Physics-Based Approaches for Neutral Density Specification and Uncertainty Quantification through Data Assimilation

by

Nicholas A. Dietrich

B.A., University of Florida, 2019

M.S., University of Colorado Boulder, 2022

A thesis submitted to the

Faculty of the Graduate School of the

University of Colorado in partial fulfillment

of the requirements for the degree of

Doctor of Philosophy

Ann and H.J. Smead Department of Aerospace Engineering Sciences

2024

Committee Members:

Tomoko Matsuo, Chair

Jeffrey Anderson

Marcus Holzinger

Jeffrey Thayer

Peter Jan van Leeuwen

Dietrich, Nicholas A. (Ph.D., Aerospace Engineering Sciences)

Physics-Based Approaches for Neutral Density Specification and Uncertainty Quantification through Data Assimilation

Thesis directed by Prof. Tomoko Matsuo

The low Earth orbit (LEO) environment ($200-2000$ km altitude) is set to become progressively crowded with an ever-increasing number of satellite and launches mega-constellation launches, and orbital debris. Accurately forecasting orbit positions is necessary for avoiding collisions and is especially difficult during geomagnetic storms due to highly variable neutral density and the associated uncertainty on atmospheric drag. It is critical to improve the predictive capabilities of neutral densities by advancing scientific understanding of the ionosphere-thermosphere (I-T)'s storm-time response. However, current physics-based I-T models are inadequate due to biases and misspecified external forcing, and with gaps in neutral observations, robust observation-model integration is challenging. Data assimilation techniques seek to address these limitations by systematically synthesizing physics-based models and observations to enable a more complete depiction of the I-T system. Additionally, more work is needed to quantify storm-time neutral density uncertainties and their impact on orbit positions. This thesis develops new physics-based data assimilation capabilities for LEO neutral density to advance 1) scientific understanding of the thermosphere's storm-time response and 2) uncertainty quantification of LEO position errors due to geophysical variability.

This thesis first makes important contributions towards neutral density specification by using strongly coupled I-T data assimilation of electron density profiles (EDPs) retrieved from radio occultation (RO) observations to constrain neutral states. Dietrich et al. (2022) demonstrates the benefits of assimilated RO EDPs to reduce orbit position errors by 70%, accomplished through improved neutral density biases with estimated neutral temperature

and neutral winds. This data assimilation framework is furthermore applied to a geomagnetic storm event to reduce overall neutral density biases by 20%, including storm recovery cooling effects. A comprehensive observing system simulation (OSSE) approach also investigates RO constellation designs as a global I-T monitoring system (Dietrich et al., 2024).

The thesis second contributes to quantifying non-Gaussian neutral density uncertainties, using a new application of a particle filter framework in a reduced forcing parameter space that incorporates a physics-based I-T model. End-to-end uncertainty quantification is accomplished using a Monte Carlo approach, wherein forcing parameter uncertainties are mapped to uncertainties of neutral density. This second component of the thesis thus opens the possibility for incorporating non-linear I-T storm dynamics into atmospheric drag and orbit position uncertainties to support future orbit positioning and conjunction analysis operations.

Acknowledgements

I would like to acknowledge all the people who have helped me along my PhD journey, starting with my advisor Tomoko Matsuo. I want to thank her for the opportunity to join her group and for spurring me to carve a research path I never knew existed before coming to CU only interested in "satellites". My thanks go out to the entire Geospace Data Science Group for being such a supportive group and where I hope to have life-long friendships. At NCAR, I want to thank all the scientists and modelers for their support in working with the TIEGCM and DART software. A particular acknowledgment to Chih-Ting Hsu for her immense help at the beginning of my PhD, for answering all my naive questions, and for her continued research guidance. I also want to thank each member of my committee for their essential feedback and support in guiding this research. Lastly, I would not be here without my fantastic community of friends at CU, and the support from my family paving the PhD path.

I would like to acknowledge financial support from the NSF Career Award AGS 1848544, the NASA FINESST award 80NSSC23K1631, and the NOAA Office of Space Weather Observations (SWO), through the UCAR subaward SUBAWD00003038. I would also like to acknowledge high-performance computing support from Cheyenne and Derecho provided by NCAR's CISL.

Contents

Chapter

1 Introduction **1**

1.1 Earth's Ionosphere-Thermosphere (I-T) System 2

1.1.1 I-T Physical Processes and Neutral Density Variability 2

1.1.2 I-T Satellite Observations 8

1.1.3 I-T Physics-based, Empirical, and Data Assimilative Models 11

1.2 Data Assimilation 15

1.2.1 Ensemble (Square Root) Kalman Filter 17

1.2.2 Particle Filter 25

1.3 Thesis Goal and Objectives, and Their Significance 28

1.3.1 I-T State Specification 28

1.3.2 Neutral Density Uncertainty Quantification 31

1.3.3 Significance of Thesis Goal and Objectives 32

2 Evaluating Radio Occultation Constellation Designs using Observing System Simulation Experiments (OSSEs) for Ionospheric Specification **33**

2.1 Background and Motivation 33

2.2 Approach 36

2.2.1 Data Assimilation: DART-TIEGCM 37

2.2.2 Nature Run (Truth) Model: WAM-IPE 38

2.2.3 Virtual Constellations 38
2.2.4 Experiment Set-up 43
2.3 OSSE Results 45
2.3.1 OSSE Ionospheric Results 45
2.3.2 Ranking Metric 52
2.3.3 Observation Performance Limit 54
2.4 Discussion 56
2.5 Conclusions 61

3 Specifying Satellite Drag Through Coupled Ionosphere-Thermosphere Data Assimilation of Radio Occultation Electron Density Profiles **63**
3.1 Background and Motivation 63
3.2 Approach 65
3.2.1 Coupled I-T Model: TIEGCM 65
3.2.2 RO Electron Density Profile Observations 66
3.2.3 Observing System Simulation Experiment (OSSE) Set-up 66
3.2.4 Orbit Propagation 68
3.3 OSSE Results 70
3.3.1 OSSE Thermospheric Results 70
3.3.2 Direct Updates to Helium 76
3.3.3 Orbit Errors 78
3.4 Discussion 81
3.5 Conclusions 86

4 Neutral Density Reanalysis during Storm-time through Coupled Ionosphere-Thermosphere Data Assimilation **88**
4.1 Background and Motivation 88
4.2 Approach 91

4.2.1 Data Assimilation: DART-TIEGCM 91
4.2.2 Storm Experiment Period 92
4.2.3 I-T Satellite Observations 92
4.3 Ensemble Filter Experiments 94
4.3.1 Ensemble Initialization 95
4.3.2 Filter Configuration 96
4.3.3 Verification with COSMIC-2 Observation 98
4.4 Reanalysis Validation and Interpretation 101
4.4.1 Validation with GRACE-FO Observations 101
4.4.2 Comparison With TIMED-GUVI O/N_2 111
4.4.3 Analysis of Storm Recovery Using TIMED-SABER NO Observations 112
4.5 Discussion 115
4.6 Conclusions 119

5 Quantifying Storm-Time Neutral Density Uncertainties using a Physics-Based Particle Filter Framework **121**
5.1 Background and Motivation 121
5.2 Approach 123
5.2.1 Coupled I-T Model: TIEGCM 123
5.2.2 Neutral Density Observations 123
5.2.3 Particle Filter Framework 125
5.2.4 Experiment Setup 130
5.3 Results 132
5.4 Discussion 140
5.5 Conclusions 144

6 Conclusions **146**
6.1 Summary and Contributions 146

6.2 Future Work 148

Bibliography **151**

Appendix

A Glossary **170**

B Control and Experiment Ensemble Configurations for Data Assimilation Experiment Runs **172**

B.1 Chapter 2 Runs 173

B.2 Chapter 3 Runs 173

B.3 Chapter 4 Runs 173

B.4 Chapter 5 Runs 178

C Supplement to Chapter 2 **179**

C.1 Supporting Figures for Chapter 2 179

D Supplement to Chapter 4 **190**

D.1 Further Experiment Testing Diagnostics 190

D.2 Altitude Data Assimilation Impact 198

Tables

Table

2.1 List of 10 OSSEs for different base LEO satellite constellation designs. For short-hand notation, the first two digits reference the constellation altitude and the last two digits reference the constellation inclination. 40

3.1 Updated State Vectors for OSSEs. 67

4.1 Configurations for the experiment (Exp) and control (Cntrl) runs for ensemble initialization and filter configurations. 98

4.2 Fitted relaxation timescales τ using a peak time defined at UT3 on July 8th. 113

5.1 Fitted Matérn parameters for GRACE-FO observations 144

B.1 Ensemble configuration for the Chapter 2 experiment runs 174

B.2 Filter configuration for the Chapter 2 experiment runs 174

B.3 Ensemble configuration for the Chapter 3 experiment runs 175

B.4 Filter configuration for the Chapter 3 experiment runs 175

B.5 Ensemble configuration for the Chapter 4 reanalysis 177

B.6 Filter configuration for the Chapter 4 reanalysis 177

B.7 Ensemble configuration for the Chapter 5 experiment runs 178

B.8 Filter configuration for the Chapter 5 experiment runs 178

Figures

Figure

1.1 Earth's I-T System 3

1.2 Thermospheric pressure level expansion as it relates to altitude and local solar time (LST), courtesy of Thayer et al. (2023). 7

1.3 The geometry of RO sounding. (Courtesy of Chi-Yen Lin) 11

1.4 Example EDPs provided by COSMIC-1 11

1.5 Data assimilation cycle 16

1.6 Strongly coupled data assimilation 21

1.7 Particle filter framework 27

2.1 The OSSE framework used in this chapter is separated by blocks for the nature run, retrieval of synthetic observations, DART-TIEGCM cycling, and post-analysis. Data are represented by parallelograms and arrows indicate workflow direction. 37

2.2 The RO observation tangent points are shown for the full day of March 13th at 300 km altitude. Shown for the four base virtual LEO constellation configurations. 40

2.3 Standard deviations attributed to EDP observations. Shown for two constellations, 5024 and 5072, at 300 km altitude on March 13th. Standard deviations are computed from the difference between synthetic EDPs and plasma density from the WAM-IPE nature run, binning data with respect to the day of the year, constellation inclination, altitude, magnetic latitude, and solar local time. 42

2.4 Binned average fractional error due to Abel retrieval, across all local times. Shown for N_mF_2, h_mF_2 and at each EDP altitude. The black line indicates the magnetic equator. Blank regions are due to a lack of observation coverage. 44

2.5 Solar (F10.7), solar wind conditions, and geomagnetic indices (Kp and Sym-H) for the week event. Solar wind states include plasma density, n, flow speed, V, and three magnetic field components, B. Vertical lines denote the OSSE quiet and storm periods. 46

2.6 a) Shows the observation rejection rate as a function of altitude. b) Shows the daily EDP observation count for each OSSE constellation configuration, separated by latitude region. 46

2.7 Electron density shown for the nature run, control, and OSSEs 1-4 posteriors at 300 km altitude at UT01 on March 13th, the first analysis step. The middle row shows posterior states, where white points are the assimilated tangent-point observations at 300 km altitude. Bias improvement, shown on the bottom row, is illustrated with blue regions providing improvement and red regions worsening. 48

2.8 The N_mF_2 RMSE for each OSSE throughout the quiet period (left) and storm period (right). Solid lines indicate single constellation OSSEs and dashed lines indicate two constellation OSSEs. Performance is assessed compared to a no-assimilation control in the dashed black curve. 51

2.9 Comparison of electron density observations at given altitudes (200 and 400 km), with the nature run WAM-IPE state shown against the Abel retrieval, TIEGCM prior, and TIEGCM posterior states. Density heat maps are shown, with counts normalized by the max bin count for that subplot. Units are all in $10^5 cm^{-3}$. 53

2.10 OSSE ranking metric for TEC. Rankings are averaged over the quiet period defined from March 13th UT01 to March 16th UT022 and averaged over the storm period defined from March 17th UT00 to March 18th UT08. Values close to 1 indicate the best performance and values close to 10 indicate the worst performance. 53

2.11 The relationship between the latitude observation counts shown in Figure 2.6b and the ranking metrics in Appendix C Figures C.12. Again noting that 1 indicates the best ranking and 10 indicates the worst ranking. All show a negative correlation (improvement with more observations) except for 200 km at low latitudes. 55

2.12 OSSE N_mF_2 RMSE fractional improvement over the control as a function of observation count, defined in Equation 2.3. Calculated for the entire N_mF_2 grid RMSE within each latitude band. Mean improvement (black dots) and notched box plots are averaged over count bins of all samples (grey dots). Non-overlapping shaded regions indicate the significant difference between medians (5% confidence). 56

2.13 Highlighting two EDPs introducing poor analysis updates. Shown using the first analysis step of Constellation 5024 (same as in Figure 2.7). EDP (a) highlights poor background covariance, and EDP (b) highlights large Abel inversion error. The bottom contour plot shows the WAM-IPE electron density at 300 km, and the observation increment (red) and the TIEGCM background correlation (black). 59

3.1 The two global plots on the left show the prior neutral temperature, prior electron density, and in black the correlation structure between the electron density at an observation location (yellow and red points) and the global neutral temperature. On the right is the EDP ensemble with two highlighted members: ensemble #81 with forcing parameters higher than the means, $d_{F107} = 78, d_{HP} = 68, d_{\Phi} = 21$, and ensemble #75 with forcing parameters lower than the mean, $d_{F107} = 63, d_{HP} = 31, d_{\Phi} = 13$. This is shown for two observations close to the equatorial ionization anomaly with one above the F2 peak at 400 km (top left) and one below the F2 peak at 250 km (bottom left). 69

3.2 Same as Figure 3.1. Observations are at longitude -10 deg and latitude -42.5 deg and priors are at UT01 on June 23rd, 2008. 69

3.3 Global RMSE for the top third pressure levels for experiments 1-3. Shown for neutral states for (a) neutral temperature, (b) neutral density, (c) helium, and (d) the neutral wind magnitude. Experiment posterior errors against truth shown in solid darker colors, and experiment prior errors shown in dashed lighter colors. Improvements are assessed in RMSE reduction over the control (black lines). Pressure levels correspond to altitudes $300 - 530$ km. 71

3.4 RMSE at each pressure level, shown in altitude, for (a) neutral temperature, (b) neutral density, (c) helium, and (d) neutral winds at UT04 on (1) June 23rd and (2) June 24th. Posterior and prior errors calculated against the truth for all three experiments are compared against control errors. 75

3.5 RMSE at each pressure level, shown in altitude, for (a) helium and (b) neutral winds at UT22 on (1) June 23rd and (2) June 24th. Posterior and prior errors calculated against the truth for all three experiments are compared against control errors. 75

3.6 Global neutral density states for the truth and experiment 1 prior bias at 500 km altitude for the first 10 hours of the OSSE period. The top rows show the truth state and the bottom rows show the experiment bias defined as the experiment prior minus the truth. Champ orbit tracks are plotted on top truth plots and EDP locations from COSMIC 1 RO are plotted on the bottom bias plots. 76

3.7 Helium mixing ratio over the south pole for the truth and experiment 1 prior bias at 500 km altitude for every fifth hour of the OSSE period. Same experiment bias as in Figure 3.6 with champ orbit tracks and COSMIC 1 RO tangent points. 77

3.8 Global helium mixing ratio for the truth and experiment 4 prior bias at 500 km altitude, shown for every fifth hour. Same experiment bias as in Figure 3.6 with champ orbit tracks and COSMIC 1 RO tangent points. Experiment 4 performs direct updates to helium compositions. 78

3.9 In-track orbit errors against the truth over the two-day OSSE period for the first three experiments, the control and the control with a 10% C_D error (left). Fractional error improvement of each experiment over the control for the two-day OSSE period (center). Extrapolated in-track orbit errors extended by 7 days (right). 80

3.10 Neutral densities sampled along the simulated orbit path from the truth, control, and experiment 1 prior. Shown for June 23rd and 24th. 80

3.11 Probability histogram of ensemble sample correlations between N_mF_2 and h_mF_2 to neutral temperature (left) and helium (right) along nearest pressure level of model grid. Computed with the prior ensemble at UT01 on June 23rd with all assimilated EDPs for that hour. 82

4.1 Solar irradiance (F10.7), solar wind IMF parameters, and geomagnetic indices (Kp and SYM-H) for the reanalysis period. Solar wind IMF parameters include plasma density, n, flow speed, V, and the three magnetic field components, B_x, B_y, and B_z. Lighter color lines indicate perturbations used to initialize the TIEGCM ensembles. Vertical lines denote phases of the reanalysis and indicate the three storm phases: initial, main, and recovery. 93
4.2 Experiment forecast reject rate performance for COSMIC-2 EDPs 99
4.3 Experiment Forecast RMSE Performance 100
4.5 GRACE-FO Neutral Density Comparison 103
4.6 GRACE-FO Neutral Density Latitude Mean 105
4.7 GRACE-FO TIEGCM COSMIC-2 Dawn-Dusk Correlation Comparisons . . 107
4.8 GRACE-FO Keogram (Dusk) compared with Control and Reanalysis 108
4.9 Along-track ensemble scale height correlations to neutral temperature and mean molecular mass 110
4.11 TIMED-GUVI O/N_2 comparison 112
4.13 Fitted relaxation timescales for each latitude, separated by dawn and dusk sides at GRACE-FO locations. Peak time defined at UT3 on July 8th. . . . 115
4.14 Normalized neutral temperature spreads, shown along two pressure levels (∼128 km and ∼539 km altitude) along the GRACE-FO orbit track. The orbit average mean is shown in darker lines. Shown for the control Cntrl_* and reanalysis $\text{Exp}_{*-Storm}$. 118

5.1 Correlations between the GRACE-FO neutral density observations and the observed F10.7 and Ap indices for July 2022. Fitted using the daily average of observations for F10.7 and the 3-hour average for Ap. Correlations are binned by latitude and solar local time (LT) for dawn (6 LT) and dusk (18 LT).124
5.2 Forcing parameter particle filter framework 127

5.3 The cycle of the forcing parameter particle filter. Not pictured are the corresponding TIEGCM states, that are propagated in the time update from their associated parameters. The TIEGCM states are additionally sorted in the reassignment step. (Inspired by Van Leeuwen (2009)). 129
5.4 Observed F10.7 and Kp indices over the week in July 2022. 131
5.5 Starting forcing parameter distribution used to initialize the particle filter. Particles are sampled from a Gamma distribution fitted for the 2022 indices, sampled using a Coupla draw with a correlation of 0.03. 132
5.6 Quiet period particle filter estimation of neutral density at GRACE-FO locations. Shows GRACE-FO observations (black), the weighted mean estimates (red), and individual particles with respective weights (shades of blue). Darker shades of blue indicate greater particle weight. The top panel shows the quiet period first half and the bottom panel shows the second half, with a noted difference in the y-axis scales. 133
5.7 Weights of particles with corresponding F10.7 and Ap weights for the quiet period running. The size of particles indicates their relative weight, and the magenta dot is the weighted mean. Shown for posterior estimates at the end of the 6-hour cycle. 134
5.8 Rank histogram for the quiet period showing particle spread relative to observations, separated by the dawn-dusk sides. 135
5.9 Same as Figure 5.6 for the storm period at 3-hour cycling. The top panel shows the storm period first half and the bottom panel shows the second half. Darker blue shades indicate greater relative particle weight. 136
5.10 Same as Figure 5.6 for the storm period at 1-hour cycling and increased stochastic forcing. The top panel shows the storm period first half and the bottom panel shows the second half. Darker blue shades indicate greater relative particle weight. 138

5.11 Storm period for particle time-series with corresponding $\mathbf{d}_{F107^*}$ and $\mathbf{d}_{Ap^*}$ weights. Shown for 3-hour cycling and increased Ap stochastic dynamics with select parameter distributions. 139

5.12 Storm period for particle time-series with corresponding $\mathbf{d}_{F107^*}$ and $\mathbf{d}_{Ap^*}$ weights. Shown for 1-hour cycling and increased Ap stochastic dynamics with select parameter distributions. 139

5.13 Rank histogram for the storm period showing particle spread relative to observations. Includes (a) 3-hour cycling and (b) 1-hour cycling, separated by the dawn-dusk sides. 140

5.14 Select posterior neutral density PDFs along GRACE-FO orbit locations, shown from the quiet period with 6-hour cycling (a-b) and the storm period with 1-hour cycling (c-d) experiments. Contains particles with their respective weights and normalized PDFs for a fitted Gaussian distribution. 141

5.15 Fitted empirical semivariogram for GRACE-FO neutral density observations, split by dawn and dusk local time and quiet and storm periods. Points represent semivariogram values and solid lines indicate the Matérn fit. 145

C.1 Same as Figure 2.3 in Chapter 2, shown instead for bin counts used to calculate standard deviation. 179

C.2 Binned average fractional error due to Abel Retrieval, across local times $10-16$. Shown for NmF2, hmF2 and at each EDP altitude, and black line indicates the magnetic equator. Blank regions are due to lack of observation coverage. 180

C.3 Same as Figure C.2, shown for local times $16-22$ 181

C.4 Electron density shown for the truth, control, and OSSEs 1-4 posteriors at 300 km altitude at UT 20 on March 17th, during the storm period. The middle row shows posterior states, where white points are the assimilated tangent-point observations at 300 km altitude. Bias improvement, shown on bottom row, is illustrated with blue regions providing improvement and red regions worsening. 182

C.5 The TEC RMSE for each OSSE throughout the quiet period (left) and storm period (right). Solid lines indicate single constellation OSSEs and dashed lines indicate two constellation OSSEs. Performance is assessed compared to a no-assimilation control in the dashed black curve. 182

C.6 The h_mF_2 RMSE for each OSSE, same as Figure C.5. 183

C.7 The 200 km electron density altitude RMSE for each OSSE, same as Figure C.5. 183

C.8 The 300 km electron density altitude RMSE for each OSSE, same as Figure C.5. 184

C.9 The 400 km electron density altitude RMSE for each OSSE, same as Figure C.5. 184

C.10 The 500 km electron density altitude RMSE for each OSSE, same as Figure C.5. 185

C.11 Comparison of electron density observations at given altitudes (300 and 500 km), with the true IPE state shown against the Abel retrieval, TIEGCM prior and TIEGCM posterior states. Density heat maps are shown, with counts normalized by the max bin count for that subplot. Units are all in $10^5 \#/cm^3$. 185

C.12 OSSE ranking metric for each electron density altitude. Contains quiet period defined from March 13th UT 01 to March 16th UT 22 and storm period defined from March 17th UT 00 to March 18th UT 08. Values of 1 indicate the best performance and values of 10 indicate the worst performance. 186

C.13 Same as Figure C.12, shown for N_mF_2. 187

C.14 Same as Figure C.12, shown for h_mF_2. 187

C.15 OSSE TEC RMSE fractional improvement over the control as a function of observation count, defined in Equation 2.1 Calculated for the entire TEC grid RMSE within each latitude band. Gray points are all samples and averaged over count bins to give the mean (black dots) and notched box plots. Shaded regions not overlapping indicate the significant difference between medians (5% confidence). 187

C.16 Same as Figure C.15, shown for h_mF_2. 188

C.17 Highlighted poor EDP observation update, with scatter showing the observation EDP and grids showing IPE electron density at that given altitude. RO EDP tangent points are quasi-vertical, with higher altitude tangent points moving into higher density regions, creating a double-peaked structure. . . . 188

C.18 GNSS ray passes for profiles (a) and (b) highlighted in the Discussion Figure 13. Black points are the RO tangent point locations and red shaded area are the occultation ray paths below the orbit height of the receiving RO satellite. 189

D.1 Locally averaged quiet period (UT01 on July 5th) correlations shown from electron density to neutral temperature. Each point shows the average correlation within a distance of 40°. Shown for a pressure surface about ∼400 km altitude. 190

D.2 Locally averaged storm period (UT01 on July 8th) correlations shown from electron density to neutral temperature. Each point shows the average correlation within a distance of 40°. Shown for a pressure surface about ∼430 km altitude. 191

D.3 Forecast COSMIC-2 EDP verification diagnostics shown for the control ($\text{Cntrl}_{*-\nu}$) and reanalysis ($\text{Exp}_{*-\nu}$). Includes the time series of RMSEs, outlier rejection rate, observation-forecast (O-F) and observation-analysis (O-A) standard deviation (std) spreads, RMSE of EDP parameters h_mF_2 and N_mF_2, and normalized standard deviation spread. 192

D.4 Rank histogram of control run Cntrl_* for the quiet period, separated by local time and altitude. 193

D.5 Rank histogram of control run Cntrl_* for the quiet period, separated by altitude and latitude. 193

D.6 Keogram of the dawn-side GRACE-FO neutral densities, Cntrl_*, and forecast $\text{Exp}_{*-Storm}$ states. Plotted with latitude slices with time moving to the left. . 194

D.7 GRACE-FO, control and reanalysis neutral density comparison for the quiet period, with the reanalysis beginning at UT01 on July 5th. Smoothed ±45 minutes. 194

D.8 Fast Fourier Transform (FFT) GRACE-FO, TIEGCM control (Cntrl_*), and TIEGCM reanalysis (Exp_*) for the full experiment period. Shown for the absolute value of frequency magnitudes. Vertical lines denote selected frequency peaks, with their corresponding period (in hours). The bottom plot shows the difference between the GRACE-FO FFT to the control and reanalysis FFTs. 195

D.9 GRACE-FO bias improvement metric defined in Equation 4.2, using the control (Cntrl_*) and reanalysis ($\text{Exp}_{*-Storm}$). Shown for magnetic latitude and separated by dawn and dusk LT sides. 195

D.10 TIEGCM control and reanalysis NO composition (in mixing ratio) at NO peak cooling altitudes, shown at TIMED-SABER observation locations. . . . 196

D.11 Rank histogram of an inflation run for the quiet period, separated by local time and altitude. Includes EDP assimilation. 196

D.12 GRACE-FO, control and experiment neutral density comparison for the storm period, using adaptive inflation to inflate plasma and neutral temperature states. Smoothed ±45 minutes. 197

D.13 Rank histogram following adding direct state perturbations to atomic oxygen and neutral density. Control TIEGCM run. Separated by latitude and altitude. Shown for the quiet period from UT01-UT04 on July 5th. 197

D.14 COSMIC-2 rejection rate profile following adding direct state perturbations to atomic oxygen and neutral density. Shown for a control TIEGCM run and is separated by day and night local times. Shown for the quiet period from UT01-UT04 on July 5th. 197

D.15 Neutral temperature data assimilation difference between the prior (forecast), ($\mathrm{Exp}_{*-Storm}$), and control, (Cntrl_{*}). Shown for neutral temperature magnitude for vertical pressure levels along GRACE-FO track locations. 199

D.16 Same as Figure D.15, normalized by the mean neutral temperature. 199

D.17 Same as Figure D.15, shown for posterior (analysis) and prior (forecast) difference, showing the analysis step impact 199

Chapter 1

Introduction

The low Earth orbit (LEO) environment ($200 - 2000$ km) is set to become increasingly crowded with more satellite and mega constellations launches, and orbital debris. Effectively monitoring and forecasting LEO satellite positions is most affected by orbit position uncertainties arising from satellite drag errors. Quantifying atmospheric drag uncertainties is especially pertinent for assessing conjunction alerts, or when two satellites' positions pass some threshold for probability of collision. The atmospheric drag force, $\mathbf{a}_{drag}$, is defined as

$$\mathbf{a}_{drag} = -\frac{1}{2} C_D \frac{A}{M} \rho v \boldsymbol{v} \tag{1.1}$$

where $\boldsymbol{v} = \boldsymbol{v}_s - \boldsymbol{w} - \boldsymbol{\Omega}$ is the satellite velocity vector, $\boldsymbol{v}_s$, relative to the atmosphere velocity, $\boldsymbol{w}$, $\boldsymbol{\Omega}$ is the co-rotation velocity, v is the velocity magnitude, C_D is the drag coefficient, $\frac{A}{M}$ is the area-to-mass ratio and ρ is the neutral mass density. The mass density of the neutral gas constitutes the thermosphere. It is the primary source of uncertainties for atmospheric drag, and various internal processes and external forcings of the upper atmosphere control its variability. This chapter provides an overview of the LEO upper atmosphere environment, currently available satellite observations, and the data assimilation (DA) approaches used in the thesis.

1.1 Earth's Ionosphere-Thermosphere (I-T) System

1.1.1 I-T Physical Processes and Neutral Density Variability

Earth's upper atmosphere (>100 km altitude) represents the region with growing specification and forecasting needs, as more ground- and space-based technologies are dependent on the knowledge of upper atmospheric states and how they are impacted by space weather. The thermosphere lies above the turbopause ($\sim$ 100 km) where the turbulent mixing of the lower and middle atmosphere ends and individual species start to experience molecular diffusion according to their respective scale heights. The thermosphere extends vertically into the exosphere ($\sim$ 600 km) where the temperature reaches an asymptotic exospheric value. Incoming solar irradiance, primarily in the form of x-ray and ultraviolet (UV) radiation, heats and photoionizes the neutral gas, along with triggering other ionization processes, to create the weakly ionized plasma region known as the ionosphere that overlaps with the thermosphere. The ionosphere-thermosphere (I-T) system is strongly coupled through ion-neutral collisions. Capturing the variability of the I-T system requires understanding both internal processes and external forcing that occur across a multitude of scales. A schematic of the I-T system and its sources of variability is illustrated in Figure 1.1.

The thermospheric neutral mass density, ρ, here referred to as simply the neutral density, is well described by the ideal gas law,

$$\rho = \frac{P\bar{M}}{k_B N_A T n} \tag{1.2}$$

where Tn is the temperature, P is the pressure, $\bar{M}$ is the mean molar mass, k_B is the Boltzmann constant and N_A is the Avogadro constant. For time scales longer than 10 minutes, hydrostatic equilibrium can be assumed. The vertical profile of individual molecular species follows the balance between the gravity and pressure-gradient forces,

$$\frac{dP_i}{dz} = -\rho_i g(z) \tag{1.3}$$

where P_i is the partial pressure of species i, and $g(z)$ is the gravitational constant. Major

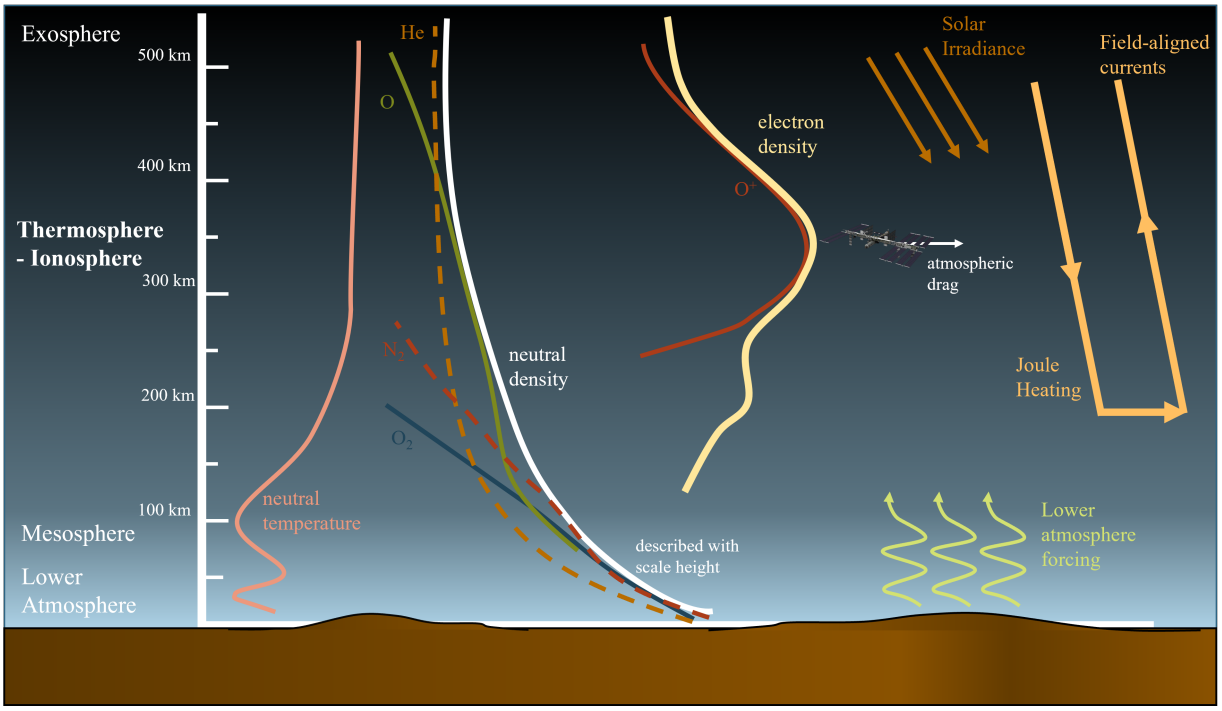

Figure 1.1: Diagram of Earth's I-T system showing vertical profiles of the neutral and plasma states, as well as sources of external forcing that influence state variability.

species of the thermosphere include atomic oxygen (O), molecular oxygen (O_2), helium (He), and nitrogen (N_2). Applying the hydrostatic equilibrium with the ideal gas law yields the neutral density profile of individual species:

$$\rho_i(z) = \rho_i(z_0) \exp\left[- \frac{z - z_0}{H_i} \right] \tag{1.4}$$

where $\rho(z)$ is the neutral density at height z from a reference height z_0, and the individual scale height, H_i, is:

$$H_i = \frac{k_B T n(z)}{m_i g(z)} \tag{1.5}$$

where m_i is the individual species mass. We can additionally define the mean scale height, H, as

$$H = \frac{k_B T n(z)}{\bar{m} g(z)} \tag{1.6}$$

where $\bar{m}$ is the mean molecular mass. Commonly Equation 1.4 can be used with H to determine the altitude profile of the total neutral density ρ. Characterizing the vertical profile of neutral temperature and individual molecular species is useful in determining the neutral density via its vertical integration (Emmert, 2015). The vertical profile of neutral temperature can be approximated with the vertical energy equation:

$$\frac{\partial Tn}{\partial t} = -w\Big(\frac{\partial Tn}{\partial z} + \frac{g}{c_p}\Big) - \frac{1}{\rho c_p}\frac{\partial}{\partial z}\Big(\lambda_n \frac{\partial Tn}{\partial z}\Big) + \frac{1}{\rho c_p}\Sigma\dot{Q} - \frac{1}{\rho c_p}\Sigma\dot{L} + \text{other terms} \tag{1.7}$$

where w is the vertical wind, c_p is the specific heat per unit mass, λ_n is the thermal conduction coefficient, $\dot{Q}$ specify sources of heat flux and $\dot{L}$ specify sources of heat loss flux. The respective terms in this heat equation are (1) adiabatic heating and cooling due to neutral winds, (2) molecular heat conduction, (3) diabatic heating and (4) cooling. General circulation models (GCMs) solve a set of three-dimensional primitive equations (Schunk and Nagy, 2009) along with this equation containing other terms including processes such as horizontal advection and eddy mixing. A steady state solution to Equation 1.7 assuming only heat conduction and diabatic heating and cooling yields the Bates temperature profile (Bates, 1959).

The ionosphere is created through the photoionization of the neutral gas by incoming solar irradiance, and is strongly coupled with the neutral temperature and composition. The balance of plasma production and loss processes defines the resulting Chapman profile (Chapman, 1931), a steady-state solution dependent on the neutral scale height. The neutral scale height is a key factor in describing this structure, determining the altitude profiles of ionization and recombination rates. A prominent feature of the ionosphere is the F-region ($200 - 500$ km) that is dominated by O^+ ions and defined by the peak electron density, N_mF_2, and its height, h_mF_2. Diffusion and transport effects influence the top-side F-region O^+, and the bottom-side F-region is influenced by photochemical processes. These bottom-side plasma layers, the D- ($60 - 100$ km) and E-regions ($100 - 150$ km), are primarily controlled by chemical processes. The bottom-side layers disappear during the night through recombination, while F-region plasma largely persists through the night due to the lower recombination rate. Neutral states further influence plasma states through recombination rates that depend on both neutral temperature and the relative ratio of O and N_2 compositions, commonly described with the O/N_2 ratio (Danilov, 2013). Additional coupling processes include meridional neutral winds moving plasma up and down magnetic field lines at mid-latitudes and neutral wind dynamo electric fields causing plasma drifts (Schunk and Nagy, 2009; Kelley, 2009).

The I-T system variability is impacted by external forcing that originates from three primary sources: solar irradiance in the form of x-rays and extreme ultraviolet (EUV), high-latitude energy input from the magnetosphere resulting from its interactions with solar winds, and atmospheric wave forcing from below (shown in Figure 1.1). Solar irradiance in the EUV range deposits energy around $120 - 160$ km altitude, and has global-scale impact as the primary driver for I-T variability (Robie, 1993; Solomon and Qian, 2005). The F10.7 index is a widely used proxy for the incoming EUV flux, a daily index for the radio flux at the 10.7 cm wavelength (Tapping, 2013). The quantity of incoming EUV greatly varies by a factor ~ 2 over the 11-year solar cycle (Solomon and Qian, 2005). The diurnal variation of solar EUV

irradiance introduces considerable solar local time changes for I-T states. Another important contributor to the day-to-day variability of the I-T system is atmospheric wave forcing from below. These waves generated in the troposphere and stratosphere upwardly propagate and transport energy and momentum into the mesosphere and thermosphere. These waves perturb both neutral and plasma states and have multi-scale impact. The variability of I-T states introduced by lower atmospheric forcing is important during geomagnetically quiet periods, and it is not the focus of the thesis.

In contrast to quiet period variation, geomagnetic storm events introduce considerable neutral density variability on time scales from hours to days, dramatically changing thermospheric states that increase atmospheric drag uncertainties. The enhanced interaction between the solar wind and Earth's magnetosphere, for example, following a coronal mass ejection, results in the deposition of large quantities of energy along geomagnetic fields into the I-T system at the polar latitudes (Prölss, 2011). Some relevant solar wind parameters include the plasma density, velocity as well as the magnetic field magnitude and orientation. The contribution of strong geomagnetic storms can be upwards of two-thirds of the upper atmospheres' energy budget during geomagnetically active periods (Knipp et al., 2004) and has complex impacts on I-T variability (Thayer and Semeter, 2004). The solar wind-magnetosphere interaction drives the convective electric fields as well as high-energy charged auroral particle precipitation at high latitudes. The increased electric field convection enhances frictional heating, transferring momentum and energy from plasma to neutrals and heating the neutral gas (Prölss, 1996). This heating at high latitudes produces a global adiabatic expansion of the neutral gas, which manifests as an expansion of constant pressure surfaces defined by the scale height. Additional upwelling of the neutral gas occurs with neutral wind divergence uplifting heavier molecular species (Rishbeth et al., 1987), as well as strengthening of equatorward meridional winds that globally alters the circulation of molecular compositions (Buonsanto et al., 1990). These storm-time neutral wind circulations from high to low latitudes exhibit solar local time dependence due to background quiet

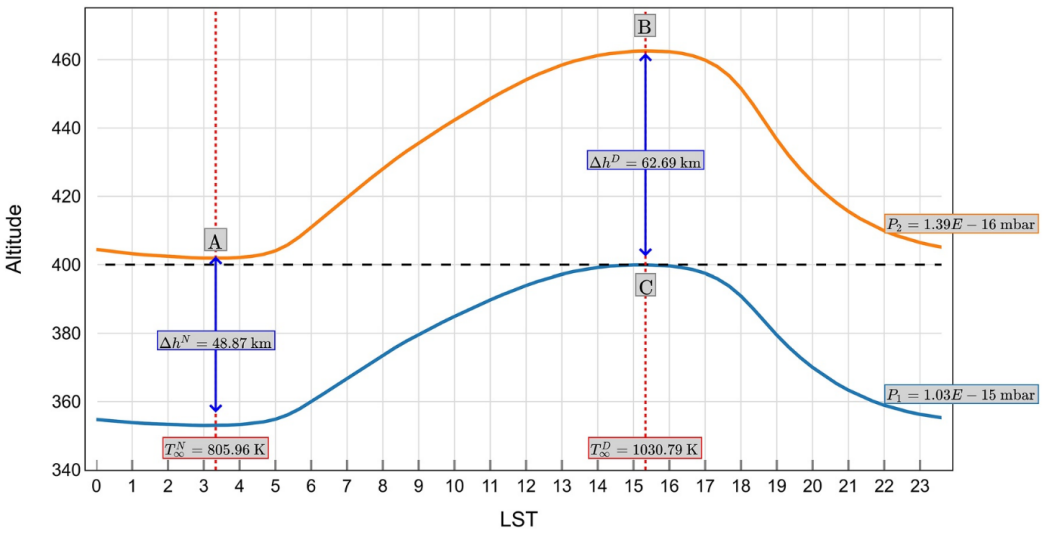

Figure 1.2: Thermospheric pressure level expansion as it relates to altitude and local solar time (LST), courtesy of Thayer et al. (2023).

wind structures (Fuller-Rowell et al., 1994). Geomagnetic activity is well depicted using the Kp index, a 3-hour, quasi-logarithmic index calculated using ground-based magnetometers around the globe. The Ap index is equivalent in a linear scale and other commonly used geomagnetic indices include the Dst index and SYM-H index.

A representative pressure-surfaces altitude change between quiet and storm times is illustrated in Figure 1.2, courtesy of Thayer et al. (2023). LEO objects at a relatively constant altitude could pass through very different neutral density regions during geomagnetic storms, considerably affecting their orbit positions.

Neutral density furthermore undergoes distinctive post-storm recovery processes to restore the thermosphere to its pre-storm states. Primary recovery-phase cooling processes include downward thermal heat conduction due to increased vertical gradients in temperature, and greater NO cooling of post-storm upper atmosphere (Maeda et al., 1992). These processes are represented by terms (2) and (4) respectively in Equation 1.7. NO cooling has been described as a "natural thermosphere thermostat" for the neutral gas and plays a critical role in introducing global cooling effects(Mlynczak et al., 2003; Knipp et al., 2017;

Zesta and Oliveira, 2019). This NO infrared cooling is driven by increases in NO production that persists throughout the storm period (Barth, 1992). From Kockarts (1980), the NO cooling term can be formulated in terms of the NO density, $n(NO)$, temperature, Tn, and chemical reaction rates as

$$L_{NO} = hv_0 n(NO_{v=0}) A_{10} \frac{g_1}{g_0} \times \exp\Big(-\frac{hv_0}{k_B Tn}\Big) \tag{1.8}$$

where h is the Planck's constant, $v_0 = c/\lambda_0$ is the frequency with c as the speed of light and $\lambda_0 = 5.3\mu$m, A_{10} is the transition probability of $NO_{v=1} \rightarrow NO_{v=0} + hv_0$, and g_1/g_0 represent the quenching of vibrationally excited NO by O, O_2 and N_2, with constants reported in Murphy et al. (1975); Hwang et al. (2003).

The changes in the temperature and compositions are affected by various fundamental I-T physical processes that give rise to the neutral density variability (e.g., Equations 1.2 and 1.5) (Prölss, 2012; Lei et al., 2010). The thesis is motivated to further advance understanding of the specific roles of storm-time I-T physical processes in causing storm-time neutral density variability.

1.1.2 I-T Satellite Observations

Observations of the upper atmosphere provide direct information on neutral and plasma states critical for understanding I-T fundamental processes. The thesis utilizes some of the currently available observations of neutral states as well as observations of plasma states from satellite observing systems.

Neutral state observations are generally limited in terms of the spatial and temporal coverage required to fully address pressing science questions related to neutral density variability. Existing neutral observations infrequently overlap, making them difficult to calibrate (Bruinsma et al., 2023). Neutral density observations are primarily derived from onboard accelerometers or precise orbit determination (POD). These observations are restricted to the satellite orbit track and available only during the lifetime of research missions, such as

CHAMP, GRACE, GRACE-FO, and Swarm (Sutton et al., 2007; van den IJssel et al., 2020; Mehta et al., 2017). Present time neutral density observations come from GRACE-FO's onboard accelerometer (March et al., 2021) and ESA Swarm's Global Navigation Satellite Systems (GNSS) positioning (van den IJssel et al., 2020). Satellite two-line elements (TLEs) are widely and routinely available; however, the derived neutral density information is integrated over space and time. A limited amount of neutral temperature information is available. GOLD (Eastes et al., 2017) provides altitude-integrated temperature information on the dayside disk. ICON (Immel et al., 2018) observes temperatures along the limb to give altitude profiles, around $100 - 150$ km altitudes, largely below LEO altitudes. ICON-MIGHTI (Immel et al., 2018) additionally provides altitude profiles of neutral winds from $\sim 90 - 300$ km on the dayside at most low-to mid-latitude locations. For compositions, remote sensing observations by ICON, GOLD, and TIMED (Immel et al., 2018; Eastes et al., 2017; Christensen et al., 2003) come mainly in the form of height integrated atomic oxygen to molecular nitrogen ratios (O/N_2), with a modest number of altitude profiles from ICON. TIMED-SABER (Esplin et al., 2023) provides profile information on NO cooling rates (Mlynczak, 1997) and NO densities (Wang et al., 2024). For lighter species such as helium, composition observations are severely restricted. Helium has been directly measured with in-situ mass spectrometers from the Atmospheric Explorer (AE) satellites (Pelz et al., 1973). There have not been any publicly available observations since the last AE missions in the early 1980s. Therefore, because of the sparse distribution and limitations in these available neutral observations, alternative methods are proposed in the thesis to specify the thermospheric states globally.

In contrast with the thermosphere, the ionosphere has a wealth of plasma observations that enable global specification. The thesis specifically leverages plasma observations from radio occultation (RO). GNSS constellations are designed for global positioning, combined with receivers on LEO platforms, enabling RO observations with global coverage of the ionosphere. Currently available GNSS constellations include GPS, GLONASS, Galileo,

and BeiDou. The development and operation of RO satellite constellations in LEO have considerably grown over recent decades, providing real-time monitoring of ionospheric space weather and supporting scientific studies of ionospheric physics. Earth-based RO constellations began in 1995 with the launch of MicroLab-1 Global Positioning System/Meteorology (GPS/MET) (Hajj and Romans, 1998; Kursinski et al., 1997), and was succeeded in 2006 by the FORMOSAT-3/COSMIC (F3/C) (Anthes et al., 2008) and its follow-on mission FORMOSAT-7/COSMIC-2 (F7/C2) (Yue et al., 2014b; Fong et al., 2019) in 2019. F3/C consisted of a 6-satellite low Earth orbit (LEO) constellation, orbiting in separate orbital planes, each at 72° latitude and 800 km altitude. RO observation counts of F3/C were doubled with the launch of the more recent F7/C2, a 6-satellite constellation in a similar orbit configuration at 24° inclination and 550 km altitude. Commercial RO sources have additionally grown to include satellites and constellations in near-polar orbit (e.g., Angling et al., 2021), promoting their use within data assimilation experiments quantifying their benefit, i.e., RO Modeling EXperiment (ROMEX) (Anthes et al., 2023). In addition to their well-recognized and valuable role as an observing system for ionospheric plasma density, recent physics-based data assimilative modeling studies Matsuo and Hsu (2021); Dietrich et al. (2022) suggest their utility as a global monitoring system of thermospheric mass density.

The slant TEC (sTEC) is measured along the radio signal's limb-sounding geometry connecting the GNSS satellite and the observing LEO satellite during an RO sounding. Electron density profiles (EDPs) are retrieved from these sTEC observations at the ray tangent point locations through Abel inversion. This inversion relies on a spherical symmetry assumption. A diagram of an EDP retrieval is shown in Figures 1.3 and 1.4 along with example sounding paths from GNSS satellites to LEO RO satellites used to generate sTEC profiles. For a typical RO sounding there is an occultation side and an auxiliary side, where the auxiliary side passes through both the upper ionosphere and plasmasphere, and the occultation side passes through the ionosphere, atmosphere, and plasmasphere. The resulting calibrated sTEC profile comes from subtracting the auxiliary side TEC profile from

the occultation side TEC profile and contains only the ionosphere plasma. EDPs are then retrieved by applying Abel inversion to the calibrated sTEC profiles. RO EDPs are highly accurate observations of the ionosphere's F-region, especially for F_2 region parameters N_mF_2 and h_mF_2 (Cherniak et al., 2021; Yue et al., 2010; Lei et al., 2007). Relatively large errors can exist for low altitudes, i.e., the E-region below 200 km altitude (Kelley et al., 2009). Sizable RO EDP errors are also reported where there are breakdowns in the spherical symmetry assumption such as near equatorial latitudes (Tsai et al., 2001; Tsai and Tsai, 2004) and beneath the crests of the equatorial ionization anomaly (EIA), peaking at 200% (Liu et al., 2010; Yue et al., 2010). Recent algorithm improvements to the Abel inversion retrieval are aided by the use of prior ionosphere information (e.g., Yue et al., 2013a; Pedatella et al., 2015; Chou et al., 2017; Lin et al., 2020; Tulasi Ram et al., 2016). A bottom-up retrieval approach has been proposed for the D- and E-regions (Wu, 2018).

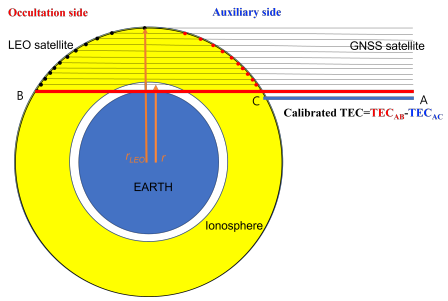

Figure 1.3: The geometry of RO sounding. (Courtesy of Chi-Yen Lin)

Abel Inversion

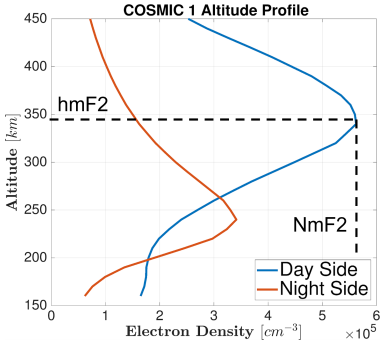

Figure 1.4: Example EDPs provided by COSMIC-1

1.1.3 I-T Physics-based, Empirical, and Data Assimilative Models

The upper atmosphere sits within an intermediary region influenced by both external and internal processes. Thus to model the upper atmosphere, both internal processes dependent on initial conditions and external forcing need to be considered. Different I-T models have been developed to specify and/or forecast the upper atmosphere state.

Commonly, empirical models are relied upon to provide neutral density states for orbit determination. These models include the Mass Spectrometer Incoherent Scatter radar (MSIS) global reference atmospheric model (Picone et al., 2002; Emmert et al., 2021; Brandt et al., 2020), the Jacchia-Bowman upper atmosphere density model (JB2008) (Bowman et al., 2008), and the semi-empirical Drag Temperature Model (DTM)(Bruinsma, 2014). The High Accuracy Satellite Drag Model (HASDM) is the leading standard for neutral density data (Storz et al., 2005), using satellite calibration data to correct JB2008. Nevertheless, while some HASDM neutral density data has been made available (Tobiska et al., 2021), the calibration data has not been made public. These neutral density models are limited in the underlying physical description; for example, JB2008 and HASDM lack composition and temperature information. While these empirical models generally perform well, specifying neutral density variability during changing solar activity and geomagnetic conditions remains a problem (Bruinsma et al., 2021).

Compared to empirical models, physics-based models can comprehensively model neutral density through changing solar and geomagnetic conditions, describing the time-variation of all relevant atmospheric states. Physics-based models have the potential to improve capabilities for neutral density forecasting and are vital for advancing scientific understanding of the I-T storm-time response. One of the widely used physics-based models of the I-T system is the Thermosphere Ionosphere Electrodynamics General Circulation Model (TIEGCM) developed by the High Altitude Observatory (HAO) at the National Center for Atmospheric Research (NCAR) (Richmond et al., 1992; Qian et al., 2014). The TIEGCM produces a three-dimensional, time-varying field of the thermosphere and ionosphere systems using a self-consistent solution to first-principle equations. The TIEGCM spans much of the relevant LEO altitudes, extending from approximately ~ 97 km to $\sim 500 - 600$ km. Solar irradiance in the TIEGCM is controlled by a solar proxy model driven by specifying the F10.7 index (F107). Magnetospheric input can be specified using the Heelis model (Heelis et al., 1982), controlled by hemispheric power (HP) and cross-polar cap potential (Φ), or using the Weimer

model (Weimer, 2005), controlled by interplanetary magnetic field (IMF) solar wind parameters. The TIEGCM is run with either a 5-degree or 2.5-degree resolution for computation feasibility using TIEGCM v2.0. The noteworthy states the TIEGCM solves are the neutral states for neutral temperature, zonal and meridional winds, species N_2, O_2, O and He as well as plasma states O^+ and electron density. Still, physics-based models are limited with gross model-observation biases due to either simplified parameterization of fundamental processes, mis-specified external forcing parameters, or incomplete physical description. For example, Lu et al. (2014) have shown modeled neutral density biases that worsen when comparing higher altitude observations. Other modeling work has shown storm recovery time scales to be too slow, which is attributed to improper NO cooling (e.g., Lei et al., 2011; Lu et al., 2014; Sheng et al., 2017; Li et al., 2019). In addition, there are known day-night neutral density biases (Waldron, 2020; Thayer et al., 2023).

DA can improve the capability of physics-based models by constraining initial conditions and forcing parameters using observations. With a limited number of available neutral observations, it is feasible to estimate a small number of the forcing parameters in physics-based models. This idea has been attempted in past studies through either estimating solar forcing parameters (Morozov et al., 2013) or both solar and geomagnetic forcing parameters (Codrescu et al., 2018; Sutton, 2018; Sutton et al., 2021) using satellite-derived neutral density observations and resulted in the removal of gross neutral density model biases. Major neutral compositions such as O and N_2 have also been estimated by using forcing parameters (Codrescu et al., 2004). Even with a limited amount of neutral observations, large numbers of state variables in physics-based models can be estimated as attempted by Minter et al. (2004); He et al. (2023). Additional corrections using satellite position data have also been performed (Gondelach and Linares, 2021). The effectiveness of these DA approaches is nonetheless hindered by a shortage of neutral observations that have sparse coverage or are time-integrated. Matsuo et al. (2013) have demonstrated the challenges in estimating both solar forcing parameters, temperatures, and compositions with sparse neutral observations,

as well as the potential use of global ionospheric observations to infer neutral temperatures and compositions. Follow-on work to Matsuo et al. (2013) has shown the direct estimation of neutral state with ionospheric observations to be effective for both solar minimum and solar maximum conditions (Kodikara et al., 2021).

Accurately quantifying neutral density uncertainties through modeling is especially critical as LEO becomes crowded with more objects, with the potential of conjunction alerts to easily outpace space domain awareness (SDA) operators' capabilities(Berger et al., 2020). Operationally, conjunction assessment assumes Gaussian position errors that greatly ease computational costs over more intensive Monte Carlo calculations NASA (2020). Previous work has quantified Gaussian neutral density uncertainties using lower-dimensional models (Gondelach and Linares, 2021; Licata et al., 2022). However, non-linear storm-time dynamics should result in non-Gaussian neutral density uncertainties. Previous studies using lower-dimensional models lack these non-linear dynamics or use time-integrated observations (i.e., TLE data) that cannot represent small-scale features present during storms. On the contrary, physics-based models can be a powerful tool for providing uncertainty quantification useful to prevent satellite collisions. It is well established that orbital dynamics produce curvilinear uncertainties (Ghrist and Plakalovic, 2012), but it has not yet been investigated the impact non-Gaussian neutral densities have on orbit positioning.

In contrast with the thermosphere, the ionosphere has an abundance of plasma observations that have enabled global ionospheric specification. This has been done through empirical and physics-based data assimilative modeling as demonstrated in numerous DA studies and applications to operational systems (e.g., Bust et al., 2004; Lin et al., 2015; Hajj et al., 2004; Hsu et al., 2014; Lee et al., 2013; Scherliess et al., 2006; Schunk et al., 2005; Yue et al., 2014a; Wang et al., 2004; Reid et al., 2023; Matsuo and Araujo-Pradere, 2011; Pedatella et al., 2020). The coupling of plasma states to neutral states has not been incorporated in most of these studies in a comprehensive manner. Forecasting plasma states has been shown to only have system memory of a few hours (Jee et al., 2007; Chartier et al.,

2013; Dietrich et al., 2024). Comparatively, neutral states have a longer forecasting memory (Chartier et al., 2013) such as oxygen composition that can improve plasma forecasting (Hsu et al., 2014).

Using the TIEGCM, the thesis focuses on fully integrating neutral-plasma state coupling into a physics-based data assimilate modeling to advance understanding of neutral density variability. The thesis targets neutral density variability during geomagnetically active periods to improve satellite orbit prediction as well as uncertainty quantification needed to prevent satellite collisions.

1.2 Data Assimilation

Data assimilation is an approach that leverages both physics-based models and observations, providing the most complete description of a given geophysical system. Data assimilation techniques optimally combine model forecasts and observations to produce state estimates, addressing model biases and facilitating uncertainty quantification. The objective of data assimilation is to obtain a posterior estimate, $p(\mathbf{x}|\mathbf{y})$. We seek to estimate a realization of the state random variable, $\mathbf{x}$, with a given probability distribution function (PDF), p. The posterior is estimated using Bayesian inference,

$$p(\mathbf{x}|\mathbf{y}) = \frac{p(\mathbf{y}|\mathbf{x})p(\mathbf{x})}{p(\mathbf{y})} \tag{1.9}$$

using a prior state estimate, $p(\mathbf{x})$, of what we think the state is, and observation information, $\mathbf{y}$, that is used to calculate the likelihood of the observations given our prior states, $p(\mathbf{y}|\mathbf{x})$. The denominator normalizes the area under the PDF to sum to one. Sequential data assimilation techniques propagate the PDF of the state estimate using a two-step cycling approach: (1) the forecast step that propagates model states with model dynamics to produce a forecast, and (2) the analysis step that optimally updates states with observation information to produce an analysis estimate. This cycling is illustrated in Figure 1.5. The forecast is alternatively called the prior and the analysis estimate is called the posterior, and

these terms are used interchangeably.

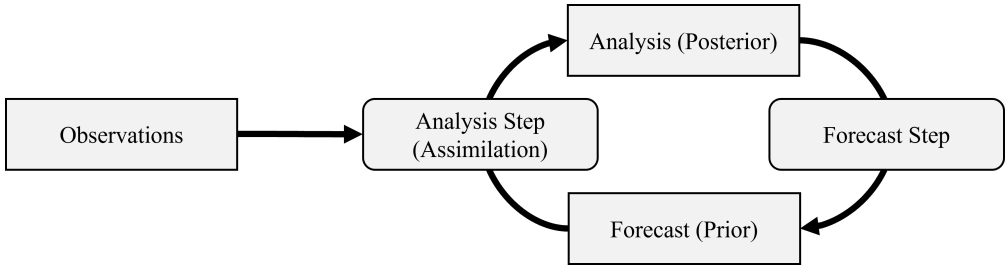

Figure 1.5: A typical sequential data assimilation cycle, with the forecast step forward propagating model states in time and the analysis step assimilating observations into the forecast model.

For the upper atmosphere, the Bayesian estimation problem can be formulated using the upper atmosphere's dependence on both initial conditions and external forcing. Suppose the model grid states are given by $\mathbf{x} \in \mathbb{R}^n$, (e.g., neutral temperature, neutral winds, electron density), and external forcing is given by $\mathbf{d} \in \mathbb{R}^q$, (e.g., solar irradiance, geomagnetic forcing). Propagating the full appended state PDF uses the two general equations from the previous cycle time t_{k-1} to the next update time at t_k:

$$\text{Forecast Step:} \quad p\big(\mathbf{x}_{k-1}, \mathbf{d}_{k-1:k} | Y_{k-1}\big) \xrightarrow{\mathcal{M}} p\big(\mathbf{x}_k, \mathbf{d}_{k-1:k} | Y_{k-1}\big) \tag{1.10}$$

$$\text{Analysis Step:} \quad p\big(\mathbf{x}_k, \mathbf{d}_{k-1:k} | Y_k\big) \propto p\big(\mathbf{y}_k | \mathbf{x}_k\big) p\big(\mathbf{x}_k, \mathbf{d}_{k-1:k} | Y_{k-1}\big) \tag{1.11}$$

where $\mathcal{M}$ is the dynamical model, Y_{k-1} includes all observations up to time t_{k-1}, and $\mathbf{d}_{k-1:k}$ indicates forcing parameters used between time-steps t_{k-1} and t_k.

In the thesis, two approaches are taken to address the estimation of I-T states and neutral density, separated into two objective components for neutral density estimation: state specification and uncertainty quantification. For neutral density specification, we focus on the estimation of I-T states, formulating the analysis update as

$$\text{Analysis Step:} \quad p\big(\mathbf{x}_k | Y_k\big) \propto p\big(\mathbf{y}_k | \mathbf{x}_k\big) p\big(\mathbf{x}_k; \mathbf{d}_{k-1:k} | Y_{k-1}\big) \tag{1.12}$$

where grid states are estimated using direct updates with observations. This is accomplished in an ensemble Kalman filter approach detailed in Section 1.2.1. For uncertainty quantifica-

tion, we focus on external forcing estimation within forcing parameter space. The analysis update is then given as

$$\text{Analysis Step:} \quad p\big(\mathbf{d}_{k-1:k}|Y_k\big) \propto p\big(\mathbf{y}_k|\mathbf{d}_{k-1:k}\big)p\big(\mathbf{d}_{k-1:k};\mathbf{x}_k|Y_{k-1}\big) \tag{1.13}$$

where the thesis applies a particle filter framework that makes no assumptions about the form of the PDF to estimate the time series of forcing parameters, $\{\mathbf{d}_k, \mathbf{d}_{k-1}, \mathbf{d}_{k-2}, \dots\}$.

Within the Bayesian update, the likelihood of an observation, $\mathbf{y}_k$, is calculated given that the prior state information, $\mathbf{x}_k^f$, would be the true state vector. This transformation is defined with the observation or forward operator, $\mathcal{H}$, to convert from state space to the observation space, $\mathbf{y}_k \in \mathbb{R}^p$, with assumed observation errors to be

$$\mathbf{y}_k = \mathcal{H}(\mathbf{x}_k^{true}) + \boldsymbol{\varepsilon}_k \tag{1.14}$$

where these observations are realizations of the true state at time t_k, $\mathbf{x}_k^{true}$, with some observation error given by $\boldsymbol{\varepsilon}_k$. These capture uncertainties including instrument, retrieval algorithm, and representativeness errors. Commonly, observation errors are assumed Gaussian with zero mean bias, i.e., $\boldsymbol{\varepsilon}_k \sim \mathcal{N}(0, \mathbf{R}_k)$, where $\mathbf{R}_k$ is the observation error covariance. The likelihood PDF, $p(\mathbf{y}_k|\mathbf{x}_k)$, assuming Gaussian observation errors is calculated to be

$$p(\mathbf{y}_k|\mathbf{x}_k) \propto \exp\Big[-\frac{1}{2}\big(\mathbf{y}_k - \mathcal{H}(\mathbf{x}_k)\big)^T\mathbf{R}_k^{-1}\big(\mathbf{y}_k - \mathcal{H}(\mathbf{x}_k)\big)\Big] \tag{1.15}$$

Additionally, a core assumption within sequential data assimilation approaches is that the PDF evolves as a Markov chain process. This assumption allows the current state estimate to only be conditioned on the state estimate at the previous time, as this previous estimate contains all the earlier included information.

1.2.1 Ensemble (Square Root) Kalman Filter

We seek to solve the estimation problem here by minimizing the state error variance. Beginning with a description of the classical Kalman filter, we assume a linear system with

errors in the form of Gaussian PDFs. This requires state PDFs to be represented only using the mean and covariance, solving Bayes' theorem as

$$p(\mathbf{x}_k|\mathbf{y}_k) \propto \exp\big(\mathcal{J}(\mathbf{x}_k)\big) \tag{1.16}$$

where the analysis state estimate, $\mathbf{x}_k^a$ is computed by minimizing the cost function, $\mathcal{J}(\mathbf{x}_k)$, given as

$$\mathcal{J}(\mathbf{x}_k) = \frac{1}{2}\big(\mathbf{x}_k - \mathbf{x}_k^f\big)^T(\mathbf{P}_k^f)^{-1}\big(\mathbf{x}_k - \mathbf{x}_k^f\big) + \frac{1}{2}\big(\mathcal{H}(\mathbf{x}_k^f) - \mathbf{y}_k\big)^T\mathbf{R}_k^{-1}\big(\mathcal{H}(\mathbf{x}_k^f) - \mathbf{y}_k\big) \tag{1.17}$$

where $\mathbf{P}_k^f$ is the forecast state error covariance, and $\mathbf{x}_k^f$ is the forecast state.

Continuing from Evensen et al. (2022), a closed-form solution to Equation 1.17 is retrieved. Assuming that $\mathcal{H}(\mathbf{x}_k)$ is linear to give $\mathbf{H}_k\mathbf{x}_k$ and observations are all assumed to be collected at the update time, we can take the gradient of Equation 1.17 and set equal to zero:

$$(\mathbf{P}_k^f)^{-1}(\mathbf{x}_k^a - \mathbf{x}_k^f) + \mathbf{H}_k^T\mathbf{R}_k^{-1}(\mathbf{H}_k\mathbf{x}_k^a - \mathbf{y}_k) = 0 \tag{1.18}$$

and then solve for $\mathbf{x}_k^a$ to give the update equation:

$$\mathbf{x}_k^a = \mathbf{x}_k^f + \mathbf{K}_k(\mathbf{y}_k - \mathbf{H}_k\mathbf{x}_k^f) \tag{1.19}$$

where $\mathbf{K}_k = \mathbf{P}_k^f\mathbf{H}_k^T(\mathbf{H}_k\mathbf{P}_k^f\mathbf{H}_k + \mathbf{R}_k)^{-1}$ is the Kalman gain. The analysis update of the state error covariance, $\mathbf{P}_k^a$, is found to be

$$\mathbf{P}_k^a = (\mathbf{I} - \mathbf{K}_k\mathbf{H}_k)\mathbf{P}_k^f \tag{1.20}$$

This retrieves the Kalman filter (KF) update equations.

Alternative approaches are needed to apply the KF to systems with large state space, $O(n) = 10^4 - 10^8$, and observation space, $O(p) = 10^2 - 10^5$. For this, ensemble Kalman filters are a Monte Carlo method using a low-rank approximation of the full state covariance, where the state mean and covariance are approximated by an ensemble with size m, with $m \ll n$. This approach gives rise to a class of ensemble KFs (EnKF) using square root

methods (Tippett et al., 2003; Evensen et al., 2022) that estimate in a much-reduced ensemble subspace with efficient and straightforward implementation. As the covariance matrices are symmetric semi-positive definite by definition, EnKFs represent the covariance matrices by square root matrices approximated by ensemble matrices:

$$\mathbf{P}^f \approx \mathcal{D}^f_{\mathbf{x}}(\mathcal{D}^f_{\mathbf{x}})^T \tag{1.21}$$

$$\mathbf{P}^a \approx \mathcal{D}^a_{\mathbf{x}}(\mathcal{D}^a_{\mathbf{x}})^T \tag{1.22}$$

where $\mathcal{D}$ is the data matrix square root constructed using ensemble members and the forecast data matrix, $\mathcal{D}^f_{\mathbf{x}}$, is given by

$$\mathcal{D}^f_{\mathbf{x}} = \frac{1}{\sqrt{m-1}}\left[(\mathbf{x}^{f,(1)} - \bar{\mathbf{x}}^f) \quad \dots \quad (\mathbf{x}^{f,(m)} - \bar{\mathbf{x}}^f)\right] \in \mathbb{R}^{n\times m} \tag{1.23}$$

and the analysis data matrix, $\mathcal{D}^a_{\mathbf{x}}$, is constructed in a similar manner. For deterministic square root KFs, the analysis state error covariance can be found as in Tippett et al. (2003) by substituting the data matrices into the KF update equation:

$$\mathbf{P}^a_k = \mathcal{D}^a_{\mathbf{x}}(\mathcal{D}^a_{\mathbf{x}})^T = [\mathbf{I} - \mathbf{P}^f_k\mathbf{H}_k(\mathbf{H}_k\mathbf{P}^f_k\mathbf{H}^T_k + \mathbf{R}_k)^{-1}\mathbf{H}_k]\mathbf{P}^f_k \tag{1.24}$$

$$= [\mathbf{I} - \mathcal{D}^f_{\mathbf{x}}(\mathcal{D}^f_{\mathbf{x}})^T\mathbf{H}_k(\mathbf{H}_k\mathcal{D}^f_{\mathbf{x}}(\mathcal{D}^f_{\mathbf{x}})^T\mathbf{H}^T_k + \mathbf{R}_k)^{-1}\mathbf{H}_k]\mathcal{D}^f_{\mathbf{x}}(\mathcal{D}^f_{\mathbf{x}})^T \tag{1.25}$$

$$= \mathcal{D}^f_{\mathbf{x}}[\mathbf{I} - \mathbf{V}_k(\mathbf{V}^T_k\mathbf{V}_k + \mathbf{R}_k)^{-1}\mathbf{V}^T_k](\mathcal{D}^f_{\mathbf{x}})^T \tag{1.26}$$

$$= \mathcal{D}^f_{\mathbf{x}}\mathbf{T}\mathbf{T}^T(\mathcal{D}^f_{\mathbf{x}})^T \tag{1.27}$$

where $\mathbf{V}_k = (\mathbf{H}_k\mathcal{D}^f_{\mathbf{x}})^T$, and $\mathbf{T}$ is some matrix transform such that $\mathcal{D}^a_{\mathbf{x}} = \mathcal{D}^f_{\mathbf{x}}\mathbf{T}$. Here, $\mathcal{D}^a_{\mathbf{x}}$ is a linear combination of $\mathcal{D}^f_{\mathbf{x}}$, where $\mathbf{T}$ is non-unique as $\text{rank}(\mathcal{D}\mathcal{D}^T) < n$. In practice, $\mathbf{T}\mathbf{T}^T = [\mathbf{I} - \mathbf{V}_k(\mathbf{V}^T_k\mathbf{V}_k + \mathbf{R}_k)^{-1}\mathbf{V}^T_k]$ finds $\mathbf{T}$ solving the matrix square root such as with singular value decomposition. Different square root Kalman filters calculate $\mathbf{T}$ by different means, e.g., the Ensemble Kalman Filter (EnKF) (Evensen, 2009), Ensemble Transform Kalman Filter (ETKF) (Bishop et al., 2001) and Ensemble Adjustment Kalman Filter (EAKF) (Anderson, 2001).

The forecast and analysis steps of the EnKF cycle are given for the mean state, $\bar{\mathbf{x}}$, as

$$\text{Forecast Step:} \quad \mathbf{x}_k^{f,(i)} = \mathcal{M}\Big(\mathbf{x}_{k-1}^{a,(i)}; \mathbf{d}_{k-1:k}\Big), \quad i = 1, \ldots, m \tag{1.28}$$

$$\text{Analysis Step:} \quad \bar{\mathbf{x}}_k^a = \bar{\mathbf{x}}_k^f + \tilde{\boldsymbol{K}}_k\Big(\mathbf{y}_k - \mathcal{H}(\bar{\mathbf{x}}_k^f)\Big) \tag{1.29}$$

where the forecast covariance $\mathbf{P}_k^f$ is implicitly propagated through the full non-linear dynamics, and the analysis step uses an equivalent Kalman gain, $\tilde{\boldsymbol{K}}_k$ to map the innovation increment to update the mean state.

The specific EnKF implementation used in the thesis is the EAKF implemented in the Data Assimilation Research Testbed (DART) at NCAR (Anderson, 2001, 2003; Anderson and Collins, 2007; Anderson et al., 2009a). DART is an open-source data assimilation tool with model support for the TIEGCM, denoted as DART-TIEGCM, and numerous other geophysical models. The EAKF within DART is implemented through a *two-step* framework developed in Anderson (2003). The first step computes a Bayesian update of a posterior distribution conditioned on observations, as generalized in Grooms (2022). This update can be accomplished with a variety of approaches, where Anderson (2003) develops this sampling for the EAKF, calculating an increment for each prior ensemble member. The second step maps these increments to state variables using linear regression, relying on the prior ensemble to provide the relationship between these two spaces. For the univariate update case, the state increment (Anderson, 2003), Δx_k, is found by

$$\Delta x_k = \frac{\sigma_{x,y}}{\sigma_{y,y}} \Delta y_k \tag{1.30}$$

where Δy_k is the observation increment, and the linearization uses the prior ensemble cross-covariance, $\sigma_{x,y}$, and prior ensemble observation covariance, $\sigma_{y,y}$, information. This linear mapping allows observation information to infer unobserved model states and have a regional impact, enabling global state estimation. Strongly-coupled data assimilation utilizing this approach is discussed in the following Section 1.2.1.1. Further algorithm implementation and specifics of the EAKF are detailed in (Anderson and Collins, 2007; Anderson et al., 2009a), with supporting theory in (Anderson, 2001, 2003).

1.2.1.1 Strongly Coupled I-T Data Assimilation

Through strongly coupled data assimilation, neutral states can be updated with ionospheric observations. This approach impacts state estimates in both the analysis and forecast steps. The analysis step includes direct updates to neutral states and specified model initial conditions impact unobserved states in the forecast step, illustrated in Figure 1.6. This framework has been used in previous work (e.g., Matsuo and Hsu, 2021; Hsu et al., 2014; Matsuo et al., 2013; Lee et al., 2012; Kodikara et al., 2021; Pedatella et al., 2020). This section details the procedure for directly updating neutral and plasma states using plasma observations, specifically using RO EDPs.

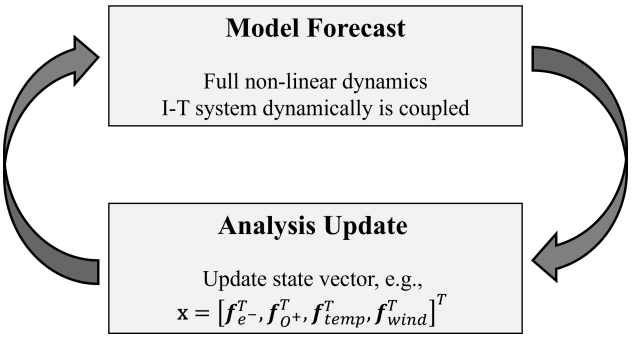

Figure 1.6: Schematic of strongly coupled data assimilation, impacting state specification through forecast and analysis step cycling.

The updated state vector is defined as $\mathbf{x} = \begin{bmatrix} \mathbf{x}_\mathrm{I} \\ \mathbf{x}_\mathrm{T} \end{bmatrix} \in \mathbb{R}^n$, as a combination of updated ionospheric states, $\mathbf{x}_I \in \mathbb{R}^{n_I}$, and updated thermospheric states, $\mathbf{x}_\mathrm{T} \in \mathbb{R}^{n_\mathrm{T}}$, where $n = n_\mathrm{I} + n_\mathrm{T}$. It is noted that all observations and states are at the update time t_k, so for simplicity, the time notation (subscript k) is assumed for all vectors.

For the analysis step, all of the nearest hour EDP observations of the ionosphere, $\mathbf{y}^\mathrm{o}_\mathrm{EDP}(t_k) \in \mathbb{R}^p$, are assimilated to update the state vector $\mathbf{x}(t_k)$ composed of neutral states, $\mathbf{x}_\mathrm{T}$, and plasma states $\mathbf{x}_\mathrm{I}$. For an analysis step at the update time t_k, model ionosphere states,

$\mathbf{x}_{\mathrm{I}}^{(i)}(t_k)$, are first transformed to observation space using the matrix operator $\mathbf{H} \in \mathbb{R}^{p \times n}$:

$$\mathbf{y}_{\mathrm{EDP}}^{(i)}(t_k) = \mathbf{H}\mathbf{x}_{\mathrm{I}}^{(i)}(t_k) \tag{1.31}$$

for each ensemble $i = 1, \ldots, m$. It is noted that the forward operator may be non-linear in the EAKF, and in this case $\mathbf{H}$ represents a linear interpolator for electron densities, transforming the TIEGCM electron density grid to be at the derived EDP locations. For simplicity, we show the update for a scalar observation $\mathrm{y}_{\mathrm{EDP}}^{(i)}$ with $p = 1$.

In the EAKF two-step update, the first step is a Bayesian update, yielding an observation variable increment for each ensemble member, $\Delta\mathrm{y}_{\mathrm{EDP}}^{(i)}$. The second step is a linear regression that can directly update unobserved states and is the enabling force behind strongly coupled data assimilation. The linear relationship is provided by the background sample covariances between EDPs and model states, constructed using the data matrix with the ensemble perturbations from the means, $\overline{\mathbf{x}}_{\mathrm{T}}^{f}$, $\overline{\mathbf{x}}_{\mathrm{I}}^{f}$ and $\overline{\mathrm{y}}_{\mathrm{EDP}}$. The updated thermosphere states data matrix is constructed as:

$$\mathcal{D}_{\mathrm{T}} = \frac{1}{\sqrt{m-1}} \begin{bmatrix} \mathbf{x}_{\mathrm{T}}^{f,(1)} - \overline{\mathbf{x}}_{\mathrm{T}}^{f} & \mathbf{x}_{\mathrm{T}}^{f,(2)} - \overline{\mathbf{x}}_{\mathrm{T}}^{f} & \cdots & \mathbf{x}_{\mathrm{T}}^{f,(m)} - \overline{\mathbf{x}}_{\mathrm{T}}^{f} \\ \mathrm{y}_{\mathrm{EDP}}^{(1)} - \overline{\mathrm{y}}_{\mathrm{EDP}} & \mathrm{y}_{\mathrm{EDP}}^{(2)} - \overline{\mathrm{y}}_{\mathrm{EDP}} & \cdots & \mathrm{y}_{\mathrm{EDP}}^{(m)} - \overline{\mathrm{y}}_{\mathrm{EDP}} \end{bmatrix} \in \mathbb{R}^{(n_{\mathrm{T}}+1) \times m} \tag{1.32}$$

and the updated ionosphere states,

$$\mathcal{D}_{\mathrm{I}} = \frac{1}{\sqrt{m-1}} \begin{bmatrix} \mathbf{x}_{\mathrm{I}}^{f,(1)} - \overline{\mathbf{x}}_{\mathrm{I}}^{f} & \mathbf{x}_{\mathrm{I}}^{f,(2)} - \overline{\mathbf{x}}_{\mathrm{I}}^{f} & \cdots & \mathbf{x}_{\mathrm{I}}^{f,(m)} - \overline{\mathbf{x}}_{\mathrm{I}}^{f} \\ \mathrm{y}_{\mathrm{EDP}}^{(1)} - \overline{\mathrm{y}}_{\mathrm{EDP}} & \mathrm{y}_{\mathrm{EDP}}^{(2)} - \overline{\mathrm{y}}_{\mathrm{EDP}} & \cdots & \mathrm{y}_{\mathrm{EDP}}^{(m)} - \overline{\mathrm{y}}_{\mathrm{EDP}} \end{bmatrix} \in \mathbb{R}^{(n_{\mathrm{I}}+1) \times m} \tag{1.33}$$

Self-multiplying these matrices by the transpose, T gives a low-rank approximation of the

covariances:

$$\mathcal{D}_{\mathrm{T}}\mathcal{D}_{\mathrm{T}}^{T} = \begin{bmatrix} \mathbf{P}_{\mathrm{T,T}} & \mathbf{P}_{\mathrm{T,EDP}} \\ \mathbf{P}_{\mathrm{T,EDP}}^{T} & \sigma_{\mathrm{EDP}}^{2} \end{bmatrix} \in \mathbb{R}^{(n_{\mathrm{T}}+1)\times(n_{\mathrm{T}}+1)} \tag{1.34}$$

$$\mathcal{D}_{\mathrm{I}}\mathcal{D}_{\mathrm{I}}^{T} = \begin{bmatrix} \mathbf{P}_{\mathrm{I,I}} & \mathbf{P}_{\mathrm{I,EDP}} \\ \mathbf{P}_{\mathrm{I,EDP}}^{T} & \sigma_{\mathrm{EDP}}^{2} \end{bmatrix} \in \mathbb{R}^{(n_{\mathrm{I}}+1)\times(n_{\mathrm{I}}+1)} \tag{1.35}$$

Using the data matrices, we have the covariance matrix for thermospheric states, $\mathbf{P}_{\mathrm{T,T}}$, the observation variance, $\sigma_{\mathrm{EDP}}^{2}$, and most importantly the covariance matrix between thermospheric states and observations, $\mathbf{P}_{\mathrm{T,EDP}}$. The same is available for ionospheric states. Using the constructed covariance matrices, the increment to electron density, $\Delta \mathrm{y}_{\mathrm{EDP}}^{(i)}$, is mapped to thermospheric and ionospheric state increments, $\Delta\mathbf{x}_{\mathrm{T}}$ and $\Delta\mathbf{x}_{\mathrm{I}}$:

$$\begin{bmatrix} \\ \Delta\mathbf{x}_{\mathrm{T}}^{(i)} \\ \\ \\ \Delta\mathbf{x}_{\mathrm{I}}^{(i)} \\ \\ \end{bmatrix} = \boldsymbol{\alpha}_{GC} \odot \begin{bmatrix} \\ \frac{\mathbf{P}_{\mathrm{T,EDP}}}{\sigma_{\mathrm{EDP}}^{2}} \\ \\ \\ \frac{\mathbf{P}_{\mathrm{I,EDP}}}{\sigma_{\mathrm{EDP}}^{2}} \\ \\ \end{bmatrix} \Delta \mathrm{y}_{\mathrm{EDP}}^{(i)} \tag{1.36}$$

where $\boldsymbol{\alpha}_{GC} \in \mathbb{R}^{n_{\mathrm{T}}+n_{\mathrm{I}}\times 1}$ is a localization parameter constructed with the Gaspari-Cohn (GC) localization function multiplied by the Schur product, $\odot$, (Gaspari and Cohn, 1999). We normalize the covariance between the updated states and the observation states, forming a linear regression coefficient (Equation 1.30) that relates the observation state increment to the model state increment, $\mathbf{P}_{\mathrm{T,EDP}}/\sigma_{\mathrm{EDP}}^{2}$. This allows us to direct-update neutral states using $\mathrm{y}_{\mathrm{EDP}}$. The sample statistics, obtained by ensemble perturbations, generate correlation structures that are more complex than an isotropic, homogeneous correlation structure. An example of these background covariance structures is illustrated in Figures 3.1 and 3.2.

The analysis step for the EAKF is performed sequentially for each observation. Sequentially updating with observations assumes that observations are independent for $j = 1, \ldots, p$. The data assimilation cycle continues for the next forecast step to propagate model states one hour into the future with initial conditions $\mathbf{x}_{k}^{a,(i)}$, $i = 1, \ldots, m$ and forcing parameters

$\mathbf{d}_{k:k+1}$. In strongly coupled data assimilation, specified initial conditions can still impact model states not directly updated in the linear regression through the coupled I-T model dynamics of the forecast step.

Within an EnKF, there are key means for improving assimilation performance through two *auxiliary* approaches: inflation and localization. To avoid ensemble spread collapse and filter divergence, inflation uses innovation statistics to boost state spread where there are larger model-observation biases. Inflation and newer adaptive inflation schemes are implemented within DART (Anderson, 2007; El Gharamti, 2018) and these approaches use an inflation parameter estimated within a filter framework. As background covariances are a low-rank approximation by ensemble members, sampling errors will inevitably be an issue leading to spurious correlations being produced. Localization limits observation impact to a "local" region around the observation location, where a compactly-supported function is commonly used, for example, the GC function (Gaspari and Cohn, 1999)). Additionally, localization can limit unrealistically large correlations, such as solar irradiance producing large-scale, global correlation structures.

While TIEGCM solves vertical coordinates in a pressure level grid, the analysis update is essentially agnostic to the model's vertical coordinate system except for within localization. This is because the analysis update of model states is purely accomplished through the linear regression mapping (Equations 1.30 and 1.36), relying only on the ensemble background covariance. Within DART-TIEGCM, the analysis update is localized around observation locations, and it is noted the thesis does not use vertical localization. Vertical localization can be applied in pressure or altitude coordinates using the distance between observations and model grid locations. When using vertical localization, the chosen distance metric limits the local extent the analysis update has on model states, and the preferred localization space would require further study.

1.2.2 Particle Filter

In the particle filter, no assumptions are needed for the state distributions, allowing complete freedom for state error representation. This allows non-Gaussian PDFs when there are non-linear dynamics.

Particle filters use a wholly Monte Carlo approach to approximate the state PDF using a sample of particles, where each particle has an associated weight representing the likelihood of that particle. In the standard or bootstrap particle filter, $i = 1, \ldots, N$ particles approximate the forecast PDF of state $\mathbf{x}_k$ as

$$p(\mathbf{x}_k) \approx \sum_{i=1}^{N} \frac{1}{N} \delta(\mathbf{x}_k - \mathbf{x}_k^i) \tag{1.37}$$

where $\delta()$ is the Dirac-delta distribution and each particle is equally weighted as $1/N$ (van Leeuwen et al., 2019). Plugging in this representation of the forecast PDF into Bayes' theorem (Equation 1.9), allows the analysis PDF to be represented as

$$p(\mathbf{x}_k|\mathbf{y}_k) \approx \sum_{i=1}^{N} w_k^i \delta(\mathbf{x}_k - \mathbf{x}_k^i) \tag{1.38}$$

where individual particle weights, w_k^i, are given by

$$w_k^i = \frac{p(\mathbf{x}_k|\mathbf{y}_k)}{N p(\mathbf{y}_k)} = \frac{p(\mathbf{x}_k|\mathbf{y}_k)}{N \int p(\mathbf{y}_k|\mathbf{x}_k) p(\mathbf{x}_k) d\mathbf{x}_k} \approx \frac{p(\mathbf{y}_k|\mathbf{x}_k)}{\sum_j p(\mathbf{y}_k|\mathbf{x}_k^j)} \tag{1.39}$$

The scalar weight of each particle can be calculated with an assumed likelihood function distribution (Van Leeuwen, 2010). Additionally in practice, the denominator of Equation 1.39 does not need to be calculated, and using the fact that PDFs must sum to one can instead be normalized using the sum of all weights. For the next time step at t_{k+1}, the next cycle's posterior weights, w_{k+1}^i, is calculated using the prior information,

$$w_{k+1}^i = w_k^i \frac{p(\mathbf{y}_{k+1}|\mathbf{x}_{k+1})}{\sum_j p(\mathbf{y}_{k+1}|\mathbf{x}_{k+1}^j)} \tag{1.40}$$

However when implementing a particle filter, cycling weights and including increasingly more observation information will quickly cause all the weight to be attributed to one particle,

and result in particle collapse and filter divergence. Therefore, resampling is introduced to produce a new, equally weighted set of particles, $w_{k+1}^i = 1/N$, where resampling uses the analysis particle weights to best reproduce the analysis PDF. Commonly used resampling schemes draw from a uniform distribution, for example, the multinominal resampling and SU sampling algorithms (Van Leeuwen, 2009; Farchi and Bocquet, 2018).

The general particle filter framework is illustrated in Figure 1.7, courtesy of Van Leeuwen (2009). It begins at time $t = 0$ with an initial set of particles with their respective probability reflected by the size of the points. Particles are propagated in the forecast step to time $t = 10$, where the posterior weight is calculated using Bayes' theorem. Particles are then resampled based on each particle's posterior weight, with each resample having equal weight, and propagated forward again within the next forecast step.

These particle filter approaches rely upon the idea of sampling importance resampling (SIR) (Farchi and Bocquet, 2018; Gordon et al., 1993). The principle of importance sampling is reconstructing a sample of the analysis PDF given forecast particles and their associated importance weights. From Farchi and Bocquet (2018), the equivalent data assimilation cycle to propagate the state and weights is

$$\text{Forecast Step:} \qquad \mathbf{x}_k^i \sim p(\mathbf{x}_k|\mathbf{x}_{k-1}^i) \tag{1.41}$$

$$w_k^i \leftarrow w_{k-1}^i \tag{1.42}$$

$$\text{Analysis Step:} \qquad w_k^i \leftarrow w_k^i p(\mathbf{y}_k|\mathbf{x}_k^i) \tag{1.43}$$

where $\mathbf{x} \sim p$ is a realization of the random vector according to PDF p and $p(\mathbf{x}_k|\mathbf{x}_{k-1}^i)$ is the transition density from the previous time step. In this formulation, the empirical density $\pi_{k+1|k}^N$ is used as an estimator of the true density $\pi_{k+1|k}$. As the number of particles increases, $N \to \infty$, it can be shown that $\pi_{k|k}^N$ converges to $\pi_{k|k}$ under weak topology (Crisan and Doucet, 2002).

The largest obstacle to the implementation of particle filters is the curse of dimensionality which is especially challenging for high-dimensional applications in geophysical systems.

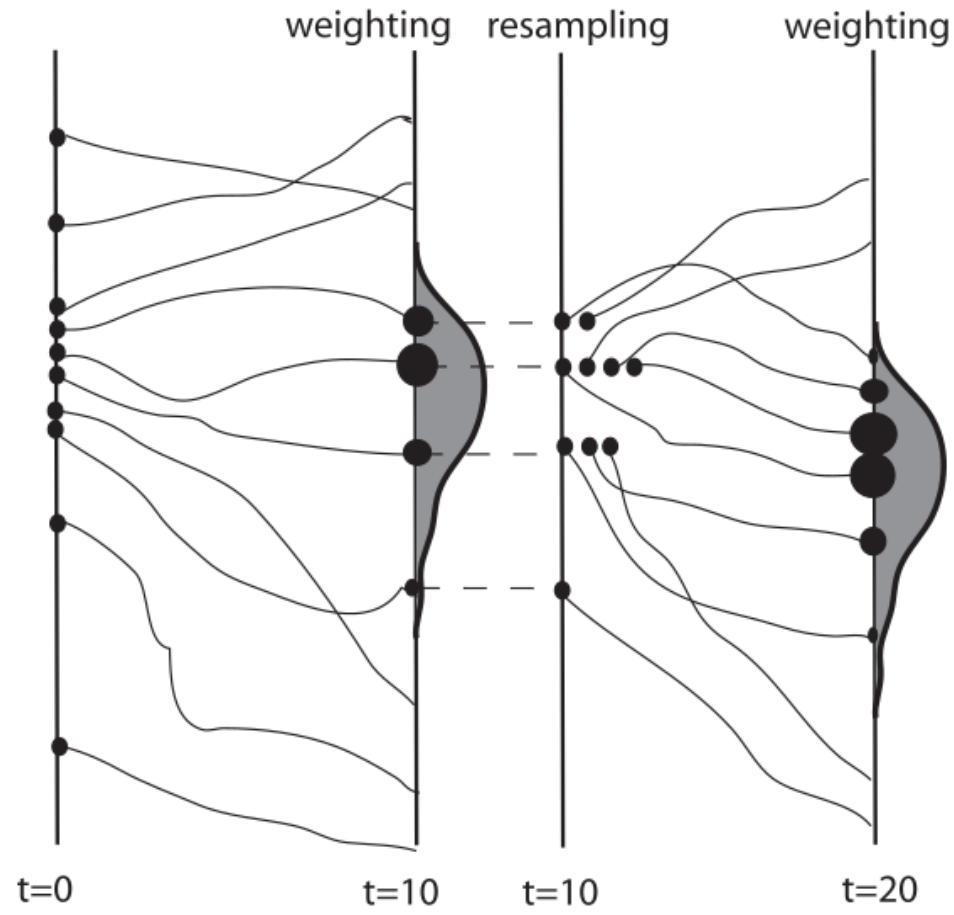

Figure 1.7: Bootstrap particle filter with sequential importance resampling, courtesy of Van Leeuwen (2009). The size of particles corresponds to their relative weight in representing the PDF. Particles are resampled according to their posterior weight and propagated through the stochastic model dynamics.

With a high number of observations, weight can quickly get assigned to a single particle and result in weight collapse. This weight collapse has been quantified in Snyder et al. (2008) in an equivalent state dimension, showing a need for N to grow exponentially with more observations. In the event of weight collapse, the resampling step re-selects the same particle and all particle spread is gone. To prevent this collapse, alternative methods for implementing particle filters are needed for high-dimensional applications (e.g., van Leeuwen et al., 2019; Farchi and Bocquet, 2018).

1.3 Thesis Goal and Objectives, and Their Significance

The thesis addresses the overarching goal stated below with specific objectives categorized into two separate components in terms of data assimilation approach types, targeting I-T state specification and neutral density uncertainty quantification, as described in Section 1.3.1 and Section 1.3.2.

Goal

The goal of the thesis is to develop new physics-based data assimilation capabilities for LEO neutral density to advance 1) scientific understanding of the thermosphere's storm-time response and 2) uncertainty quantification of LEO position errors due to geophysical variability.

The significance of these goals and objectives are summarized in Section 1.3.3.

1.3.1 I-T State Specification Using Ensemble Filters

The thesis first addresses the goal of advancing scientific understanding of the thermosphere's storm-time response with the following three objectives. These objectives are implemented by applying an ensemble filter to I-T state specification and focusing on enhancing the ability of physics-based modeling to capture neutral density variability.

Objective 1.1, Objective 1.2, Objective 1.3

1.1 Evaluate GNSS radio occultation constellation design for ionospheric specification, comprehensively characterizing observation and model error impacts to inform future mission planning.

1.2 Infer thermospheric states from ionospheric observations from radio occultation constellations and quantify their benefits to neutral density specification and orbit propagation errors.

1.3 Better characterize the global thermospheric dynamics and energetics behind neutral density variability during geomagnetic storms by improving neutral state estimation with RO plasma observations.

Current physics-based models adequately describe the I-T system climatologically, but their ability to accurately model specific storm events is insufficient. The applied ensemble filter data assimilation framework is motivated to directly address the limitations of physics-based models and a lack of global neutral observations to constrain the model. The framework enables the use of global ionospheric observations provided by RO constellations to inform internal I-T dynamics, through a strongly coupled I-T data assimilation framework. It is in distinct contrast to other typical thermospheric data assimilation approaches that assimilate neutral observations to constrain thermospheric dynamical variables (e.g., temperature and neutral winds). Section 1.2.1.1 details this framework of using ionospheric observations to directly estimate unobserved thermospheric states such as neutral temperature, compositions, and neutral winds. This approach leverages the I-T coupling processes of ionospheric formulation (Section 1.1.1) using cross-covariance information supplied by the physics-based model.

The thesis uses two data assimilation experiment frameworks to accomplish Objectives 1.1, 1.2, and 1.3. The first is Observing System Simulation Experiments (OSSEs), wherein data assimilation frameworks can quantitatively assess hypothetical observing systems for their relative value and benefit. Within an OSSE, synthetic data are generated from a nature-run model simulation (that serves as a truth model state) and then assimilated into a biased forecast model to assess improvement. Section 2.2 provides details about the OSSE

framework adopted in the thesis. The second approach is Observing System Experiments (OSEs) which quantitatively assess existing observing systems and further their integration into data assimilation systems. Specifically, the thesis uses an OSE framework to produce a reanalysis of thermospheric states during a geomagnetic storm event. Reanalysis has been a valuable tool for Earth science investigations, with some notable examples including ECMWF's ERA5 (Hersbach et al., 2020), NASA's MERRA (Rienecker et al., 2011), and the NCEP/DOE Reanalysis II (Kanamitsu et al., 2002). Reanalysis has also been beneficial for the ionosphere, such as in Rajesh et al. (2021), which enabled the quantification of hourly tidal variations.

Objective 1.1 evaluates hypothetical RO constellation designs for plasma specification using a comprehensive OSSE approach. This objective is implemented by incorporating an I-T coupled model in the ensemble data assimilation framework, realistically accounting for the forecast model and observation errors. Chapter 2 details using this OSSE approach to evaluate RO constellation configurations quantitatively. This study informs RO constellation designs for maximizing observational impact as well as characterizes the data assimilation impacts of Abel inversion observation retrieval errors. Objective 1.2 successfully demonstrates the use of RO EDPs to infer neutral densities and reduce orbit position errors. Chapter 3 details an OSSE study wherein a strongly coupled I-T data assimilation framework uses these plasma observations to constrain neutral temperature and neutral winds. The study additionally demonstrated the potential of estimating unobserved helium compositions and has been published in Dietrich et al. (2022). Objective 1.3, detailed in Chapter 4, builds on Objective 1.2 to produce a reanalysis of thermospheric states during a storm event. The resulting reanalysis and the data assimilation impact are investigated and validated against independent neutral state observations. These efforts support the validity of using RO EDPs to constrain neutral temperature and compositions to improve the physics-based description of storm-time neutral density changes.

1.3.2 Neutral Density Uncertainty Quantification Using a Particle Filter

The second thesis component addresses the goal of advancing uncertainty quantification of LEO position errors due to geophysical variability with the following objective by incorporating physics-based modeling into a particle filter framework.

Objective 2.1

2.1 Quantify non-Gaussian uncertainties of neutral density variability associated with non-linear thermospheric dynamics during geomagnetically active and quiet times.

By quantifying non-Gaussian neutral density uncertainties, the thesis aims to advance the quantification of LEO position errors, especially during storm time. Estimating non-Gaussian neutral density uncertainties using a Bayesian approach presents two obstacles. The first obstacle is the lack of prior knowledge of neutral density error distributions. The thesis addresses this by developing a particle filter framework that does not require prior distribution assumptions. Second, the high dimensionality of neutral states is a considerable challenge for a particle filter implementation. Therefore, the particle filter is implemented as parameter estimation in a reduced space containing two forcing parameters, while still using a complete physics-based model to capture the non-linear storm dynamics. This component focuses on assimilating in-situ neutral density observations. Forcing parameter estimation is feasible as the upper atmosphere is strongly controlled by external forcing during storm time (Jee et al., 2007; Chartier et al., 2013). Others have used this dependence to estimate the solar and geomagnetic forcing parameters for improving physics-based models (Morozov et al., 2013; Sutton, 2018; Sutton et al., 2021; Codrescu et al., 2018, 2004).

Objective 2.1 quantifies non-Gaussian neutral density uncertainties during a geomagnetic storm by incorporating the TIEGCM into a particle filter framework. Chapter 5 details this objective and shows how resulting non-Gaussian distributions of forcing parameter estimates can be used to produce a global, time-varying specification of neutral density non-

Gaussian uncertainties during a storm event, through end-to-end uncertainty quantification.

1.3.3 Significance of Thesis Goal and Objectives

The thesis paves the way for bridging space weather research and SDA by transforming scientific understanding of geophysical variability of thermospheric neutral density into practical solutions useful to SDA. While Objective 1.1 directly supports decision-making for RO mission constellation designs for plasma density specification and forecasting, Objectives 1.2 and 1.3 are highly relevant for establishing the basis of a global GNSS-based monitoring system for LEO neutral density specification and forecasting. Objectives 1.2 and 1.3 contribute towards the broader goal of adapting physics-based models for neutral density specification and forecasting. Objective 2.1 is relevant as it suggests a viable path for propagating uncertainty end-to-end from forcing to neutral density and then to orbit positioning. The characterization of non-Gaussian LEO position errors resulting from non-linear storm dynamics is valuable to future SDA capabilities including conjunction analysis.

Chapter 2

Evaluating Radio Occultation Constellation Designs using Observing System Simulation Experiments (OSSEs) for Ionospheric Specification

This chapter uses OSSE studies to evaluate hypothetical RO constellation designs and assess their impacts on ionospheric specification. We employ a comprehensive OSSE approach, the first ionospheric study to realistically account for the forecast model and Abel inversion errors. The experiment period is the 2015 St. Patrick's Day storm, including quiet and storm periods. As expected, this chapter finds that increased EDP spatial coverage leads to improved specification at altitudes 300 km and above, with the 520 km altitude constellations performing best due to yielding the highest observation counts. Results also suggest a potential performance limit with two 6-satellite constellations. Lastly, uncharacterized Abel inversion errors highlight limitations of EDPs with negative impact at altitudes below 200 km and dayside equatorial regions with large horizontal gradients and low electron density magnitudes. The results from this chapter inform future RO constellation mission designs and future integration of RO observations into future DA systems. The results of this chapter are published in Dietrich et al. (2024).

2.1 Background and Motivation

Monitoring the near-Earth space environmental conditions for space weather nowcasting and forecasting is increasingly pertinent to maintaining critical ground- and space-based technological systems. One such critical impact is ionospheric plasma disturbances

affecting navigational systems via the propagation of radio waves for Global Navigation Satellite Systems (GNSS) and very low-frequency signals, along with other communication systems utilizing high-frequency and ultra-high frequency radio signals. The peak heights and magnitudes of plasma density affect whether radio signals are reflected or absorbed, the index of refraction that bends these signals, and small-scale plasma density irregularities can cause radio signals to scatter or scintillate. These space weather effects on radio signals can be characterized using parameters, such as the F-region peak electron density, N_mF_2, and its height, h_mF_2, the total electron content (TEC), the rate of change of TEC index (ROTI), and the S_4 index. Geomagnetic storms can induce considerable variations and disturbances of the near-Earth plasma environments, stressing our radio-based systems as indicated by dramatic changes in ROTI and S_4 index (e.g., Moreno et al., 2011). As underscored by the Promoting Research and Observations of Space Weather to Improve the Forecasting of Tomorrow (PROSWIFT) Act in 2020 (Lugaz, 2020) and space weather gap analysis findings (Vourlidas et al., 2023), continuing and developing new ionospheric observing systems, as well as their integration into forecast models with the help of data assimilation (DA), is essential for advancing space weather now-casting and forecasting capabilities. Moreover, the Weather Research and Innovation Forecasting Act of 2017 specifically mandates the National Oceanic and Atmospheric Association (NOAA) to perform Observing System Simulation Experiments (OSSEs), wherein DA frameworks are used to quantitatively assess hypothetical observing systems for their relative value and benefit.

OSSEs have been used to evaluate the quantitative value of RO observations (e.g., Yue et al., 2014a; Lee et al., 2013; Hsu et al., 2018b; He et al., 2019; Lin et al., 2015, 2017; Scherliess et al., 2004; Pedatella et al., 2020; Forsythe et al., 2021). Within an OSSE, synthetic data are generated from a nature run model simulation (that serves as a truth model) and then assimilated into a biased forecast model to assess improvement. Yue et al. (2014a) performed an OSSE study before the launch of F7/C2, assessing the multiple planned RO EDPs from F7/C2 using the NeQuick model as the nature run and assimilating EDPs into

the empirical ionospheric model IRI. Lee et al. (2013) assimilated synthetic F7/C2 EDPs into a coupled ionosphere-thermosphere (I-T) physics-based model, and saw global improvements in electron density states over previous F3/C EDPs. Further to realistically assess the value of observing systems, it is crucial to quantify observation errors for DA. In particular, RO EDP assimilation can be negatively impacted by Abel retrieval errors if not properly characterized, with the most recent RO error quantification performed in Yue et al. (2010); Liu et al. (2010). Even though OSSEs have been proven to be useful for mission planning and in informing the most effective constellation designs, previous OSSE work has yet to account for both forecast model errors and Abel retrieval errors comprehensively. For example, the tropospheric weather forecasting community has been investing considerable efforts to design standard and fair nature runs for OSSE studies (e.g., Masutani et al., 2007; Andersson and Masutani, 2010; Errico et al., 2013; Hoffman and Atlas, 2016). These standardized nature runs use state-of-the-art numerical model simulations that climatologically match the real atmosphere and contain realistic differences from the forecast model.

This chapter aims to evaluate different RO constellation designs by quantifying the ionospheric specification impact of assimilating EDP observations into a coupled I-T model. We do this by adopting a comprehensive OSSE approach that overcomes the limitations of past RO EDP OSSE studies. The nature run is performed using the Whole Atmosphere Model-Ionosphere Plasmasphere Electrodynamics (WAM-IPE) (Akmaev, 2011; Maruyama et al., 2016), and the forecast coupled I-T model used in the DA framework is the TIEGCM developed by NCAR (Qian et al., 2014; Richmond et al., 1992). Here, synthetic EDPs are retrieved from the nature run WAM-IPE simulation through an extensive Abel inversion procedure combined with simulated RO limb sounding geometries between the GNSS and hypothetical RO constellations. This Abel inversion procedure is built on the operational procedure used for the COSMIC-2 EDP data product. Synthetic EDP observations used in this chapter therefore include realistic Abel inversion errors, that cannot be represented by directly sampling electron density from the nature run at RO tangent points. A widely-

used ensemble DA framework, the EAKF (Anderson, 2001), developed by NCAR's DART (Anderson et al., 2009a) is run with the TIEGCM, denoted as DART-TIEGCM. The OSSEs are run for a popularly studied event, the week of the March 2015 St. Patrick's Day storm. A total of ten OSSEs are performed for the different permutations of the four base virtual LEO constellation configurations. To address what constellation design is "best", evaluated across different ionospheric regions, the results from these OSSEs are compared using various metrics including key ionospheric parameters of TEC, N_mF_2 and h_mF_2, as well as the three-dimensional plasma density structure.

In the following sections, Section 2.2 provides details for the EDP Abel retrieval and its errors as well as the OSSE design. Section 2.3 provides the OSSE results, including assimilation impact, a relative OSSE ranking metric, and a potential limit to observation impact. Section 2.4 contains a general discussion assessing observation impact from DART-TIEGCM and Abel inversion errors, along with future work. Finally, Section 2.5 provides the conclusions.

2.2 Approach

A general overview of the OSSE framework is shown in Figure 2.1 with four workflow blocks: nature run, synthetic RO observations, DART-TIEGCM, and post-analysis. In the nature run block, a single model run instance is used to represent the "true" atmosphere, here using the WAM-IPE model that is detailed in Section 2.2.2. In the synthetic RO observation block, the assimilated observations are retrieved from the nature run output through simulating RO events between the RO and GNSS constellations. Each OSSE has an associated set of retrieved EDP observations as well as corresponding observation uncertainty quantification that is detailed in Section 2.2.3. The DART-TIEGCM block contains the data assimilation cycle where synthetic observations and the TIEGCM experiment model are combined and are discussed in Section 2.2.1. More details of how the TIEGCM ensemble is initialized and other experiment information are included in Section 2.2.4. The remaining

block is the post-analysis in which the estimated TIEGCM states (posteriors) are directly compared against the WAM-IPE nature run, discussed in Section 2.3.

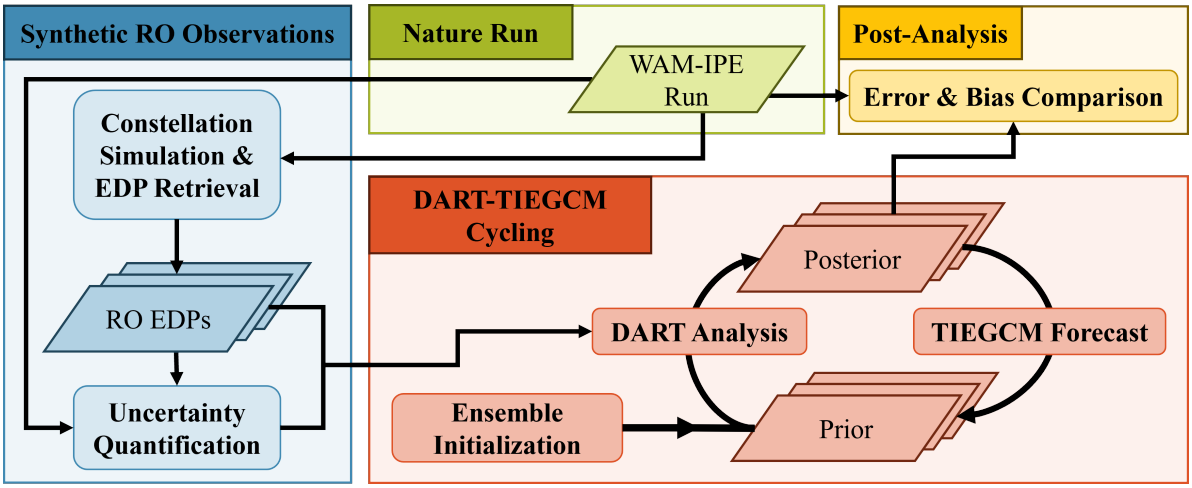

Figure 2.1: The OSSE framework used in this chapter is separated by blocks for the nature run, retrieval of synthetic observations, DART-TIEGCM cycling, and post-analysis. Data are represented by parallelograms and arrows indicate workflow direction.

2.2.1 Data Assimilation: DART-TIEGCM

In this chapter, the EAKF is employed as developed and implemented by DART (Anderson, 2001; Anderson et al., 2009a). In the EAKF, each observation has a spatially localized impact on model states determined by ensemble covariance information. This covariance information determines the statistical relationship between an observation and nearby surrounding model states and is dynamically estimated from the model ensemble that reflects nonlinear dynamics and physics. Further background for DART-TIEGCM is found from other studies (e.g., Hsu et al., 2014; Dietrich et al., 2022; Matsuo et al., 2013; Chartier et al., 2016; Chen et al., 2016; Lee et al., 2012; Kodikara et al., 2021). The DART software is detailed in Anderson et al. (2009a); Anderson and Collins (2007).

The TIEGCM v2.0 at 5° resolution developed by NCAR as the forecast model was used, solving a self-consistent set of first-principle equations of the I-T system and producing the three-dimensional, time-varying field of the thermosphere and ionosphere states. External

forcing in TIEGCM is specified through solar UV irradiance parameterized with respect to a daily value of the F10.7 index (F10.7), and lower boundary tides through the Global Scale Wave Model (GSWM) (Hagan and Forbes, 2002, 2003). The empirical Heelis convection model and an empirical auroral model specified magnetospheric forcing in TIEGCM.

2.2.2 Nature Run (Truth) Model: WAM-IPE

The nature run simulation, which serves as the truth model, is achieved with a free run of the I-T coupled physics-based model WAM-IPE developed by NOAA. There are several differences in how the I-T physics and dynamics are solved between the TIEGCM and WAM-IPE. These differences are expected to manifest as forecast model biases and likely widen during the storm period. WAM is a spectral whole atmosphere model, containing 150 pressure levels that solve neutral states from the surface up to $400 - 600$ km altitudes, output at about 2° horizontal resolution (Akmaev, 2011). IPE solves plasma state physics along flux tubes in the semi-Lagrangian reference frame, extending up into the plasmasphere encompassing 90 km to 10,000 km altitudes (Maruyama et al., 2016). In contrast, the TIEGCM solves both neutral and plasma states in the Euler reference frame, approximating the O^+ flux at the upper boundary, and using lower boundary tide conditions specified by GSWM. In WAM-IPE, solar irradiance is also parameterized using daily F10.7 but magnetospheric forcing is specified by an empirical Weimer convection model driven by solar wind states at 1-minute cadence. These model differences are expected to introduce distinctive ionosphere biases partly corrected by the assimilation of EDP observations. The details for the WAM-IPE nature run and the TIEGCM experiment ensemble are available in Section 2.2.4.

2.2.3 Virtual Constellations

This chapter uses four base virtual LEO constellation configurations, derived from the F3/C and F7/C2 constellations, to design ten hypothetical RO constellation configurations.

Each base constellation consists of six satellites with the same inclination and altitude and at separate orbital planes. In a similar mode of operation to that used by F7/C2, we simulate the LEO constellation orbits and the GPS and GLONASS radio ray paths to generate synthetic RO events. The base constellation parameters are as follows: (i) a 520 km altitude and 24° inclination constellation (similar to F7/C2), (ii) a 520 km altitude and 72° inclination constellation, (iii) an 800 km altitude and 24° inclination constellation, and (iv) an 800 km altitude and 72° inclination constellation (similar to F3/C). All ten OSSE combinations of one or two base virtual constellations are listed in Table 2.1. Each OSSE is referenced according to a short-hand notation, with the first two digits referencing the constellation altitude, and the second two digits referencing the constellation inclination. For instance, OSSE 1, with the short-hand notation 5024, is performed using the LEO constellation of satellites at 520 km altitude and 24° inclination.

Within each OSSE, we assimilate EDPs from 160 km to 500 km altitude at 10 km vertical sampling intervals to update the DART state vector containing electron density, e^-, and atomic oxygen ion, O^+. Observation errors are assigned to each electron density using the variances determined from the EDP uncertainty quantification process detailed in Section 2.2.3.2. The RO tangent point locations for each of these base constellations for a full day of observations are shown in Figure 2.2 to illustrate their respective coverage. As expected, the low-inclination constellations provide only low- and mid-latitude observations, while the high-inclination constellations provide observations in all latitude regions, at the cost of less dense spatial coverage.

2.2.3.1 Synthetic EDP Retrieval Using RO Simulation and Abel Inversion

Synthetic RO EDPs are generated from the WAM-IPE nature run simulation with the typical EDP retrieval processes, as detailed in Hajj and Romans (1998); Gorbunov and Kornblueh (2001). Specifically, we use the Abel inversion algorithm adapted from the operational data product procedure used to generate ionPrf files from F3/C and F7/C2. The sounding

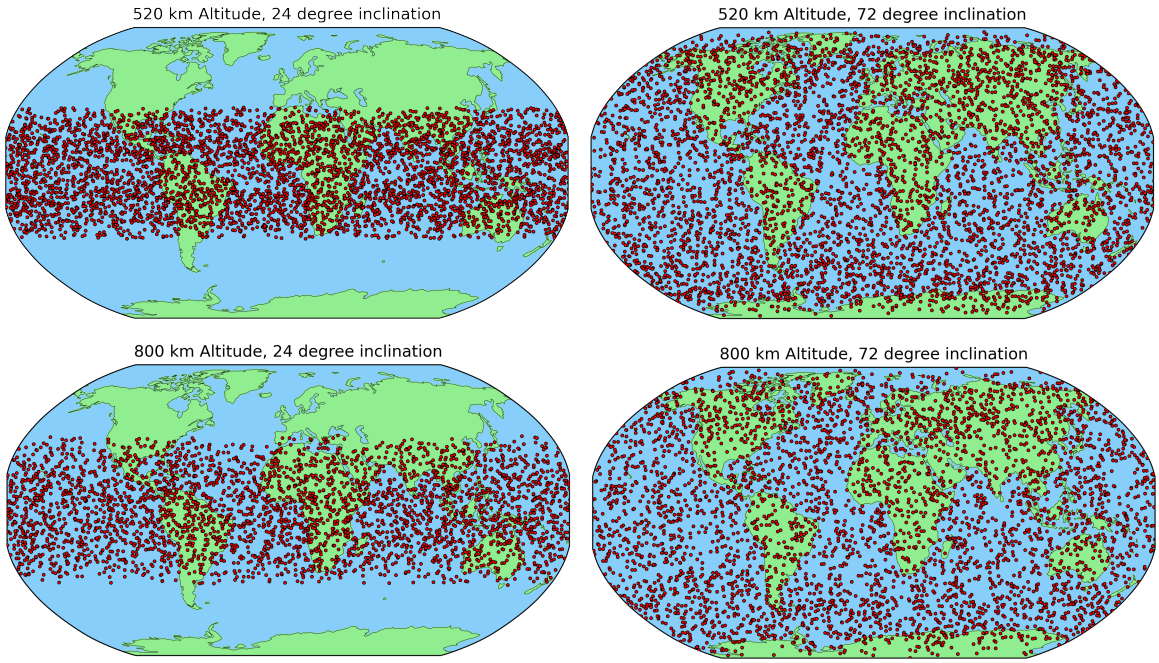

Figure 2.2: The RO observation tangent points are shown for the full day of March 13th at 300 km altitude. Shown for the four base virtual LEO constellation configurations.

Table 2.1: List of 10 OSSEs for different base LEO satellite constellation designs. For short-hand notation, the first two digits reference the constellation altitude and the last two digits reference the constellation inclination.

Experiment Name	LEO Constellations	Short-Hand Notation
OSSE 1	520 km alt, 24° inc	5024
OSSE 2	520 km alt, 72° inc	5072
OSSE 3	800 km alt, 24° inc	8024
OSSE 4	800 km alt, 72° inc	8072
OSSE 5	520 km alt, 24° inc & 800 km alt, 72° inc	5024 & 8072
OSSE 6	520 km alt, 24° inc & 520 km alt, 72° inc	5024 & 5072
OSSE 7	520 km alt, 24° inc & 800 km alt, 24° inc	5024 & 8024
OSSE 8	800 km alt, 24° inc & 800 km alt, 72° inc	8024 & 8072
OSSE 9	520 km alt, 72° inc & 800 km alt, 72° inc	5072 & 8072
OSSE 10	520 km alt, 72° inc & 800 km alt, 24° inc	5072 & 8024

paths from GNSS satellites to LEO RO satellites are used to generate the synthetic slant TEC profiles. For a typical RO sounding there is an occultation side and an auxiliary side, where the auxiliary side passes through both the upper ionosphere and plasmasphere, and the occultation side passes through the ionosphere, atmosphere, and plasmasphere. Here, WAM-IPE's ionosphere extension provides plasmasphere information. The resulting calibrated slant TEC profile comes from subtracting the auxiliary side TEC profile from the occultation side TEC profile and contains only the impact of the ionosphere. The synthetic EDPs are then retrieved by applying Abel inversion to these synthetic calibrated slant TEC profiles. The synthetic EDP data retrieved in this chapter thus contain the same systemic error as real ionPrf data products, ensuring the OSSE results more closely reflect reality.

2.2.3.2 Uncertainty Quantification of Synthetic EDPs

To determine observation uncertainties necessary for DA, the EDP errors due to Abel inversion are quantified. Observation errors are calculated using the difference between synthetic EDPs and the modeled electron density distribution from the WAM-IPE nature run. Sample standard deviations are computed after binning difference data for the following parameters: day of year, constellation inclination, altitude, magnetic latitude, and solar local time. Four solar local time (LT) bins are used: LTs $4-10$, LTs $10-16$, LTs $16-22$, and LTs $22-4$. LEO constellation altitude was found to have a negligible effect on errors. Similar studies with EDP observations have used percentage errors over local time, altitude, and magnetic latitude (Lee et al., 2013; Liu et al., 2010; Yue et al., 2010), while we quantify errors using standard deviation. Standard deviations are computed from EDP samples within ± 5 km for a given altitude, and within $\pm 5^{\circ}$ for a given latitude. An example of the calculated EDP uncertainties for March 13th at 300 km is shown in Figure 2.3. Notable features are the distinct difference in the error magnitude for the four solar local time bins and the impact that constellation inclination has on error magnitudes for the LT $16-22$ in the equatorial latitudes. Over these local times, there are highly variable spatial features such as the EIA

and the prereversal enhancement. The pronounced dependence on constellation inclinations can also be due to smaller low-latitude observation counts for the high-inclination orbit (shown in Appendix C Figure C.1).

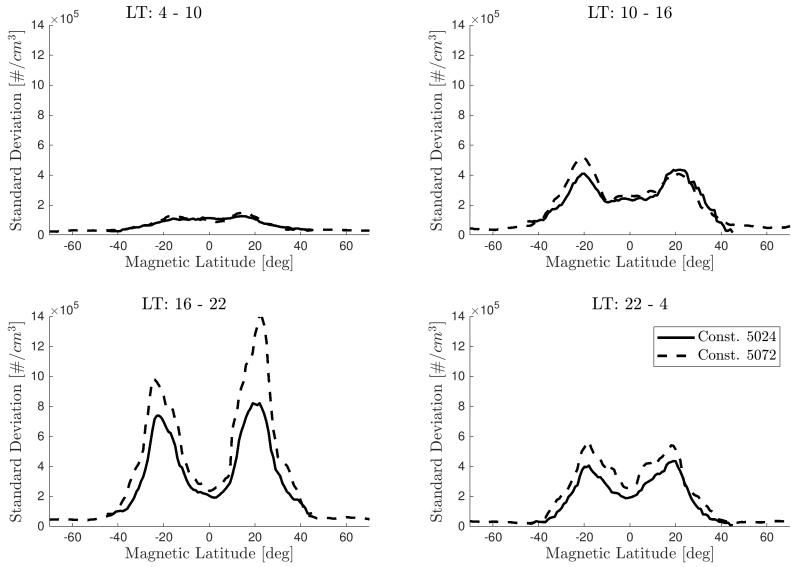

Figure 2.3: Standard deviations attributed to EDP observations. Shown for two constellations, 5024 and 5072, at 300 km altitude on March 13th. Standard deviations are computed from the difference between synthetic EDPs and plasma density from the WAM-IPE nature run, binning data with respect to the day of the year, constellation inclination, altitude, magnetic latitude, and solar local time.

The Abel retrieval errors are furthermore characterized for N_mF_2, h_mF_2 and over multiple EDP altitudes as shown in Figure 2.4. For N_mF_2, we see peak errors of 85% near the South Atlantic Anomaly (SAA), while the global error average is 18%, with structures following Earth's magnetic field lines. As expected, we see very small errors for h_mF_2 with percentage errors peaking at 17% and averaging 4%. As for the altitude variations of errors, we see substantial errors at 200 km altitude, where these errors are considerably higher than previous studies that showed low altitude errors to peak around 200% (Liu et al., 2010; Yue et al., 2010). In these two studies, Liu et al. (2010) uses IRI as the truth model, and Yue et al. (2010) uses NeQuick as the truth model, two very different models from WAM-IPE. These large errors are captured in the calculated observation uncertainties, and the data assimilation impact is discussed later in Section 2.3. Errors are smaller at 300 km, with peaks along the magnetic and near the SAA. Outside these two regions, errors are below 40%, with a median error of 25%. For 400 and 500 km altitudes, we see increasingly smaller errors, with a peak error near the SAA and a global average of 17%. There are some spurious high

errors seen at high latitudes where there are low observation counts. It is noted these errors are highly dependent on solar LT, with two example local time cases shown in Appendix C Figures C.2 and C.3.

These large errors seen in Figure 2.4 come primarily from break-downs of the spherical symmetry assumption used in Abel inversion. The breakdowns of this assimilation are expected to impact regions with large horizontal gradients in electron density distribution, such as near and below the magnetic equator and EIA. The impact is less acute with increasing altitude. These errors are well-captured within uncertainty calculations considered in this chapter. An additional source of RO errors is from onboard GNSS receivers as well as receiver errors, but these errors are not considered here.

2.2.4 Experiment Set-up

The OSSE period is the St. Patrick's Day storm of March 2015, with observed solar and geomagnetic indices and IMF solar wind parameters shown in Figure 2.5. The nature run of WAM-IPE is a model free-run, specifying geomagnetic forcing using the Weimer model with input IMF solar wind parameters and the F10.7 index for solar irradiance. The OSSE is broken into two periods, the preceding quiet period and storm-time. The quiet period begins at UT00 on March 13th and ends at UT23 on March 16th. Localization is done using the Gaspari-Cohn (GC) function (Gaspari and Cohn, 1999) with a GC radius of 0.2 radians ($\sim$ 1300 km) without vertical localization, so observations have an impact on all pressure levels. We do not use ensemble inflation. As the upper atmosphere is strongly influenced by external forcing, the TIEGCM ensemble is initialized using perturbed solar irradiance with the F10.7 index and geomagnetic indices driven with the Heelis model for 90 ensemble members. These perturbations are normally distributed and kept constant through the quiet period. The sampled F10.7 indices are sampled from $d_{F10.7} \sim \mathcal{N}(120, 4^2)$ and Heelis input is defined through the hemispheric power, $d_{HP} \sim \mathcal{N}(22, 4^2)$ and the cross-tail potential $d_{\Phi} \sim \mathcal{N}(46, 8^2)$. The ensemble is initialized through a 7-day spin-up period to reach a steady state

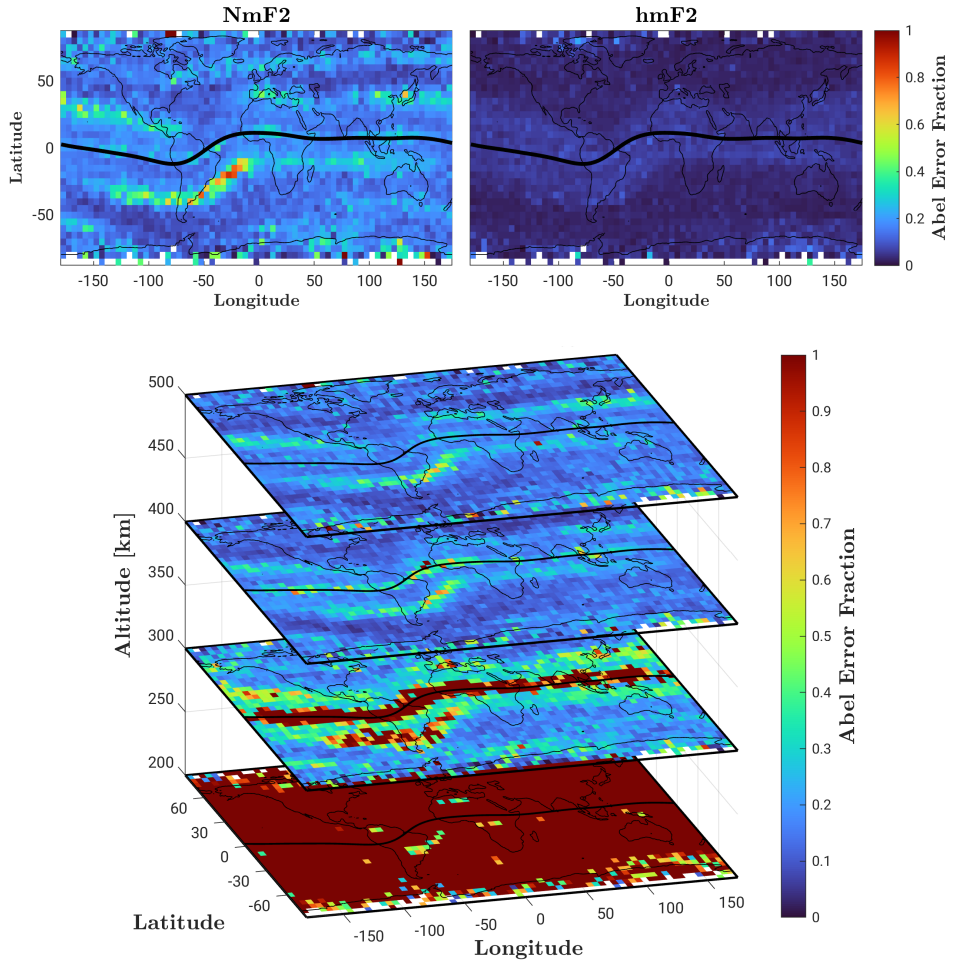

Figure 2.4: Binned average fractional error due to Abel retrieval, across all local times. Shown for N_mF_2, h_mF_2 and at each EDP altitude. The black line indicates the magnetic equator. Blank regions are due to a lack of observation coverage.

for the start of the OSSE. For the storm period, the TIEGCM magnetospheric drivers have updated samples, sampling from $d_{HP} \sim \mathcal{N}(115, 10^2)$ and $d_{\Phi} \sim \mathcal{N}(135, 20^2)$ with the same quiet period F10.7 samples. Results for this chapter are assessed on a vertical altitude grid, where observations and the TIEGCM and WAM-IPE grids are all interpolated to constant altitudes. For OSSE post-analysis, the performance of the experiment ensemble (with EDP assimilation) is assessed against an identical control ensemble without data assimilation. Information detailing the truth run and experiment ensemble are tabulated in Appendix B.

Additional quality control is necessary for DA with observation flags and rejection to avoid assimilating poor-quality observations. We reject observations for three reasons: negative values, outside an outlier threshold, and a failed forward operator, with rejection rates shown in Figure 2.6a. Negative values are the most common reason for rejection, notably at low altitudes where observation quality is worst. Between $10-50\%$ of observations are rejected between $160 - 250$ km altitude, with rejection rates considerably improving at higher altitudes. We reject observations that are extreme outliers using a 10 standard deviation threshold. In the OSSE observation counts shown in Figure 2.6b, 520 km altitude constellations show greater observation counts than the 800 km altitude constellations.

2.3 OSSE Results

2.3.1 OSSE Ionospheric Results

First highlighting the quiet period, we show the impact of the first analysis step at UT01 on March 13th in Figure 2.7, for 300 km altitude. In the top row is the WAM-IPE nature run, where synthetic observations are derived, and the no-assimilation control (identical to the prior here), for electron densities at 300 km altitude. In the middle row are the posterior electron densities for OSSEs $1 - 4$, each containing a single constellation. The first notable bias between the WAM-IPE and TIEGCM control is the EIA, where WAM-IPE produces higher magnitudes and sharper horizontal gradients. High electron densities

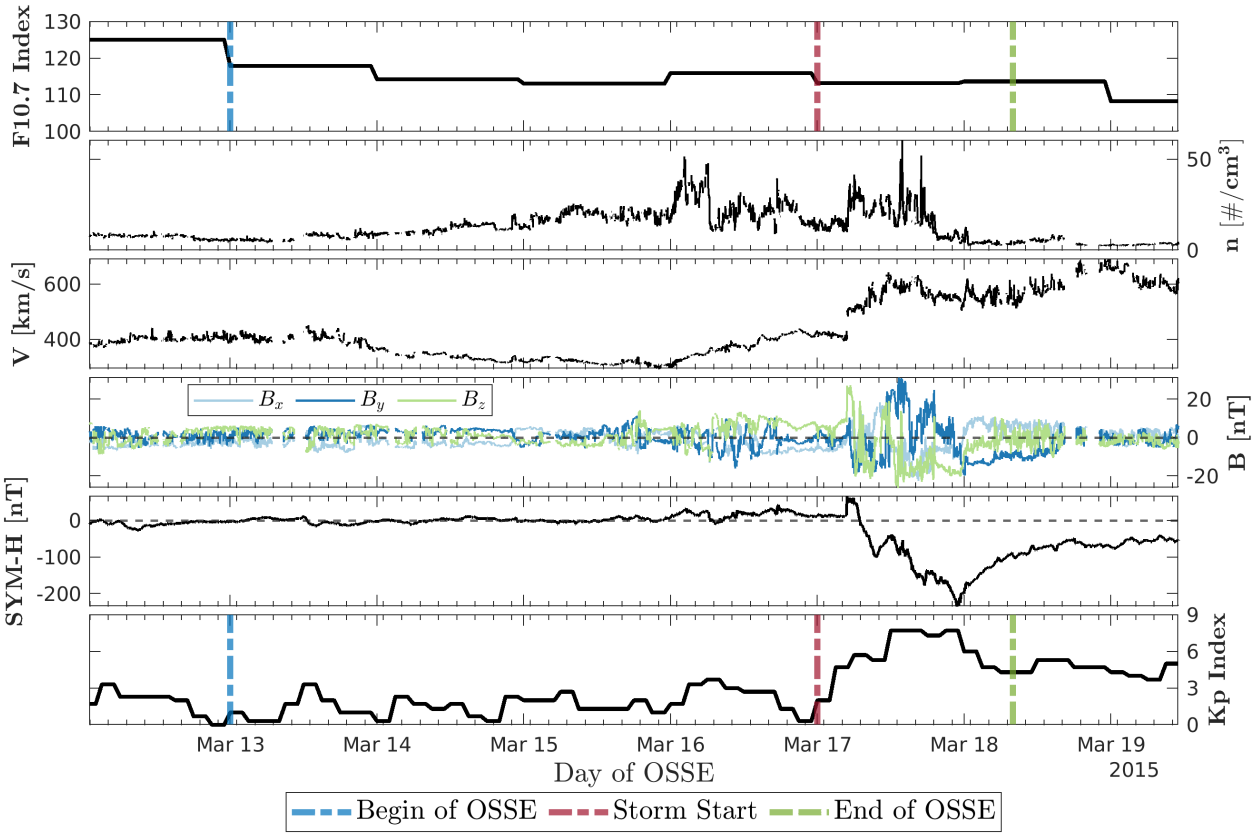

Figure 2.5: Solar (F10.7), solar wind conditions, and geomagnetic indices (Kp and Sym-H) for the week event. Solar wind states include plasma density, n, flow speed, V, and three magnetic field components, B. Vertical lines denote the OSSE quiet and storm periods.

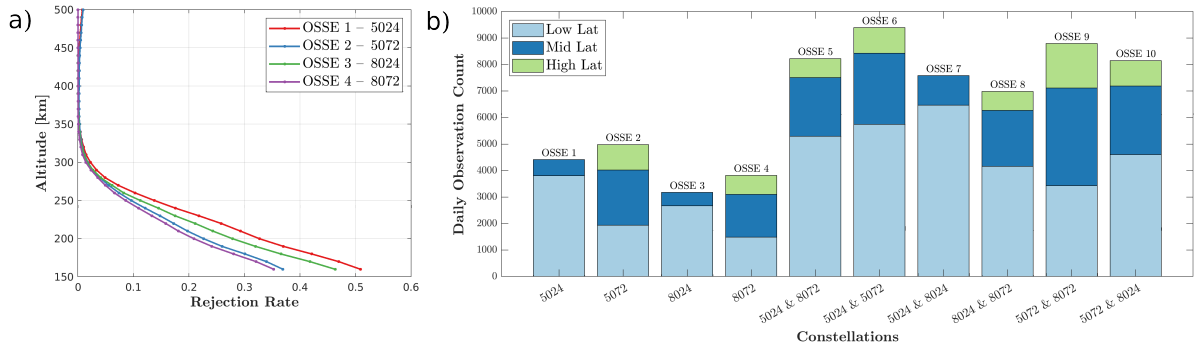

Figure 2.6: a) Shows the observation rejection rate as a function of altitude. b) Shows the daily EDP observation count for each OSSE constellation configuration, separated by latitude region.

additionally extend into the night side for WAM-IPE. In contrast, the TIEGCM has a less prominent EIA peak and smoother spatial gradients, stretching for longer length scales, and has EIA peaks westward of what WAM-IPE shows. Comparing electron density magnitudes between the TIEGCM and WAM-IPE, the TIEGCM under-represents electron densities on the day side and over-represents electron densities on the night side. Assessing the posterior electron density states, seen in the middle row of Figure 2.7, the analysis step is as expected positively impacting posterior states, such as in increasing the EIA magnitude and better replicating the extension of higher electron density magnitudes into the low-latitude night side. For high inclination constellations 5072 and 8072, electron density magnitudes are noticeably reduced in the night side high-latitudes.

An illustration of the performance of the analysis update is shown in the bottom row of Figure 2.7. The analysis bias improvement is defined as

$$\textbf{Bias Improve} = |\bar{\boldsymbol{x}}^{prior} - \boldsymbol{x}^{NR}| - |\bar{\boldsymbol{x}}^{post} - \boldsymbol{x}^{NR}| \tag{2.1}$$

where $|\boldsymbol{x}|$ is the element-wise absolute value of mean OSSE state vectors $\bar{\boldsymbol{x}}^{prior}, \bar{\boldsymbol{x}}^{post} \in \mathbb{R}^n$ and nature run state vector $\boldsymbol{x}^{NR} \in \mathbb{R}^n$. Bias improvement is shown in the bottom row of Figure 2.7, with blue regions indicating improved electron density biases and red regions indicating worsened biases. For state grid point comparisons between the two models, we down-sample the WAM-IPE and interpolate as needed to the TIEGCM's 5° grid resolution. At locations where WAM-IPE shows large electron density magnitudes, biases overall improve when observations are available. This is most evident for constellations 5024 and 8024 at peak EIA magnitudes. In red regions directly off WAM-IPE's EIA, we see the analysis step worsen biases. Generally, there are red worsen regions where there is a large gradient in WAM-IPE electron densities. More discussion of these worsening regions is addressed in Section 2.4, and they are largely explained by Abel retrieval errors and improper background covariance. A similar figure for the storm period is shown in Appendix C Figure C.4.

As the primary metric to assess OSSE performance, we use the root-mean-square error

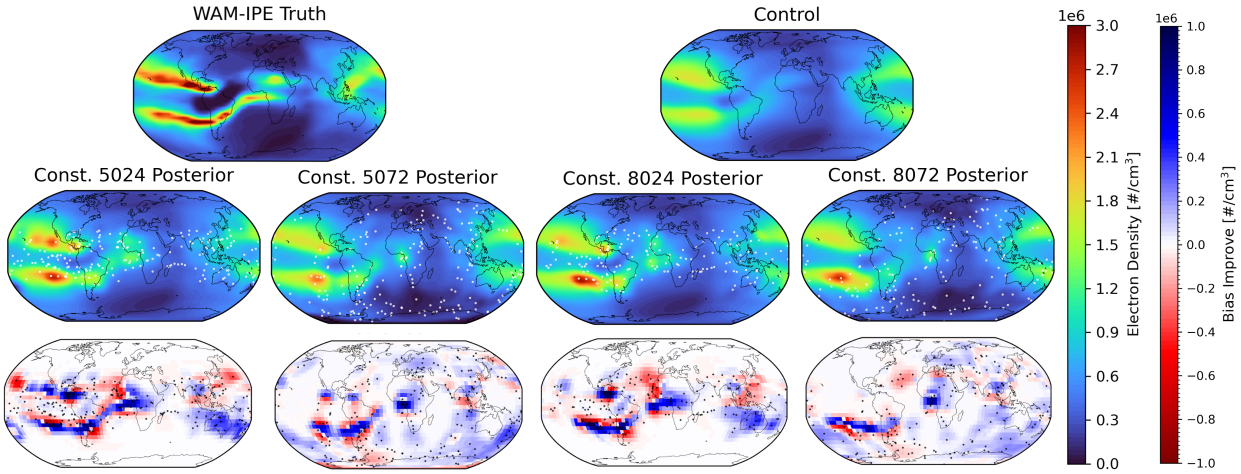

Figure 2.7: Electron density shown for the nature run, control, and OSSEs 1-4 posteriors at 300 km altitude at UT01 on March 13th, the first analysis step. The middle row shows posterior states, where white points are the assimilated tangent-point observations at 300 km altitude. Bias improvement, shown on the bottom row, is illustrated with blue regions providing improvement and red regions worsening.

(RMSE) defined as

$$\text{RMSE} = \sqrt{\frac{\sum_{j=1}^{N} \left(x_j^{NR} - \overline{x}_j^{exp}\right)^2}{N}} \tag{2.2}$$

where x_j^{NR} is the jth WAM-IPE state, $\overline{x}_j^{exp}$ is the jth ensemble mean OSSE state, and N is the total number of states. As RMSE is a magnitude-dependent quantity, we separate results into three latitude regions, where low latitude is between $-30°$ and $+30°$, middle latitude is between $-30°$ and $-60°$ as well as $30°$ and $+60°$, and high latitude is below $-60°$ and above $60°$. We show results for N_mF_2, h_mF_2, TEC, and altitude electron densities. We compare relative posterior RMSE performance against a no-assimilation control.

The N_mF_2 RMSE for all ten OSSEs is shown in Figure 2.8 for both quiet and storm periods. At high latitudes, the best performance is seen from OSSE 9 including constellations 5072 and 8072, the constellations with the most high-latitude coverage. As expected, OSSEs 1, 3, and 7 have no high-latitude coverage resulting in negligible impact on high-latitude errors. At low latitudes, OSSE 7, containing constellations 5024 and 8024, performs the best with the highest coverage of observations. Additionally, OSSEs 3 and 4 containing only constellations 5072 and 8072 have the least error improvement. At mid-latitudes, the OSSEs containing just constellations 5024 or 8024 have the worst performance, OSSEs 1,3 and 7. High inclination OSSEs show consistent improvement in N_mF_2 RMSE at low latitudes and in high latitudes.

The N_mF_2 posterior RMSEs for the storm period are also shown in Figure 2.8. As with the quiet period at low and high latitudes, there is a consistent improvement in RMSE over the control for the storm period, with more observation coverage of a region providing better performance. OSSE 7 with constellations 5024 and 8024 performs the best at low latitudes, and OSSE 9 with constellations 5072 and 8072 performs the best at high latitudes. It is also noted that the control RMSE increases for the storm period due to increasing model biases between the TIEGCM and WAM-IPE.

Further RMSE time-series plots are available in Appendix C. The TEC RMSE time

series is shown in Appendix C Figure C.5, showing very similar performance to N_mF_2 RMSEs. h_mF_2 RMSEs are additionally shown in Appendix C Figure C.6. For h_mF_2, we see only a slight impact on posterior RMSEs as compared with the no-assimilation control. This negligible performance is primarily attributed to a lack of state spread in h_mF_2, as we expect h_mF_2 observation quality to be very high, see Figure 2.4. Additional figures, including RMSE at each altitude (200, 300, 400 and 500 km) are available in the Appendix C Figures C.7, C.8, C.9 and C.10. Altitude RMSEs show similar performance results as the N_mF_2 RMSEs except at 200 km altitude.

Observation comparisons at 200 km and 400 km altitude are shown in Figure 2.9, where these contain all observations from all OSSEs and are shown for the quiet period at a given altitude. Here, WAM-IPE electron density states at EDP observation tangent points are shown against the Abel retrieval, TIEGCM prior and TIEGCM posterior, and separated by latitude region. Each plot is a density map of the observations in each range, normalized by the respective max binned observation count, shown in units of 10^5 cm^{-3}. The goodness of fit to the line $x = y$, R^2, and the number of observations, N, are provided for each sub-figure. For 400 km altitude, there is quite good agreement among the WAM-IPE states and Abel retrievals. The TIEGCM prior biases are most noticeable at the low latitudes and for the 400 km altitudes, there is consistent improvement in posterior agreement and R^2. Posterior states at 400 km perform best at high latitudes and worst at low latitudes, likely due to EIA biases. We see all Abel retrieval values of R^2 greater than or equal to 0.78. Observation comparisons for 300 and 500 km altitudes are shown in Appendix C Figure C.11 and show similar results to 400 km altitude.

In the left sub-figure of Figure 2.9 for 200 km altitude, we see very different results. For all latitude regions, the Abel retrieval and the TIEGCM prior and posterior are all severely under-biased to the WAM-IPE nature run electron densities. Still, we do see improvement in agreement for posterior states at the middle and high latitudes, while the 200 km low latitudes show worsening error. The low and middle latitudes priors have surprisingly good

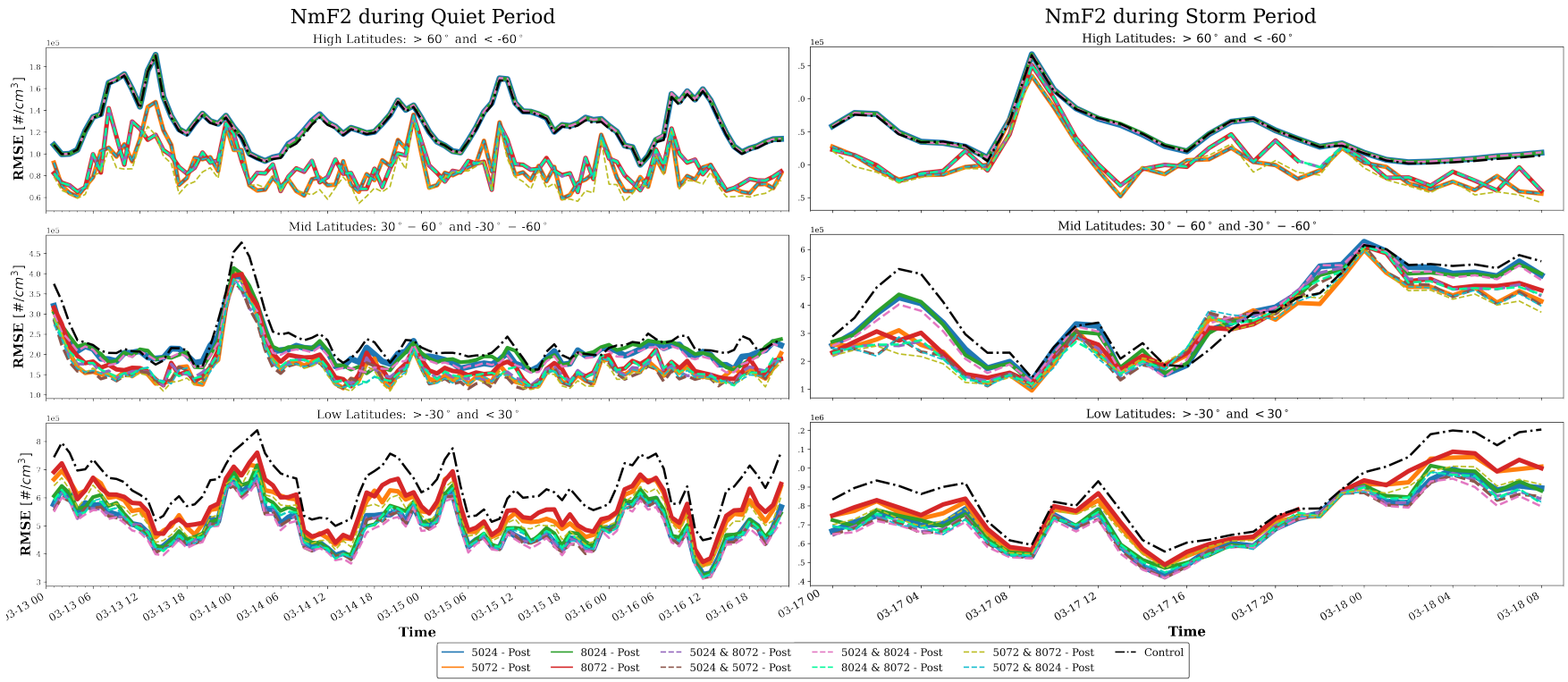

Figure 2.8: The N_mF_2 RMSE for each OSSE throughout the quiet period (left) and storm period (right). Solid lines indicate single constellation OSSEs and dashed lines indicate two constellation OSSEs. Performance is assessed compared to a no-assimilation control in the dashed black curve.

R^2 values, due to many states being very low magnitude (not very visible on this plot axis scale), while the Abel retrieval at low latitudes has a negative R^2 value.

2.3.2 Ranking Metric

To further quantify relative OSSE performance, we devise a simple high-level ranking metric. Using the time series of RMSEs calculated for N_mF_2, h_mF_2, TEC, and altitude electron densities, each OSSE is ranked for each hour. The ten OSSEs are ordered and ranked according to each OSSE's RMSE, 1 through 10, with 1 having the lowest error (best performance) and 10 having the highest error (worst performance). Averaging hourly OSSE ranks over the whole experiment period then gives the ranking metric.

The vertically integrated TEC ranking metric is shown in Figure 2.10 for the three latitude bins and globally, for both the quiet and storm periods. Table cells are color-coated with deep green indicating the best performance (close to 1) and deep red indicating the worst performance (close to 10). For low latitudes, OSSE 7 (5024 and 8024) performs the best with the highest coverage of low latitudes. For high latitudes, OSSE 9 (5072 and 8072) performs the best with the highest coverage in that respective region. OSSEs that mix high and low inclination constellations, OSSE 5, 6, 8, and 10, generally do well across the board. OSSE performances are similar for quiet and storm conditions as most quiet and storm rankings are within a rank of 1. For global rankings, these typically reflect performance at the low and mid-latitudes, where the largest electron density magnitudes are present and thus dominate RMSEs. Additional ranking metric tables are available for N_mF_2, h_mF_2, and electron density at altitudes 200, 300, 400, and 500 km in Appendix C Figures C.13, C.14 and C.12. It is noted that TEC, N_mF_2, and 300-500 km altitude ranking values all indicated similar results.

To explain ranking metrics performance, we collect all the rankings for the quiet period at 200, 300, 400, and 500 km electron density altitudes (Appendix C Figure C.12) and plot them against their daily average observation count, shown in Figure 2.11. The left sub-figure

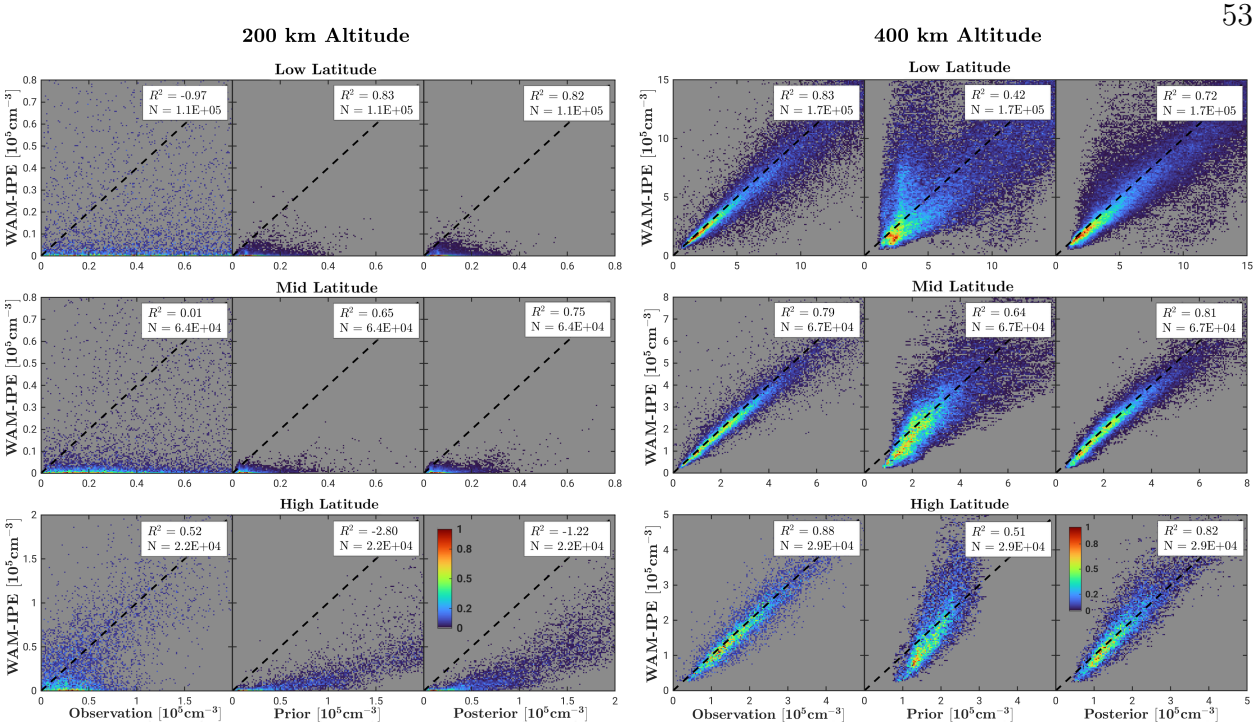

Figure 2.9: Comparison of electron density observations at given altitudes (200 and 400 km), with the nature run WAM-IPE state shown against the Abel retrieval, TIEGCM prior, and TIEGCM posterior states. Density heat maps are shown, with counts normalized by the max bin count for that subplot. Units are all in $10^5 cm^{-3}$.

		Low Lat	*Mid Lat*	*High Lat*	*Global*	*Low Lat*	*Mid Lat*	*High Lat*	*Global*
Experiment Name	**Constellations**	**Quiet**				**Storm**			
OSSE 1	5024	4.98	9.31	8.8	5.85	5.7	8.42	8.58	6.79
OSSE 2	5072	9.09	5.37	3.97	9.03	7.97	4.09	3.06	7.09
OSSE 3	8024	6.8	9.28	8.96	7.24	5.82	6.94	9.06	6.48
OSSE 4	8072	9.91	6.9	4.27	9.91	9.67	5.18	4.55	9.03
OSSE 5	5024 & 8072	3.6	4	4.84	3.05	4.91	6.3	5.42	4.88
OSSE 6	5024 & 5072	2.27	2.55	4.37	1.64	3.09	4.7	3.85	2.76
OSSE 7	5024 & 8024	1.34	7.71	8.93	2.79	2.21	7.82	8.73	4.42
OSSE 8	8024 & 8072	5.43	4.53	4.55	4.93	4.85	5.15	5.48	4.82
OSSE 9	5072 & 8072	7.83	2.31	2.19	7.43	7.33	2.82	2.45	5.94
OSSE 10	5072 & 8024	3.77	2.81	4.13	3.13	3.45	3.58	3.82	2.79

Figure 2.10: OSSE ranking metric for TEC. Rankings are averaged over the quiet period defined from March 13th UT01 to March 16th UT022 and averaged over the storm period defined from March 17th UT00 to March 18th UT08. Values close to 1 indicate the best performance and values close to 10 indicate the worst performance.

shows results collected for altitudes 300, 400, and 500 km, and the right shows rankings for 200 km, also splitting for low, mid, and high latitudes. Very simply, where we have more observations, we see better OSSE performance with lower metric ranks as shown by a strong negative correlation. This finding holds for all regions except for one: 200 km altitude at low latitudes. These values are reflected in Appendix C Figure C.12 where worsening ranking is seen for 200 km in OSSEs, as well as in Figure 2.9 at 200 km with little agreement between WAM-IPE states and Abel retrieved EDPs. Regardless, we still see improvement in the ranking metric at 200 km altitudes for mid- and high-latitudes.

A couple of additional results are as follows. First, we see more observations from the 520 km altitude constellations than the 800 km altitude constellations, and this directly corresponds to better ranking metrics for these OSSEs. With this, it is arguable that OSSE 6 with 5024 and 5072 is the best performing OSSE (as reflected in the global ranking metric in Figure 2.10). We see Constellation 8024 has 27% fewer profiles than Constellation 5024; we see Constellation 8072 has 24% fewer profiles than Constellation 5072. The differences are likely explained by the shorter orbit period of the 520 km altitude constellations, enabling more limb passes and RO events. Secondly, OSSE 9 with 5072 and 8072 performs poorly for low latitude observations, as one might expect; however from Figure 2.6, OSSE 9 performs worse than OSSEs 1 (5024) and 3 (8024) with comparable low-latitude coverage. This worse performance can potentially be explained by larger observation errors that the high inclination constellations show at low latitudes, as illustrated most evidently in the bottom left panel of Figure 2.3. Thus a combination of a low- and high-inclination constellation provides the best global coverage.

2.3.3 Observation Performance Limit

An additional question was raised when designing an observing system and adding more observations: what is the potential performance limit? We define a "performance limit" as the point when assimilating more observations plateaus improving OSSE errors.

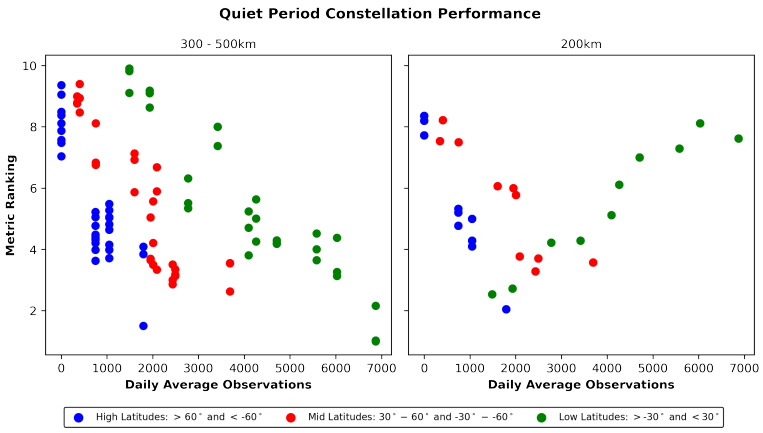

Figure 2.11: The relationship between the latitude observation counts shown in Figure 2.6b and the ranking metrics in Appendix C Figures C.12. Again noting that 1 indicates the best ranking and 10 indicates the worst ranking. All show a negative correlation (improvement with more observations) except for 200 km at low latitudes.

To address this question with available OSSE results, we compute the RMSE for all grid points for the low-, mid-, and high-latitude regions of each OSSE, as well as for the control. We then define the OSSE fractional improvement over the control as

$$\text{Fractional Improvement} = \frac{\text{RMSE}_{cntrl} - \text{RMSE}_{exp}}{\text{RMSE}_{cntrl}} \tag{2.3}$$

This is done for every hour of the OSSE and all ten OSSEs. Next binning over hourly observation counts we show the mean and notched box plot for the N_mF_2 RMSEs in Figure 2.12. For the low- and mid-latitudes, there is a steady improvement in performance with more observations and a visible leveling off, as the improvement is no longer statistically significant at the peak observation counts. For the endpoints of each latitude region, shaded regions have very small or very large spreads due to a limited number of samples. For high latitudes, the results are more noisy as we have fewer samples due to having only two constellations with high-latitude coverage. We see a positive trend in the high-latitude fractional improvement that does not appear to plateau. Results for TEC show very similar results to N_mF_2 (Appendix C Figure C.15), and h_mF_2 fractional improvement are less consistent (Appendix C Figure C.16). Further study is needed to investigate the cause of this performance limit, such as due to observation errors, background covariance, localization and other DA parameters, model errors, model resolution, or observation spatial density.

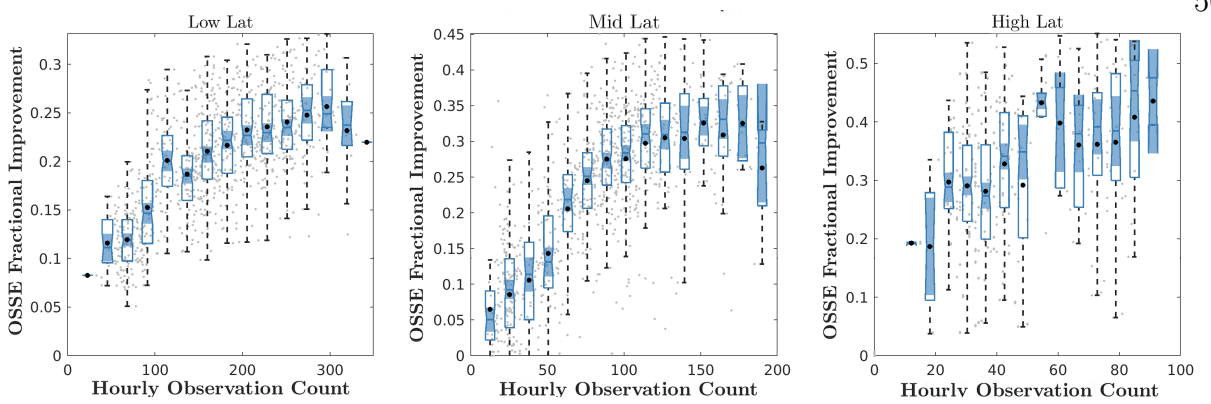

Figure 2.12: OSSE N_mF_2 RMSE fractional improvement over the control as a function of observation count, defined in Equation 2.3. Calculated for the entire N_mF_2 grid RMSE within each latitude band. Mean improvement (black dots) and notched box plots are averaged over count bins of all samples (grey dots). Non-overlapping shaded regions indicate the significant difference between medians (5% confidence).

2.4 Discussion

Returning to the initial question we first posed as to what constellation configuration is best: it depends. Simply put, with more observation coverage in a given region, we gain better ionosphere specification, with a combination of a low- and high-inclination constellation providing the best global coverage. Therefore, designing an RO constellation observing system depends on what regions we desire to study or monitor.

Fully simulating the Abel inversion retrieval for EDP observations allows us to evaluate the impact of Abel inversion errors within a DA framework, as compared with studies such as Hsu et al. (2014); Lee et al. (2013) that only perturbed using Gaussian errors. Previously documented Abel inversion errors are evident, notably at the low latitudes and low altitudes (Tsai et al., 2001), resulting in poor analysis updates. Abel inversion particularly has trouble reproducing the low electron densities in "plasma caves" beneath the EIA crests (Liu et al., 2010; Yue et al., 2010), as this is the one region (200 km, low latitude) we see the DA hurts electron density states. These were also expected from Figure 2.4 where there are considerably high Abel retrieval errors. Nevertheless, we do see a positive impact for 200

km altitudes at the mid- and high-latitudes. Additionally, as we move to higher altitudes, we see observations consistently provide positive data impact.

OSSE results suggest this region of very low electron densities is likely an inherent limitation of RO and the Abel inversion technique. As we move to lower altitudes, the radio signal passes become increasingly longer, comprising more of the ionosphere and yielding larger slant TEC observations. The Abel retrieved EDPs cannot resolve the WAM-IPE's low electron densities using large TEC observations, especially if the spherical symmetry assumption is increasingly broken, adding increasingly more observation noise. We also see many negative observations in this region, reducing data available for assimilation. Therefore we see RO EDPs to not be useful for ionospheric specification in this low latitude, low altitude region, supporting the conclusions of Lee et al. (2012).

To detail poor EDP performance, we highlight two assimilated profiles shown in Figure 2.13. We focus on the worsening regions of Constellation 5024 from Figure 2.7. We show the WAM-IPE nature run, Abel retrieval, and the TIEGCM prior and posterior at profile locations.

One source of poor analysis updates comes from DART-TIEGCM, exhibited by profile (a) of Figure 2.13. At this location, there is good agreement between the Abel retrieved EDP (and its assigned 1 standard deviation (std) uncertainty) and the WAM-IPE nature run. The RO event details of profile (a) are additionally shown in Appendix C Figure C.18 where the black tangent points are close to vertical and the red RO ray-passes align with the EIA gradients. This observation point is within EIA peak electron density, and as the EAKF locally updates states using the ensemble background covariance, an over-correction is performed for grid points off WAM-IPE's EIA structure. The regional impact of this observation is shown in the bottom plot of Figure 2.13, including the nature run WAM-IPE state at 300 km, TIEGCM's background electron density correlation, and the observation increment. The TIEGCM shows high background correlations extending beyond WAM-IPE's sharper electron density gradient, and the update is very much defined by

the isotropic GC localization. This poor update underscores the importance of having a good background covariance and is a necessary filter feature for global specification. Many studies have been devoted to improving the local update impact, either through improved background covariance or through localization (e.g., Lin et al., 2015; Hsu et al., 2018b; Forsythe et al., 2020; Zhang et al., 2023).

Another source of poor analysis updates, one very much a focus of this chapter, comes from Abel inversion errors, shown at point (b) of Figure 2.13. At this location, the prior EDP has fine agreement with WAM-IPE; however, the Abel inverted EDP is considerably more biased, and we see worse posterior error. This profile deviates from the typical Chapman function, instead showing a double peak structure in both the EDP observation and WAM-IPE RO tangent points. A view of this profile and the WAM-IPE states are shown in Appendix C Figure C.17, where the tangent points' quasi-vertical profile at high altitudes includes higher magnitude electron densities. The RO event geometry for profile (b) is also shown in Appendix C Figure C.18, where the tangent points span a large horizontal region. There is a large electron density gradient that the RO view angle crosses over two distinct ionospheric regions, introducing sizable errors into the Abel inversion retrieval. Ideally, this observation profile should be flagged for quality control and not assimilated, or the observation uncertainty should be considerably increased to more sufficiently account for the Abel inversion error.

It is noted as a caveat that the devised ranking metrics only provide a big-picture view of the relative OSSE results. These rankings do not indicate the magnitude of the relative OSSE performance and should be viewed in conjunction with the RMSE time series plots to gain a full perspective. Regardless, conclusions from these rankings generally support the findings from the RMSE time series. Additionally assessing errors through RMSE and with parameters TEC and N_mF_2 can simplify the global impression of ionosphere specification. These metrics are decidedly magnitude dependent, sometimes representing only the highest magnitude locations, e.g., the EIA or F_2 peak. The altitude profile of the electron density

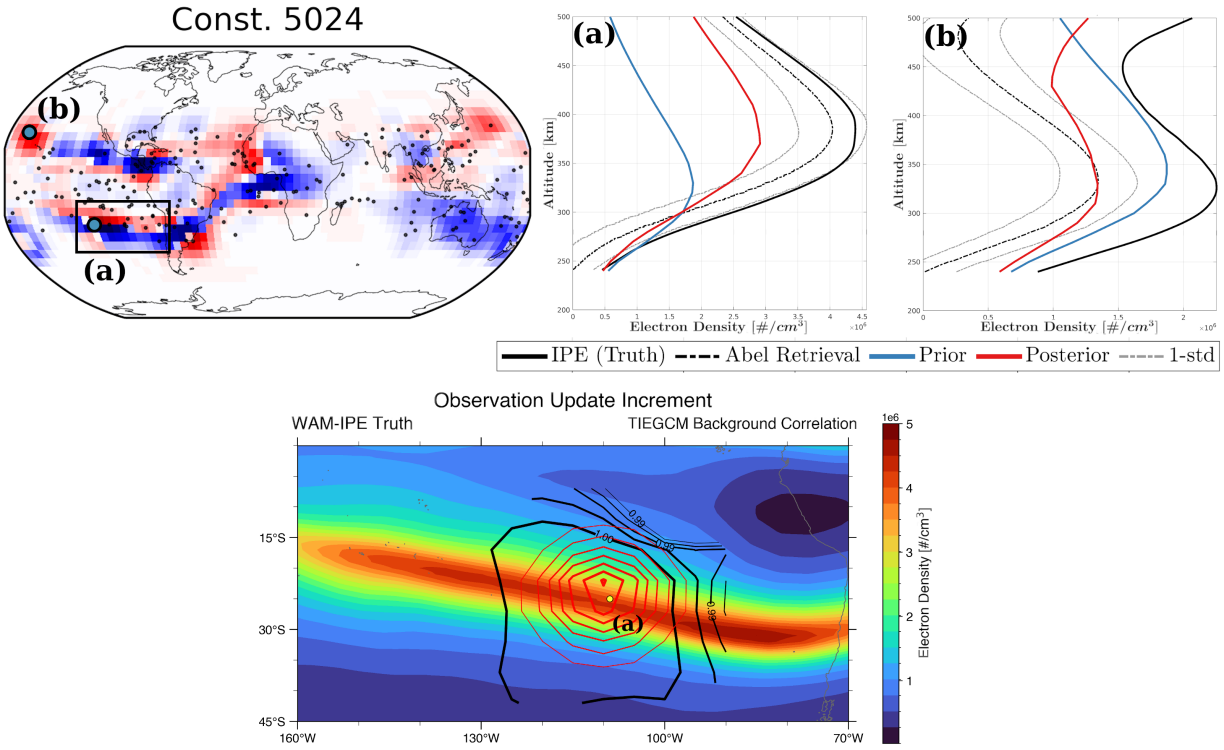

Figure 2.13: Highlighting two EDPs introducing poor analysis updates. Shown using the first analysis step of Constellation 5024 (same as in Figure 2.7). EDP (a) highlights poor background covariance, and EDP (b) highlights large Abel inversion error. The bottom contour plot shows the WAM-IPE electron density at 300 km, and the observation increment (red) and the TIEGCM background correlation (black).

can be very important for space weather influences, making ionospheric specification a three-dimensional problem that needs to be addressed through multiple metrics.

We focus in this chapter on the relative performance of all OSSEs, and the filter performed well enough for assessment. Filter features such as tuned localization, implementing inflation, and better ensemble initialization with more realistic geomagnetic forcing would all help to improve the data impact of the synthetic EDPs. One evident source of poor impact is the lack of h_mF_2 spread in the TIEGCM, as previously noted in Lee et al. (2012), that causes h_mF_2 improvement to be considerably less than expected given their low errors.

Another large restriction in filter performance was achieving sustained RMSE improvement from using a coupled I-T model due to plasma states having limited memory in the system. Non-updated neutral states in the TIEGCM quickly rebound posterior plasma states back to control states in the forecast step, showing only a 1-2 hour system memory. Previous studies have shown plasma forecasting only on the order of hours with ionosphere assimilation in coupled I-T models (Jee et al., 2007; Chartier et al., 2013). Neutral states have a longer forecasting memory (Chartier et al., 2013), and specifying neutral states such as oxygen composition has been shown to greatly improve plasma forecasting (Hsu et al., 2014). This would help the system retain plasma RMSE improvements when forecasting and see greater OSSE performance. Another possibility not included in this chapter is the potential to estimate neutral states using the EDP observations, which has been shown to positively impact composition, neutral temperature, and neutral winds (Matsuo and Hsu, 2021; Dietrich et al., 2022).

Accounting for realistic Abel inversion and forecast model errors in this chapter underscores the need for a more complete EDP error quantification and observation quality control. There still remains work needed to fully quantify Abel inversion errors, and quantify their impacts from breakdowns in the spherical symmetry assumption. In this chapter, there are two main error sources included in these OSSEs: errors from Abel inversion and errors within the DART-TIEGCM DA framework, and it is challenging to fully deconvolve

these two error sources. Future OSSE work could apply the same OSSE set-up while also running equivalent OSSEs with synthetic EDPs directly sampled at WAM-IPE locations, enabling direct comparisons of error impacts and more complete quantification of Abel inversion errors. Abel error fitting over altitude, magnetic latitude, and local time, as in Yue et al. (2010); Liu et al. (2010), was shown to not be sufficient in some cases. Additional error analysis capturing exactly how the spherical symmetry assumption is being broken is needed by analyzing the radio ray paths taken through the ionosphere. Better quantification of these Abel errors should improve DA performance in negatively impacted regions, and provide means for better observation quality control. Further, more advanced Abel inversion algorithms have improved low altitude observations errors and improved their DA impact (e.g., Pedatella et al., 2015; Wu, 2018; Chou et al., 2017; Tulasi Ram et al., 2016) and were not included in this chapter.

2.5 Conclusions

To inform future RO constellation mission planning and design, this chapter uses a comprehensive OSSE approach to evaluate the ionospheric specification impact of assimilating RO EDPs into a coupled I-T model. We perform ten OSSE configurations to evaluate four base hypothetical RO constellations. These RO constellations are modeled after F3/C and F7/C2, at either 24° or 72° inclination and 520 or 800 km altitude orbits. Each OSSE's relative performance is evaluated through multiple metrics during the St. Patrick's Day storm on March 13-18, 2015, including quiet and storm-time conditions, using the DART-TIEGCM and a nature run simulation provided by WAM-IPE. This chapter is the first ionospheric OSSE study to comprehensively and realistically account for forecast model and observation errors by using a distinct nature run simulation and forecast model, as well as retrieving synthetic EDP observations from the WAM-IPE nature run with an extensive Abel inversion procedure.

Overall, better spatial coverage of EDP observations from a given RO constellation

design corresponds to a better OSSE performance. For low-inclination constellations with greater low-latitude coverage, the best performance is obtained for the low-latitude ionosphere, and likewise, for high-inclination constellations, the best performance is achieved for the high-latitude ionosphere. The increased spatial coverage of EDPs directly corresponding to improved results is best reflected in a ranking metric, with higher observation counts seen for the 520 km altitude constellations, arguably making OSSE 6 (5024 and 5072) the best performing OSSE. This combination of a low- and high-inclination constellation additionally provides the best global coverage. Consistent posterior improvement is seen at all latitudes for altitudes 300 to 500 km, demonstrating evident benefits to EDP assimilation. A performance limit is also conceivably illustrated for two 6-satellite constellations, and further study is needed to uncover its causes and validity.

Another notable finding is the limitations of RO EDP data impact on the dayside equatorial region at low altitudes. Worsening Abel inversion errors cause negative DA impact in this region due to both breakdowns in the spherical symmetry as well as RO's inherent shortcoming in accurately retrieving very low, low altitude plasma densities. Additional large retrieval errors are seen when vertical plasma density structures deviate from the typical Chapman function, such as double-peaked EDPs.

Ultimately, RO EDPs offer a unique, three-dimensional global ionospheric perspective advantageous for global ionospheric specification. While Abel retrieval and uncertainty quantification may still be improved, as considered in the discussion, RO EDPs offer clear operational space weather benefits for the upper atmosphere. Further assessment of space weather observing systems using comprehensive OSSE studies will considerably enhance future observation integration into DA systems, as well as greatly aid in future constellation design.

Chapter 3

Specifying Satellite Drag Through Coupled Ionosphere-Thermosphere Data Assimilation of Radio Occultation Electron Density Profiles

In this chapter, OSSE studies demonstrate the capability to specify neutral density using RO data assimilation. This chapter shows the benefits of RO EDP observations in overcoming neutral observation limitations, acting as a global monitoring system for neutral and plasma states. Directly updating states using strongly coupled data assimilation improves errors for neutral temperature (70%), neutral winds (20%), and helium composition (60% and 40%), where neutral temperature estimation corresponds to improved neutral density errors (70%) when compared against a no-assimilation control. These neutral density estimates correspond to a reduction of 2-day orbit position errors by 1.2 km, an error reduction of 70% over the control. The results of this chapter are published in Dietrich et al. (2022).

3.1 Background and Motivation

Using RO-derived electron density data has been shown to improve neutral state estimates in Matsuo and Hsu (2021) and Matsuo et al. (2013), notably in improving neutral densities through direct neutral temperature updates. In Matsuo and Hsu (2021), EDPs given by COSMIC-1 RO are assimilated in both an OSSE and OSE. EDP updates showed improvement to neutral temperatures, lower-thermosphere compositions, and neutral winds along with reduced neutral density errors in comparison with CHAMP neutral densities.

However, the past study did not show the impacts the estimated neutral states would have on atmospheric drag and orbit errors. Additionally, helium was not studied as to whether it could be estimated.

In the absence of global observing systems for directly monitoring LEO neutral states, data assimilation of alternative observations offers the ability to globally specify and forecast neutral states. The capability to estimate global atmospheric states from abundant ionospheric observations can be a valuable tool for understanding the evolution of neutral densities during space weather events and filling in knowledge gaps.

The goal of this chapter is to build upon the work of Matsuo and Hsu (2021), further developing and evaluating the effectiveness of this data assimilation tool. This chapter assesses the ability to use RO-derived EDPs to directly update neutral states for neutral temperature, neutral winds, and helium. We focus on higher altitudes ($300 - 500$ km) that are well within the LEO altitude ranges. The same TIEGCM OSSE framework as in Matsuo and Hsu (2021) is used, generating COSMIC EDPs from a truth run and assimilating them into biased experiment runs. Furthermore, we attempt to estimate helium from EDPs. There are two ways helium may be estimated: through direct updates using electron densities, or improved specification of the transport mechanisms that control helium's movement. For the latter case, early models only accounting for species diffusive equilibrium were found to diverge from direct helium observations from satellite and rocket observations (Reber et al., 1971; Kasprzak, 1969). Additionally, helium compositions have been seen to be strongly controlled by neutral winds (Reber et al., 1971) in observations and by wind divergence dynamics in simulations (Sutton, 2016). Thus we seek to estimate helium's transport mechanisms in the vertical and horizontal directions through specified temperatures and neutral winds. In this chapter, we also extend neutral state error improvements to corresponding improvements to orbit errors through a simulated orbit and demonstrate the potential of estimating neutral states for neutral temperature, neutral winds, and helium where current observations have fallen short. With improved, globally available thermospheric state speci-

fication and forecast capabilities, we look to advance atmospheric drag forecasts and provide benefits to orbital errors.

In the following sections, the methods in Section 3.2 detail the TIEGCM (Section 3.2.1), the RO electron density data (Section 3.2.2), the OSSE set-up (Section 3.2.3) and the simulated orbit propagation (Section 3.2.4). The results in Section 3.3 detail the OSSE neutral state results (Section 3.3.1) and the corresponding orbit errors (Section 3.3.3), followed by discussion and future work in Section 3.4, and then the conclusions in Section 3.5.

3.2 Approach

3.2.1 Coupled I-T Model: TIEGCM

For the dynamical forecast model to specify the relationship between the thermosphere and ionosphere, NCAR's TIEGCM (Richmond et al., 1992; Qian et al., 2014) is used. The TIEGCM spans much of the relevant LEO altitudes, extending from approximately ~ 97 km to ~ 600 km. Solar irradiance in the TIEGCM is controlled by a solar proxy model driven by specifying the F10.7 index (F107). Magnetospheric input is specified by an empirical ion convention model, the Heelis model, controlled by hemispheric power (HP) and cross-polar cap potential (Φ) and by an empirical auroral model (Heelis et al., 1982). Lower boundary conditions are specified using the Global Scale Wave Model (GSWM) to specify migrating diurnal tides and migrating semidiurnal tides (Hagan and Forbes, 2002, 2003). The TIEGCM v2.0 is used. The TIEGCM vertical grid is defined by 29 pressure levels with half-scale height resolution, and the horizontal grid is defined by 72 longitude and 36 latitude points with 5-degree resolution. Since ensemble filter methods require a large number of ensemble simulations ($\sim 80 - 100$), we use the TIEGCM with a 5-degree resolution for its computational feasibility. A model integration time step of 100s is used. The neutral density ρ is calculated from neutral grid states using the ideal gas law in Equation 1.2.

3.2.2 RO Electron Density Profile Observations

RO observations of Earth's ionosphere are assimilated for this chapter, where global coverage is enabled with the inherent global coverage of GPS radio signals, allowing observations to be made at all longitudes and latitudes. In this chapter, we use synthetic COSMIC 1 (Anthes et al., 2008) observations, a constellation of 6 satellites at 72 degrees inclination in LEO typically making $2,000-3,000$ ionosphere occultations a day. As RO provides both terrestrial and space weather observations, RO data products are continuously and quickly accessible, and are increasingly available from commercial sources. Therefore, RO data has the potential to be used in real-time, global space weather forecasts to estimate neutral densities.

3.2.3 Observing System Simulation Experiment (OSSE) Set-up

Four OSSEs are run to evaluate the effectiveness of estimating neutral density and composition, detailed in Table 3.1, where each run has updated electron density, (e^-) and atomic oxygen ion, (O^+), and has some combination of updated temperature (Tn), helium (He), zonal wind (UN) and meridional wind (VN). O^+ density is assumed equal to electron density in the TIEGCM, so it is additionally updated as further discussed in Hsu et al. (2014). The vector of state variables being updated is defined as $\mathbf{x} = [\mathbf{x}_{\mathrm{I}}^T, \mathbf{x}_{\mathrm{T}}^T]^T \in \mathbb{R}^n$, a combination of updated ionospheric states, $\mathbf{x}_{\mathrm{I}} \in \mathbb{R}^{n_{\mathrm{I}}}$, and updated thermospheric states, $\mathbf{x}_{\mathrm{T}} \in \mathbb{R}^{n_{\mathrm{T}}}$, where $n = n_{\mathrm{I}}+n_{\mathrm{T}}$. The TIEGCM is used as the truth run with conditions $d_{F107} = 74$, $d_{HP} = 55$ and $d_{\Phi} = 18$. Synthetic observations are generated by sampling the truth run at real COSMIC 1 observation locations and adding perturbations. Perturbations are generated according to random draws from the Gaussian probability distribution defined with altitude-dependent variance (Lee et al., 2012; Lee, 2013). Synthetic EDPs are assimilated into the TIEGCM for altitudes 160 to 450 km at a 10 km interval. On average 65 profiles per hour are assimilated. Each experiment consists of a 90-member ensemble driven with forcing parameters sampled

Table 3.1: Updated State Vectors for OSSEs.

Name	Number of Updating States	Updated State Vector, $\mathbf{x} = [\mathbf{x}_I^T, \mathbf{x}_T^T]^T$
Exp 1	$72 \times 36 \times 29 \times 3 = 225,504$	$\mathbf{x}_\mathrm{I} = [\boldsymbol{f}_{e^-}^T, \boldsymbol{f}_{\mathrm{O}^+}^T]^T$, $\mathbf{x}_\mathrm{T} = [\boldsymbol{f}_{\mathrm{Tn}}]$
Exp 2	$72 \times 36 \times 29 \times 4 = 300,672$	$\mathbf{x}_\mathrm{I} = [\boldsymbol{f}_{e^-}^T, \boldsymbol{f}_{\mathrm{O}^+}^T]^T$, $\mathbf{x}_\mathrm{T} = [\boldsymbol{f}_{\mathrm{UN}}^T, \boldsymbol{f}_{\mathrm{VN}}^T]^T$
Exp 3	$72 \times 36 \times 29 \times 5 = 375,840$	$\mathbf{x}_\mathrm{I} = [\boldsymbol{f}_{e^-}^T, \boldsymbol{f}_{\mathrm{O}^+}^T]^T$, $\mathbf{x}_\mathrm{T} = [\boldsymbol{f}_{\mathrm{Tn}}^T, \boldsymbol{f}_{\mathrm{UN}}^T, \boldsymbol{f}_{\mathrm{VN}}^T]^T$
Exp 4	$72 \times 36 \times 29 \times 3 = 225,504$	$\mathbf{x}_\mathrm{I} = [\boldsymbol{f}_{e^-}^T, \boldsymbol{f}_{\mathrm{O}^+}^T]^T$, $\mathbf{x}_\mathrm{T} = [\boldsymbol{f}_{\mathrm{He}}]$

from $d_{F107} \sim \mathcal{N}(69, 5^2)$, $d_{HP} \sim \mathcal{N}(45, 10^2)$ and $d_\Phi \sim \mathcal{N}(16, 2^2)$. The experiment ensemble is initialized through a 15-day spin-up period to reach a steady state. Each OSSE begins at UT00 on June 23rd, 2008, and synthetic EDP observations are assimilated at each subsequent hour until the experiment ends at UT22 on June 24th, 2008. Experiment results are evaluated against a no-assimilation control run with the same ensemble members without assimilated observations. Improvements of experiment states over the control states are assessed on pressure levels for quantifying impacts in neutral states. Model neutral density states are interpolated to a constant altitudes to inform orbit position impacts. Information detailing the truth run and experiment ensemble are tabulated in Appendix B.

The strongly coupled I-T DA approach, as detailed in Section 1.2.1.1, uses the EAKF (Anderson et al., 2009a) to provide direct updates to neutral and plasma model states, as well as provide impact through the model forecast. Localization is performed with a GC radius of 0.2 radians (∼1300 km). No vertical localization is used, so data can impact all pressure levels in each analysis step. Adaptive inflation is additionally performed on prior states to avoid ensemble spread collapse (Anderson, 2007). In addition to assessing the DA impact of estimating neutral temperature and neutral winds, helium estimation is also assessed. Helium estimation is focused on through the DA impact within multiple cycles of the forecast step as impacted by direct updates to neutral temperature and neutral winds.

An example of the background correlation used in this chapter to directly update neutral states is shown in Figures 3.1 and 3.2. The sample statistics, obtained by ensemble perturbations, generate correlation structures that are more complex than an isotropic,

homogeneous correlation structure, with examples shown in Figure 3.1. The correlation between neutral temperature and electron density is shown in the black contour, illustrated at a point for two different altitudes above and below the F2 peak electron density. Around the equatorial ionospheric anomaly (EIA) on the low-latitude day-side of Figure 3.1, the electron density in the top and bottom side ionosphere shows a positive correlation with neutral temperature. Two ensemble members are highlighted with one higher than the mean and one lower than the mean. These high positive correlations can be explained by the changes in solar flux control both increasing and decreasing the neutral temperature and ionization rate. Additionally, it should be noted that the black contour curves in Figure 3.1 are global correlations; however, in the ensemble data assimilation implementation, the covariance localization limits the observation in a close region about the observation location. It is also noted that these correlation structures are optimistic in the large correlations they show, as plasma correlations are expected to act on much smaller scales than neutral states.

3.2.4 Orbit Propagation

The connection of neutral densities and orbit determination errors is accomplished through a simulated orbit that is propagated through the generated TIEGCM grids. Neutral density, composition, and neutral wind states can all affect the atmospheric drag calculation. CHAMP's orbit during this period is used as the basis for the simulated orbit; a near-circular, ~ 90 minute period, polar orbit raised to 500 km altitude. The satellite's orbit is simulated including dynamics for two-body, J_2 perturbations, and atmospheric drag:

$$\mathbf{a} = \frac{\mu_{Earth}}{r^3}\mathbf{r} + \mathbf{a}_{J_2} - \frac{1}{2}C_D\frac{A}{m}\rho v\mathbf{v} \tag{3.1}$$

With a drag coefficient of $C_D = 4$ and an area to mass ratio of $\frac{A}{m} = 4/490\ [m^2/kg]$. While the drag coefficient is dependent on composition, for simplicity C_D is kept constant which is a reasonable assumption for this chapter. Since atmospheric drag is predominately anti-parallel to the velocity direction, in-track orbit errors (in the direction of the velocity vector),

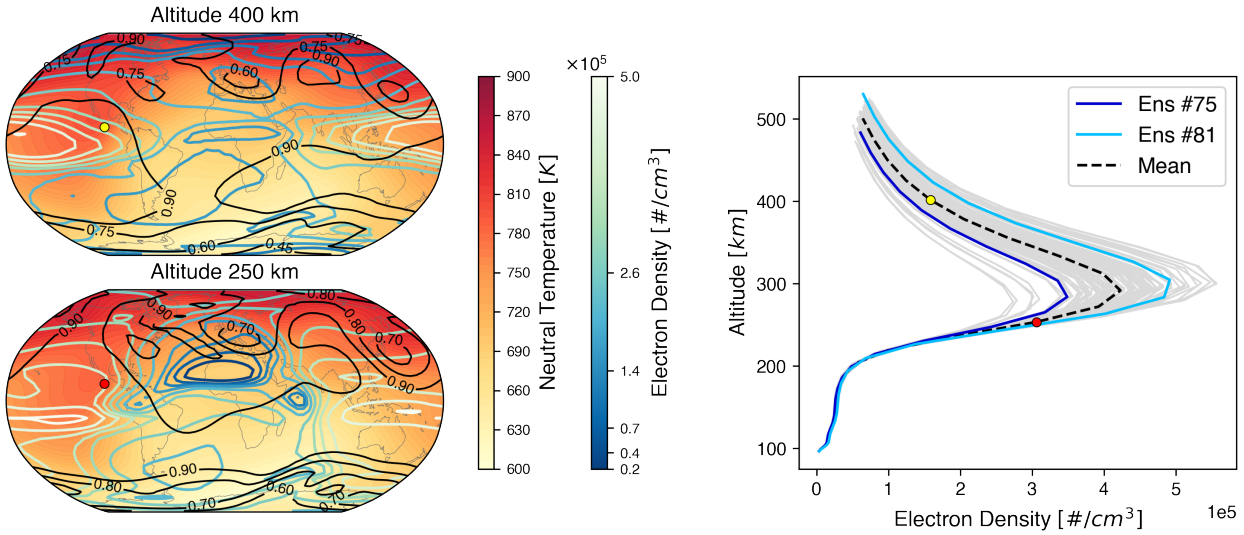

Figure 3.1: The two global plots on the left show the prior neutral temperature, prior electron density, and in black the correlation structure between the electron density at an observation location (yellow and red points) and the global neutral temperature. On the right is the EDP ensemble with two highlighted members: ensemble #81 with forcing parameters higher than the means, $d_{F107} = 78, d_{HP} = 68, d_{\Phi} = 21$, and ensemble #75 with forcing parameters lower than the mean, $d_{F107} = 63, d_{HP} = 31, d_{\Phi} = 13$. This is shown for two observations close to the equatorial ionization anomaly with one above the F2 peak at 400 km (top left) and one below the F2 peak at 250 km (bottom left).

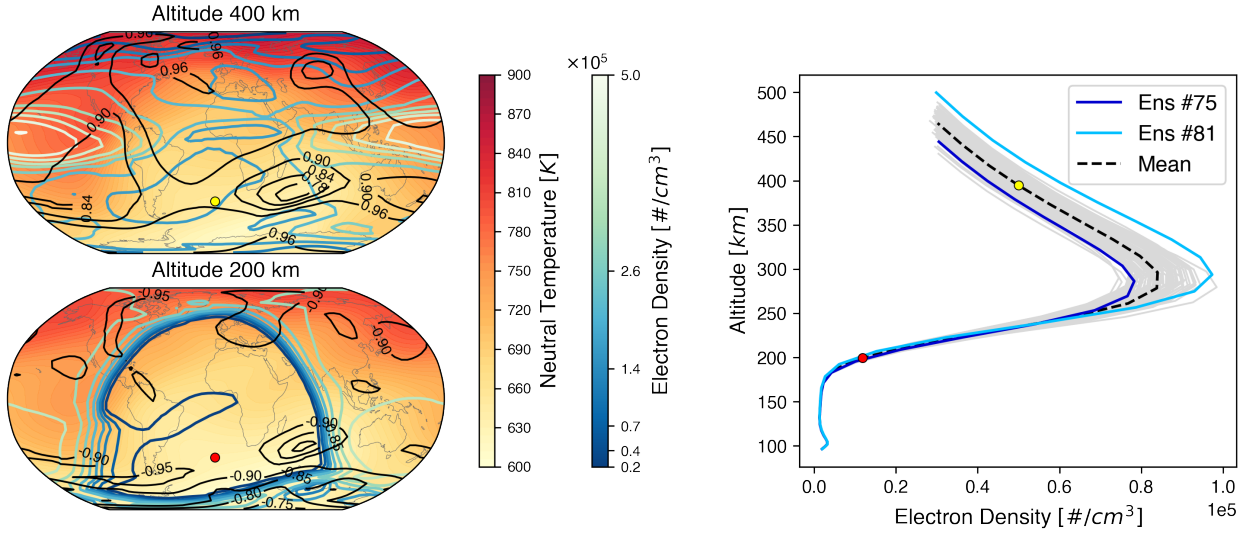

Figure 3.2: Same as Figure 3.1. Observations are at longitude -10 deg and latitude -42.5 deg and priors are at UT01 on June 23rd, 2008.

are calculated for the two-day OSSE period against an orbit propagation through the true TIEGCM state grid.

3.3 OSSE Results

3.3.1 OSSE Thermospheric Results

We focus on the OSSE results for the upper third pressure levels of the TIEGCM, encompassing the altitudes $300-530$ km that cover the LEO regime. The root mean squared errors (RMSEs) are calculated for the first three experiments and the control against the truth using

$$RMSE = \sqrt{\frac{\sum_{j=1}^{N}\left(x_j^{true} - \overline{x}_j^{exp}\right)^2}{N}} \tag{3.2}$$

where N is the total number of points, x^{true} are the truth states and $\bar{x}^{exp}$ are the experiment state means. We assess the results of each experiment through their percentage improvement over the control as defined as follows:

$$\frac{RMSE_{control} - RMSE_{exp}}{RMSE_{control}} \tag{3.3}$$

The experiment denotes the ensemble with EDP assimilation and is identical to the control ensemble which does not have data assimilation. A time series of the total RMSEs for the top third pressure levels of the TIEGCM is shown in Figure 3.3 for neutral temperature, neutral density, helium composition, and neutral wind.

As first shown in (Matsuo and Hsu, 2021), direct updates to neutral temperature show an immediate drop in the posterior error for experiments 1 and 3, reaching a 65% improvement over the control, shown in Panel (a) of Figure 3.3. These improved temperatures correspond to similar error reductions in neutral density at high altitudes, achieving an improvement of 70% over the control, shown in Panel (b) of Figure 3.3. The control neutral temperature RMSE has peak and minimum errors repeated every 24 hours. Experiment neutral temperature and neutral density RMSEs show this same repeating behavior, with

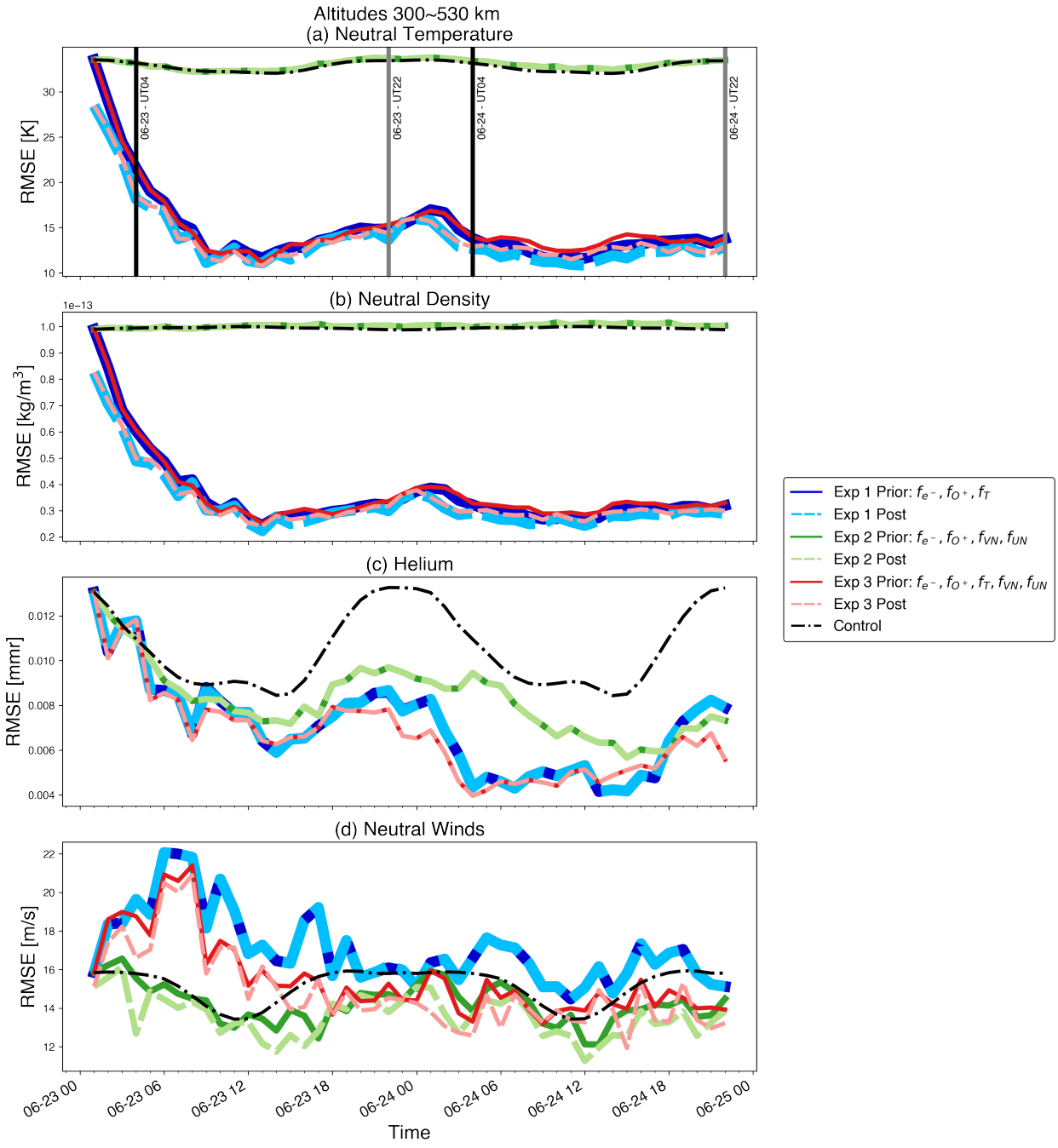

Figure 3.3: Global RMSE for the top third pressure levels for experiments 1-3. Shown for neutral states for (a) neutral temperature, (b) neutral density, (c) helium, and (d) the neutral wind magnitude. Experiment posterior errors against truth shown in solid darker colors, and experiment prior errors shown in dashed lighter colors. Improvements are assessed in RMSE reduction over the control (black lines). Pressure levels correspond to altitudes $300 - 530$ km.

experiments 1 and 3 RMSEs reaching a minimum at about UT13 on June 23rd and reaching another minimum 24 hours later. Updating only neutral winds in experiment 2 shows no impact on improving neutral density or neutral temperature.

A new question to be answered is whether helium may be estimated using EDPs. In experiment 1 where the neutral temperature is updated, there is continuous improvement in helium estimation over the control, achieving a 60% improvement, shown in Panel (c) of Figure 3.3. While neutral temperature RMSEs reach a minimum at hour 13, helium errors do not reach a minimum until around UT04 on June 24th. Updating only neutral winds additionally sees an improvement in helium estimation by 40%, as shown by experiment 2. Thus in experiment 3, the helium error improvements are due to better specified neutral temperature and neutral winds. Since there are no direct updates to helium in experiments 1, 2, and 3, the helium state is adjusted through the TIEGCM's forecast step. There is additionally a 24-hour period in the helium RMSE variation in the control and experiments 1-3.

As for neutral wind errors in Figure 3.3, experiment 2 shows direct updates to neutral winds improve their RMSE. It is noted that the wind RMSEs are shown for the magnitude of the horizontal wind vector, containing errors from both the zonal and meridional wind directions. In experiment 2, direct updates to the winds reduce the RMSE in 87% of analysis steps, shown in Panel (d) of Figure 3.3. Nonetheless, the improvements do not impact neutral density errors. In experiments 1 and 3, there is an initial jump in the neutral wind RMSE due to updated neutral temperatures disturbing the neutral winds. Eventually, as more data are assimilated, the initial increase in wind errors for experiments 1 and 3 is corrected. By the end of the OSSE period, experiments 2 and 3 perform about the same in neutral wind RMSE. In experiment 3, we see the posterior improving wind errors in 80% of analysis steps and the prior worsened neutral wind errors in 80% of forecast steps. The lowest achieved wind RMSE error reduction over the control is 20% for experiment 3.

It is noted that for Figure 3.3, while there is a wide span of altitudes represented within

each calculated RMSE, each experiment's error evolution shows the same behavior for each included pressure level. The exception is neutral density which shows dramatic changes in error magnitudes when changing altitude, however, the relative errors for each experiment remain the same.

Examining Figure 3.4, the RMSE for neutral temperature, neutral density, helium composition, and neutral wind at each pressure level at UT04 on June 23rd and 24 hours later at UT04 on June 24th is shown. Experiments 1 and 3 show improvement to neutral temperature and neutral density at all altitudes, shown in Panels (a) and (b) of Figure 3.4. The posterior neutral temperatures for experiments 1 and 3 at UT04 on June 23rd show considerable improvement, shown in Panel (1a) of Figure 3.4. After 24 hours, the posterior and prior neutral temperature errors are more closely aligned and improvement to neutral density is visible for all altitudes, shown in Panel (2a) of Figure 3.4. These improvements to neutral density are from improved neutral temperatures. As for helium, there are little differences in RMSE between experiments and the control at UT04 on June 23rd, but 24 hours later at UT04 on June 24th, there is a noticeable error improvement over the control in experiments 1 and 3, shown in Panels (c) of Figure 3.4. Helium composition become a dominant species above 400 km, so composition errors below 400 km are negligible.

For neutral wind errors in Panel (1d) of Figure 3.4, the initial error increase is again apparent for experiments 1 and 3 at all altitudes at UT04 on June 23rd, but experiments 2 and 3 do show an improvement in posterior wind errors. Following 24 cycles, neutral wind for both experiments 2 and 3 show improvements over the control in RMSE, and experiment 1 sees errors aligned with the control, shown in Panel (2d) of Figure 3.4. Neutral wind errors improve for all altitudes above 150 km.

Vertical RMSE for helium composition and neutral winds at two additional times at UT22 on June 23rd and UT22 on June 24th are shown in Figure 3.5. Over the 24 hours, both helium errors and neutral wind errors improve for all three experiments. At the end of the OSSE, experiment 1 wind errors have improved over the control, shown in Panel (2b) of

Figure 3.5, as compared with the initial jump in RMSE seen from UT01 to UT08 on June 23rd in Panel (d) of Figure 3.3. While Figure 3.5 shows experiment 3 performing better at estimating winds than experiment 2, both experiments 2 and 3 show relatively similar performance over UT12 to UT23 on June 24th as seen in Panel (d) of Figure 3.3.

To provide evidence that errors are globally improving, the true states and the experiment 1 bias from the truth for neutral density and helium at 500 km altitude are plotted in Figures 3.6 and 3.7, respectively. The top rows show the truth state and the bottom rows show the experiment prior minus the truth. The simulated 500 km polar orbit is plotted for the corresponding hour in the truth plots. The orbit passes through the day (around 12 local time)and night (around 0 local time) sides, passing through the peak and minimum neutral density regions. EDP locations from COSMIC 1 ROs are additionally plotted at their corresponding hour in the bias plots. Since these are COSMIC 1 observation locations, they reach high-latitude locations and include all longitudes. In Figure 3.6, the neutral density bias for experiment 1 is negatively biased, with the largest negative bias occurring on the day side. As shown in Figure 3.3, there is an immediate drop in neutral density RMSE that continues to decrease through UT10 on June 23rd. For experiment 1, the bias in neutral temperature and neutral density is considerably reduced but is not fully corrected. While there are still some regions of higher neutral density bias in experiment 1, say around the peak day side and on the night side, improvements occur globally.

For helium composition, improvements in bias are shown in Figure 3.7 over the south pole at 500km altitude where helium is dominant. Helium concentration can become the dominant species over the winter pole through the winter helium bulge phenomenon (Keating and Prior, 1967). The top rows in Figure 3.7 show the truth helium composition and the bottom rows show the experiment 1 bias from the truth. To show the lagged improvement in helium RMSE over the control, times in Figure 3.7 are plotted every 5 hours, with the minimum bias occurring within UT05 to UT16 on June 24th. It is again noted that neutral temperature is the only neutral state updated in experiment 1. At 500 km altitude, the

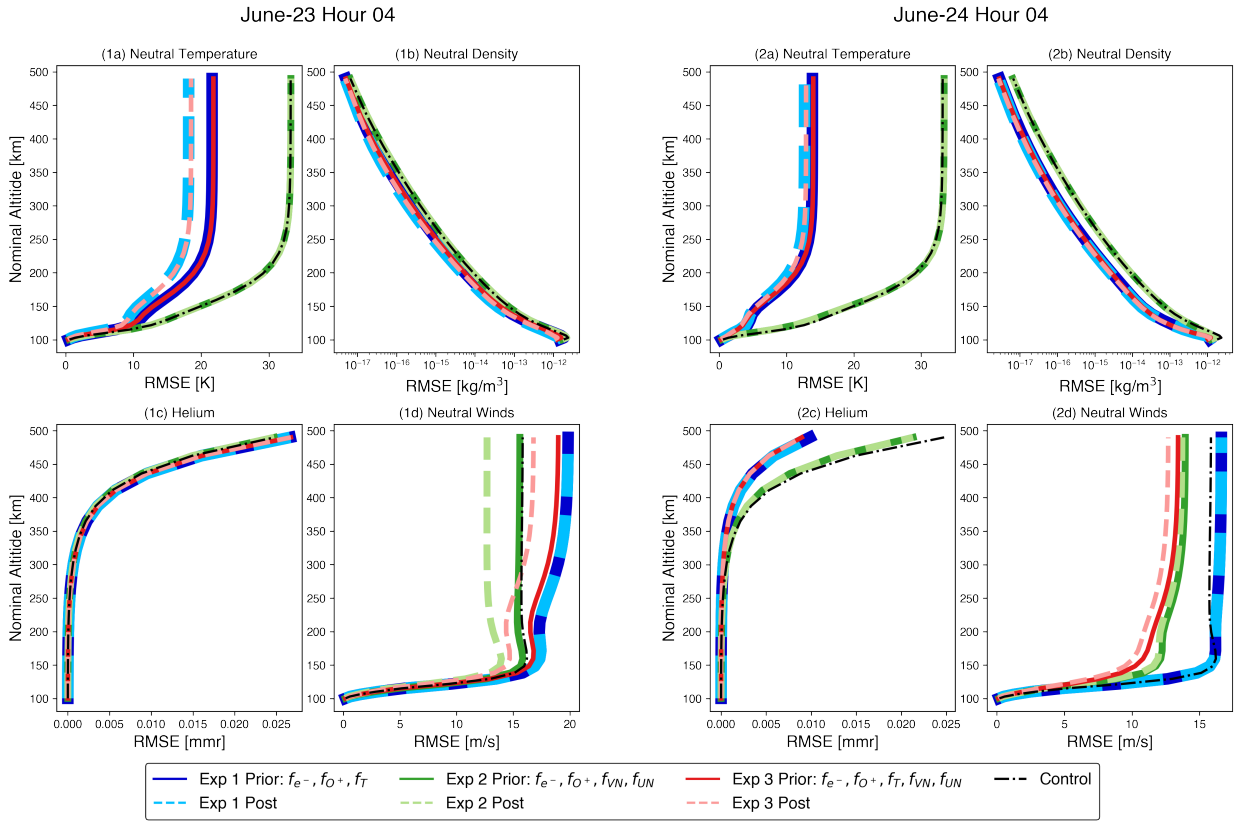

Figure 3.4: RMSE at each pressure level, shown in altitude, for (a) neutral temperature, (b) neutral density, (c) helium, and (d) neutral winds at UT04 on (1) June 23rd and (2) June 24th. Posterior and prior errors calculated against the truth for all three experiments are compared against control errors.

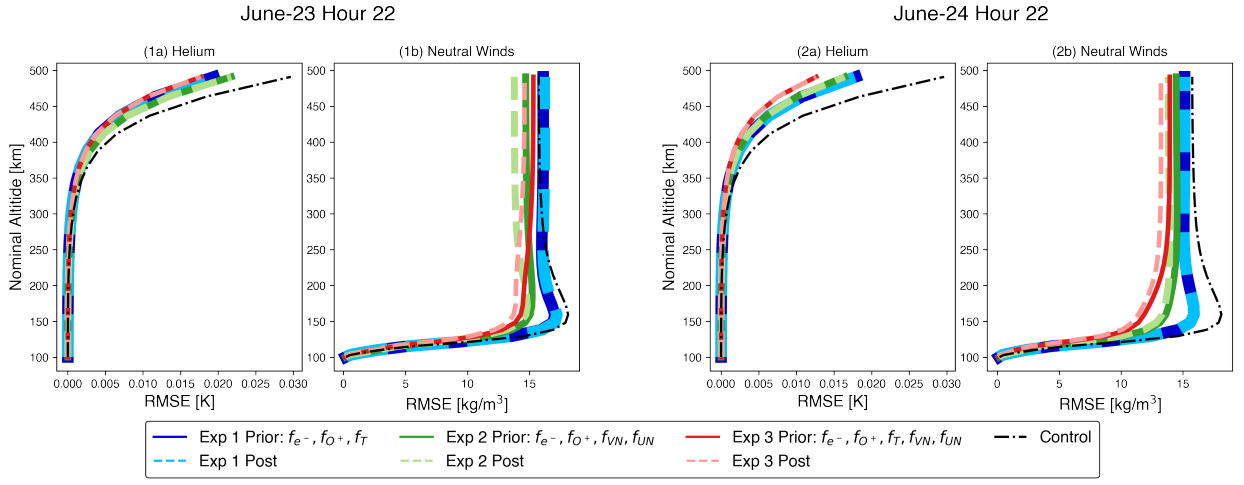

Figure 3.5: RMSE at each pressure level, shown in altitude, for (a) helium and (b) neutral winds at UT22 on (1) June 23rd and (2) June 24th. Posterior and prior errors calculated against the truth for all three experiments are compared against control errors.

helium mole mixing ratio for experiment 1 sees a 0.16 molecular mixing ratio (MMR) bias at UT01 on June 23rd. This bias corresponds to an initial peak composition error of 56%. As each day progresses, the peak helium content rotates with the solar angle, showing very similar composition structures when looking at 24-hour differences in the truth 500km helium compositions. Additionally, the 500km polar orbit passes through this peak helium region.

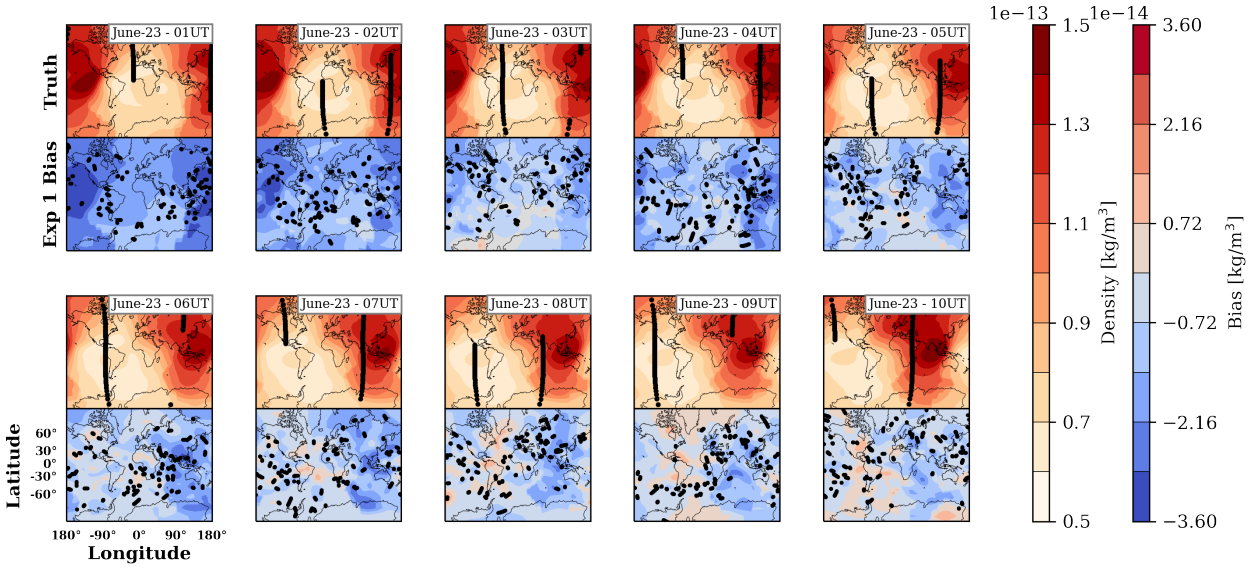

Figure 3.6: Global neutral density states for the truth and experiment 1 prior bias at 500 km altitude for the first 10 hours of the OSSE period. The top rows show the truth state and the bottom rows show the experiment bias defined as the experiment prior minus the truth. Champ orbit tracks are plotted on top truth plots and EDP locations from COSMIC 1 RO are plotted on the bottom bias plots.

3.3.2 Direct Updates to Helium

The results from experiment 4 have not yet been discussed. We apply RO EDPs to directly update helium composition. In experiment 4, state estimates for helium diverge from the truth, as shown in Figure 3.8, with experiment 4 biases plotted every fifth hour of the day. The top rows show the truth state and the bottom rows show the experiment prior minus the truth. Helium compositions begin with a positive bias at 500 km, and while some improvements are initially made, helium bias for the entire globe grows over the OSSE

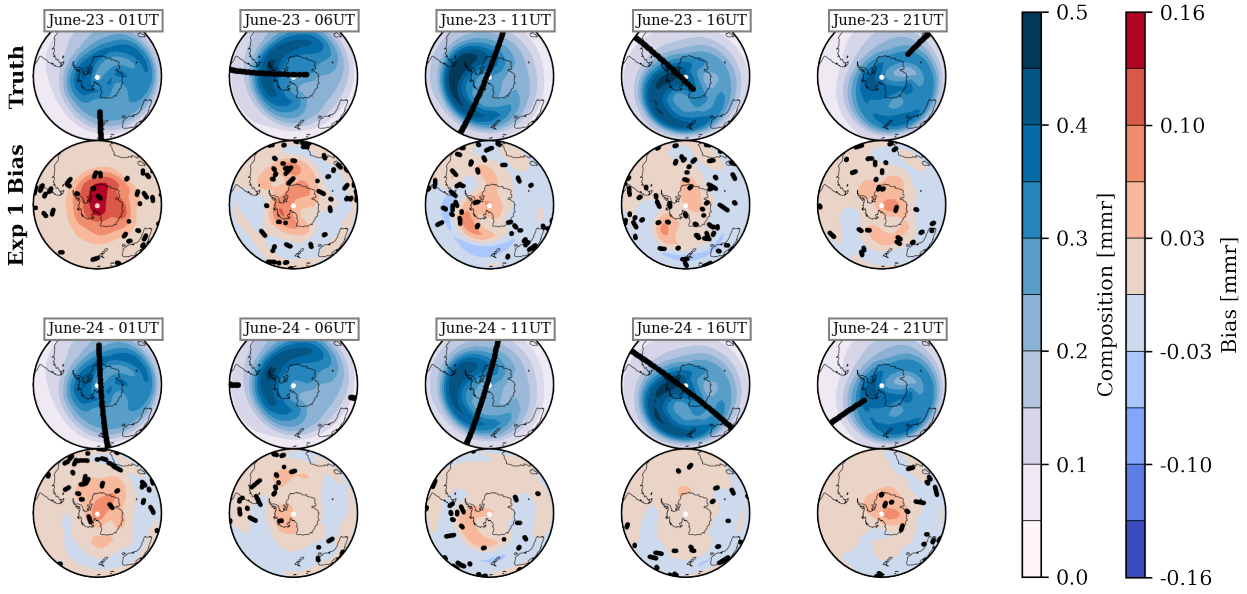

Figure 3.7: Helium mixing ratio over the south pole for the truth and experiment 1 prior bias at 500 km altitude for every fifth hour of the OSSE period. Same experiment bias as in Figure 3.6 with champ orbit tracks and COSMIC 1 RO tangent points.

period. Helium is increasing in composition above −30° latitude where helium composition should be low. Thus, helium composition was not successfully estimated with direct updates and we instead rely on strongly coupled data assimilation with direct updates to neutral temperature and neutral winds to dynamically correct helium composition.

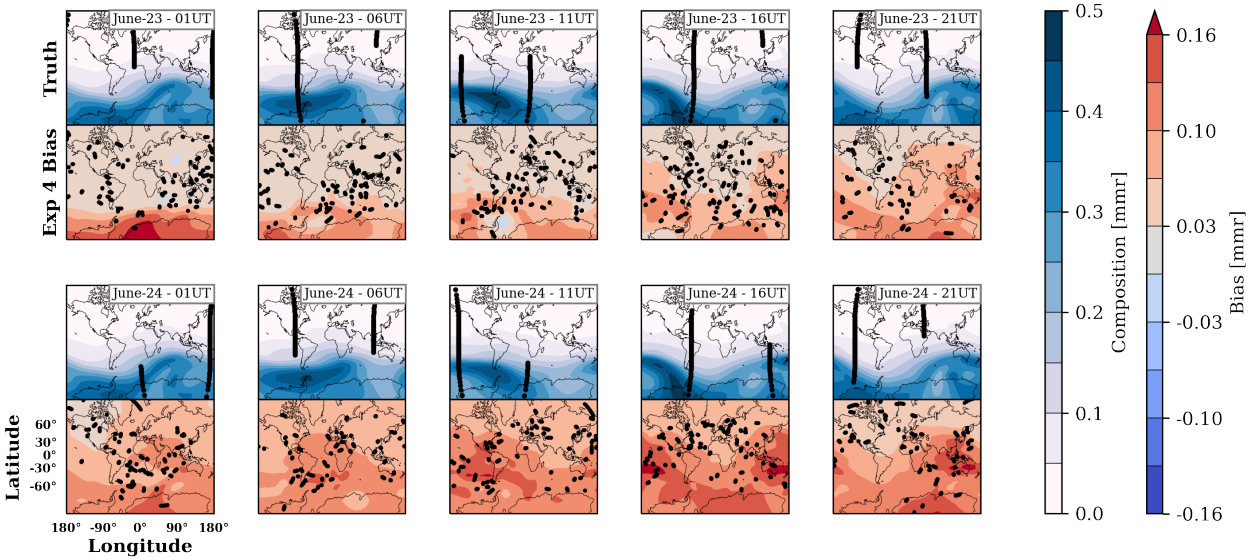

Figure 3.8: Global helium mixing ratio for the truth and experiment 4 prior bias at 500 km altitude, shown for every fifth hour. Same experiment bias as in Figure 3.6 with champ orbit tracks and COSMIC 1 RO tangent points. Experiment 4 performs direct updates to helium compositions.

3.3.3 Orbit Errors

The simulated orbit is propagated through the atmospheric fields for experiments 1-3 and the control. Orbit positions are compared against a propagation through the truth. Orbit errors in calculating atmospheric drag can come from three atmospheric states: neutral density, composition, and neutral winds. Orbit position errors for the in-track direction are shown in Figure 3.9. After two days, experiments 1 and 3 show a 1.2 km error reduction, a 70% error reduction over the control, as shown in the center panel of Figure 9 where the two-day experiment errors are normalized by the control error. Experiment 2, where winds are updated, shows a negligible improvement over the control. The percent improvement for

each experiment begins to level out after two days, capping the relative improvement. Orbit errors were extrapolated for an additional 7 days using the 2-day error growths, as shown in the right panel of Figure 3.9. Errors in the control grow to 38 km, while the errors for experiments 1 and 3 extend to less than 9 km, an improvement of 29 km.

Composition errors are known to have an impact on the drag coefficient. For this chapter, however, incorrect compositions were not found to have a considerable impact. Using the drag coefficient model VECTOR (Pilinski, 2011) with a cylinder shape, the peak error in C_D amounts to less than 3%. The C_D errors will come from errors in relative composition, peaking within the helium winter bulge in the He to O ratio. Experiment 1 does improve C_D estimates through an improved He to O ratio; however, a corresponding decrease in neutral temperatures could have counterbalanced this impact, resulting in minimal C_D changes (Thayer et al., 2012). Additionally, the winter helium bulge is quite small in comparison to the rest of the globe, so the integrated position error is negligible. To analyze what would happen if there were a much greater C_D error, an orbit is simulated with a constant 10% C_D error and plotted additionally in Figure 3.9. As compared with the errors caused by the biased neutral densities, the biased C_D has considerably less impact on orbit errors, worsening in-track error by less than 3%.

Errors from the neutral winds manifest within the relative velocity in Equation 1.1 and dynamically improved composition impacts the neutral density magnitude. While experiment 2 shows improvement in neutral wind RMSE and helium compositions, position errors for experiment 2 remain close to the control.

Along the simulated orbit path, neutral densities are sampled from the TIEGCM grids for the truth, control, and experiment 1, shown in Figure 3.10. The satellite orbit passes through two local times for the day and night side, sampling peak and minimum neutral density magnitudes. After an initial experiment 1 bias of 1×10^{-12} $[kg/m^3]$ at UT01 on June 23rd, neutral densities quickly align with the truth with data assimilation cycles. These improvements are sustained for the whole OSSE period.

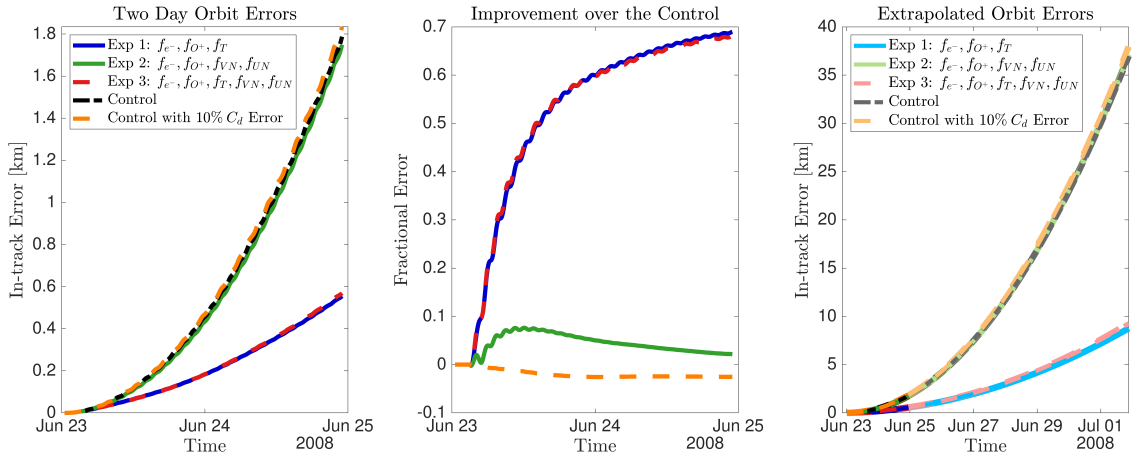

Figure 3.9: In-track orbit errors against the truth over the two-day OSSE period for the first three experiments, the control and the control with a 10% C_D error (left). Fractional error improvement of each experiment over the control for the two-day OSSE period (center). Extrapolated in-track orbit errors extended by 7 days (right).

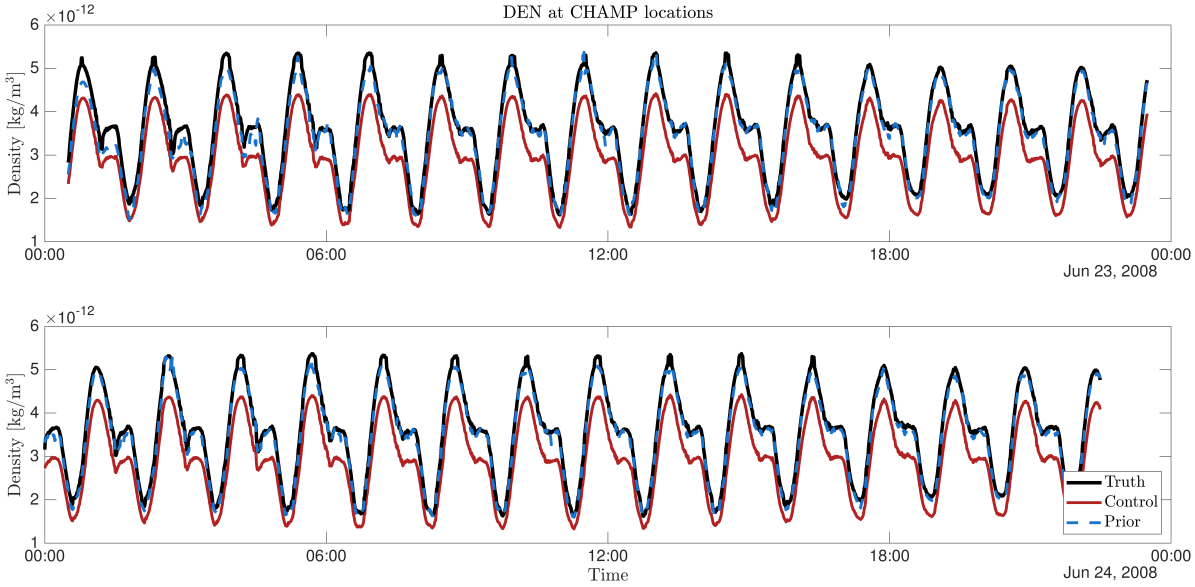

Figure 3.10: Neutral densities sampled along the simulated orbit path from the truth, control, and experiment 1 prior. Shown for June 23rd and 24th.

3.4 Discussion

Applications of data assimilation techniques to estimate neutral densities are not new (Sutton, 2018; Morozov et al., 2013; Codrescu et al., 2018); however, important differences make this chapter distinct from previous attempts. Instead of estimating model forcing parameters from mass density data, this chapter focuses on directly estimating atmospheric states from a large ionospheric data set. This enables the estimation of individual neutral states and state uncertainties globally. For example, we show that EDPs retrieved from RO are effective in direct updates to neutral temperature and neutral winds, as shown in Figure 3.3, and these improvements correspond to improvements to LEO neutral density across the globe as shown in Figure 3.6. Not all of the bias in temperature is removed partly due to the TIEGCM forcing parameters for each ensemble being kept unchanged for the OSSE period. Through updating neutral temperature and neutral winds, helium compositions are also shown to improve, especially in the vicinity of the winter helium bulge, as shown in Figure 3.7. All these would be difficult to achieve via the estimation of forcing parameters by data assimilation.

The observability of neutral temperature by EDP observations is difficult to quantify. We offer empirical evidence as to why COSMIC EDPs are effective in estimating neutral temperature through sample correlations calculated between characteristic features of the EDP and neutral temperature. The EAKF's analysis step relies on a linear regression fit obtained from the ensemble statistics to map the EDP increments in observation space to the neutral state increments in model space, as shown in Equation 1.36. Thus, the correlations between states and observations can indicate how effective the EAKF analysis step is. First, the peak density of the EDP, N_mF_2, and the peak density height, h_mF_2, are calculated for each synthetic RO EDP. Correlations of N_mF_2 and h_mF_2 with neutral temperature and helium states along the nearest model pressure level are calculated using the prior ensemble, at UT01 on June 23rd, before the first analysis step. This results in a correlation structure

on the 2D longitude and latitude grids. The correlation structures are the same as displayed with the black contours in Figures 3.1 and 3.2 which show correlation structures between electron density at a given point and neutral temperature on the model grid. These calculated neutral temperature and helium correlations are collected into probability histograms, shown in Figure 3.11. The high correlations between h_mF_2 and neutral temperature are apparent, and support the observability of neutral temperature by EDP capabilities for COSMIC EDPs to update neutral temperature states. This is explained by the fact that peak heights of EDP (h_mF_2) move up and down with the pressure level as neutral temperatures go up and down. There are considerably high correlations between N_mF_2 and neutral temperatures as well. High correlations of N_mF_2 and h_mF_2 with neutral temperatures is an encouraging result for using real COSMIC EDP data to estimate neutral temperature (Matsuo and Hsu, 2021), as COSMIC RO can measure h_mF_2 with high precision (Cherniak et al., 2021; Yue et al., 2010).

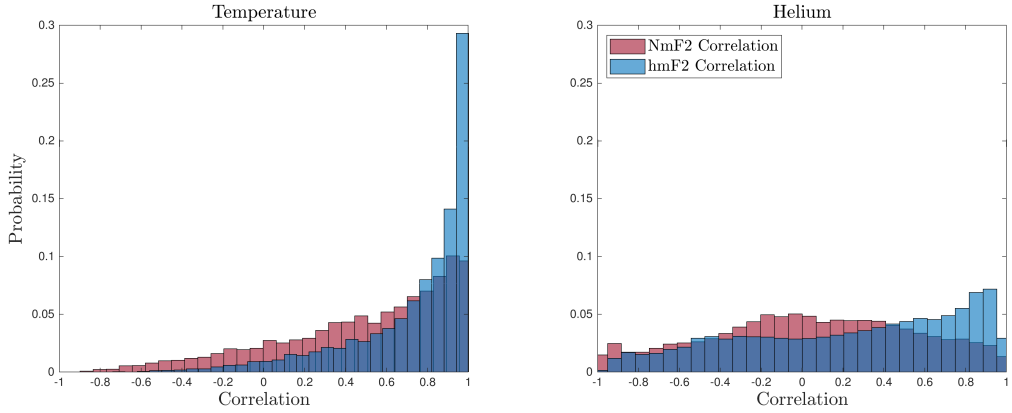

Figure 3.11: Probability histogram of ensemble sample correlations between N_mF_2 and h_mF_2 to neutral temperature (left) and helium (right) along nearest pressure level of model grid. Computed with the prior ensemble at UT01 on June 23rd with all assimilated EDPs for that hour.

Helium is best estimated using dynamical updates from directly updated neutral temperatures and neutral winds. Again examining Figure 3.11, high correlations of h_mF_2 or N_mF_2 are less common for helium compared with temperature. This helps to explain why experiment 4 has performed badly and resulted in filter divergence. Instead of direct adjust-

ments, helium estimation can be improved over a succession of the forecast steps through better-specified temperatures and neutral winds, and is supported by the observed lag time between neutral temperature improvement and helium improvement. Assimilating EDPs to specify neutral temperature and neutral winds provides constraints on the transport of helium in both the horizontal and vertical directions, resulting in a global redistribution of helium. For instance, it has been shown by (Sutton, 2016) through the TIEGCM simulation that the vertical flux resulting from the horizontal wind convergence plays a major role in forming the winter helium bulge at solar minimum. This chapter suggests that subseasonal and day-to-day variations of the winter helium bulge can be examined by imposing constrained dynamics using direct updates to neutral temperature and neutral winds.

There is an issue with updating neutral temperature that needs some attention, wherein there is a jump in the neutral winds RMSE, notably over the first several analysis-forecast cycles as shown in Figure 3.3. In experiments 1 and 3 in which the neutral temperature variables are direct-updated by EDPs, the updated temperature distributions become dynamically imbalanced with the neutral wind distributions. This dynamical imbalance generates non-physical waves in the first few data assimilation cycles when there are larger temperature increments. However, after continuously informing the wind dynamics with 2 days of analysis-forecast cycling, wind errors are reduced. The wind and temperature distribution become more consistent with those represented in the truth through assimilation. Note that synthetic EDP observations are sampled from the truth. This dynamical adjustment occurs faster when neutral winds are directly updated with EDPs. These experiments show that the states' dynamical adjustment process during forecast steps eventually has wind RMSE improve beyond the control. Thus, wind RMSEs after the second day when a steady-state error is achieved are more representative of OSSE performance. On the other hand, in experiments 1-3, a steady improvement in helium compositions is seen, so adjusting with dynamically inconsistent increments is not a detriment to estimating helium.

We show that orbit error reduction is predominantly achieved through the estimation

of neutral densities over neutral winds and drag coefficients. We quantitatively assess the neutral state RMSE improvements through orbit position errors from orbit propagation. As shown in Figure 3.9, experiments 1 and 3, which have the greatest neutral density improvements, result in the greatest orbit error improvements. These improvements to neutral density primarily stem from improved neutral temperatures, and not from improved composition affecting the drag coefficient. Drag coefficient errors from composition were found to be minor, and even after inflating the drag coefficients to a larger error, we see negligible positional errors as compared with those from neutral densities. Improved neutral winds would manifest in relative velocity errors and improved compositions, but are again dwarfed by the impact of reducing neutral density errors. The neutral density errors can introduce large orbit position errors, and the error magnitudes can markedly grow over a short period as shown by the extrapolated position errors in Figure 3.9.

While drag coefficient improvements due to assimilation of EDP are small and make a small impact on orbit errors, drag coefficients do play a crucial role in deriving neutral density observations as their largest error sources (Sutton et al., 2007; Mehta et al., 2017). Drag coefficient models are reliant on accurate atmospheric models to provide composition and temperature information. Neutral densities are consequently used to infer knowledge of the rest of the thermosphere; however, those derived densities rely on prior thermospheric information, creating an error feedback loop (Ray, 2021). The drag coefficient magnitude will additionally affect the size of orbit position errors, where it is noted that CHAMP has a smaller drag coefficient, $C_D = 3.2$, than the simulated orbit used in this chapter. Data assimilation of EDPs can potentially provide an independent data source for composition estimation, leading to improved C_D values and derived neutral densities.

This chapter reveals the potential for improving orbit errors with ensemble data assimilation of RO electron densities, but the effectiveness of this approach will need to be assessed in more realistic conditions. In this chapter, we use a simplified model to assign EDP errors. Abel inversion errors primarily come from breakdowns of the spherical sym-

metry assumption (Liu et al., 2010; Yue et al., 2010). When assimilating real data, it is important to incorporate more realistic Abel inversion error uncertainties.

One question needs to be addressed in future work: how does the data assimilation approach presented in this chapter contribute to space weather forecasting of neutral density? During quiet periods with steady conditions, empirical models perform well for satellite operators. However, it is during geomagnetic storms that these empirical models struggle. Thus, the next step is to evaluate the performance of this data assimilation approach under realistic storm-time conditions with real data to prove its efficacy in neutral density forecasting. Since the analysis step relies on the TIEGCM's dynamics to define the multivariable correlations, model biases, and inadequately specified forcing parameters need to be examined. (Matsuo and Hsu, 2021) has performed OSEs using real COSMIC 1 derived EDPs and shown improvements in neutral density as compared with CHAMP neutral densities, a data source that is used for assimilation. During geomagnetic storms when state biases can be large, it is important to estimate forcing parameters along with neutral states. Research by Sutton (2018) has shown estimating the TIEGCM forcing parameters leads to neutral density improvements under real storm conditions. Considerable computing power is needed to run a large ensemble number, which has limited the OSSE period to over two days and with 90 ensemble members. However, with growing computational power, this data assimilation approach will become increasingly practical to use. Additionally, future work needs to address how to mitigate numerical instabilities when EDP direct updates to neutral states cause dynamically imbalanced assimilation increments. Adjusting the model integration time step, introducing prior state inflation, and rejecting poor quality observations are all necessary to ensure the data assimilation scheme runs robustly.

The next question is how effectively this work may be applied to contribute to the scientific understanding of magnetosphere-ionosphere-thermosphere coupling. Future work needs to address issues of model bias. In particular, the relative biases between electron densities and neutral states need to be focused on with attention to missing or inadequately

represented fundamental processes in the current I-T models. For this chapter, the existing bias issues in the TIEGCM do not arise when using a simulated experiment, but they will with real observations. Another scientific question of interest is how changes in neutral winds, compositions, and neutral densities in response to magnetospheric driver changes impact LEO neutral mass densities. The state estimation enabled by the data assimilation approach presented in this chapter can allow for quantifying the relative contribution of neutral density changes due to composition and neutral temperature as well as winds.

3.5 Conclusions

For the first time, this chapter demonstrates the ability to use RO electron density profiles to estimate atmospheric drag and improve LEO satellite position errors. By assimilating RO EDPs through strongly coupled data assimilation into a physics-based model, we show a reduction in neutral density and helium composition errors in LEO and consequently show considerable improvement in orbit errors. These results are significant in that it is necessary to reduce satellite drag errors through better estimates for neutral densities and drag coefficients. This chapter overcomes the limited number of direct atmospheric observations by using globally available electron density observations of the ionosphere. This was enabled by two main methods to estimate neutral density and helium: the physics-based, I-T coupling in the TIEGCM and strongly coupled data assimilation. The TIEGCM provides the physics-based coupling of the I-T system, providing a dynamical relationship connecting ionospheric and thermospheric model states. Strongly coupled data assimilation then takes advantage of the I-T coupling to provide statistical relationships among ionospheric and thermospheric states, enabling direct updates to neutral states with EDPs. To assess the capabilities of using electron densities to estimate atmospheric drag, synthetic EDPs from COSMIC RO are assimilated into the TIEGCM to directly update neutral temperature and neutral winds. The data assimilation was performed using the EAKF implemented by DART. Using sample statistics determined by the TIEGCM ensemble, analysis step increments for electron

densities are mapped to update neutral temperature, neutral winds, and helium. A 500 km polar orbit was simulated and propagated through the generated TIEGCM fields to connect atmospheric state errors to orbit position errors.

Specific findings are as follows. Using EDPs to constrain neutral temperatures, neutral densities RMSEs were improved by 70% over the control at all longitudes, latitudes, and altitudes as shown in Figure 3.3. Direct updates to neutral temperature were effective partially through high correlations between h_mF_2 and neutral temperatures shown in Figure 3.11. The improvement to neutral densities corresponds to reduced orbit errors of 1.2 km over 2 days, a 70% reduction over the control, and a 29 km improvement over 9 days. Errors in neutral density dominate orbit errors over other atmospheric state errors from neutral winds and drag coefficients. Helium estimation is demonstrated for the first time through EDP updates. While helium was not able to be directly estimated, helium composition estimation was presumably due to improvements to helium's transport mechanisms. Helium's vertical and horizontal transport mechanisms were seemingly improved with better specified neutral winds and neutral temperature with a 20% reduction in RMSE. Direct updates to neutral temperature showed a 60% helium RMSE reduction and direct updates to neutral winds saw a 40% helium RMSE reduction.

These results further demonstrate the potential for using RO data as a means for estimating neutral states, building on results from Matsuo and Hsu (2021). RO data is leveraged through strongly coupled data assimilation and physics-based modeling to provide direct updates to neutral states and specify neutral densities and compositions. With COSMIC 2 providing more RO data than its predecessor and growing commercial RO data sources, RO constellations offer a potent data source to be used in data assimilation and space weather forecasting. Adapting RO observations has the potential to overcome our current neutral observation limitations, allowing us to infer more information on the LEO environment to predict atmospheric drag and provide a safer, collision-free space environment.

Chapter 4

Neutral Density Reanalysis during Storm-time through Coupled Ionosphere-Thermosphere Data Assimilation

This chapter presents the first study to infer neutral temperature from RO EDPs during a storm event using strongly coupled data assimilation. This study marks an important step in producing a reanalysis by improving the model representation of storm-time neutral density variability using the data assimilation framework demonstrated in Chapter 3. Considerable effort is devoted to achieving a 10% observation rejection rate by improving observation-model comparisons through ensemble initialization and filter tuning. The reanalysis is validated against independent Gravity Recovery and Climate Experiment Follow-On (GRACE-FO) neutral density data, improving neutral density errors by 20%, with better represented global recovery timescales. Quantitative comparisons against TIMED-SABER NO cooling suggest that the cause of slow recovery time scales is likely due to underestimated peak cooling magnitudes in TIEGCM. Further analysis indicates that in addition to the temperature changes, composition changes contribute to improved neutral density errors. The resulting thermospheric reanalysis shows promise for aiding future scientific investigations of dynamics and energetics associated with neutral density variability during storm periods.

4.1 Background and Motivation

Properly capturing the storm-time neutral density variability requires fully coupled physics-based models to represent non-linear, complex physical processes of a coupled I-T

system on a wide range of temporal and spatial scales. However, leveraging observation constraints through data assimilation to improve the physics-based representation of the storm response is challenging due to a lack of direct, global coverage of neutral state dynamical observations. To overcome this limitation, this chapter extends the framework established in Chapter 3 and uses RO EDPs in strongly coupled I-T data assimilation to improve the model representation of neutral density variability. The creation of I-T reanalyses has been previously demonstrated to provide scientific insights, such as in assimilating middle atmosphere observations for neutral states (Pedatella et al., 2014, 2018), or assimilating plasma observations to analyze tidal variation (Rajesh et al., 2021).

Currently available physics-based models are insufficient to reproduce neutral density variability due to biases resulting from misspecified external forcing and misrepresented internal processes. These biases include inadequately represented diurnal differences, traveling atmospheric disturbances (TADs) associated with storms, and radiative cooling processes during a storm recovery phase. This chapter uses the TIEGCM as the coupled I-T model. The TIEGCM has previously been shown to not well reproduce detailed storm-enhancement structures (Pham et al., 2022) and cooling time-scales, which is often attributed to poorly specified NO cooling (Lei et al., 2011; Lu et al., 2014; Sheng et al., 2017; Li et al., 2019). The TIEGCM neutral density also shows a stronger sensitivity to neutral temperature than seen in observations (Thayer et al., 2023). Efforts to improve NO cooling biases have led to an adjustment of particle precipitation and implemented a temperature-dependent reaction rate; however, further biases remain (Sheng et al., 2017; Chen and Lei, 2018). The NO cooling rate, shown in Equation 1.8, is directly proportional to NO concentration and exponentially dependent on neutral temperature, and the relative bias contributions from each state are unclear. While NO cooling is the main mechanism of temperature recovery at low altitudes (< 200 km), downward thermal conduction (Maeda et al., 1992) due to temperature gradients is conversely the primary recovery process at higher altitudes. The relative influence of each process is an open question in the upper atmosphere.

Data assimilation studies focusing on a storm event have often used a separate data assimilation procedure, such as with the Assimilated Mapping of Geospace Observations (AMGeO) (Matsuo et al., 2020) or the Assimilative Mapping of Ionospheric Electrodynamics (AIME) (Richmond and Kamide, 1988; Lu, 2017). These tools use publicly available high-latitude geospace observations and have been shown to improve model biases, e.g., polar wind dynamics (Lu et al., 2014; Lu, 2017), over empirical models of magnetospheric forcing. Estimation of forcing parameters, such as the Kp and F10.7 indices, has also been previously done using neutral density observations (Codrescu et al., 2018; Sutton, 2018; Sutton et al., 2021). High latitude magnetospheric forcing has been studied for its impact in an ensemble sensitivity study coupling the TIEGCM with AMGeO (Hsu et al., 2021a). Assimilation of NO cooling flux observations has shown to improve neutral density behavior in the storm recovery phase (He et al., 2023); however, direct state estimation of model states over an entire storm period has not been extensively developed due to the lack of global neutral observations to constrain states. Assimilating real observations for the I-T system requires considerable effort to improve the observation-model agreement, with previous studies assimilating RO EDPs showing large observation rejection rates Lee et al. (2012). Representing the model uncertainty realistically (e.g., Hsu and Pedatella, 2023) is thus an important step to provide model background error covariances for the successful assimilation of real observations.

This chapter aims to improve the model representation of neutral density variability for a storm-time event through constraining neutral states with globally available plasma observations. Specifically, the DART-TIEGCM is used to assimilate COSMIC-2 EDPs to estimate neutral temperatures. Using abundant ionospheric observations, with full longitudinal coverage, has been previously shown to effectively constrain neutral states and overcome neutral observation limitations (Matsuo and Hsu, 2021; Hsu et al., 2014; Matsuo et al., 2013; Lee et al., 2012; Kodikara et al., 2021; Pedatella et al., 2020). The resulting thermospheric reanalysis is validated against available independent observations. The primary focus is to evaluate the improvement of TIEGCM biases, attained through EDP assimilation

during the storm main and recovery phases, against GRACE-FO neutral densities. Using TIMED-SABER NO cooling flux, potential sources of NO cooling biases in the TIEGCM are investigated, along with their impact on neutral density recovery time scales. Composition analysis is furthermore compared with TIMED-GUVI O/N_2 ratios.

The rest of the chapter is structured as follows. Section 4.2 details the DART-TIEGCM framework and observations that are used in the study, and the ensemble initialization and filter configuration are described in Section 4.3. Verification of data assimilation experiments with respect to assimilated COSMIC-2 observations is shown in Section 4.3.3. The reanalysis results presented in Section 4.4 include validation with independent data sets of GRACE-FO neutral densities (Section 4.4.1), TIMED-SABER NO cooling (Section 4.4.3), and TIMED-GUVI O/N_2 (Section 4.4.2). The following sections include a discussion in Section 4.5 and conclusions in Section 4.6.

4.2 Approach

4.2.1 Data Assimilation: DART-TIEGCM

The EAKF implemented in the DART(Anderson, 2001; Anderson et al., 2009a), along with TIEGCM, is used for data assimilation, specifically the DART-TIEGCM using the Manhattan version of DART (Hsu et al., 2024). This version includes more efficient parallel computations and additional filter features. The Apex magnetic coordinates system (Emmert et al., 2010; Richmond, 1995) in the TIEGCM v2.0 is updated to the most recent epoch time. Solar irradiance is specified with a proxy model with the F10.7 index as input. The TIEGCM has a horizontal grid of 2.5-degree resolution with 144 longitude and 72 latitude grid points, with the vertical grid defined with quarter scale height resolution defined with 57 pressure levels. Lower boundary conditions are defined using the GSWM including diurnal and semi-diurnal migrating tides along with diurnal and semi-diurnal non-migrating tides (Hagan and Forbes, 2002, 2003). Magnetospheric forcing is specified with the Weimer model, with input

from the interplanetary magnetic field (IMF) solar wind parameters, to generate the high-latitude electric field convection pattern (Weimer, 2005) and an empirical auroral model included within the TIEGCM v2.0. Specific model input is detailed in Section 4.3.1 and Appendix B.

4.2.2 Storm Experiment Period

The experiment is conducted for July 5th - July 10th, 2022, and includes an isolated geomagnetic storm with a maximum Dst drop of -85 nT on July 7th and a peak Kp of 5. The F10.7 index (solar irradiance proxy), solar wind IMF parameters, and geomagnetic indices are shown in Figure 4.1. The experiment period includes a quiet period that begins at UT01 on July 5th. The beginning of the storm's initial phase is marked by the increase in SYM-H at UT07 on July 7th, with the storm's main phase starting at UT13 on July 7th as the SYM-H index drops to negative values. The minimum SYM-H index occurs at UT02 on July 8th at -85 nT, marking the beginning of the storm recovery phase, with the solar wind B_z component turning northward after UT03 on July 8th. Solar wind characteristics, typically associated with geomagnetic storms, are seen in the large spike in IMF density, velocity, and the negative B_z component of the magnetic field.

4.2.3 I-T Satellite Observations

The experiment assimilates EDPs retrieved from the COSMIC-2 RO data into the TIEGCM. COSMIC-2 is a constellation of 6-satellites in LEO with separate orbital planes all at 24° inclination and 550 km altitude and has full operational coverage for 2022 following its launch in 2019 (Yue et al., 2014b; Fong et al., 2019). Thus COSMIC-2 provides full longitudinal coverage and low- and mid-latitude coverage from $-40°$ to $+40°$ latitude. COSMIC-2 RO EDP retrieval uses Abel inversion, relying on the spherical symmetry assumption. The EDP retrieval errors are expected to improve with altitude, as shown in Chapter 2. EDP error analysis provided by Yue et al. (2010); Liu et al. (2010); Lee (2013) are used to inform

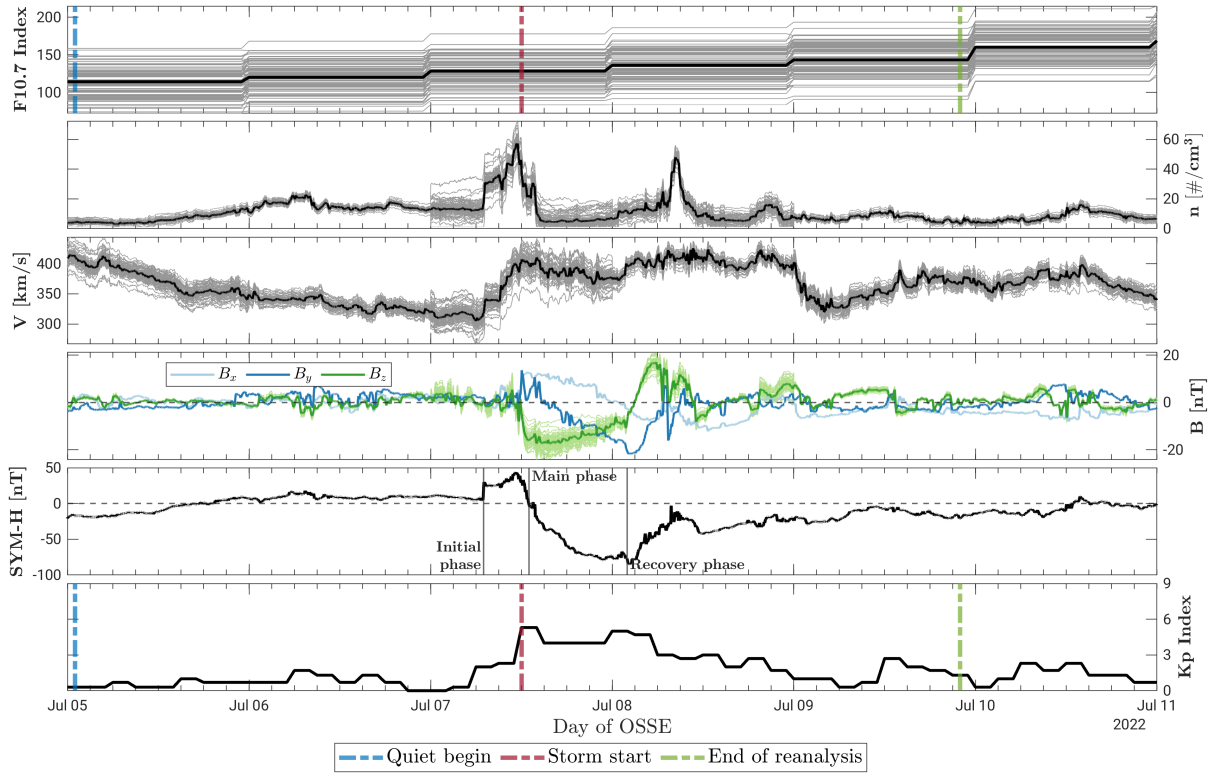

Figure 4.1: Solar irradiance (F10.7), solar wind IMF parameters, and geomagnetic indices (Kp and SYM-H) for the reanalysis period. Solar wind IMF parameters include plasma density, n, flow speed, V, and the three magnetic field components, B_x, B_y, and B_z. Lighter color lines indicate perturbations used to initialize the TIEGCM ensembles. Vertical lines denote phases of the reanalysis and indicate the three storm phases: initial, main, and recovery.

observation error covariances used in this study. EDPs from 160 to 500 km altitude at 10 km increments are assimilated. Quality control of EDP data is performed before assimilation and is addressed in Section 4.3.2.

The reanalysis neutral density field is validated against GRACE-FO neutral density observations (March et al., 2021), derived from onboard accelerometers. The GRACE-FO data sets are the highest resolution neutral density data available, provided every 10 seconds with a $\sim$ 95 minute orbit period. GRACE-FO is in a near-polar orbit, providing neutral density samples at two solar local times: $\sim$ 7 LT (dawn) and $\sim$ 19 LT (dusk).

TIMED provides two types of measurements useful for the validation of reanalysis fields. TIMED-SABER has continuous measurements of NO cooling flux (Esplin et al., 2023; Mlynczak, 1997; Mlynczak et al., 2003). The SABER instrument scans the Earth's limb of NO cooling irradiances at the 5.3 μm infrared wavelength, and following an Abel transform, outputs a vertical profile of energy loss per volume from 100 to 250 km. For July 2022, TIMED-SABER observes from $\sim -83 - 53$ deg latitude at a dawn median of $LT \sim 7$, and a dusk median of $LT \sim 22$. A new NO concentration data product has recently been made available (Wang et al., 2024) but does not yet include 2022. TIMED-GUVI makes measurements of far ultraviolet (FUV) airglow (Christensen et al., 2003) to provide the altitude integrated O/N_2 ratio (Meier, 2021) in the dusk LTs $6 - 10$ and for latitudes between -60 and 60 degrees.

4.3 Ensemble Filter Experiments

The following three sections describe the trial-and-error experiments performed to produce the thermospheric reanalysis of the storm event. The ensemble initialization effort is detailed in Section 4.3.1, followed by the filter configuration in Section 4.3.2, and experiment verification against COSMIC-2 plasma observations in Section 4.3.3. Data assimilation experiment results and their relative improvement are assessed against a control experiment with an identical ensemble but without data assimilation.

4.3.1 Ensemble Initialization

Ensemble initialization is critical to provide ensemble state spread and realistic background covariance structures. Previous data assimilation studies have primarily performed ensemble initialization using external forcing (Dietrich et al., 2022; Hsu et al., 2021a; Lee et al., 2012; Matsuo et al., 2013). External forcing perturbations are introduced through three means: solar irradiance through the F10.7 index, magnetospheric forcing through the Weimer model with input solar wind parameters, and lower boundary conditions through GSWM. It is noted the mean external forcing is kept unchanged from observed values and only the perturbation spread is adjusted. One additional perturbation is included to account for internal process uncertainties: the collision factor between O^+ and O, defined as ν_{O^+-O}. Specific ensemble initialization details are outlined in Appendix B, with the perturbed parameters illustrated in Figure 4.1.

Adding perturbations for ensemble initialization are shown in Figures D.1 and D.2 for their impact on background correlation structures. The locally averaged correlation between electron density and neutral temperature is shown along a pressure surface, where correlations are expected to be better described along a constant pressure level. Ensemble initialization examples include using constant F10.7, a perturbed time-series of F10.7, adding perturbations to the lower boundary, and adding perturbations to ν_{O^+-O}. Figure D.1 illustrates example correlations for the quiet period, with adding time-series perturbations for the F10.7 index and ν_{O^+-O} perturbations visibly reducing correlation magnitudes. The lowest correlations are seen near dawn, where there is the least solar irradiance influence, and in the vicinity of the dusk terminator where the EIA remains strong. During the peak storm time in Figure D.2, correlation structures are consistent and close to zero in some regions. Solar wind parameter perturbations are the same for each ensemble run, and as expected have a strong influence on I-T variability during a storm. Regardless, these modeled correlation structures do not likely reflect actual correlation structures. For example, it is

likely correlations near one are unrealistic, and plasma correlation structures are expected to have much smaller scales (Allen et al., 2023).

4.3.2 Filter Configuration

The model state vector updated by data assimilation in this chapter is given as $\mathbf{x} = [\boldsymbol{f}_{e^-}^T, \boldsymbol{f}_{O^+}^T, \boldsymbol{f}_{Tn}^T]^T$. The specific data assimilation approach is detailed in Section 1.2.1.1. Updating neutral temperature results in the best impact for neutral density estimation, whereas updating neutral winds and composition leads to mixed results (not shown). The total number of ensemble members is 90 and forecast cycling is set to one hour. Concurrent with ensemble initialization, tuning of the EAKF parameters is carried out. Tuned filter parameters include localization and outlier thresholding. In addition, observation quality control is applied before data assimilation.

Implementing localization is necessary to counter spurious correlations and correct correlation structures with overestimated correlation length scales likely introduced due to the F10.7 perturbation, as shown in Figures 3.1 and D.1. The localization function is given by the isotropic GC function (Gaspari and Cohn, 1999), with a GC half-length of 0.4 radians ($\sim$2600 km) found to be most effective. Increasing the half-length to 0.8 radians saw degrading filter performance. Vertical localization was not found to have a positive impact and thus was not used in the study. It is noted that adding lower boundary perturbations was effective in introducing more realistic vertical correlation structures.

For observation quality control, errors due to poor observation quality are weighted against insufficient model variability and spread. Poor quality observations could come from breakdowns in the spherical symmetry assumptions (Chapter 2), or from strong radio signal scintillations. Thus plasma profiles deviating too much in shape from the TIEGCM are flagged and rejected, which also helps to ensure more effective neutral temperature updates. These rejection criteria include when >50% of the EDP are "far" from the TIEGCM ensemble profiles, defined as more than four innovation standard deviations (STDs) away,

and when the EDP h_mF_2 is outside of the $220 - 450$ km altitude range. This pre-processing removes on average 10% of observations, a reasonable trade-off. Following this observation quality control, the filter outlier thresholding was relaxed to a threshold of 4.5 STDs. DART implements this as rejecting observations past some specified number of STDs away from the ensemble forecast spread as defined by the innovation statistics. Increasing the outlier threshold to 6 STDs begins to degrade filter performance.

Sensibly extracting more observation information is found to positively impact data assimilation performance, but does come at the cost of tighter model spreads with assimilated observations assumed independent. This tightening of model spread most evidently affects the quiet period results with stagnating filter performance (discussed in Section 4.5). This spread issue is most commonly countered with inflation, where specifically adaptive inflation El Gharamti (2018) was tested but did not have a strictly positive impact. Inflation uses the innovation statistics to artificially boost state spread, and while testing found some improvement to electron density errors, adjustments to neutral temperature caused model neutral density states to diverge from observations. For this reanalysis, state spread issues are overcome by starting the experiment assimilation 12 hours before the storm at UT00 on July 7th, and was found to be an adequate spin-up period to settle neutral state disturbances. During the storm period, we avoid issues of filter diverging from improper initial conditions as the storm enhancement is strongly driven by external magnetospheric forcing, and has the benefit of providing an additional source of state spread. It is noted that the I-T initial conditions are still important as the initial energy determines the relative state impact of input magnetospheric energy (e.g., Burns et al., 2004).

The foremost benefits we achieve from ensemble initialization and filter tuning are improvements to the observation rejection rate, while the issues of model spread inhibited sufficiently uniform rank histograms from being achieved. COSMIC-2 EDP rank histograms for the best no-assimilation run are shown in Figures D.4 and D.5, separated by solar local time, altitude, and magnetic latitude. These observations have complex spatial biases making

it challenging to simply fix. For example in Figure D.5, the southern latitudes are plasma are generally over-biased while the northern latitudes are generally under-biased.

4.3.3 Verification with COSMIC-2 Observation

Experiment verification is done by comparing forecast plasma states against COSMIC-2 EDP observations over the full experiment period. Experiments for ensemble initialization and filter configurations are listed in Table 4.1, separated by no-assimilation controls (denoted Cntrl) and assimilation experiments (denoted Exp). These configurations include adding lower boundary perturbations (GSWM), adjusting horizontal localization (Local), adding observation quality control (QC), adjusting outlier rejection (outlier thresh), and adding internal perturbations (ν_{O^+-O}), as detailed in Sections 4.3.1 and 4.3.2.

Table 4.1: Configurations for the experiment (Exp) and control (Cntrl) runs for ensemble initialization and filter configurations.

Run Name	**EDP Assim**	**Ensemble Initialization**				**Ensemble Filter**		
		F10.7	**Weimer**	**GSWM**	$\boldsymbol{\nu_{O^+-O}}$	**Local**	**QC**	**Outlier Thresh**
Cntrl_0		✓	✓					
Cntrl_*		✓	✓	✓			✓	
$\text{Cntrl}_{*-\nu}$		✓	✓	✓	✓		✓	
Exp_0	✓	✓	✓					
Exp_G	✓	✓	✓	✓				
Exp_{QC}	✓	✓	✓				✓	
Exp_{HL}	✓	✓	✓			✓		
$\text{Exp}_{G-HL-QC}$	✓	✓	✓	✓		✓	✓	
Exp_*	✓	✓	✓	✓		✓	✓	✓
$\text{Exp}_{*-\nu}$	✓	✓	✓	✓	✓	✓	✓	✓
$\text{Exp}_{*-Storm}$	✓	✓	✓	✓		✓	✓	✓

The altitude profile of the rejection rate is shown in Figure 4.2 for select ensemble runs including observations from UT 01 on July 5th to UT22 on July 8th. For the initial control run, Cntrl_0, there is around a 50% rejection rate at low altitudes that reduces to around $15-30\%$ for the mid and high-altitudes. The initial experiment run, Exp_0, with a reduction in

state spread, has around a 45% rejection rate at all altitudes. From this starting point, added features reduce the rejection rate and improve data assimilation performance. Adding lower boundary perturbations in Exp_G did not significantly positively impact rejection rates. The greatest benefits come from observation quality control and adjusting the outlier threshold, where including these features in Exp_* show peak rejection rates of 30% at low altitudes and less than 20% at high altitudes. $\text{Exp}_{G-HL-QC}$ that includes quality control, lower boundary perturbations, and horizontal localization mostly show benefits from quality control. The best model-observation agreement is in control runs Cntrl_* and $\text{Cntrl}_{*-\nu}$, with a 30% rejection rate at low altitudes and $< 5\%$ rejection at high altitudes, for an average rejection rate of 10%. Adding ν_{O^+-O} slightly improves experiment rejection rates in $\text{Exp}_{*-\nu}$. These reject rates are improved over the results of Lee et al. (2012) with an average EDP rejection rate of 35%. We note experiment rejection rate increases come primarily from the night side.

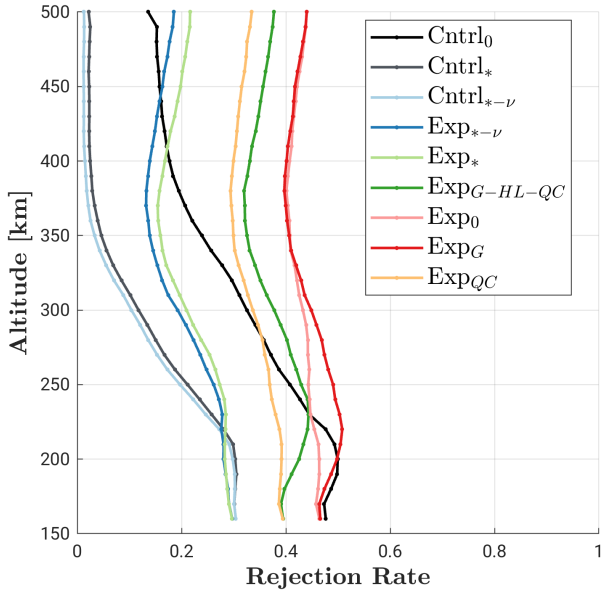

Figure 4.2: Rejection rate profile as a function of altitude for COSMIC-2 EDPs. Rates are averaged over UT 01 on July 5th to UT22 on July 8th.

The total forecast plasma RMSEs are shown in Figure 4.3, and generally where the rejection rate is reduced, RMSEs are improved. These RMSEs are time-smoothed with a moving window of ± 1.5 hours. The assimilation experiments consistently improve the forecast RMSE over their respective control, such as between Exp_0 and Cntrl_0. The RMSE improvement is most evident during the peak storm period (UT12 on July 7th - UT12 on July

8th) with RMSEs in Exp_* and $\text{Exp}_{*-\nu}$ considerably lower than their control counterparts. Comparing Exp_0 and Exp_G, while lower boundary perturbations did not improve rejection rates, they did improve the mean biases. Thus adding lower boundary conditions, increasing horizontal localization, performing observation quality control, and adjusting outlier rejection all positively impact assimilation experiment performance. Over the quiet and storm periods, Exp_* and $\text{Exp}_{*-\nu}$ perform the best, with added ν_{O^+-O} perturbations providing a slight improvement .

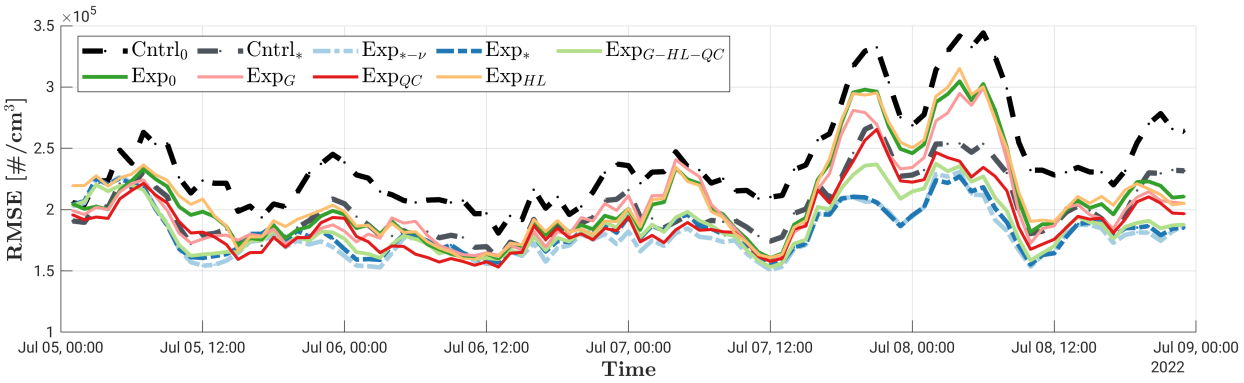

Figure 4.3: Time-series of RMSEs from control and experiment runs over the full experiment period, comparing forecast electron densities against COSMIC-2 EDPs.

Forecast error results for one of the best-performing experiments $\text{Exp}_{*-\nu}$ are further illustrated in Figure 4.4. The top panel shows the percentage reduction in RMSE compared against $\text{Cntrl}_{*-\nu}$, defined as

$$\text{RMSE Reduction} = -1 \times \frac{RMSE_{exp} - RMSE_{cntrl}}{RMSE_{cntrl}} \tag{4.1}$$

where RMSEs are separated by low (defined as < 250 km), middle ($250 - 350$ km), and high (> 350 km) altitudes. Total forecast RMSEs generally improve around $10 - 20\%$ over the control, where the best performance is seen for high altitudes with a 20% RMSE reduction. These relative RMSE errors also consistently improve over time. In the bottom panel of Figure 4.4, the STD$(obs - forecast)$ (O-F) spread is shown describing the closeness of forecast states to observations. There is consistent improvement in O-F spread at the

middle and high altitudes and negligible assimilation impact on the low altitudes. The EDP retrieval is the best at F-region altitudes with the lowest observation errors (Chapter 2); this region contains the strongest dynamical correlations from plasma-neutral coupling and is most relevant for LEO neutral density variability. Additional plasma state diagnostics for $\text{Exp}_{*-\nu}$ are shown in Figure D.3 for altitude-dependent RMSEs, observation rejection rate time-series, data assimilation spread impacts, and h_mF_2 and N_mF_2 RMSEs.

Following this experiment testing, Exp_* is found to have the best performance for both plasma and neutral states. For storm-period results, as previously stated in Section 4.3.2, we begin the experiment at UT01 on July 7th and denote this as $\text{Exp}_{*-Storm}$. Thus for the following neutral state validation, $\text{Exp}_{*-Storm}$ is selected as the reanalysis field.

4.4 Reanalysis Validation and Interpretation

4.4.1 Validation with GRACE-FO Observations

Comparing the reanalysis field beginning at UT00 on July 7th against GRACE-FO neutral densities, forecast $\text{Exp}_{*-storm}$ neutral densities are validated at $\sim$ 500 km altitude in the dawn and dusk LT regions, shown in Figure 4.5. The top panel (a) shows the time series of GRACE-FO, the reanalysis mean, the ensemble spread, and the control mean. The TIEGCM generally follows the neutral density response seen in GRACE-FO, with most differences in the main storm phase where the TIEGCM does not replicate some small-scale structures of density enhancement. During the recovery phase, the TIEGCM follows the relaxation that GRACE-FO observes, and the reanalysis better matches observations. The reanalysis additionally performs better than the control in the quiet period preceding the storm.

Smoothing the neutral density magnitudes using a rolling mean orbit average ($\pm$90 minutes), the mean response of the storm event is shown in Figure 4.5b. The reanalysis improvement is seen here for both quiet and storm periods, as the reanalysis more closely

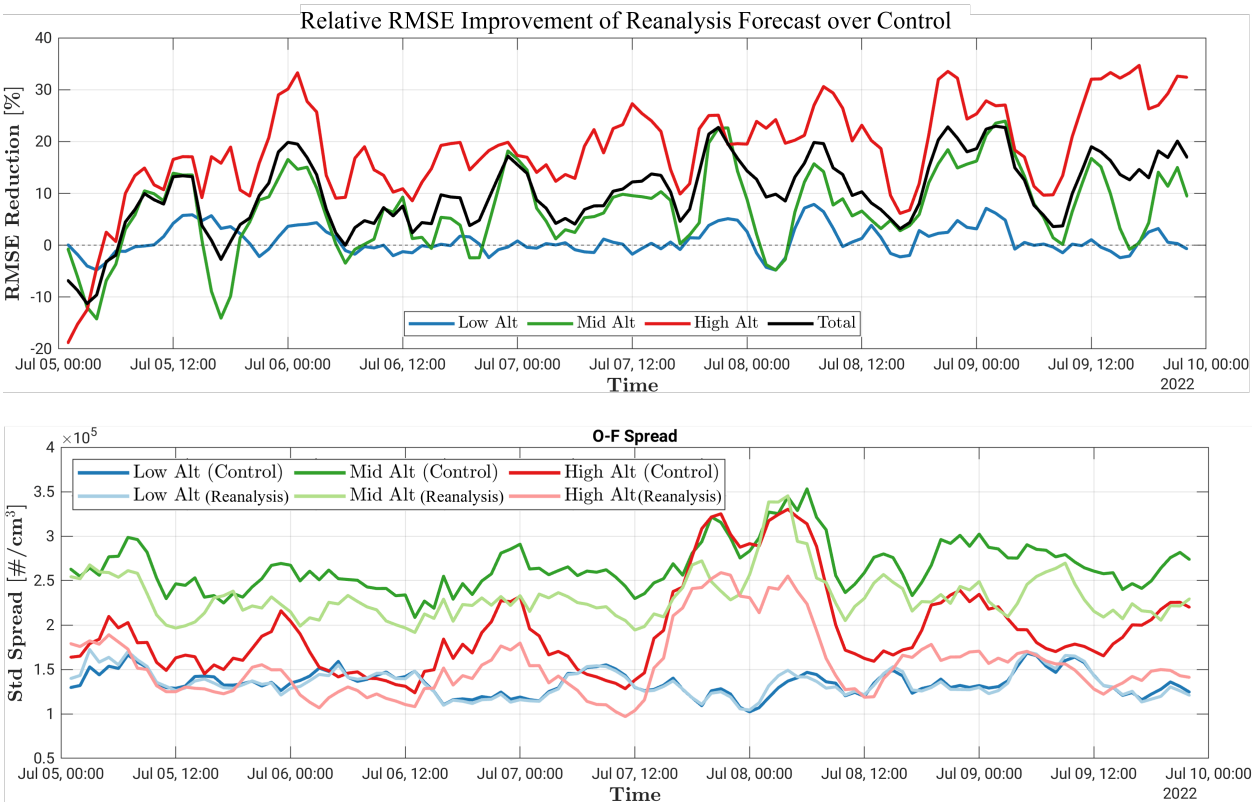

Figure 4.4: Relative plasma improvement of $\text{Exp}_{*-\nu}$ compared over $\text{Cntrl}_{*-\nu}$. Observation minus background (O-F) spread is defined as 1 standard deviation.

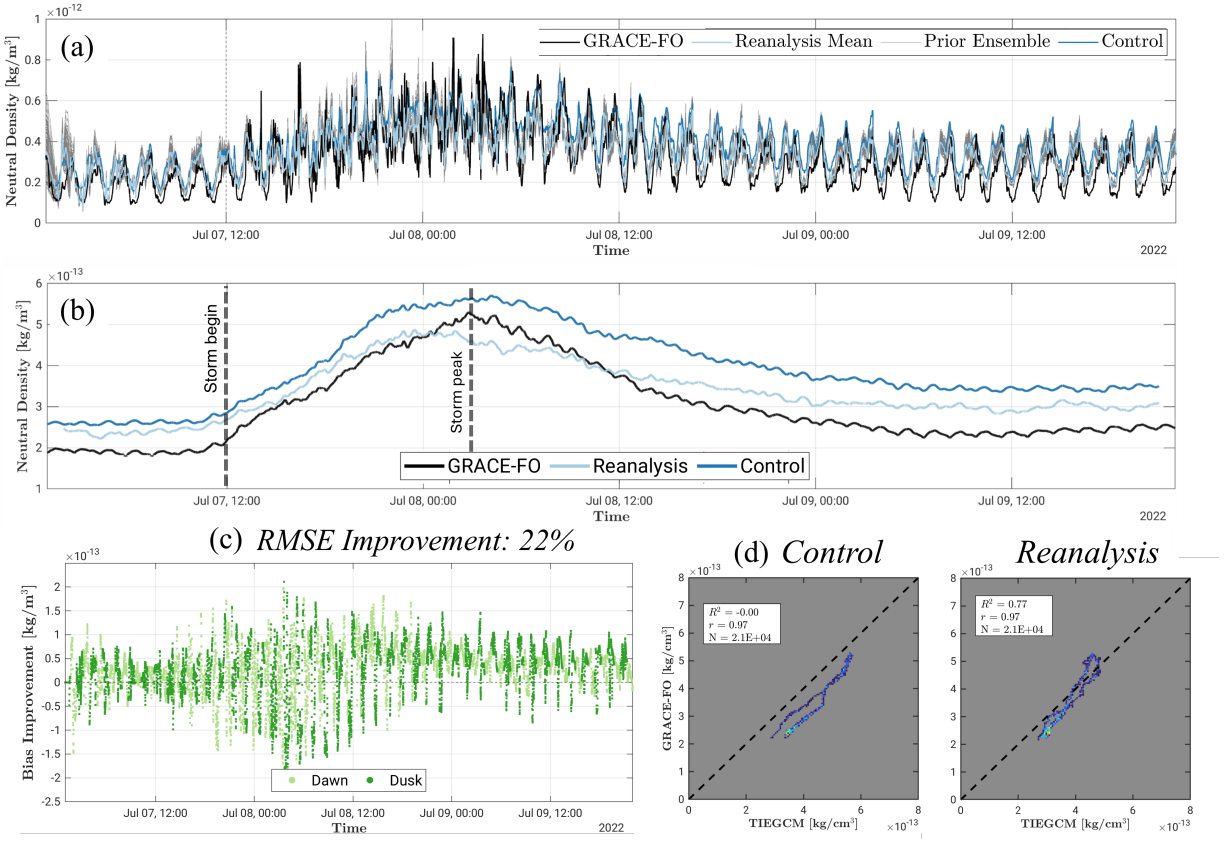

Figure 4.5: GRACE-FO neutral density comparisons, with the TIEGCM control (Cntrl$_*$) and reanalysis (Exp$_{*-Storm}$) results.

matches GRACE-FO neutral densities than the control, except for the peak neutral density being underestimated in the reanalysis. The reanalysis shows the best performance as the thermosphere cools, where GRACE-FO shows a faster cooling response than the TIEGCM, and this improvement begins to plateau after UT12 on July 9th. We note the GRACE-FO average neutral density recovers to a magnitude on July 10th greater than the prior quiet state and is attributed to the rising solar EUV flux (shown by the F10.7 index in Figure 4.1). A comparison of the relative biases for individual observations is shown in Figure 4.5c, where the bias improvement of the reanalysis over the control is defined as

$$\textbf{Bias Improve} = |\bar{\boldsymbol{x}}_{control} - \boldsymbol{y}_{GRACE-FO}| - |\bar{\boldsymbol{x}}_{reanalysis} - \boldsymbol{y}_{GRACE-FO}| \tag{4.2}$$

where $|\boldsymbol{x}|$ is the absolute value operator, $\bar{\boldsymbol{x}}_{control}$ are the mean control states, $\bar{\boldsymbol{x}}_{reanalysis}$ are the mean reanalysis states, and $\boldsymbol{y}_{GRACE-FO}$ are GRACE-FO observations. Positive values indicate reanalysis improvement and are split for the dawn and dusk LTs, with a total reduction in reanalysis RMSEs of 22% over the control. Clear improvements are seen for the quiet period and mixed bias impacts during the storm's main phase. During the storm recovery phase, we see the best performance of reanalysis, from UT12 on July 8th to the end of the reanalysis, where the reanalysis corrects biases due to internal processes rather than external forcing errors driving biases in the storm main phase. For the mixed reanalysis performance during the storm main phase, errors were not found to have a strong magnetic latitude or dawn-dusk dependence, as shown in Appendix D Figure D.9.

The agreement of smoothed experiment neutral densities with GRACE-FO is quantified in the bottom right panel in Figure 4.5d. Quantifying agreeing using a best-fit value R^2 along the line $x = y$, the reanalysis improves biases to $R^2 = 0.77$ compared with the control value of $R^2 = 0$. Quantified correlations remain constant between the control and reanalysis and both show high correlations with GRACE-FO observations.

The separation of neutral density results by dawn-dusk LTs and latitude is shown in Figure 4.6. The left panel shows the latitude average of the dawn and dusk LTs, where

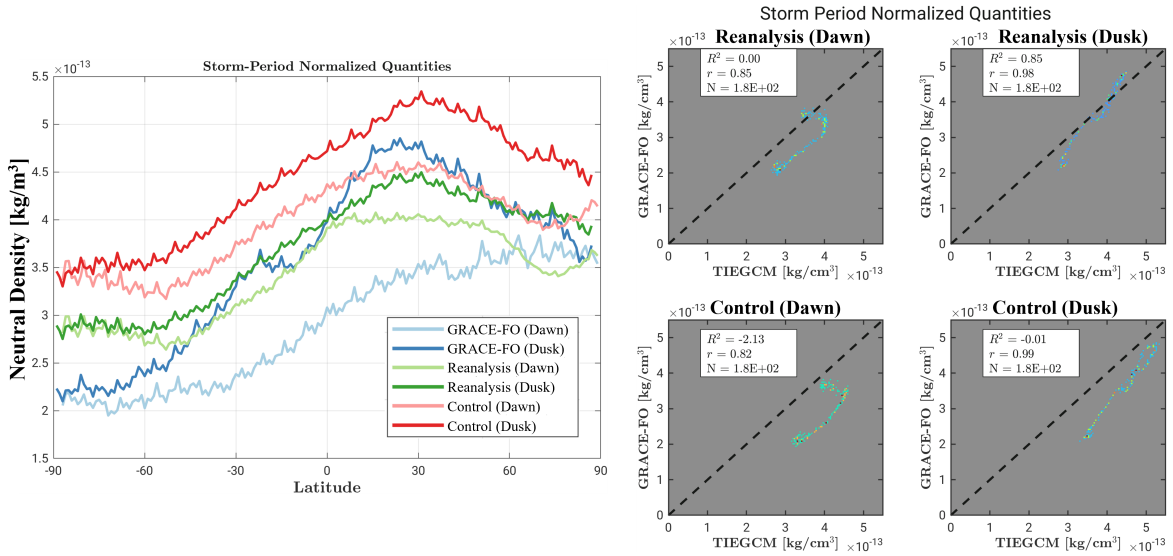

Figure 4.6: GRACE-FO, Cntrl$_*$, and Exp$_{*-Storm}$ neutral densities separated by dawn-dusk LT sides and averaged over latitude, shown for the storm period.

the reanalysis produces lower neutral densities compared with the control, more closely aligning with GRACE-FO observations. The reanalysis also overcorrects and subsequently underestimates the dusk neutral densities near 0-45 degrees latitude. Notably, a larger bias separation is seen between the two LT sides for GRACE-FO observations than in the TIEGCM. The reanalysis additionally produces an even closer dawn-dusk separation than the control and points to other sources of model biases.

The right panel of Figure 4.6 quantifies the agreement of the control and reanalysis to GRACE-FO observations. The reanalysis improves agreement on the dawn side from a control value of $R^2 = -2.13$ to a value of $R^2 = 0$. For the dusk side, reanalysis improves over the control from $R^2 = -0.01$ to $R^2 = 0.85$ and represents the best-performing validation region of the reanalysis.

To explain the difference in performance between the dawn and dusk sides, observation correlations, r_{xy}, are assessed between GRACE-FO and the TIEGCM states to COSMIC-2 EDP parameters N_mF_2 and h_mF_2. These correlations are shown in Figure 4.7 for (a) COSMIC-2 N_mF_2 to GRACE-FO density, (b) COSMIC-2 h_mF_2 to GRACE-FO density, (c)

COSMIC-2 h_mF_2 to the TIEGCM density, and (d) COSMIC-2 h_mF_2 to the TIEGCM temperature. These correlations are calculated using co-located points between COSMIC-2 and GRACE-FO observations over the full reanalysis period, collected at the nearest hour when within 2600 km. Comparing (a) COSMIC-2 N_mF_2 to GRACE-FO, higher correlations exist on the dusk side, $r_{xy} = 0.43$, compared with the dawn side, $r_{xy} = -0.08$. The same difference is seen in (b) comparing COSMIC-2 h_mF_2 to GRACE-FO, with dawn correlation $r_{xy} = 0.16$ and dusk correlation $r_{xy} = 0.38$. The TIEGCM neutral densities show similar correlations in (c), with dawn and dusk correlations at $r_{xy} = 0.12$ and $r_{xy} = 0.41$, respectively. These correlations can be explained through the impact of neutral temperature, where COSMIC-2 h_mF_2 has dawn and dusk correlations at $r_{xy} = 0.27$ and $r_{xy} = 0.43$, respectively. The TIEGCM showing similar correlations as GRACE-FO supports the TIEGCM representing realistic correlations. It is this general relationship that we rely upon in this data assimilation framework where solar irradiance heating of the day-side thermosphere changes scale height, affecting both neutral and plasma densities. Additionally, this can potentially explain the reduction of dawn-dusk separation biases in the reanalysis seen in Figure 4.6, with greater analysis impact on the dusk side. These weaker dawn LT correlations can be explained by incoming O^+ flux or other processes controlling plasma variability. Nonetheless, there is a positive reanalysis impact on the dawn side, whether accomplished through direct updates or forecast step coupling influences at other LTs.

A keogram of the dusk-side storm response at GRACE-FO locations is shown in Figure 4.8, qualitatively illustrating the improvement of the reanalysis $\text{Exp}_{*-Storm}$ over Cntrl_*. The large improvement in the recovery period cooling is most evident, while the reanalysis dampens some misplaced neutral density enhancement structures albeit without placing new enhancement structures not already present in Cntrl_*. Additionally, the reanalysis has positive impacts at high latitudes, where there is no EDP observation coverage, with impacts likely through forecast dynamical coupling. A dawn-side keogram is also shown in Appendix D Figure D.6.

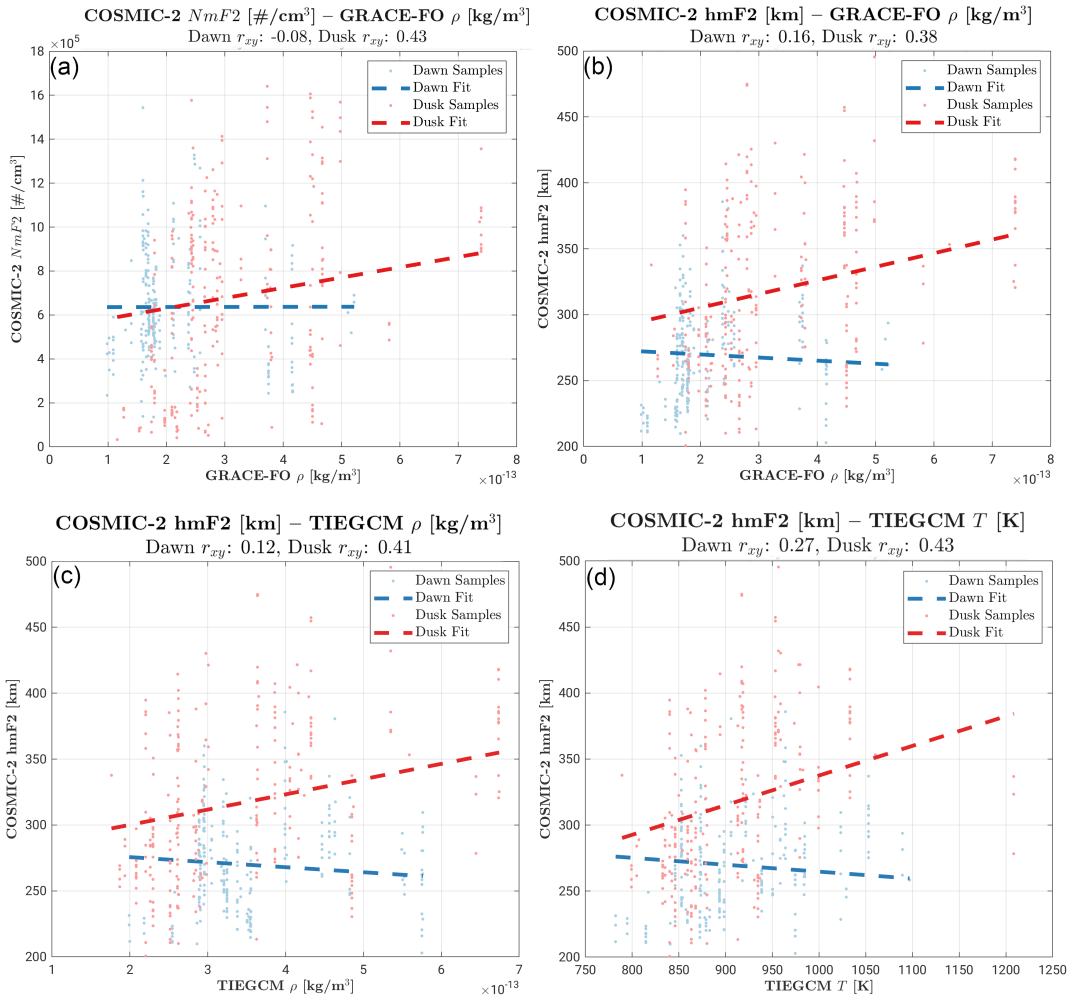

Figure 4.7: Comparison of dawn-dusk correlations from COSMIC-2 EDP parameters N_mF_2 and h_mF_2 to GRACE-FO neutral densities and the TIEGCM states. Observations and states are co-located within a 2600 km radius, at the nearest hour, for July 5th - July 9th. Respective dawn and dusk correlations, r_{xy} are quantified for each grouping.

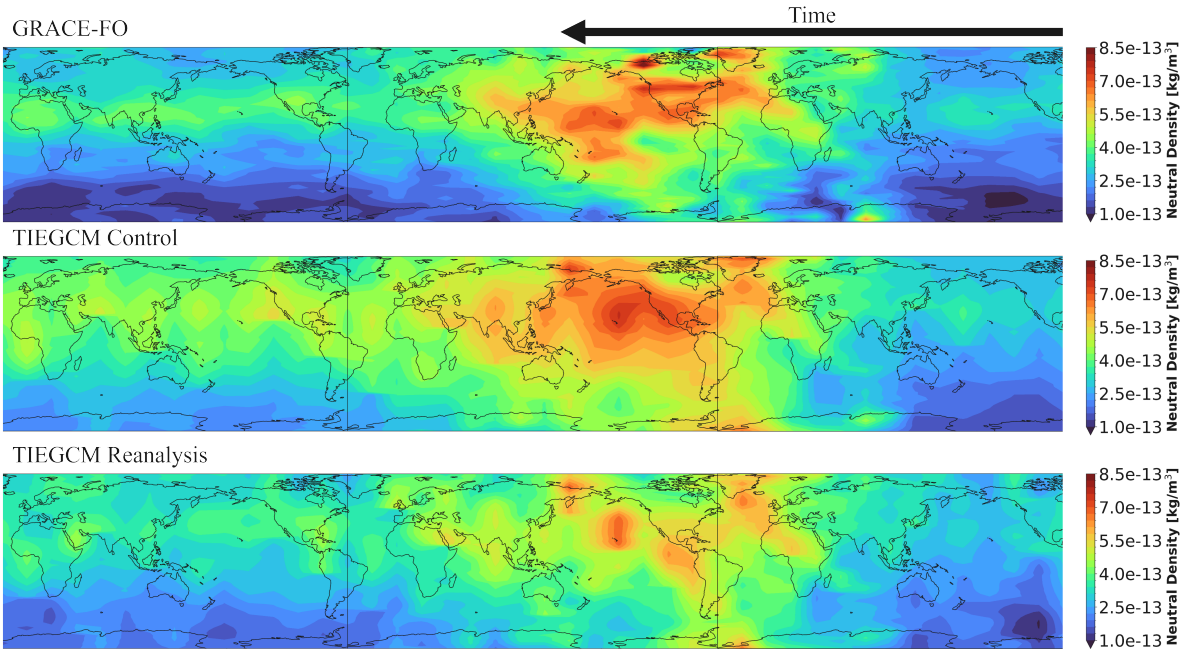

Figure 4.8: Keogram of the dusk-side GRACE-FO neutral densities, Cntrl$_*$, and forecast Exp$_{*-Storm}$ states. Plotted by latitude slices with time moving to the left.

4.4.1.1 Along-track Scale Height Correlations

Reanalysis estimation of neutral density is accomplished through neutral temperature and composition changes, where their impact can be explained through adjustments to scale height (Equation 1.5) as a dominant means for controlling neutral density variability. Correlations of the Cntrl_* and $\text{Exp}_{*-Storm}$ ensembles between scale height to neutral temperature and mean molecular mass are shown in Figure 4.9 along a pressure-level surface at GRACE-FO locations. In the control, temperature is highly correlated with scale height variability throughout the quiet and storm periods, remaining near 1. The mean molecular mass shows lower correlations, with a mean correlation of 0.6 during the quiet period and 0.4 during the storm peak. In the reanalysis, temperature and mean molecular mass more equally contribute to scale height variability. During the quiet period, the temperature remains very high ($\sim$1 correlation) with spikes toward zero, and mean molecular mass averages 0.8 correlation. During peak storm time, mean molecular mass and neutral temperature correlations drop to 0.6, with intervals where mean molecular mass correlations are greater than those with neutral temperature. The increased storm state variability is illustrated in the quiet-to-storm drop in correlation, where the mean molecular mass correlation drops 0.2 for both the control and reanalysis, while the reanalysis temperature correlation drops considerably more (0.2) compared with the control temperature.

From these correlations, the reanalysis neutral temperature and composition states more comparably impacted scale height variability than in the TIEGCM control. The question of how real these relative contributions are needs further investigation to uncover what "realistic" features the reanalysis adds versus non-physical characteristics that the analysis update introduces. In Thayer et al. (2023), the TIEGCM was found to be more sensitive to temperature as a means for adjusting neutral densities over mean molecular composition, supporting correlations seen here in the control ensemble. It is also noted for the quiet period, the two shown orbit passes are representative of the entire quiet period cor-

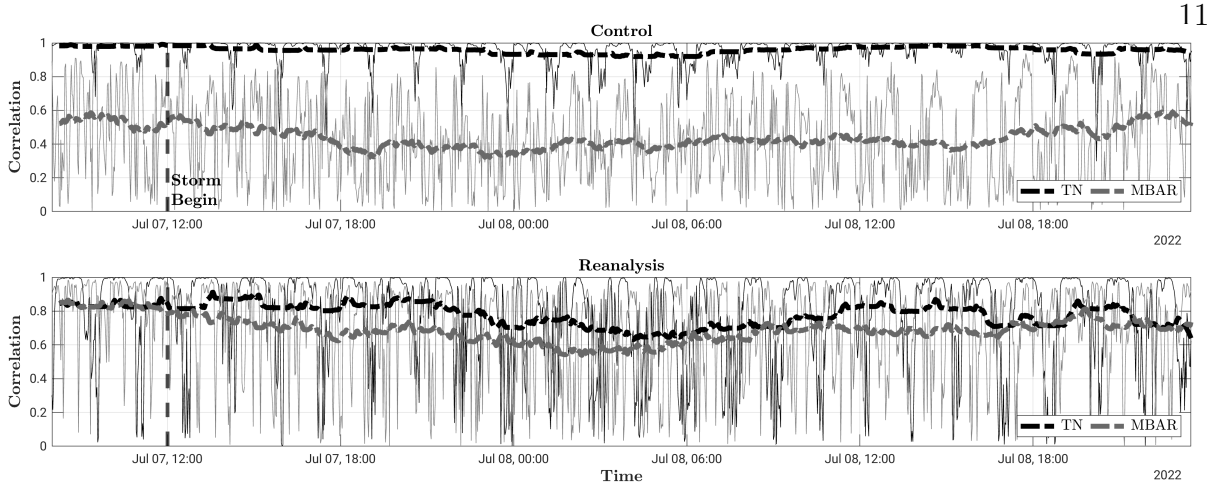

Figure 4.9: The TIEGCM ensemble correlations of Cntrl_* and $\text{Exp}_{*-Storm}$ between scale height to neutral temperature (TN) and mean molecular mass (MBAR) (absolute value). Shown along a constant pressure surface (1.1×10^{-7} Pa, $520 \sim 580$ km altitude) at GRACE-FO longitude and latitude locations. Thicker dashed lines are a rolling mean of ± 45 minutes.

relation variability with consistent orbit period cycle behavior. The reanalysis quiet period shows very high mean molecular mass correlations possibly explained by analysis updates disturbing the neutral wind field that in effect alter composition circulation. Additionally, the correlations for temperature and mean molecular mass are not strictly anti-correlated in their relationship, with periods where both state correlations peak and periods where state correlations have an inverse relationship.

These scale height-to-state correlations show a strong latitude dependence, with this relationship shown in Figure 4.10 for Cntrl_* and $\text{Exp}_{*-Storm}$. The control neutral temperature correlation is highly positive at all latitudes (as expected from Equation 1.5), and mean molecular mass correlations are generally negative and more evenly distributed. The reanalysis still shows high neutral temperature correlations in the northern hemisphere, but now shows low correlations in the southern hemisphere. This is likely explainable by the greater solar irradiance in the summer northern hemisphere affecting temperatures and effectively controlling scale height changes, whereas temperature updates disturb the winter southern hemisphere. For mean molecular mass, the reanalysis correlations strongly change with lati-

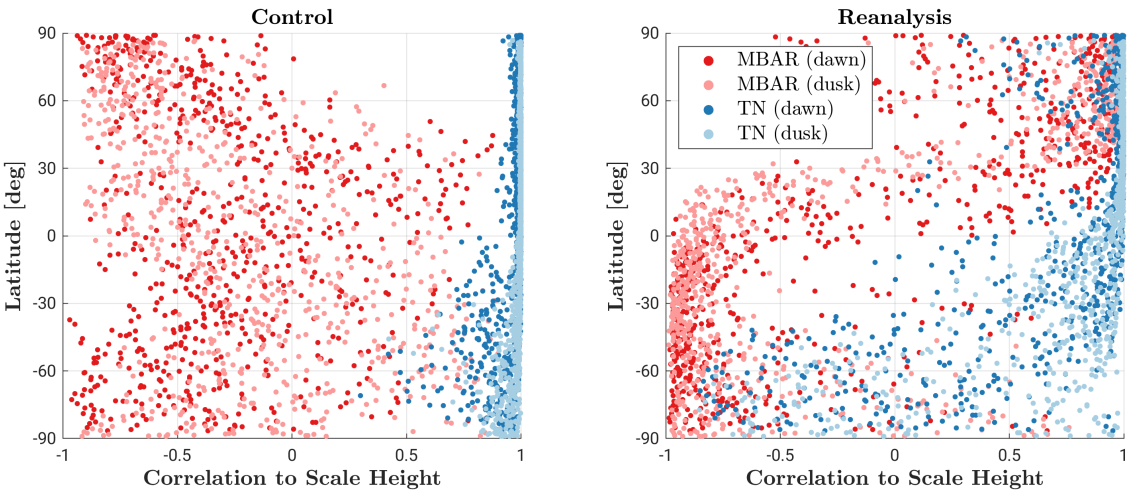

Figure 4.10: Correlation of the TIEGCM scale height states to neutral temperature (TN) and mean molecular mass (MBAR) as a function of latitude. Shown for point samples in Figure 4.9 for the TIEGCM control and reanalysis.

tude between northern positive correlations and southern negative correlations, with a visible transition near the equator. These large mean molecular mass correlations in the southern hemisphere can alternatively explain the drop in neutral temperature correlations, where composition adjustments due to circulation are more dominant, notably with changes to the O/He ratio in the cooler winter hemisphere (Thayer et al., 2012; Liu et al., 2014). An interesting finding is the positive correlations for mean molecular mass in the reanalysis northern hemisphere, possibly due to some transport mechanism reducing the mean molecular mass. There additionally is no apparent dawn and dusk LT dependence for correlations.

4.4.2 Comparison With TIMED-GUVI O/N_2

Reanalysis and control comparisons with TIMED-GUVI O/N_2 ratio are shown in Figure 4.11 using the vertically integrated atomic oxygen (O) and molecular nitrogen (N_2) densities (Meier, 2021). There is a qualitative agreement in O/N_2 between GUVI and the TIEGCM, where at the storm peak large O/N_2 values reach low latitudes due to storm-induced neutral wind transport and circulation. It is noted the periodic low O/N_2 values near $-30°$ latitude are artifacts due to SAA impacts. The bias improvement (Equation 4.2)

of the reanalysis over the control is shown in the bottom right of Figure 4.11, where we see mixed results in reanalysis performance. The best performance is arguably just past the storm peak when the reanalysis neutral densities also perform best. TIMED-GUVI O/N_2 structures in the southern hemisphere at peak storm time are more southern than in the TIEGCM, and the reanalysis slightly corrects this bias.

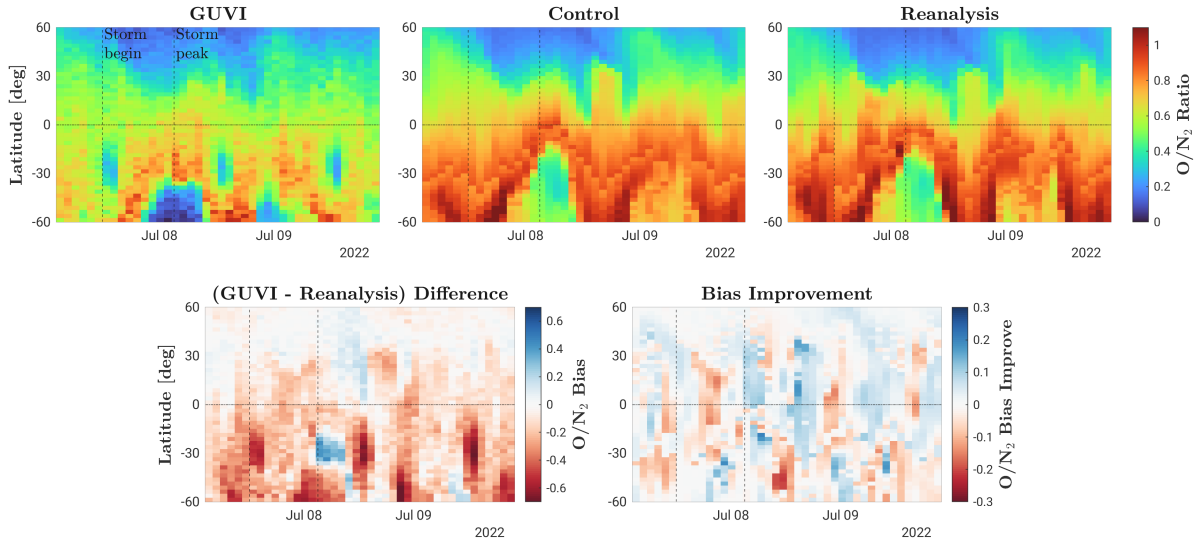

Figure 4.11: TIMED-GUVI O/N_2 ratio comparison with Cntrl_* and $\text{Exp}_{*-Storm}$. The top panel shows the observed and calculated O/N_2 ratios and the bottom panel shows the difference ($\text{GUVI} - \text{Exp}_{*-Storm}$) on the left, and the bias improvement of the reanalysis over the control, defined in Equation 4.2. Blue regions indicate improving and red regions are worsening biases.

4.4.3 Analysis of Storm Recovery Using TIMED-SABER NO Observations

To explain recovery response following the storm, NO cooling changes are assessed against TIMED-SABER observations. Splitting the SABER observations by the two dominant local time samples (dawn median of LT $\sim$ 7, dusk median of LT $\sim$ 22), the vertically integrated NO flux is shown in Figure 4.12. The reanalysis and control results for NO flux do not significantly differ other than from slightly lowering NO flux magnitudes presumably due to lower neutral temperatures. NO cooling enhancements begin at the high latitudes and migrate towards the equator as the storm period progresses, where SABER shows large

NO cooling fluxes to reach about $-20-30$ degrees latitude in both hemispheres. For the dawn-side NO flux observations, the TIEGCM generally agrees with SABER-NO during the storm main phase but underestimates the peak NO cooling and misses NO cooling flux peaks around UT11 on July 8th. On the dusk side, the TIEGCM again underestimates NO cooling 12 hours into the recovery phase in both hemispheres. The enhancements in the TIEGCM NO cooling correspond extremely well with regions where NO composition peaks, as shown in Appendix D Figure D.10. NO compositions persisting into the storm recovery are thus potentially lacking in the TIEGCM and could explain this underestimation of NO cooling; however, temperature biases cannot be ruled out either.

The relaxation timescales for neutral states to return to their quiet period states are quantified using the same approaches as in Maeda et al. (1992) and Lei et al. (2011), assuming the form:

$$\rho(t) = \rho_0 + (\rho_{peak} - \rho_0)\exp\Big(-t/\tau\Big) \tag{4.3}$$

where t is time, ρ_0 is the relaxation state value, ρ_{peak} is the peak state value, and τ is the relaxation timescale found through an optimized fit. ρ_{peak} is defined as the neutral density at UT3 on July 8th, the time when the B_z component of the solar wind turns northward, and ρ_0 is defined as the average density between UT6-UT12 on July 9th. Fitted τ values for the time-smoothed neutral density of Figure 4.5c are shown in Table 4.2. GRACE-FO shows a faster recovery than the TIEGCM, and the reanalysis improves the timescale by 1 hour, validating the improved reanalysis recovery at least for global scales.

Table 4.2: Fitted relaxation timescales τ using a peak time defined at UT3 on July 8th.

	GRACE-FO	Control	Reanalysis
Relaxation Timescale	10.9 hrs	12.9 hrs	11.9 hrs

Relaxation timescales are also fit for GRACE-FO, Cntrl_* and $\text{Exp}_{*-Storm}$ separating the relaxation timescales by local time and latitude, shown in Figure 4.13. Calculated τ

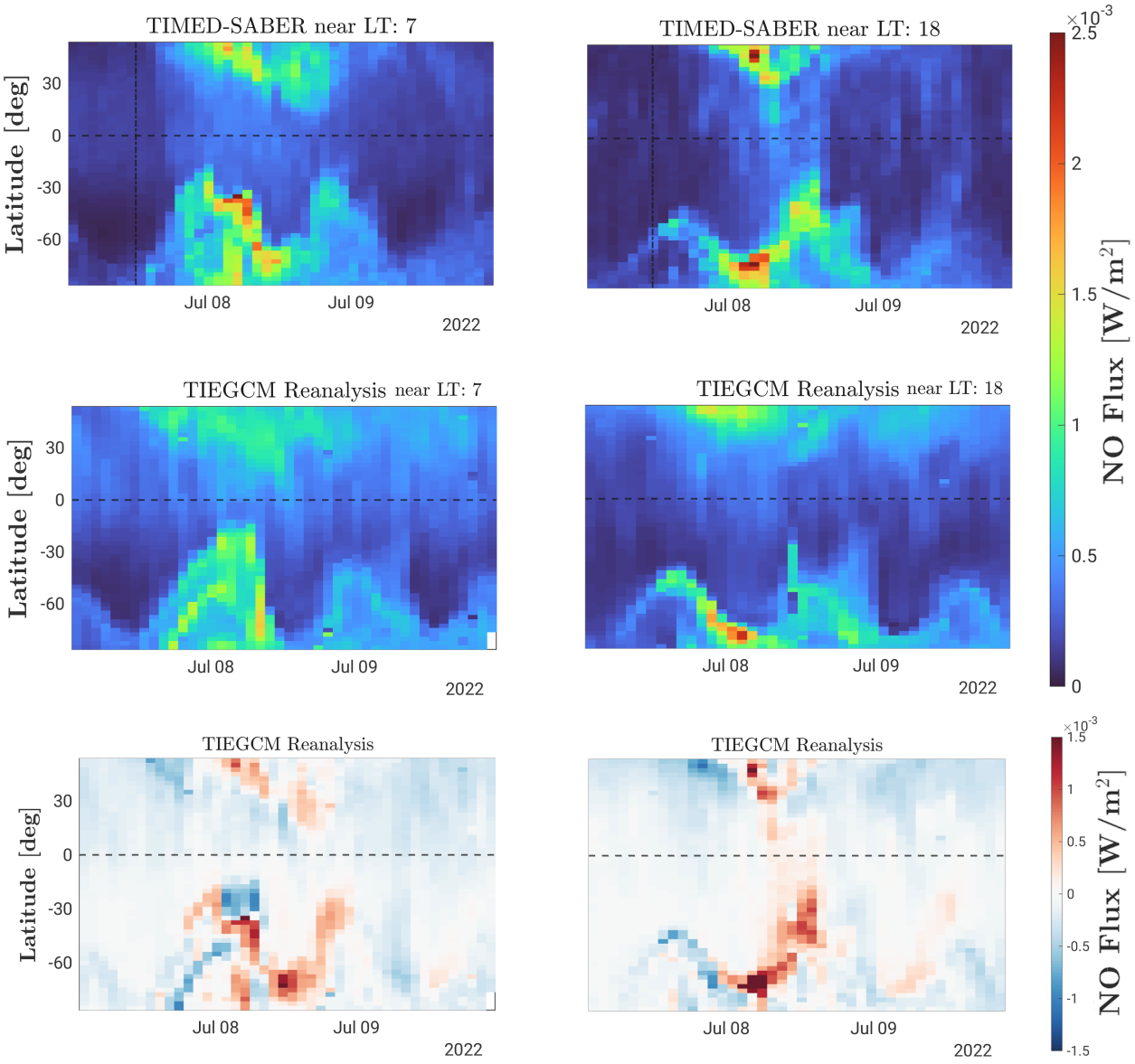

Figure 4.12: Vertically integrated TIMED-SABER NO cooling flux over the storm period, compared against $\text{Exp}_{*-Storm}$.

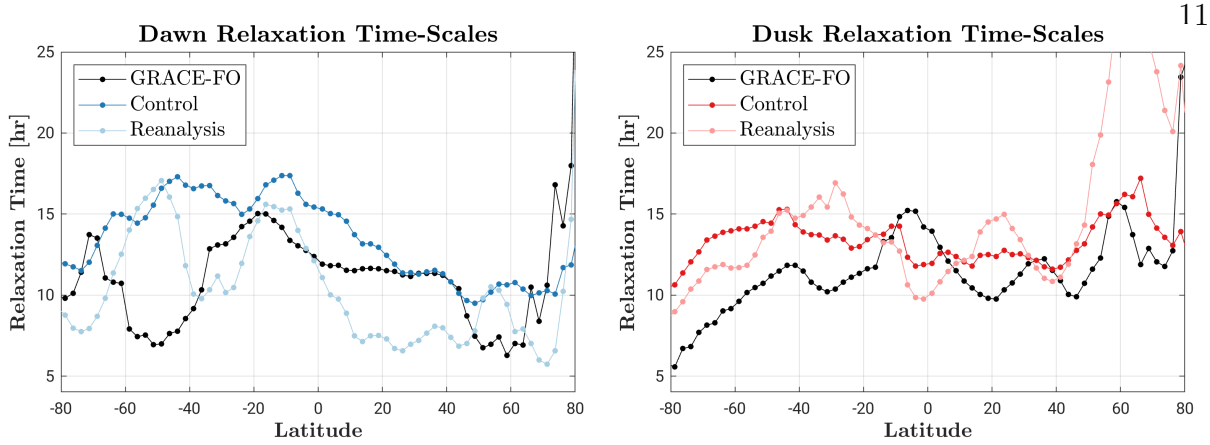

Figure 4.13: Fitted relaxation timescales for each latitude, separated by dawn and dusk sides at GRACE-FO locations. Peak time defined at UT3 on July 8th.

values show a strong dependence on latitude, with GRACE-FO generally showing faster timescales than the TIEGCM, but still with relatively good agreement with GRACE-FO. For the dawn side, the reanalysis generally lowers the relaxation time with overcorrections in the northern low latitudes. For the dusk side, reanalysis τ increases and decreases relaxation times compared with the control, with mixed results in improving agreement with GRACE-FO. The TIEGCM showing slower recovery is consistent with previous studies using the TIEGCM (Lei et al., 2011); however, this storm event does not show the quick recovery times seen by Lei et al. (2011) for two 2003 October storm events. Likely, the higher geomagnetic activity (Kp = 9) of these storm events in 2003 created considerably greater NO cooling rates compared with the fairly moderate Kp = 5 for this storm event, where increases in Joule heating have been found to correspond to greater NO cooling rates (Lu et al., 2010).

4.5 Discussion

The creation of this reanalysis strongly depends on the background covariance structures for prescribing plasma-to-neutral state correlations and for representing realistic state variability. Thus there are model limitations in creating this reanalysis, such as from relative neutral and plasma biases. These issues are most evident in neutral density enhancements

in the storm main phase, where neutral density structures were largely unchanged between the reanalysis and the control, and illustrated in a fast-Fourier transform (FFT) comparison shown in Appendix D Figure D.8. Here, frequency peaks in the TIEGCM differ from GRACE-FO observations above 0.3 Hz. While these enhancement biases are likely due to external forcing, whether more general biases come from internal parameters or external forcing is beyond this chapter's scope. Regardless, this chapter finds that adding state spread and variability through perturbing solar irradiance and magnetospheric forcing has the most positive impact, although solely relying on the F10.7 index likely introduces unrealistically large correlation structures. Introducing lower boundary variability through perturbations in tides only slightly impacted ensemble spread, but other studies perturbing lower boundary conditions though full atmosphere coupling (Hsu and Pedatella, 2023) have shown greater spread benefits. Adding further sources of state variability is still required, especially for low altitudes in the E- and D- regions where the spread is most limited. For high-altitude plasma states, benefits could be found by coupling plasmasphere models (Chou et al., 2023). Introducing internal process uncertainties through perturbing ν_{O^+-O} saw slightly positive effects, but not enough to impact reanalysis performance greatly. In any case, this chapter utilizes external forcing perturbations as a dominant means for ensemble initialization.

Another approach for ensemble initialization is to directly perturb neutral states, similar to approaches used for the lower atmosphere where perturbed states diverge due to chaotic dynamics. In Figures D.13 and D.14 in Appendix D, rank histograms and COSMIC-2 EDP rejection rates are shown for experiments directly perturbing neutral temperature and atomic oxygen compositions. Doing this shows the best rank histogram performances out of all the testing. However, one issue with perturbing these states is their limited forecast system memory, with improved spreads from neutral temperatures lasting around $2-4$ hours, and atomic oxygen sees spreads persisting for a day, as also shown in Chartier et al. (2013); Jee et al. (2007). The second issue is these perturbations are not physically justified and randomly disturb background correlation structures. This testing is still promising for

introducing model spread into the TIEGCM capabilities, but questions of how to induce state spread realistically and over sustained periods require future investigation.

Regardless of the TIEGCM's limitations, there are considerable benefits to using the TIEGCM for this reanalysis. Running the TIEGCM is comparatively faster and more stable than other upper atmospheric models with more comprehensive coupling. The ability to quickly run many experiments and ensemble initialization testing allows for much faster experiment tuning and a deeper understanding of the impact of each tuning node, providing a better idea of the model capabilities. Model stability enables longer runs without debugging model crashing, and is particularly important for countering non-physical state adjustments in the analysis update. Additionally, a more efficient model allows for longer experiments to assess performance through multiple periods. Information learned here is also transferable to other upper atmosphere models.

With large model state biases, there are limits to the reanalysis performance with poor rank histograms and a lack of sustained bias improvements. Insufficient state spread is most frequently countered using inflation, but for this reanalysis, adaptive inflation (El Gharamti, 2018) shows mixed results. The impact of no inflation is seen in Exp_* beginning at UT01 on July 5th, where following two days of DA cycling state spread has collapsed and the reanalysis performs similarly to the control, shown in Figure D.7. When adding adaptive inflation, there are slightly improved rank histograms (Figure D.11), but at the cost of negative impacts on neutral temperature estimation. These worsening neutral states are shown in Figure D.12 with worse reanalysis agreement with GRACE-FO observations. The artificially induced state spread from inflation likely has a negative effect of increasing neutral temperatures, whereas inflation uses EDP innovation statistics and the background covariance to inform neutral temperature spreads. Either providing a static background covariance could be beneficial, or an updated inflation framework is needed for the upper atmosphere to enable more effective inflation. This reanalysis works around the lack of inflation by beginning the storm reanalysis on UT00 on July 7th, balancing a sufficiently long 12-hour cycle spin-up

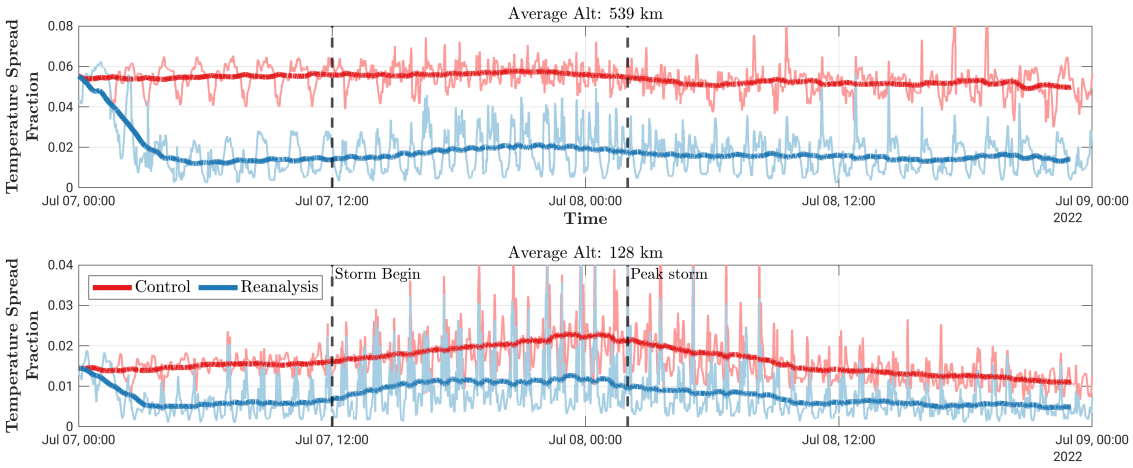

Figure 4.14: Normalized neutral temperature spreads, shown along two pressure levels (∼128 km and ∼539 km altitude) along the GRACE-FO orbit track. The orbit average mean is shown in darker lines. Shown for the control Cntrl$_*$ and reanalysis Exp$_{*-Storm}$.

period to settle analysis-induced neutral temperature perturbations, without too much cost of lost ensemble spread.

Despite the lack of inflation, the reanalysis performs best during the storm recovery phase, with a notable increase in DA impact following UT00 on July 8th in Figure 4.5c. This DA impact is most explainable by increased state spreads from magnetospheric forcing perturbations. It is noted the storm minimally affects electron density spread, and Figure D.3 shows normalized standard deviation spread to instead decrease during peak storm time. Conversely, neutral temperature spreads greatly increase during the storm period, showing an altitude relationship in Figure 4.14. For low altitude spreads, there is a greater percentage increase near where the Pedersen and Hall currents peak (∼ 128 km) than at high altitudes (∼ 539 km). This raises questions about the DA vertical impact, where there are competing impacts of the vertical reach of analysis updates versus thermal conduction vertically coupling the lower and upper altitudes. Questions about the vertical controllability of the upper atmosphere require future investigation and are further discussed in Section D.2 in Appendix D.

While not the focus of this reanalysis, the continuous improvements shown for forecast

electron density RMSEs are noteworthy, even through the quiet period where reanalysis neutral densities performance stagnates. This plasma error improvement is coming from neutral state estimation impact on model initial conditions, where without neutral updates, as shown in Chapter 2, plasma forecasts quickly revert to what neutral states dictate. Reanalysis neutral state impacts come through constraining neutral temperature, but dynamical coupling adjusting compositions, particularly atomic oxygen, is a likely source of the improved plasma forecasts Chartier et al. (2013); Hsu et al. (2014). This is supported by the changes in the reanalysis to the O/N_2 ratio and for improving plasma forecasting capabilities.

4.6 Conclusions

Leveraging an abundant source of plasma observations, this chapter establishes the value of plasma RO data to specify neutral densities during a storm event, particularly in improving the recovery response. This chapter produces a thermospheric reanalysis of a moderate storm event in July 2022, assimilating COSMIC-2 EDPs to constrain neutral temperatures that via cycling constrain other neutral states. The evaluation of the reanalysis points to the need for future investigation necessary for advancing the specification and forecasting capabilities of physics-based models, by addressing model representation of geomagnetic storm variability. Physics-based models have inherent advantages over empirical models in capturing non-linear storm-time changes, and these reanalysis results take another step in demonstrating a proof of concept for accurately quantifying variability seen in real observations and advancing understanding of fundamental physical processes and coupling during geomagnetic storms.

In this reanalysis, considerable effort is devoted to improving observation-model agreement through ensemble initialization and filter tuning to achieve an EDP rejection rate averaging 10% and is near zero for high altitudes. Filtering experiment tuning and testing entails introducing perturbations for external forcing and internal processes, as well as adjusting horizontal localization length scales and performing observation quality con-

trol. Reanalysis forecasts compared against COSMIC-2 EDPs improve total RMSEs up to 20%, with high altitudes showing an RMSE reduction of over 30% compared with the no-assimilation control, verifying reanalysis performance. Validating reanalysis neutral densities against GRACE-FO shows an RMSE improvement of 20%, with the best performance occurring on the dusk side which has greater influence by solar irradiance, and during the storm recovery. We see comparable recovery timescales between the TIEGCM and GRACE-FO neutral densities for this moderate storm event; however, the TIEGCM underestimates NO cooling fluxes within the recovery period. The reanalysis additionally shows temperature and composition to comparably influence scale height with a strong latitudinal dependence.

The development of this reanalysis raises many questions for future upper atmosphere data assimilation efforts as detailed in the discussion. Nevertheless, this reanalysis helps to establish the potential for using abundant plasma observations to constrain neutral states and serve as a global I-T monitoring system. With the current lack of a true global neutral state observing system, alternative approaches for global upper atmosphere specification should be developed and leveraged. Further DA efforts to synthesize together physics-based models and observations will aid in the future development of reanalysis capabilities and further understanding of the fundamental processes behind storm-time neutral density variability.

Chapter 5

Quantifying Storm-Time Neutral Density Uncertainties using a Physics-Based Particle Filter Framework

This chapter develops a forcing parameter particle filter framework to quantify non-Gaussian uncertainties present during geomagnetic storms due to non-linear dynamics. Estimating in a much-reduced forcing parameter space allows us to overcome filter degeneracy issues common to particle filter implementations and relax state distribution assumptions. The outcome of this chapter is a time-varying uncertainty quantification characterizing non-Gaussian uncertainties. We apply this particle filter framework to the same storm event assessed in Chapter 4, assimilating GRACE-FO neutral densities to estimate proxy forcing parameters of the F10.7 index and Ap index. These results reveal non-Gaussian distributions for forcing parameter estimates during the storm period, where increased stochastic parameter dynamics allow the particle filter to follow the storm density enhancement and somewhat lag behind the storm recovery. Additionally, during quiet periods, filter results show different bias fits introducing bimodal distributions for the separate dawn and dusk LT sides. These results of estimated non-Gaussian distributions will aid future efforts to quantify neutral density uncertainties and their impacts on orbit position errors.

5.1 Background and Motivation

Geomagnetic storm events introduce considerable neutral density variability on hours to days time scales, dramatically changing atmospheric states that increase atmospheric drag

uncertainties. These storm-time dynamics are especially non-linear and are likely to result in non-Gaussian neutral density uncertainties. However, operationally, conjunction assessment assumes Gaussian position errors that greatly ease computational costs over more intensive Monte Carlo calculations (NASA, 2020). Quantifying Gaussian neutral density uncertainties has previously been done using lower-dimensional models (Gondelach and Linares, 2021; Licata et al., 2022). However, these models lack the fully non-linear dynamics or use time-integrated observations (i.e., TLEs) that are unable to represent small-scale features present during storms. It is well established that orbital dynamics produce curvilinear uncertainties (Ghrist and Plakalovic, 2012), but it has not yet been investigated as to the impact that non-Gaussian neutral densities would have on orbit positioning.

With the particle filter, fully non-linear data assimilation is achievable. The particle filter enables a purely Bayesian update, requiring no assumptions for the prior, likelihood, or posterior distributions, in contrast to base Kalman filters that use Gaussian assumptions. The difficulty in implementing particle filters comes from the curse of dimensionality (Snyder et al., 2008). Still, adapting particle filters for geophysical systems has seen considerable advancements in recent years (e.g., van Leeuwen et al., 2019; Farchi and Bocquet, 2018).

The purpose of this chapter is to quantify non-Gaussian neutral density uncertainties for quiet and storm periods. This is accomplished by developing a new particle filter framework to estimate states in a much reduced forcing parameter space. Estimating in a much smaller parameter space will help to alleviate degeneracy issues by using the F10.7 index as a proxy for solar irradiance and the Ap index as a proxy for geomagnetic activity. This particle filter is applied to a geomagnetic storm event and accelerometer neutral density observations are assimilated to estimate these external forcing parameters.

This chapter is outlined as follows. Section 5.2 gives the details for the TIEGCM version and assimilated GRACE-FO observations are detailed in Section 5.2.2. The particle filter framework is detailed in Section 5.2.3 and the experiment setup is given in Section 5.2.4. Section 5.3 provides the results of the particle filter experiments, followed by a general

discussion in Section 5.4 and conclusions in Section 5.5.

5.2 Approach

5.2.1 Coupled I-T Model: TIEGCM

For the physics-based model to represent the I-T variability, we use the TIEGCM developed by NCAR HAO(Richmond et al., 1992; Qian et al., 2014). Since particle filters require a large number of ensemble simulations, for computational feasibility we use the TIEGCM v2.0 with a 5-degree resolution, with the vertical grid defined by 29 pressure levels with half-scale height resolution, spanning much of the relevant LEO altitudes from approximately $\sim$ 97 km to $\sim$ 600 km. Solar irradiance in the TIEGCM is specified by the F10.7 index and magnetospheric input is specified by the Heelis model, an empirical ion convention model controlled by the Kp index. In the observation likelihood calculation, neutral densities ρ are interpolated from model pressure levels to observation altitudes using the ideal gas law (Equation 1.2).

5.2.2 Neutral Density Observations

Neutral density observations used in this study are from the Gravity Recovery and Climate Experiment Follow-On (GRACE-FO), where neutral density observations are retrieved using the onboard accelerometer (March et al., 2021). GRACE-FO currently orbits nominally near 500 km altitude, with a 95 minute period, near-polar orbit, and a 10-second retrieval frequency. We assign observation errors as 15% of the neutral density magnitude, a reasonable assumption for GRACE-FO neutral densities (March et al. (2021), personal communications, 2023).

The correlations between GRACE-FO neutral density observations and the observed F10.7 and Ap indices are shown in Figure 5.1 for July 2022. As GRACE-FO has full latitude sampling at consistent solar mean local time (LT), correlations are binned for latitude and

local time. The two LT samplings are nearly all around LT 6 and LT 18, corresponding to the dawn and dusk regions, respectively. For F10.7 correlations, we see consistent correlations with LT 18, with latitudes just past the dusk terminator, and are still very influenced by solar irradiance. For LT 6 near dawn, we see a strong latitude dependence in correlation. This is explainable by seasonal asymmetry, where during this period the northern hemisphere is in summer and thus is much more sunlit than the winter southern hemisphere. Locations in the southern hemisphere have passed much longer through the night side, reducing the influence of solar irradiance. It is noted there are available LT bin samples near LT 0 and LT 12, but are only over the poles and thus not included.

Correlations with Ap show the inverse latitudinal relationship as from F10.7 correlations. Both dawn and dusk sides show greater correlations over the winter southern hemisphere than the summer northern hemisphere. This is possibly explainable by the stronger influence of solar irradiance over the northern hemisphere compared with geomagnetic input having greater influence in less sun-lit regions. Additionally as expected, dusk shows lower correlations than dawn due to the greater solar irradiance influence over the dusk side.

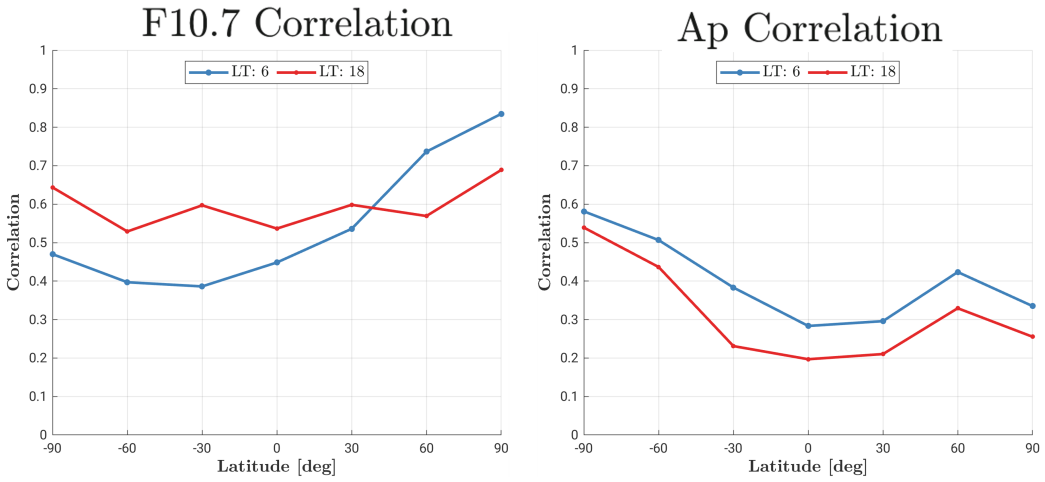

Figure 5.1: Correlations between the GRACE-FO neutral density observations and the observed F10.7 and Ap indices for July 2022. Fitted using the daily average of observations for F10.7 and the 3-hour average for Ap. Correlations are binned by latitude and solar local time (LT) for dawn (6 LT) and dusk (18 LT).

5.2.3 Particle Filter Framework

The particle filter enables complete Bayesian inference with no assumptions on distributions, allowing for non-Gaussian state estimation with the limitation of more frequent filter degeneracy issues. In Bayesian estimation, we seek to obtain the best estimate of our state $\mathbf{x}$, given a prior state $p(\mathbf{x})$ and observation information $\mathbf{y}$. The standard or bootstrap particle filter uses $i = 1, \ldots, N$ particles to approximate the probability density function of the posterior state estimate defined as

$$p(\mathbf{x}|\mathbf{y}) \approx \sum_{i=1}^{N} w^i \delta(\mathbf{x} - \mathbf{x}^i) \tag{5.1}$$

where $\delta()$ is the Dirac-delta distribution and where the particle weights are given by:

$$w^i = \frac{p(\mathbf{y}|\mathbf{x}^i)}{\sum_{j=1}^{N} p(\mathbf{y}|\mathbf{x}^j)}. \tag{5.2}$$

Here, $p(\mathbf{y}|\mathbf{x})$ is the likelihood, and weights here are normalized so that they sum to one. The particles' relative weights thus represent the distribution. Like most Monte Carlo methods, the larger N is, the better the approximation in Equation 5.1 becomes. The posterior at time t_k is calculated using observations, $\mathbf{y_k}$, the prior weights, $\boldsymbol{w}_{k-1}$, and the transition probability, $p(\mathbf{x}_k|\mathbf{x}_{k-1})$, from the previous time, t_{k-1}, as

$$p(\mathbf{x}_k|\mathbf{y}_k) \approx \sum_{i=1}^{N} w_{k-1}^i \frac{p(\mathbf{y}_k|\mathbf{x}_k)p(\mathbf{x}_k|\mathbf{x}_{k-1})}{p(\mathbf{y}_k)} \tag{5.3}$$

where $p(\mathbf{y}_k)$ is the observation marginal probability. The data assimilation framework cycles between prior and posterior estimates, where new weights are assigned to particles by multiplying the particle's prior weight by the new likelihood. This multiplication will quickly cause weights to collapse, so resampling is performed and weights are re-normalized to $1/N$.

For the forcing parameter particle filter, the estimated state vector is composed of two proxy parameters for the F10.7 index describing solar irradiance, and the Ap index describing

geomagnetic forcing:

$$\mathbf{d} = \begin{bmatrix} \mathbf{d}_{F10.7^*} \\ \mathbf{d}_{Ap^*} \end{bmatrix} \tag{5.4}$$

While these indices have real observed values, this filter considers them tuning parameters. These parameters will take values to match observations, performing as proxies for the external energy input into the upper atmosphere. For this filter implementation, the TIEGCM is being used as a *time-dependent* forward model as $\mathbf{d}$ do not have dynamics themselves. Due to this, atmospheric states, $\boldsymbol{f}$, are needed as initial conditions for the model, and as such are carried in the filter cycle along with an associated particle $\mathbf{d}^i$.

The framework for the forcing parameter estimation particle filter is outlined in Figure 5.2, illustrated in Figure 5.3, and a step-by-step outline is as follows.

To initialize in Step 0, the prior distribution of parameters is set based on the yearly F10.7 and Ap index data and further discussed in the Experiment Setup. These sampled particles are then used to initialize $i = 1, \ldots, N$ particles to time t_0 through a $\sim$ 10-day spin-up period, yielding the prior particle parameter, $\mathbf{d}_0^i$, and the initial TIEGCM states, $\boldsymbol{f}_0^i$. The initial particle distribution is shown at t_0 of Figure 5.3.

For the Step 1 time update, particles from the previous time step, $t_{k-1} = t_0$, are propagated to the next observation time at time t_k. This step is especially distinct from the standard particle filter as there are no parameter dynamics. However, as the observed parameters evolve with time, this time motion is modeled with added random noise:

$$\mathbf{d}_k^i = \mathbf{d}_{k-1}^i + \boldsymbol{\varepsilon}_k^i \tag{5.5}$$

where $\boldsymbol{\varepsilon}_k^i$ represents the parameter model error and is assumed to be sampled from a zero-mean, independent and identically distributed Gaussian, $\boldsymbol{\varepsilon}_k^i \sim \mathcal{N}(0, \mathbf{Q})$, where $\mathbf{Q}$ is the model error covariance. It is noted that the parameter "model" here is the time-evolution uncertainty of the forcing parameters. Additionally, this stochastic forcing can be accounted

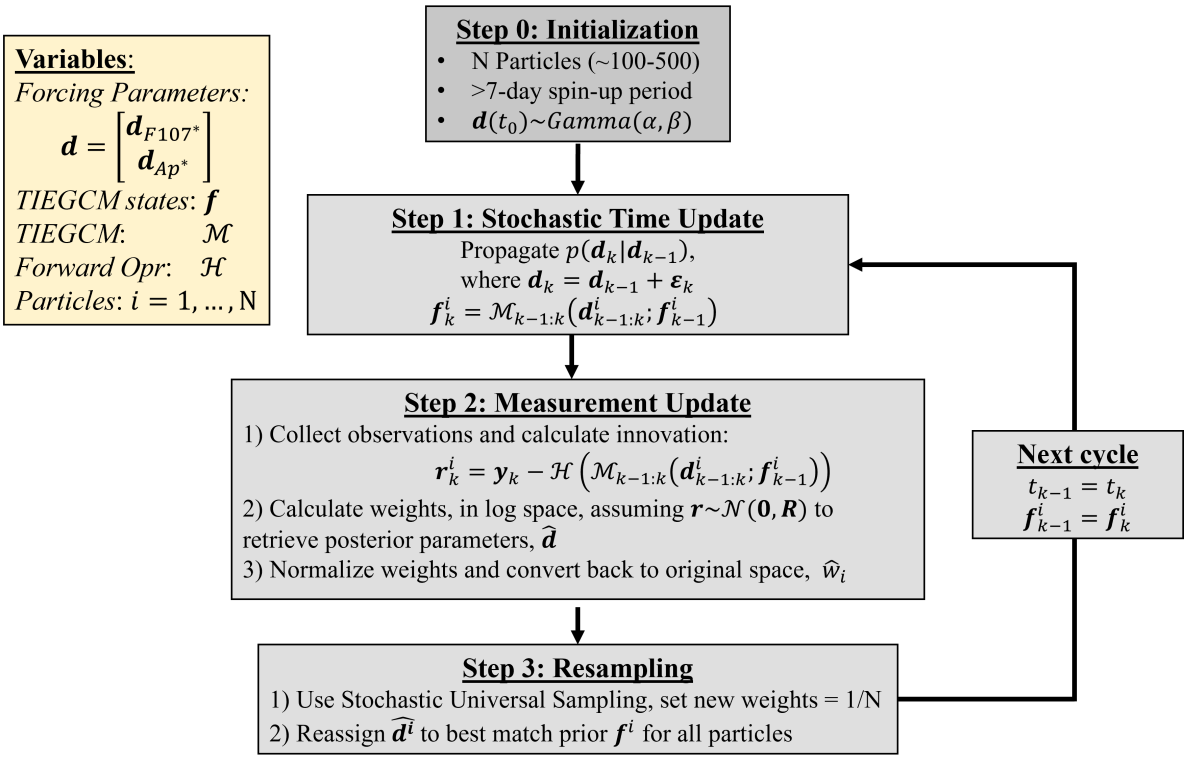

Figure 5.2: Forcing parameter particle filter framework

for in the prior weights (Van Leeuwen, 2009) as

$$\boldsymbol{w}_i^* = p\Big(\mathbf{d}_k; \boldsymbol{f}_k | \mathbf{d}_{k-1}; \boldsymbol{f}_{k-1}\Big) p\Big(\mathbf{d}_{k-1}\Big) \tag{5.6}$$

where the likelihood of the transition density is a single value calculated from the Gaussian parameter model error distribution. This step likewise increases particle spread to mitigate filter divergence. The time propagation of these parameters is illustrated in the time update of Figure 5.3. Each particles' associated states $\boldsymbol{f}_{k-1}^i$ are propagated with the TIEGCM, $\mathcal{M}_{k-1,k}$, from t_{k-1} to t_k using time-varying parameters $\mathbf{d}_{k-1:k}^i$:

$$\boldsymbol{f}_k^i = \mathcal{M}_{k-1,k}\Big(\mathbf{d}_{k-1:k}^i; \boldsymbol{f}_{k-1}^i\Big) \quad \forall i = 1, \ldots, N \tag{5.7}$$

where the time-series $\mathbf{d}_{k-1:k}$ influence the atmospheric states through the TIEGCM's full non-linear dynamics.

Next in Step 2, a measurement update that resembles the traditional particle filter is made where $\boldsymbol{f}_k^i$ is used in the likelihood calculation of the weights. These weights are calculated using Equation 5.2, and there is freedom in choosing any distribution to represent the likelihood. For simplicity, we choose the likelihood to be Gaussian with observation variances contained in $\boldsymbol{R}$. The innovation vector of each particle, $\boldsymbol{r}^i$, is then calculated using observations at time t_k:

$$\boldsymbol{r}_k^{(i)} = \mathbf{y}_k - \mathcal{H}\Bigg(\mathcal{M}_{k-1,k}\Big(\mathbf{d}_{k-1:k}^{(i)}; \boldsymbol{f}_{k-1}^{(i)}\Big)\Bigg) \tag{5.8}$$

Here, $\mathcal{H}$ is an operator that resembles the traditional forward operator. It takes in neutral states output from the TIEGCM and produces states at the observation location using Equations 1.2 and 1.5. The resulting likelihood weight, $\tilde{w}^i = p(\mathbf{d}_{k-1:k}|\mathbf{y}_k)$, is then multiplied by the prior weight, $w^i = \tilde{w}^i \times w^{i*}$, to get the relative weights. Weights are then normalized to sum to one, producing the full posterior distribution of weights w^i associated with parameters $\hat{\mathbf{d}}$. These posterior weights are illustrated in the measurement update step of Figure 5.3. It is noted that the likelihood and non-normalized weights are calculated in log space to avoid

numerical precision errors. Additionally, this measurement update at time t_k includes states and observations matched at intermediate times between t_{k-1} and t_k. These intermediate times are illustrated as time steps in Figure 5.3, and are easily controlled by adjusting the frequency of model history output. Using intermediate times includes more observations into the likelihood and provides better posterior estimates.

For Step 3, particle resampling is done to mitigate filter degeneracy. This is performed using stochastic universal sampling (Kitagawa, 1996), which resamples using posterior weights and then sets prior weights to $w^i = 1/N$. The resampled parameter distribution is also reassigned in this step. This reassignment minimizes the effects of initial conditions by realigning the particles with atmospheric states, where the newly generated $\hat{\mathbf{d}}^i$ are optimally matched to the prior atmospheric states, $\boldsymbol{f}_k^{(i)}$, based on the prior particles, $\mathbf{d}^i$.

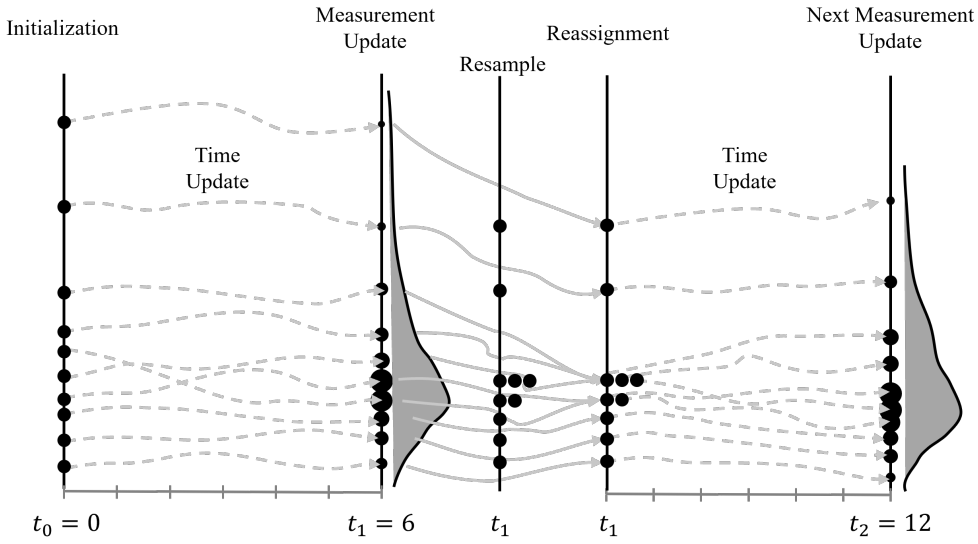

Figure 5.3: The cycle of the forcing parameter particle filter. Not pictured are the corresponding TIEGCM states, that are propagated in the time update from their associated parameters. The TIEGCM states are additionally sorted in the reassignment step. (Inspired by Van Leeuwen (2009)).

To complete the filter cycle, the reassigned particle distribution is set as the previous distribution at t_{k-1} and the filter continues to the next cycle.

As a note, a considerable assumption has to be made to properly utilize the posterior

particle distribution. This is that the parameter distribution is independent of its initial conditions,

$$p\Big(\mathbf{d}_k; \boldsymbol{f}_k|\mathbf{y}_k\Big) \approx p\Big(\mathbf{d}_k|\mathbf{y}_k)\Big) \tag{5.9}$$

This assumption as it stands relies on the fact that the upper atmosphere is strongly dependent on external forcing, where the model will "forget" its initial conditions. Having a longer time update makes this a stronger assumption, as well as introduces more non-linearity into the model states.

While estimating in the forcing parameter space increasing filter feasibility, there is a large amount of uncertainty associated with calculating likelihoods for forcing parameters in neutral density state space. Representing this uncertainty mapping is particularly challenging as we use a fully coupled physics-based model in the TIEGCM to map between parameter and state space. It is extremely likely that only using the GRACE-FO observation error magnitude, σ^2_{obs}, in the likelihood would greatly overestimate the likelihood certainty due to not considering the representativeness error of estimating forcing parameters in state space. Thus we look to capture these unknown errors by inflating the observation error with $\sigma^2_R = \sigma^2_{rep} \times \sigma^2_{obs}$ to account for representativeness errors, σ^2_{rep}, where σ^2_R is the variance in $\boldsymbol{R}$. This variance scaling is tuned to improve filter performance and has been found to counter particle filter degeneracy in other geophysical applications (Cluzet et al., 2021, 2022).

5.2.4 Experiment Setup

To demonstrate this particle filter framework, we test for an isolated storm event in July 2022, over a period from UT00 on July 5th to UT00 on July 10th. The storm event begins at UT 12 on July 7th with a peak Kp value of 5, with peak geomagnetic activity occurring at UT02 on July 8th. The observed F10.7 and Kp indices for this event are shown in Figure 5.4.

Initializing particles is accomplished using samples based on the observed F10.7 and Ap

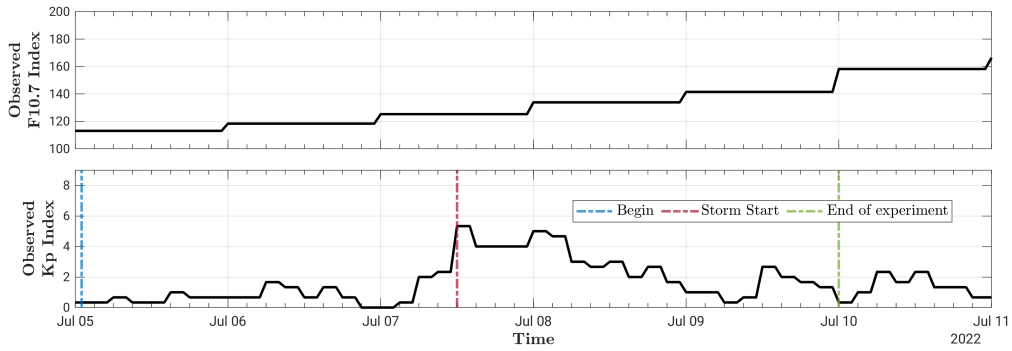

Figure 5.4: Observed F10.7 and Kp indices over the week in July 2022.

indices for the full year of 2022. These indices most commonly have lower values greater than 0 and are positively skewed, so a Gamma distribution was chosen to fit the data and sample particles, Gamma(α, β), where α is the shape parameter and β is the rate parameter. We thus sample from $\mathbf{d}_{F107^*} \sim \text{Gamma}(1.7, 6.6)$ that is positively shifted to by 80, and sample from $\mathbf{d}_{Ap^*} \sim \text{Gamma}(3, 15)$. Starting the TIEGCM states are initialized through a 10-day spin-up period with these constant forcing parameters.

We split this experiment into two periods: the quiet period between UT00 on July 5th to UT12 on July 7th and the storm period from UT12 on July 7th to UT12 on July 9th. For the quiet period, we use 6-hour long cycling periods where forcing estimation should be primarily determined by the F10.7 index. A representativeness error scaling of $\sigma_{rep} = 32$ is used for the quiet period. For the storm period, we test both 3-hour and 1-hour cycling frequencies to better capture the rapid changes in geomagnetic forcing. We use $\sigma_{rep} = 32$ for the 3-hour cycling and $\sigma_{rep} = 22$ for the 1-hour cycling. The parameter model covariance, $\mathbf{Q}$, is calculated using the standard deviations of the real observed parameters within some window of the cycle start time, enabling a time-dependent, dynamic stochastic forcing. This stochastic forcing assumes we know the observed indices; however, for operational applications, machine learning approaches (Camporeale, 2019) could be leveraged to predict the parameter variability. It is also noted that $\mathbf{Q}_{Ap}$ is multiplied by 2 for the 1-hour cycling to further increase stochastic forcing. Assimilated GRACE-FO observations are assumed to be

independent for all experiments. Particle and model initialization information is listed in Appendix B.

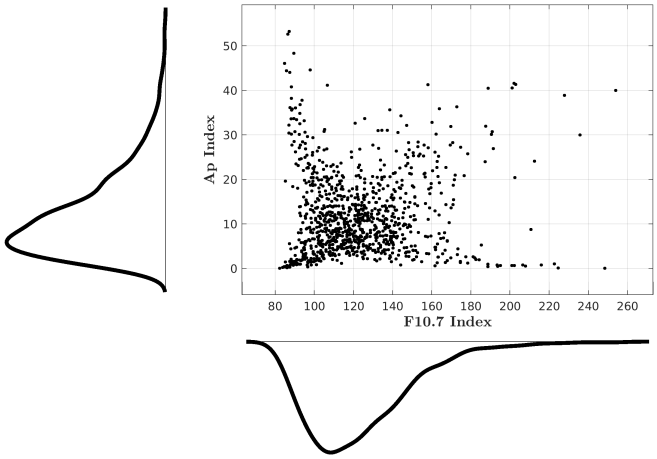

Figure 5.5: Starting forcing parameter distribution used to initialize the particle filter. Particles are sampled from a Gamma distribution fitted for the 2022 indices, sampled using a Coupla draw with a correlation of 0.03.

5.3 Results

With our initialized set of particles, we run the particle filter over the 2-day quiet period with 6-hour cycling and assess the performance of the filter in estimating neutral densities. The resulting estimates and particle distribution are shown in Figure 5.6, containing the GRACE-FO observations in black, particle distribution in shades of blue, and the weighted mean estimate in red. Darker shades of blue for the particle distribution indicate greater relative weight while whiter colors indicate lesser weight. At the beginning of the experiment period, we see considerable particle spread from our initialized states that converge to the assimilated GRACE-FO observations following a day of running the filter. The weighted mean shows good agreement with observations, and we note the greater weights for particles close to observations and smaller weights for far away particles. In the increased zoom of the second half bottom panel, we see in detail between UT18 on July 6th and UT00 on July 7th a visible bimodal weight distribution. Here, the filter appears to fit separate weights for the two LTs sampled by GRACE-FO. While the weighted mean generally estimates GRACE-FO well, we see the worst agreement for the larger neutral density magnitudes on the dusk side.

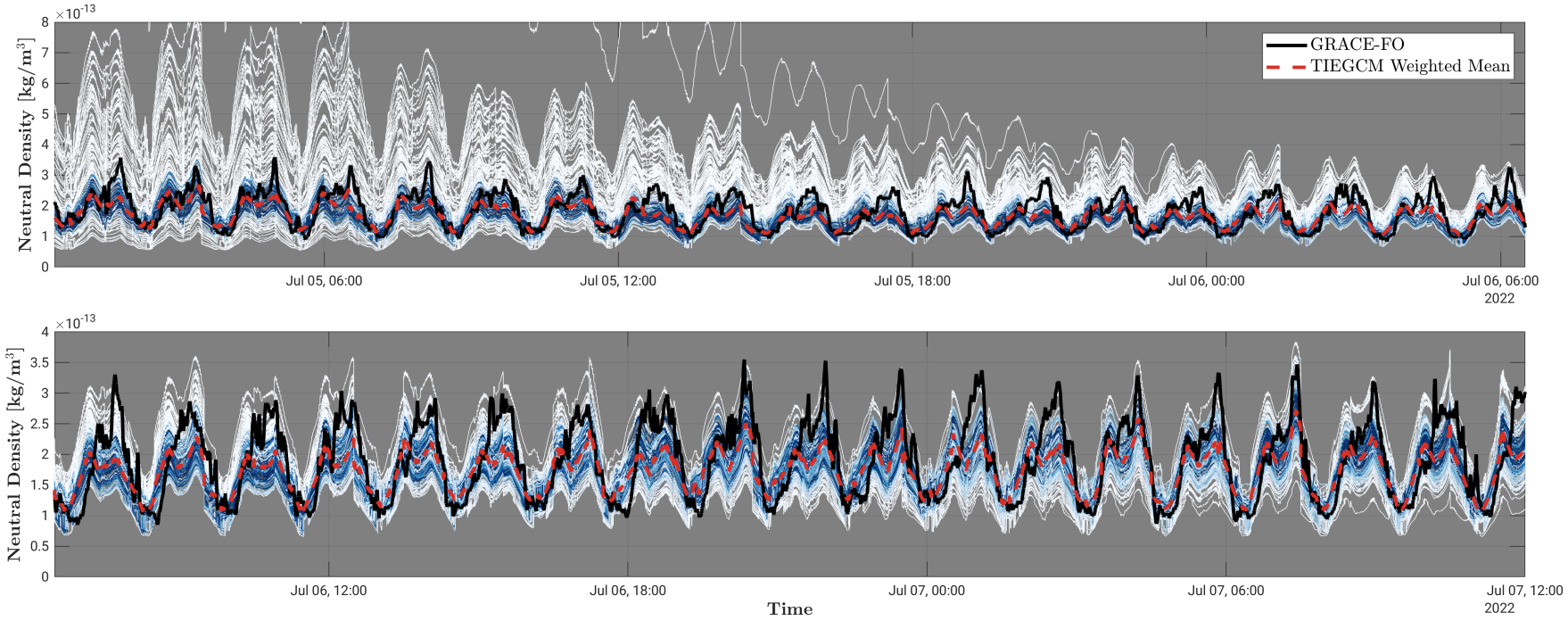

Figure 5.6: Quiet period particle filter estimation of neutral density at GRACE-FO locations. Shows GRACE-FO observations (black), the weighted mean estimates (red), and individual particles with respective weights (shades of blue). Darker shades of blue indicate greater particle weight. The top panel shows the quiet period first half and the bottom panel shows the second half, with a noted difference in the y-axis scales.

As we are performing the estimation in parameter space, a time series of the estimated forcing parameters is shown in Figure 5.7, with the size of particles indicating their relative weight as well as their weighted mean. We see consistent weights for $\mathbf{d}_{F107^*}$ over the quiet period that generally looks well distributed. For $\mathbf{d}_{Ap^*}$ weights, we see the initial spread to be large and decrease over time due to little geomagnetic activity.

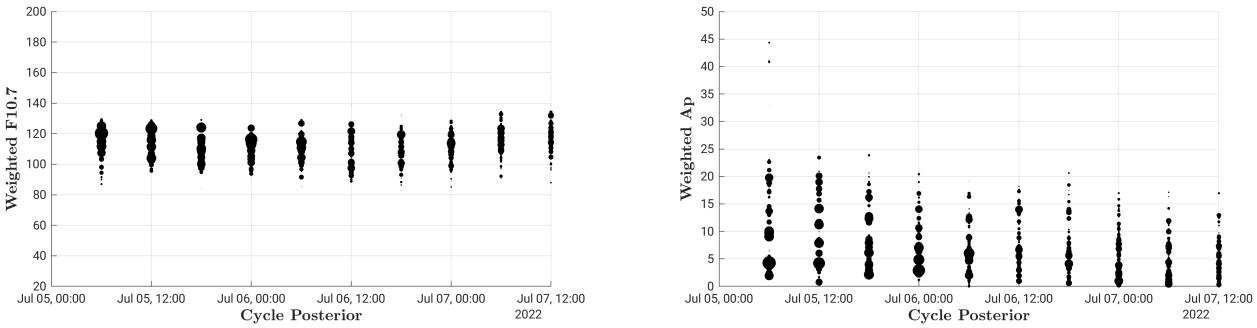

Figure 5.7: Weights of particles with corresponding F10.7 and Ap weights for the quiet period running. The size of particles indicates their relative weight, and the magenta dot is the weighted mean. Shown for posterior estimates at the end of the 6-hour cycle.

Lastly, for the quiet period, we assess the neutral density spread through a rank histogram shown in Figure 5.8. In a rank histogram, we assign a rank to each observation based on where it falls within our particle distribution. In the quiet period rank histogram, we see a relatively uniform set of ranks, signifying quite good particle spread. We additionally see a bias asymmetry when separating by the dawn and dusk sides. The particle filter estimates global weights to match biases on both LT sides, with the dawn side skewed to the right, indicating particles are over-biased, while the dusk side skews to the left.

Following running the particle filter through the quiet period, we run the storm period estimation at two cycling frequencies. The neutral density estimates for the 3-hour cycling are first shown in Figure 5.9. During this storm period, the geomagnetic activity rapidly intensifies at UT12 as indicated by a spike in Ap index, causing dramatic changes in the neutral density variability. As the neutral density enhances from UT12 on July 7th to UT4 on July 8th, the particle filter lags in response and underestimates neutral density obser-

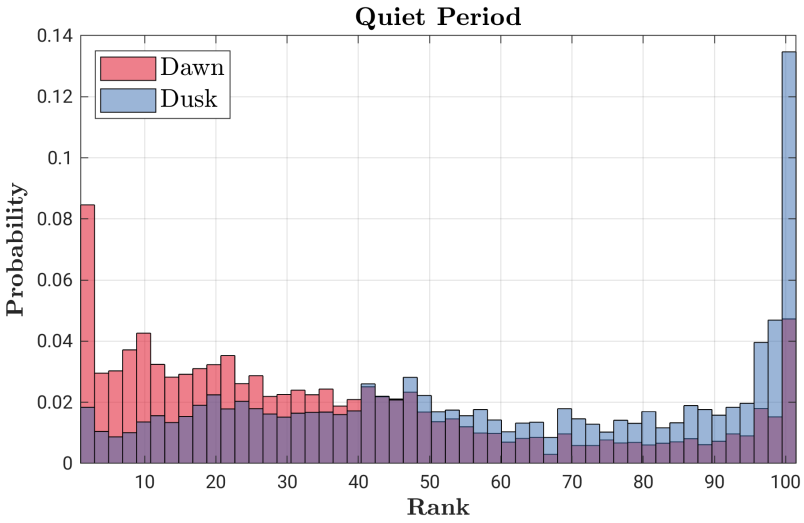

Figure 5.8: Rank histogram for the quiet period showing particle spread relative to observations, separated by the dawn-dusk sides.

vations Following this peak, the thermosphere begins cooling and there is good agreement between the particle filter and GRACE-FO observations near UT10 on July 8th. However, the recovery time scales shown in GRACE-FO observations are faster than in the TIEGCM, and all the particle weight is assigned to the lowest magnitude particles. It is noted there is a single particle sample with a lower neutral magnitude and it considerably gains weight near UT16 on July 8th. This particle sample highlights the benefits of having greater particle spread and particle sample size. By the end of the storm period at UT10 on July 9th, we see the particle filter estimate matching well with GRACE-FO observations.

The neutral density estimate results for the 1-hour cycling experiment are shown in Figure 5.10. In the storm enhancement phase, particles have more spread and the weighted mean better matches neutral density observations. Nevertheless, the post-storm recovery rate is faster than the TIEGCM's representation, and all the particle weights are again placed in the particles with the lowest magnitude. Still, we see particle spreads for 1-hr cycling much more quickly match neutral density observations at about UT0 on July 9th, shown in the diversity of particle blue colors, where 3-hour cycling had yet to produce this spread diversity even 12 hours later. The better observation agreement from increasing the cycling frequency to 1 hour and increasing the stochastic noise greatly improves the particle filter's ability to evolve quickly and highlights the importance of increased noise and spread

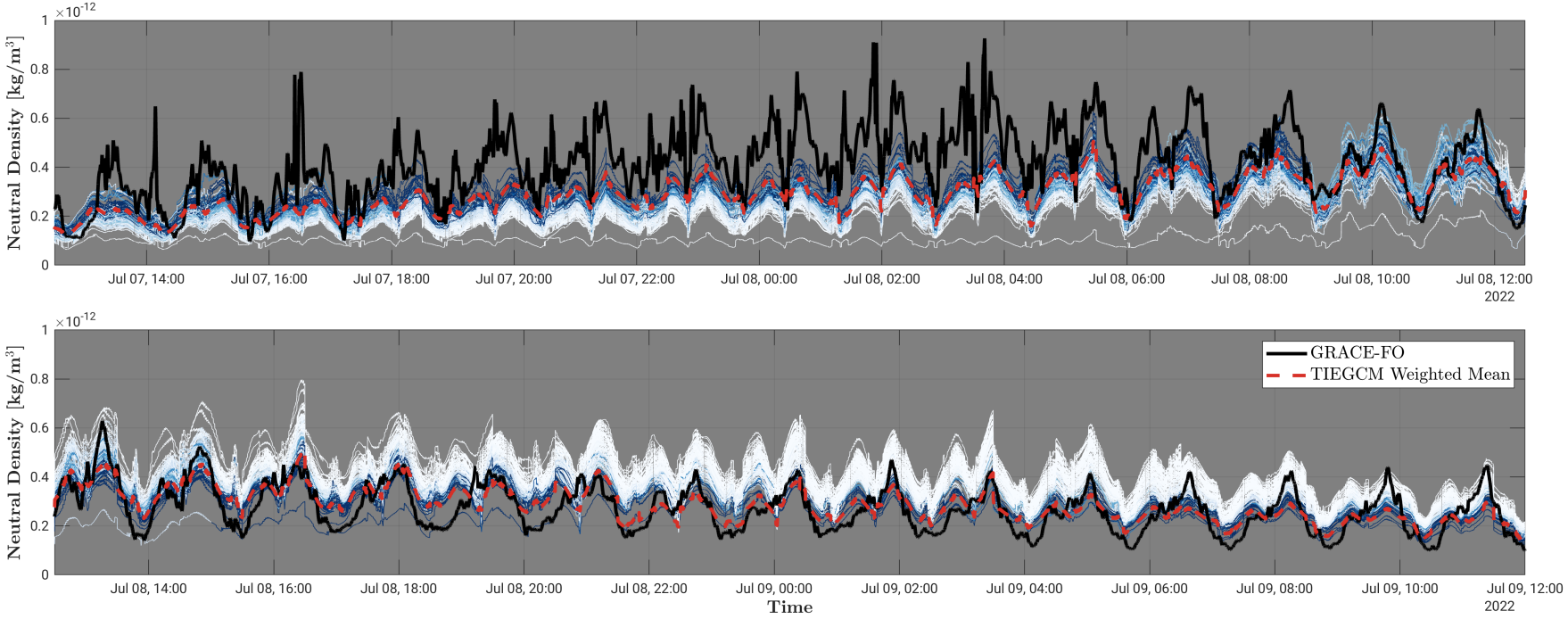

Figure 5.9: Same as Figure 5.6 for the storm period at 3-hour cycling. The top panel shows the storm period first half and the bottom panel shows the second half. Darker blue shades indicate greater relative particle weight.

in the system.

The storm time series of the weights for the forcing parameters are shown in Figures 5.11 and 5.12. For 3-hour cycling in Figure 5.11, we see during the storm enhancement phase a rise in both $\mathbf{d}_{F107^*}$ and $\mathbf{d}_{Ap^*}$, and consequently decrease during the recovery phase. Here we see neutral density changes compensated within both $\mathbf{d}_{F107^*}$ weighting. In reality, the weighting of $\mathbf{d}_{Ap^*}$ should primarily account for enhancements, and the recovery is more of an internally driven process, where the actual observed F10.7 index shows an increase over this period as seen from Figure 5.4. The time-series of $\mathbf{d}_{Ap^*}$ show a slight rise that is considerably less than the observed Ap increase, and shows a fall during the recovery phase followed by a collapse in the spread at UT00 on July 9th when the observed Kp index drops below 2. We observe non-Gaussian forcing parameter distributions in the enhancement phase, and very non-Gaussian distributions in the recovery phase.

In Figure 5.12, we see the impact of the increased cycling frequency and stochastic forcing. There is a similar increase in $\mathbf{d}_{F107^*}$ as with 3-hour cycling, and a considerably greater increase in $\mathbf{d}_{Ap^*}$ than with 3-hour cycling. We see skewed distributions for $\mathbf{d}_{F107^*}$ and $\mathbf{d}_{Ap^*}$ in this enhancement phase. During the recovery phase, parameter distributions become considerably non-Gaussian around UT12 on July 8th, with strong multi-modal distributions taking shape for both $\mathbf{d}_{F107^*}$ and $\mathbf{d}_{Ap^*}$ that we can capture through a particle filter framework. These non-Gaussian distributions are highlighted in time-slice (c) in Figure 5.12. The recovery phase shows parameter estimates fall as with the 3-hour cycling case, with $\mathbf{d}_{F107^*}$ falling below their initial quiet period values and $\mathbf{d}_{Ap^*}$ collapsing with the lack of geomagnetic activity.

An additional means for describing the 1-hour cycling improvement we see over the 3-hour cycling case is illustrated in a rank histogram comparison in Figure 5.13. Here the 1-hour cycling produces an improved model spread over the 3-hour cycling case with a more uniform distribution. Still, these storm period rank histograms show noticeably less uniform spread than the quiet period, and further experimentation is needed to improve

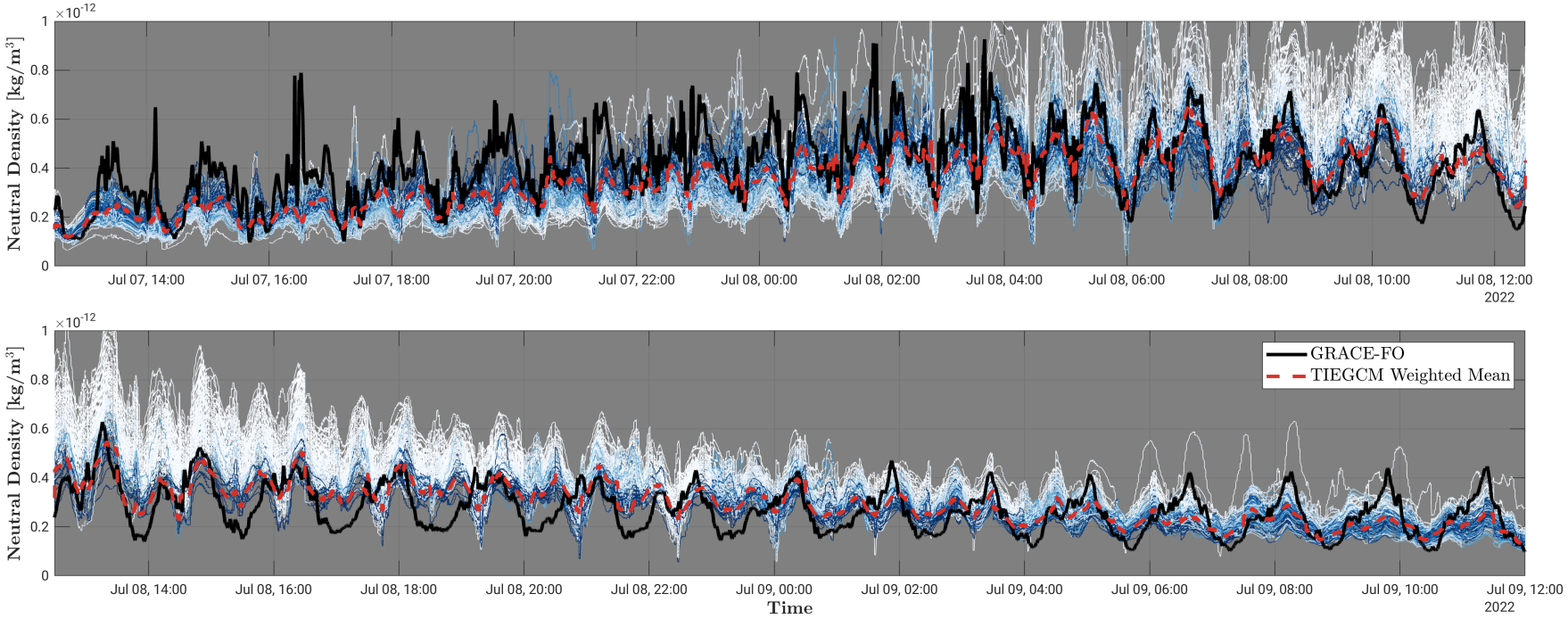

Figure 5.10: Same as Figure 5.6 for the storm period at 1-hour cycling and increased stochastic forcing. The top panel shows the storm period first half and the bottom panel shows the second half. Darker blue shades indicate greater relative particle weight.

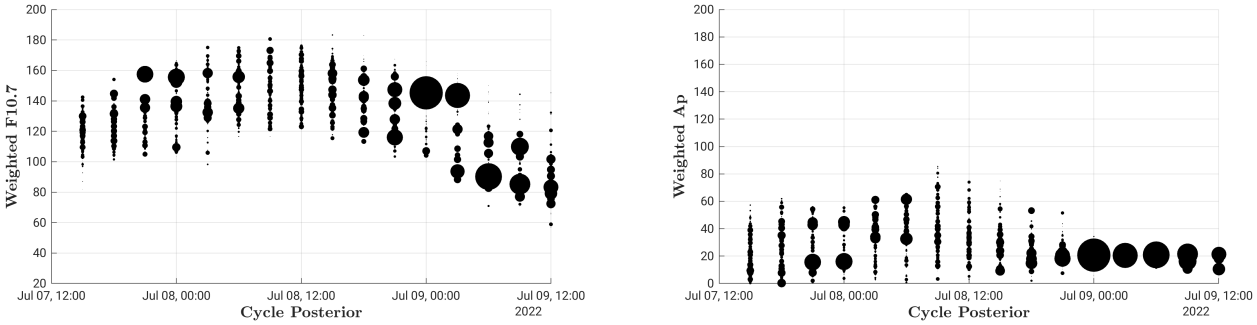

Figure 5.11: Storm period for particle time-series with corresponding $\mathbf{d}_{F107^*}$ and $\mathbf{d}_{Ap^*}$ weights. Shown for 3-hour cycling and increased Ap stochastic dynamics with select parameter distributions.

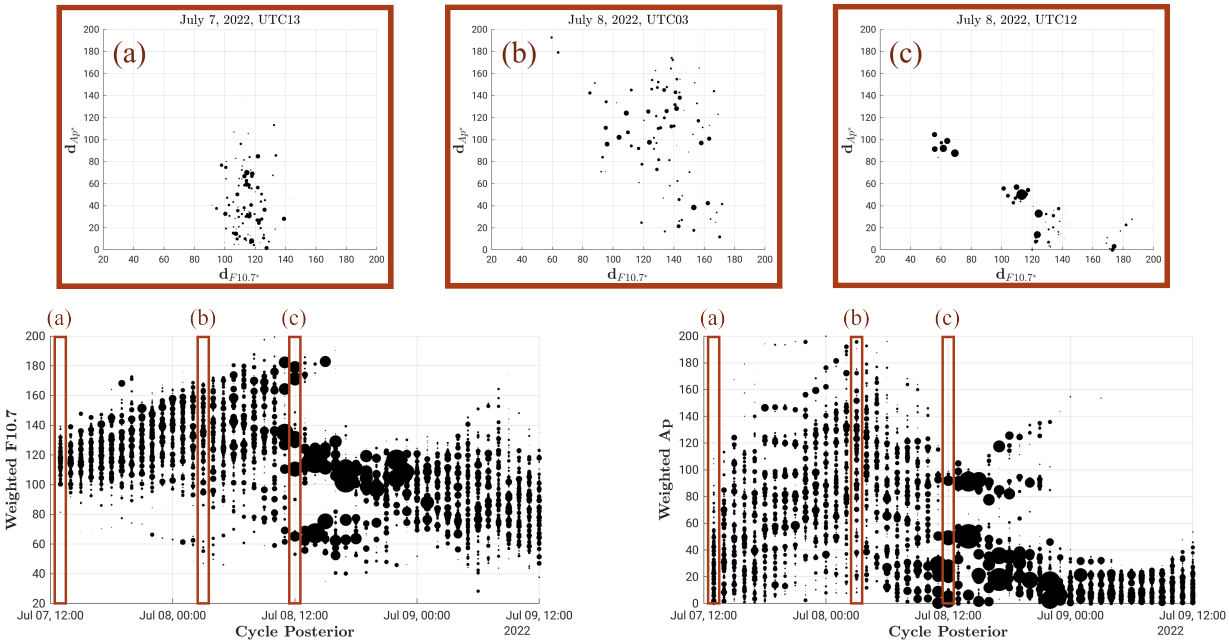

Figure 5.12: Storm period for particle time-series with corresponding $\mathbf{d}_{F107^*}$ and $\mathbf{d}_{Ap^*}$ weights. Shown for 1-hour cycling and increased Ap stochastic dynamics with select parameter distributions.

model spread and consequently filter performance. We additionally see much less difference in model spread between the dawn and dusk sides.

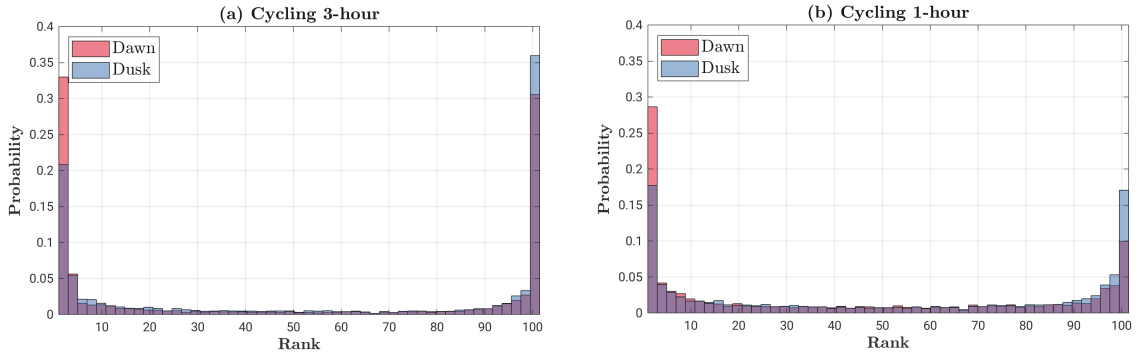

Figure 5.13: Rank histogram for the storm period showing particle spread relative to observations. Includes (a) 3-hour cycling and (b) 1-hour cycling, separated by the dawn-dusk sides.

Posterior neutral density pdfs are shown in Figure 5.14 to address the original question posed of quantifying neutral density uncertainties. Here, we show the posterior particle weights along with a fitted Gaussian distribution of the weighted particle mean and variance. PDF (a) in the quiet period shows the bimodal distribution as seen in Figure 5.6, likely showing separate fits for the two sampled LTs. An additional quiet period PDF is shown in panel (b) for the dusk LTs. For the storm period, a non-Gaussian distribution is seen for the high latitude dawn side in panel (c) where we would expect more non-linear forcing influence, as quantified in Figure 5.1. The fitted distribution matches a Gaussian assumption well for a mid-latitude dusk side location in Figure 5.14d.

5.4 Discussion

In this particle filter approach, we simplify the estimation problem by estimating a global weight for two global parameters. As such, there is a considerable limitation in the resolution of neutral density variability we can quantify, as these dynamical processes, particularly during storm events, can produce variability on much smaller spatial and temporal scales. This indicates why the particle filter performed relatively better during the quiet pe-

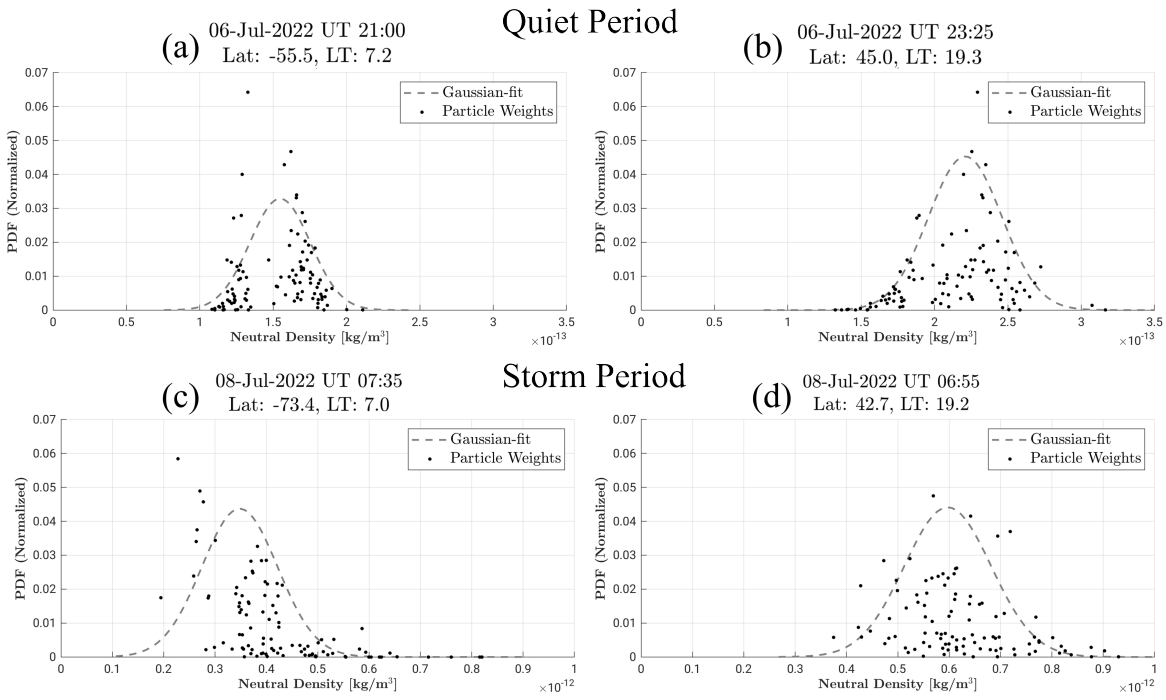

Figure 5.14: Select posterior neutral density PDFs along GRACE-FO orbit locations, shown from the quiet period with 6-hour cycling (a-b) and the storm period with 1-hour cycling (c-d) experiments. Contains particles with their respective weights and normalized PDFs for a fitted Gaussian distribution.

riod than the storm period. Additionally, in our filter assumptions, the temporal resolution is limited by the assumption of condensing observations to their nearest hour and limiting the spatial resolution by using the 5-degree TIEGCM. These spatial and temporal resolution restrictions are balanced against computational costs for memory and run-time. Investigating runs with more particle samples is also needed. Additionally, by having a longer cycling frequency, longer integration windows increase the influence of input forcing parameters, allowing time for the non-linear storm processes to develop and increase divergent state spread. Regardless, capturing smaller-scale neutral density structures is less critical due to their lesser impact on orbit propagation errors (Anderson et al., 2009b).

The use of global weights in simplifying our estimation is evident even in the quiet period of day-night biases. From the quiet period rank histograms shown in Figure 5.8, different bias directions are present in the dawn and dusk sides. These day-night biases have been previously studied and are known to exist within the TIEGCM (Waldron, 2020; Thayer et al., 2023). Additionally, all local time observations are equally weighed, meaning a day-side observation has an equal influence in determining a weight for $\mathbf{d}_{F107^*}$ as night-side observation, where there is no direct solar influence. This is likewise true for high-latitude observations when estimating $\mathbf{d}_{Ap^*}$. longer cycling windows somewhat account for these issues and can be further addressed in future work. Nevertheless, this estimation is complicated as the F10.7 index is a global solar irradiance parameter, and as such its influence cannot be independently separated by solar local time. The same is true for the Ap index.

While we show rapidly increasing Ap stochastic noise greatly helps to capture the storm enhancement, the same does not hold for the recovery phase where neutral density processes are more internally driven. The particle filter attempts to compensate for this recovery gap by lowering $\mathbf{d}_{F107^*}$, where instead the real solar irradiance increases during this period. The slow recovery response in physics-based models is a well-documented issue, and commonly attributed to lack of sufficient nitric oxide (NO) cooling (Lei et al., 2011; Lu et al., 2014; Li

et al., 2019), a primary means for recovery in the thermosphere (Barth, 1992). Assimilating NO cooling observations into the TIEGCM has been shown to improve recovery (He et al., 2023), and internal parameter terms should be investigated as adjusting external forcing does not adequately capture these processes. This additionally shows a gap of only estimating external forcing parameters.

In this particle filter implementation, we assume observations are independent and this assumption is a common cause of particle collapse. This weight collapse has been quantified in (Snyder et al., 2008) in an equivalent state dimension, showing a need for N_e to grow exponentially with more observations, p. Thus it would be beneficial to fill $\mathbf{R}$ with correlated observations so that the filter is not overconfident in the provided observation information; however, how to accomplish this is challenging. First, within $\mathbf{R}$, we are not just including observation error covariance, but also quantifying the representativeness errors of estimating forcing parameters in observation space. These include errors from the model, parameterizations, and the relation between forcing parameters and observations.

To investigate how neutral density observations vary spatially, we fit an empirical semivariogram for the quiet and geomagnetically active periods, shown in Figure 5.15. To fit the semivariogram, we assume an isotropic Matérn correlation function, defined as

$$C_\nu(r) = \frac{2^{1-\nu}}{\Gamma(\nu)} \left(\frac{r}{\rho} \right)^{\nu} K_\nu \left(\frac{r}{\rho} \right) \tag{5.10}$$

where r is the distance given by some metric, $\rho > 0$ is the length-scale range parameter, $\nu > 0$ is the shape function, $\Gamma()$ is the gamma function and $K_\nu()$ is the modified Bessel function of the second kind. We fix a shape parameter of $\nu = 20$ for all fitting, and a table of fitted Matérn parameters are listed in Table 5.1. The sill is defined as the limit of the semivariogram, and the nugget is defined as the height jump at the origin.

For the quiet period, there is good agreement between the dawn and dusk regions of the semivariogram fit, where there are similar fits for the sill and nugget, and the quiet-dawn range is slightly greater than the quiet-dusk range. For the storm period, the correlation is

Table 5.1: Fitted Matérn parameters for GRACE-FO observations

Region	ν	ρ	Sill	Nugget
Quiet-Dawn	20	11.87	0.28	0.009
Quiet-Dusk	20	9.86	0.26	0.01
Storm-Dawn	20	8.11	0.18	0.07
Storm-Dusk	20	8.5	0.15	0.13

noisier than the quiet period, with shorter range parameters and greater nugget fit. Additionally, we see less correlation for observations on the dawn side than on the dusk side. It is noted that there were a similar number of samples used for the quiet and storm periods, with 7×10^5 samples for the closest r separation and 8×10^4 samples for the furthest r separation.

While the particle filter substantiates the emergence of non-Gaussian neutral density and forcing parameter distributions, the performance must be improved to better match neutral density variability for all periods in addressing the motivating goal to quantify neutral density uncertainties. This can be accomplished through better stochastic noise, improved quantification of the σ_{rep}, as well as accounting for observation correlations within $\boldsymbol{R}$. Over-compensating for σ_{rep} will cause weights to over-disperse, restricting the filter's ability to rapidly change, and under-specifying σ_{rep} will cause the filter to become overconfident and cause weights to collapse. Additionally, more particles and estimating weights on smaller scales are needed to represent non-global processes. Once neutral density spreads better neutral density observations, validated through rank histograms, we may then look into higher order moments for neutral density uncertainty and assess their impacts on orbit position uncertainties relevant to conjunction analysis.

5.5 Conclusions

This chapter demonstrates a new particle filter framework for estimating neutral densities in a reduced forcing parameter space, enabling the estimation of non-Gaussian uncertainties. Applying this framework to a storm event demonstrates the emergence of non-Gaussian

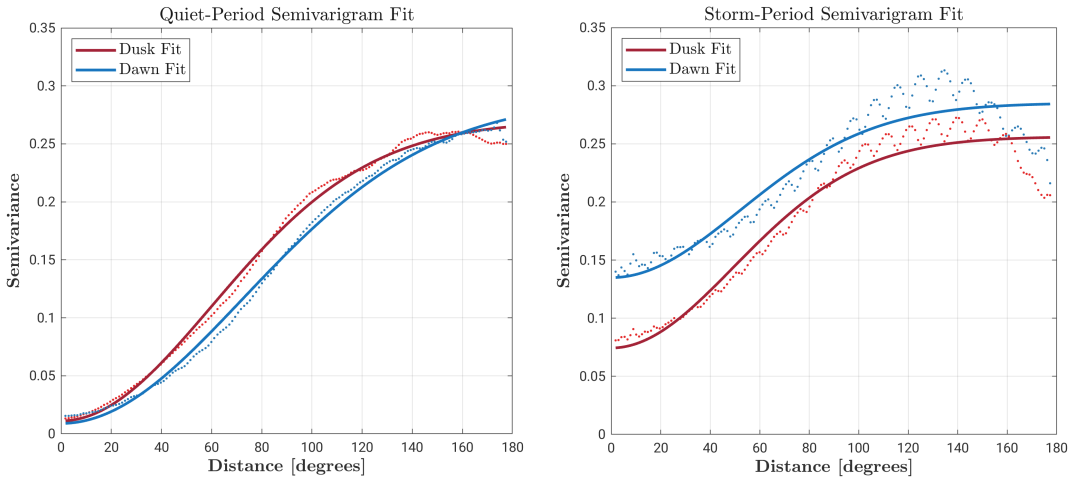

Figure 5.15: Fitted empirical semivariogram for GRACE-FO neutral density observations, split by dawn and dusk local time and quiet and storm periods. Points represent semivariogram values and solid lines indicate the Matérn fit.

distributions, and periods where Gaussian assumptions are suitable, and is promising for future applications. Limitations remain in capturing neutral density variability from sources not included in the F10.7 and Ap parameterizations, and simplifying assumptions needed for computational ease. Nevertheless, this framework shows the ability of the particle filter to accurately represent quiet-period neutral density variability and adequately represent storm enhancements through stochastic parameter forcing. Quantifying the shape and magnitude of neutral density uncertainties and how they map to orbit position errors will inform LEO conjunction analysis and enhance future SDA capabilities.

Chapter 6

Conclusions

6.1 Summary and Contributions

With the LEO environment becoming increasingly crowded and society's dependence on satellite technologies, advancing space weather understanding and incorporating this understanding into practical LEO environment monitoring tools is crucial. The thesis particularly focuses on the problem of LEO position uncertainties driven by geophysical neutral density variability. The ever-increasing LEO population will only exasperate challenges tracking orbit position uncertainties; however, with proper space management, the LEO environment can be kept safe and collision-free. To realize the potential of physics-based models for neutral density predictive capabilities, the thesis makes important contributions to capture the complex and non-linear I-T variability during storm time. Specifically, the thesis advances the capabilities of physics-based models to accurately capture neutral density variability by synthesizing models with observations through data assimilation. The data assimilation approach developed in the thesis leverages an abundantly available source of plasma observations from RO and overcomes the lack of a global thermospheric monitoring system. The estimation approaches adopted by the thesis are specifically tailored to the upper atmosphere that depends on initial conditions and external forcing. The thesis first underscores the potential to use GNSS RO observations as a global monitoring system for I-T states and overcome current neutral observation limitations. The second thesis component addresses currently used Gaussian error assumptions by incorporating non-linear storm

dynamics and supports future operations for conjunction assessment and orbit positioning. Specific contributions made by the thesis through developing and applying physics-based approaches toward neutral density specification (Objectives 1.1, 1.2, and 1.3) and uncertainty quantification (Objective 2.1) are summarized below.

(1) Objective 1.1 accomplished in Chapter 2 evaluates hypothetical RO constellations for ionospheric specification, informing better mission designs and evaluating Abel inversion error limitations for RO EDP assimilation. This is achieved through a simulation study that comprehensively accounts for the impact of forecast model and observation errors.

(2) Objective 1.2 detailed in Chapter 3 leverages GNSS RO observations to estimate thermospheric states directly. This chapter demonstrates that using strongly coupled data assimilation with RO EDPs, we can specify neutral densities to reduce corresponding orbit position errors, as well as infer unobserved states like helium compositions.

(3) Objective 1.3 accomplished in Chapter 4 produces a storm thermospheric reanalysis, building upon the framework demonstrated in Objective 1.2. This objective signifies the first case study using RO observations to estimate storm-time neutral densities, reducing overall neutral density biases and better capturing the storm recovery response. In producing this reanalysis, Objective 1.3 facilitates a systematic comparison of models with observations, shedding light on the current model and filter limitations.

(4) Objective 2.1 contributes a first attempt to quantify non-Gaussian neutral density uncertainties during storm time. Chapter 5 details this particle filter framework that facilitates non-Gaussian neutral density estimation in the reduced space of forcing parameters, utilizing the non-linear storm dynamics of physics-based modeling.

This particle filter framework accomplishes end-to-end uncertainty quantification to demonstrate the emergence of non-Gaussian error distributions during storm time.

6.2 Future Work

Work presented in Chapters 4 and 5 highlight current I-T model shortcomings and motivate further investigation. Through applying OSSE and OSE frameworks the thesis takes important steps forward towards accomplishing thermospheric data assimilation, especially the extensive experiment testing in Chapter 4. Further details are found in the Section 4.5 discussion. Chapter 2 details the need for RO EDP observation uncertainty quantification due to Abel inversion errors. For the particle filter framework in Chapter 5, Section 5.4 details filter features needed in the future to better capture the neutral density storm-time evolution. A more effective filter could quantify higher-order neutral density moments, such as by capturing smaller-scale variability with finer-scale weight implementations.

Applying the upper atmosphere data assimilation approaches described in Chapters 3 and 4 are exceptionally informative at reconciling model and observation differences. The process of directly comparing observations with the model in both OSSE and OSE frameworks helps to highlight I-T model shortcomings and offers a new perspective for further model development. Additionally, deeper analysis into how the data assimilation is impacting model states in both the forecast and analysis steps will offer great insights into the most beneficial observations and approaches for thermospheric specification. Within reanalysis experiments and development, we exhausted many available tools for improving data assimilation performance, which were insufficient in reducing model biases and introducing adequate state spreads. Ensemble filter approaches fundamentally rely on the background covariance structures to inform correlations for analysis updates, and inadequately representative or realistic covariances were found to be a particularly limiting factor in reanalysis performance. Errors in the background covariance are evident with inflation that heavily depends on covariance structures, and resulted in mixed impact and increased model insta-

bility. Toward efforts to operationalize ensemble filters for thermospheric data assimilation, there is a critical limitation in tools effective for introducing model spread, adjusting biases, and creating representative background covariance structures. Future work, such as understanding why inflation had mixed performance, is needed to develop these tools for thermospheric ensemble estimation.

As for the future, the goal would be to develop a unified estimation framework comprising of I-T states and forcing parameter space, as defined in Equations 1.10 and 1.11. For the thesis, the ensemble and particle filters are rather complementary, where the particle filter can address issues of large-scale model spreads and biases, and local time and latitudinal biases that cannot be addressed by adjusting global parameters can be corrected using an ensemble filter. Further validation into other effective data assimilation approaches for the thermospheric specification also warrants future investigation.

With TIEGCM using boundary approximations for the lower atmosphere and above plasmasphere, using other fully coupled models would add much-needed I-T state variability and spread. TIEGCM coupled with realistic lower atmospheric perturbations has been shown to improve model spreads (Hsu and Pedatella, 2023), and I-T models with coupled plasmaspheres have shown better agreement with plasma observations (Chou et al., 2023). Further, more realistic magnetospheric coupling can improve storm enhancement neutral density structures (Pham et al., 2022). Coupling models will add more sources of realistic forcing and decrease the reliance on solar irradiance to provide model spreads, where more complex solar irradiance models are also needed. Nevertheless, as discussed in Section 4.5, using an efficient and stable model like TIEGCM offers tremendous benefits over computationally heavier models, where we may run longer and more extensive experiment testing with ample ensemble members.

Another important application is to use the resulting estimated neutral density fields to inform orbit position uncertainties. Mapping the impact of these storm-time neutral densities on orbit positions can be accomplished through a Monte Carlo experiment applying

the atmospheric drag equation to produce satellite position estimates. This approach can generate uncertainties, Gaussian or non-Gaussian, useful for conjunction assessment (NASA, 2020), and be used to assess resulting error distribution shapes and magnitudes.

Bibliography

Akmaev, R. A. (2011). Whole atmosphere modeling: Connecting terrestrial and space weather. Reviews of Geophysics, 49(4).

Allen, D. R., Hodyss, D., Forsythe, V. V., and Mcdonald, S. E. (2023). Low latitude monthly total electron content composite correlations. Journal of Space Weather and Space Climate, 13(9).

Anderson, J., Hoar, T., Raeder, K., Liu, H., Collins, N., Torn, R., and Avellano, A. (2009a). The data assimilation research testbed a community facility. Bulletin of the American Meteorological Society, 90(9):1283–1296.

Anderson, J. L. (2001). An ensemble adjustment Kalman filter for data assimilation. Monthly Weather Review, 129(12):2884–2903.

Anderson, J. L. (2003). A local least squares framework for ensemble filtering. Monthly Weather Review, 131(4):634–642.

Anderson, J. L. (2007). An adaptive covariance inflation error correction algorithm for ensemble filters. Tellus, Series A: Dynamic Meteorology and Oceanography, 59(2):210–224.

Anderson, J. L. and Collins, N. (2007). Scalable implementations of ensemble filter algorithms for data assimilation. Journal of Atmospheric and Oceanic Technology, 24(8):1452–1463.

Anderson, R. L., Born, G. H., and Forbes, J. M. (2009b). Sensitivity of orbit predictions to density variability. Journal of Spacecraft and Rockets, 46(6):1214–1230.

Andersson, E. and Masutani, M. (2010). Collaboration on observing system simulation experiments (Joint OSSE). ECMWF Newsletter, 123:14–16.

Angling, M. J., Nogués-Correig, O., Nguyen, V., Vetra-Carvalho, S., Bocquet, F. X., Nordstrom, K., Melville, S. E., Savastano, G., Mohanty, S., and Masters, D. (2021). Sensing the ionosphere with the Spire radio occultation constellation. Journal of Space Weather and Space Climate, 11(2001).

Anthes, R. A., Bernhardt, P. A., Chen, Y., Cucurull, L., Dymond, K. F., Ector, D., Healy, S. B., Ho, S. P., Hunt, D. C., Kuo, Y. H., Liu, H., Manning, K., McCormick, C., Meehan, T. K., Randel, W. J., Rocken, C., Schreiner, W. S., Sokolovskiy, S. V., Syndergaard, S., Thompson, D. C., Trenberth, K. E., Wee, T. K., Yen, N. L., and Zeng, Z. (2008). The COSMIC/Formosat-3 mission: Early results. Bulletin of the American Meteorological Society, 89(3):313–333.

Anthes, R. A., Hui Shao, Christian Marquardt, and Benjamin Ruston (2023). Radio Occultation Modeling Experiment (ROMEX) Framework. Technical report, International Radio Occultation Working Group (IROWG).

Banks, P. M. and Kockarts, G. (1973). Aeronomy. Academic Press, New York, London.

Barth, C. A. (1992). Nitric oxide in the lower thermosphere. Planetary and Space Science, 40(2-3):315–336.

Bates, D. R. (1959). Some problems concerning the terrestrial atmosphere above about the 100 km level. Proceedings of the Royal Society of London. Series A. Mathematical and Physical Sciences, 253(1275):451–462.

Berger, T. E., Holzinger, M. J., Sutton, E. K., and Thayer, J. P. (2020). Flying Through Uncertainty. Space Weather, 18(1):e2019SW002373.

Bernstein, V., Pilinski, M., and Knipp, D. (2020). Evidence for drag coefficient modeling errors near and above the oxygen-to-helium transition. Journal of Spacecraft and Rockets, 57(6):1246–1263.

Bilitza, D., Pezzopane, M., Truhlik, V., Altadill, D., Reinisch, B. W., and Pignalberi, A. (2022). The International Reference Ionosphere Model: A Review and Description of an Ionospheric Benchmark. Reviews of Geophysics, 60(4).

Bishop, C. H., Etherton, B. J., and Majumdar, S. J. (2001). Adaptive sampling with the ensemble transform Kalman filter Part I: Theoretical aspects. Monthly Weather Review, 129(3):420–436.

Bowman, B. R., Tobiska, W. K., Marcos, F. A., Huang, C. Y., Lin, C. S., and Burke, W. J. (2008). A new empirical thermospheric density model JB2008 using new solar and geomagnetic indices. AIAA/AAS Astrodynamics Specialist Conference and Exhibit, 6438(August).

Brandt, D. A., Bussy-Virat, C. D., and Ridley, A. J. (2020). A Simple Method for Correcting Empirical Model Densities During Geomagnetic Storms Using Satellite Orbit Data. Space Weather, 18(12).

Bruinsma, S. (2014). The DTM-2013 thermosphere model. Journal of Space Weather and Space Climate, 5.

Bruinsma, S., Boniface, C., Sutton, E. K., and Fedrizzi, M. (2021). Thermosphere modeling capabilities assessment: Geomagnetic storms. Journal of Space Weather and Space Climate, 11(2018).

Bruinsma, S., Siemes, C., Emmert, J. T., and Mlynczak, M. G. (2023). Description and comparison of 21st century thermosphere data. Advances in Space Research, 72(12):5476–5489.

Buonsanto, M. J. (1999). Ionospheric storms – a review m. j. buonsanto. Space Science Reviews, 88(February):563–601.

Buonsanto, M. J., Foster, J. C., Galasso, A. D., Sipler, D. P., and Holt, J. M. (1990). Neutral winds and thermosphere/ionosphere coupling and energetics during the geomagnetic disturbances of March 6–10, 1989. Journal of Geophysical Research: Space Physics, 95(A12):21033–21050.

Burke, W. J., Huang, C. Y., Marcos, F. A., and Wise, J. O. (2007). Interplanetary control of thermospheric densities during large magnetic storms. Journal of Atmospheric and Solar-Terrestrial Physics, 69(3):279–287.

Burns, A. G., Killeen, T. L., Wang, W., and Roble, R. G. (2004). The solar-cycle-dependent response of the thermosphere to geomagnetic storms. Journal of Atmospheric and Solar-Terrestrial Physics, 66(1):1–14.

Bust, G. S., Garner, T. W., and Gaussiran, T. L. (2004). Ionospheric Data Assimilation Three-Dimensional (IDA3D): A global, multisensor, electron density specification algorithm. Journal of Geophysical Research: Space Physics, 109(A11).

Cai, Y., Yue, X., Wang, W., Zhang, S. R., Liu, H., Lin, D., Wu, H., Yue, J., Bruinsma, S. L., Ding, F., Ren, Z., and Liu, L. (2022). Altitude Extension of the NCAR-TIEGCM (TIEGCM-X) and Evaluation. Space Weather, 20(11):1–17.

Camporeale, E. (2019). The Challenge of Machine Learning in Space Weather: Nowcasting and Forecasting. Space Weather, 17(8):1166–1207.

Chapman, S. (1931). The absorption and dissociative or ionizing effect of monochromatic radiation in an atmosphere on a rotating earth. Proceedings of the Physical Society, 43(1):26–45.

Chartier, A. T., Jackson, D. R., and Mitchell, C. N. (2013). A comparison of the effects of initializing different thermosphere- ionosphere model fields on storm time plasma density forecasts. Journal of Geophysical Research: Space Physics, 118(11):7329–7337.

Chartier, A. T., Matsuo, T., Anderson, J. L., Collins, N., Hoar, T. J., Lu, G., Mitchell, C. N., Coster, A. J., Paxton, L. J., and Bust, G. S. (2016). Ionospheric data assimilation and forecasting during storms. Journal of Geophysical Research: Space Physics, 121(1):764–778.

Chen, C. H., Lin, C. H., Matsuo, T., Chen, W. H., Lee, I. T., Liu, J. Y., Lin, J. T., and Hsu, C. T. (2016). Ionospheric data assimilation with thermosphere-ionosphere-electrodynamics general circulation model and GPS-TEC during geomagnetic storm conditions. Journal of Geophysical Research: Space Physics, 121(6):5708–5722.

Chen, X. and Lei, J. (2018). A Numerical Study of the Thermospheric Overcooling During the Recovery Phases of the October 2003 Storms. Journal of Geophysical Research: Space Physics, 123(7):5704–5716.

Cherniak, I., Zakharenkova, I., Braun, J., Wu, Q., Pedatella, N., Schreiner, W., Weiss, J. P., and Hunt, D. (2021). Accuracy assessment of the quiet-time ionospheric F2 peak parameters as derived from COSMIC-2 multi-GNSS radio occultation measurements. Journal of Space Weather and Space Climate, 11:1–14.

Chou, M., Yue, J., Wang, J., Huba, J. D., El Alaoui, M., Kuznetsova, M. M., Rastätter, L., Shim, J. S., Fang, T., Meng, X., Fuller-Rowell, D., and Retterer, J. M. (2023). Validation of Ionospheric Modeled TEC in the Equatorial Ionosphere During the 2013 March and 2021 November Geomagnetic Storms. Space Weather, 21(6).

Chou, M. Y., Lin, C. C., Tsai, H. F., and Lin, C. Y. (2017). Ionospheric electron density inversion for Global Navigation Satellite Systems radio occultation using aided Abel inversions. Journal of Geophysical Research: Space Physics, 122(1):1386–1399.

Christensen, A. B., Paxton, L. J., Avery, S., Craven, J., Crowley, G., Humm, D. C., Kil, H., Meier, R. R., Meng, C. I., Morrison, D., Ogorzalek, B. S., Straus, P., Strickland, D. J., Swenson, R. M., Walterscheid, R. L., Wolven, B., and Zhang, Y. (2003). Initial observations with the Global Ultraviolet Imager (GUVI) in the NASA TIMED satellite mission. Journal of Geophysical Research: Space Physics, 108(A12).

Cluzet, B., Lafaysse, M., Cosme, E., Albergel, C., Meunier, L. F., and Dumont, M. (2021). CrocO-v1.0: A particle filter to assimilate snowpack observations in a spatialised framework. Geoscientific Model Development, 14(3):1595–1614.

Cluzet, B., Lafaysse, M., Deschamps-Berger, C., Vernay, M., and Dumont, M. (2022). Propagating information from snow observations with CrocO ensemble data assimilation system: a 10-years case study over a snow depth observation network. Cryosphere, 16(4):1281–1298.

Codrescu, M. V., Fuller-Rowell, T. J., and Minter, C. F. (2004). An ensemble-type Kalman filter for neutral thermospheric composition during geomagnetic storms. Space Weather, 2(11).

Codrescu, S. M., Codrescu, M. V., and Fedrizzi, M. (2018). An Ensemble Kalman Filter for the Thermosphere-Ionosphere. Space Weather, 16(1):57–68.

Cousins, E. D. and Shepherd, S. G. (2010). A dynamical model of high-latitude convection derived from SuperDARN plasma drift measurements. Journal of Geophysical Research: Space Physics, 115(12).

Crisan, D. and Doucet, A. (2002). A survey of convergence results on particle filtering methods for practitioners. IEEE Transactions on Signal Processing, 50(3):736–746.

Danilov, A. D. (2013). Ionospheric F-region response to geomagnetic disturbances. Advances in Space Research, 52(3):343–366.

Dietrich, N., Matsuo, T., and Hsu, C. T. (2022). Specifying Satellite Drag Through Coupled Thermosphere-Ionosphere Data Assimilation of Radio Occultation Electron Density Profiles. Space Weather, 20(8).

Dietrich, N., Matsuo, T., Lin, C.-Y., DiLorenzo, B., Lin, C. C., and Fang, T.-W. (2024). Evaluating Radio Occultation (RO) Constellation Designs Using Observing System Simulation Experiments (OSSEs) for Ionospheric Specification. Space Weather, 22(8):e2024SW003958.

Eastes, R. W., McClintock, W. E., Burns, A. G., Anderson, D. N., Andersson, L., Codrescu, M., Correira, J. T., Daniell, R. E., England, S. L., Evans, J. S., Harvey, J., Krywonos, A., Lumpe, J. D., Richmond, A. D., Rusch, D. W., Siegmund, O., Solomon, S. C., Strickland, D. J., Woods, T. N., Aksnes, A., Budzien, S. A., Dymond, K. F., Eparvier, F. G., Martinis, C. R., and Oberheide, J. (2017). The Global-Scale Observations of the Limb and Disk (GOLD) Mission. Space Science Reviews, 212(1-2):383–408.

Eckermann, S. D., Ma, J., Hoppel, K. W., Kuhl, D. D., Allen, D. R., Doyle, J. A., Viner, K. C., Ruston, B. C., Baker, N. L., Swadley, S. D., Whitcomb, T. R., Reynolds, C. A., Xu, L., Kaifler, N., Kaifler, B., Reid, I. M., Murphy, D. J., and Love, P. T. (2018). High-altitude (0-100 km) global atmospheric reanalysis system: Description and application to the 2014 austral winter of the Deep Propagating Gravity Wave Experiment (DEEPWAVE). Monthly Weather Review, 146(8):2639–2666.

El Gharamti, M. (2018). Enhanced adaptive inflation algorithm for ensemble filters. Monthly Weather Review, 146(2):623–640.

Emmert, J. T. (2015). Thermospheric mass density: A review. Advances in Space Research, 56(5):773–824.

Emmert, J. T., Drob, D. P., Picone, J. M., Siskind, D. E., Jones, M., Mlynczak, M. G., Bernath, P. F., Chu, X., Doornbos, E., Funke, B., Goncharenko, L. P., Hervig, M. E., Schwartz, M. J., Sheese, P. E., Vargas, F., Williams, B. P., and Yuan, T. (2021). NRLMSIS 2.0: A Whole-Atmosphere Empirical Model of Temperature and Neutral Species Densities. Earth and Space Science, 8(3).

Emmert, J. T., Richmond, A. D., and Drob, D. P. (2010). A computationally compact representation of magnetic-apex and Quasi-Dipole coordinates with smooth base vectors. Journal of Geophysical Research: Space Physics, 115(8):1–13.

England, S. L., Maus, S., Immel, T. J., and Mende, S. B. (2006). Longitudinal variation of the E-region electric fields caused by atmospheric tides. Geophysical Research Letters, 33(21):1–5.

Errico, R. M., Yang, R., Privé, N. C., Tai, K. S., Todling, R., Sienkiewicz, M. E., and Guo, J. (2013). Development and validation of observing-system simulation experiments at NASA's global modeling and assimilation office. Quarterly Journal of the Royal Meteorological Society, 139(674):1162–1178.

Esplin, R., Mlynczak, M. G., Russell, J., and Gordley, L. (2023). Sounding of the Atmosphere Using Broadband Emission Radiometry (SABER): Instrument and Science Measurement Description. Earth and Space Science, 10(9).

Evensen, G. (2009). Data assimilation: the ensemble Kalman filter. Springer.

Evensen, G., Vossepoel, F. C., and van Leeuwen, P. J. (2022). Data Assimilation Fundamentals: A Unified Formulation of the State and Parameter Estimation Problem. Springer Nature.

Farchi, A. and Bocquet, M. (2018). Review article: Comparison of local particle filters and new implementations. Nonlinear Processes in Geophysics, 25(4):765–807.

Fong, C. J., Chu, C. H., Lin, C. L., and Curiel, A. D. S. (2019). Toward the Most Accurate Thermometer in Space: FORMOSAT-7/COSMIC-2 Constellation. IEEE Aerospace and Electronic Systems Magazine, 34(8):12–20.

Forbes, J. M., Palo, S. E., and Zhang, X. (2000). Variability of the ionosphere. Journal of Atmospheric and Solar-Terrestrial Physics, 62(8):685–693.

Forsythe, V. V., Azeem, I., Blay, R., Crowley, G., Gasperini, F., Hughes, J., Makarevich, R. A., and Wu, W. (2021). Evaluation of the New Background Covariance Model for the Ionospheric Data Assimilation. Radio Science, 56(8):1–10.

Forsythe, V. V., Azeem, I., and Crowley, G. (2020). Ionospheric Horizontal Correlation Distances: Estimation, Analysis, and Implications for Ionospheric Data Assimilation. Radio Science, 55(12):1–14.

Fuller-Rowell, T. J., Codrescu, M. V., Moffett, R. J., and Quegan, S. (1994). Response of the thermosphere and ionosphere to geomagnetic storms. Journal of Geophysical Research: Space Physics, 99(3):3893–3914.

Gaspari, G. and Cohn, S. E. (1999). Construction of correlation functions in two and three dimensions. Quarterly Journal of the Royal Meteorological Society, 125(554):723–757.

Ghrist, R. W. and Plakalovic, D. (2012). Impact of non-gaussian error volumes on conjunction assessment risk analysis. In AIAA/AAS Astrodynamics Specialist Conference 2012, page 4965.

Godinez, H. C., Lawrence, E., Higdon, D., Ridley, A., Koller, J., and Klimenko, A. (2015). Specification of the ionosphere-thermosphere using the ensemble kalman filter. In Ravela, S. and Sandu, A., editors, Lecture Notes in Computer Science (including subseries Lecture Notes in Artificial Intelligence and Lecture Notes in Bioinformatics), volume 8964, pages 274–283, Cham. Springer International Publishing.

Gondelach, D. J. and Linares, R. (2021). Real-Time Thermospheric Density Estimation Via Radar and Gps Tracking Data Assimilation. Advances in the Astronautical Sciences, 175:1797–1814.

Gorbunov, M. E. and Kornblueh, L. (2001). Analysis and validation of GPS/MET radio occultation data. Journal of Geophysical Research Atmospheres, 106(D15):17161–17169.

Gordon, N. J., Salmond, D. J., and Smith, A. F. (1993). Novel approach to nonlinear/non-gaussian Bayesian state estimation. In IEE Proceedings, Part F: Radar and Signal Processing, volume 140, pages 107–113. IET.

Grooms, I. (2022). A comparison of nonlinear extensions to the ensemble Kalman filter. Computational Geosciences, 26(3):633–650.

Gupta, A. D., Basu, S., Bhar, J. N., and Bhattacharyya, J. C. (1975). Ionospheric electron content and equivalent slab thickness in the equatorial region. Journal of Geophysical Research, 80(4):699–701.

Hagan, M. E., Burrage, M. D., Forbes, J. M., Hackney, J., Randel, W. J., and Zhang, X. (1999). GSWM-98: Results for migrating solar tides. Journal of Geophysical Research: Space Physics, 104(A4):6813–6827.

Hagan, M. E. and Forbes, J. M. (2002). Migrating and nonmigrating diurnal tides in the middle and upper atmosphere excited by tropospheric latent heat release. Journal of Geophysical Research Atmospheres, 107(24):ACL 6–1–ACL 6–15.

Hagan, M. E. and Forbes, J. M. (2003). Migrating and nonmigrating semidiurnal tides in the upper atmosphere excited by tropospheric latent heat release. Journal of Geophysical Research: Space Physics, 108(A2):1–14.

Hajj, G. A. and Romans, L. J. (1998). Ionospheric electron density profiles obtained with the Global Positioning System: Results from the GPS/MET experiment. Radio Science, 33(1):175–190.

Hajj, G. A., Wilson, B. D., Wang, C., Pi, X., and Rosen, I. G. (2004). Data assimilation of ground GPS total electron content into a physics-based ionospheric model by use of the Kalman filter. Radio Science, 39(1):243–259.

He, J., Pedatella, N. M., Astafyeva, E., Yue, X., Ren, Z., and Yu, T. (2023). Improved Thermosphere Mass Density Recovery During the 5 April 2010 Geomagnetic Storm by Assimilating NO Cooling Rates in a Coupled Thermosphere-Ionosphere Model. Journal of Geophysical Research: Space Physics, 128(11):1–12.

He, J., Yue, X., Wang, W., and Wan, W. (2019). EnKF Ionosphere and Thermosphere Data Assimilation Algorithm Through a Sparse Matrix Method. Journal of Geophysical Research: Space Physics, 124(8):7356–7365.

Heelis, R. A., Lowell, J. K., and Spiro, R. W. (1982). A model of the high-latitude ionospheric convection pattern. Journal of Geophysical Research: Space Physics, 87(A8):6339–6345.

Heelis, R. A., Stoneback, R. A., Perdue, M. D., Depew, M. D., Morgan, W. A., Mankey, M. W., Lippincott, C. R., Harmon, L. L., and Holt, B. J. (2017). Ion Velocity Measurements for the Ionospheric Connections Explorer. Space Science Reviews, 212(1-2):615–629.

Hersbach, H., Bell, B., Berrisford, P., Hirahara, S., Horányi, A., Muñoz-Sabater, J., Nicolas, J., Peubey, C., Radu, R., Schepers, D., Simmons, A., Soci, C., Abdalla, S., Abellan, X., Balsamo, G., Bechtold, P., Biavati, G., Bidlot, J., Bonavita, M., De Chiara, G., Dahlgren, P., Dee, D., Diamantakis, M., Dragani, R., Flemming, J., Forbes, R., Fuentes, M., Geer, A., Haimberger, L., Healy, S., Hogan, R. J., Hólm, E., Janisková, M., Keeley, S., Laloyaux, P., Lopez, P., Lupu, C., Radnoti, G., de Rosnay, P., Rozum, I., Vamborg, F., Villaume, S., and Thépaut, J. N. (2020). The ERA5 global reanalysis. Quarterly Journal of the Royal Meteorological Society, 146(730):1999–2049.

Hoffman, R. N. and Atlas, R. (2016). Future observing system simulation experiments. Bulletin of the American Meteorological Society, 97(9):1601–1616.

Hogan, T. F., Liu, M., Ridout, J. A., Peng, M. S., Whitcomb, T. R., Ruston, B. C., Reynolds, C. A., Eckermann, S. D., Moskaitis, J. R., Baker, N. L., McCormack, J. P., Viner, K. C., McLay, J. G., Flatau, M. K., Xu, L., Chen, C., and Chang, S. W. (2014). The navy global environmental model. Oceanography, 27(3):116–125.

Hsu, C. T., Matsuo, T., Kershaw, H., Dietrich, N., Smith, M., Anderson, J., Garcia-Sage, K., Yue, J., Hozumi, Y., and Chou, M. Y. (2024). A Community Ionosphere-Thermosphere Observing System Simulation Experiment (OSSE) Tool: Geospace Dynamics Constellation Example. Earth and Space Science, 11(7):e2024EA003684.

Hsu, C. T., Matsuo, T., and Liu, J. Y. (2018a). Impact of Assimilating the FORMOSAT-3/COSMIC and FORMOSAT-7/COSMIC-2 RO Data on the Midlatitude and Low-Latitude Ionospheric Specification. Earth and Space Science, 5(12):875–890.

Hsu, C. T., Matsuo, T., Maute, A., Stoneback, R., and Lien, C. P. (2021a). Data-Driven Ensemble Modeling of Equatorial Ionospheric Electrodynamics: A Case Study During a Minor Storm Period Under Solar Minimum Conditions. Journal of Geophysical Research: Space Physics, 126(2):1–21.

Hsu, C. T., Matsuo, T., Wang, W., and Liu, J. Y. (2014). Effects of inferring unobserved thermospheric and ionospheric state variables by using an Ensemble Kalman Filter on global ionospheric specification and forecasting. Journal of Geophysical Research: Space Physics, 119(11):9256–9267.

Hsu, C. T., Matsuo, T., Yue, X., Fang, T. W., Fuller-Rowell, T., Ide, K., and Liu, J. Y. (2018b). Assessment of the Impact of FORMOSAT-7/COSMIC-2 GNSS RO Observations on Midlatitude and Low-Latitude Ionosphere Specification: Observing System Simulation Experiments Using Ensemble Square Root Filter. Journal of Geophysical Research: Space Physics, 123(3):2296–2314.

Hsu, C. T. and Pedatella, N. M. (2023). Effects of Forcing Uncertainties on the Thermospheric and Ionospheric States During Geomagnetic Storm and Quiet Periods. Space Weather, 21(4).

Hsu, C. T., Pedatella, N. M., and Anderson, J. L. (2021b). Impact of Thermospheric Wind Data Assimilation on Ionospheric Electrodynamics Using a Coupled Whole Atmosphere Data Assimilation System. Journal of Geophysical Research: Space Physics, 126(12):1–16.

Hsu, V. W., Thayer, J. P., Wang, W., and Burns, A. (2016). New insights into the complex interplay between drag forces and its thermospheric consequences. Journal of Geophysical Research: Space Physics, 121(10):10,417–10,430.

Huba, J. D., Joyce, G., and Krall, J. (2008). Three-dimensional equatorial spread F modeling. Geophysical Research Letters, 35(10).

Huba, J. D. and Liu, H. L. (2020). Global Modeling of Equatorial Spread F with SAMI3/WACCM-X. Geophysical Research Letters, 47(14):1–9.

Hunt, B. R., Kostelich, E. J., and Szunyogh, I. (2007). Efficient data assimilation for spatiotemporal chaos: A local ensemble transform Kalman filter. Physica D: Nonlinear Phenomena, 230(1-2):112–126.

Hwang, E. S., Castle, K. J., and Dodd, J. A. (2003). Vibrational relaxation of NO(v = 1) by oxygen atoms between 295 and 825 K. Journal of Geophysical Research: Space Physics, 108(A3).

Immel, T. J., England, S. L., Mende, S. B., Heelis, R. A., Englert, C. R., Edelstein, J., Frey, H. U., Korpela, E. J., Taylor, E. R., Craig, W. W., Harris, S. E., Bester, M., Bust, G. S., Crowley, G., Forbes, J. M., Gérard, J. C., Harlander, J. M., Huba, J. D., Hubert, B., Kamalabadi, F., Makela, J. J., Maute, A. I., Meier, R. R., Raftery, C., Rochus, P., Siegmund, O. H., Stephan, A. W., Swenson, G. R., Frey, S., Hysell, D. L., Saito, A., Rider, K. A., and Sirk, M. M. (2018). The Ionospheric Connection Explorer Mission: Mission Goals and Design. Space Science Reviews, 214(1):1–36.

Immel, T. J., Sagawa, E., England, S. L., Henderson, S. B., Hagan, M. E., Mende, S. B., Frey, H. U., Swenson, C. M., and Paxton, L. J. (2006). Control of equatorial ionospheric morphology by atmospheric tides. Geophysical Research Letters, 33(15):2–5.

Jacchia, L. G. (1981). Empirical models of the thermosphere and requirements for improvements. Advances in Space Research, 1(12):81–86.

Jee, G., Burns, A. G., Wang, W., Solomon, S. C., Schunk, R. W., Scherliess, L., Thompson, D. C., Sojka, J. J., and Zhu, L. (2007). Duration of an ionospheric data assimilation initialization of a coupled thermosphere-ionosphere model. Space Weather, 5(1):1–11.

Kanamitsu, M., Ebisuzaki, W., Woollen, J., Yang, S. K., Hnilo, J. J., Fiorino, M., and Potter, G. L. (2002). NCEP-DOE AMIP-II reanalysis (R-2). Bulletin of the American Meteorological Society, 83(11):1631–1644.

Kasprzak, W. T. (1969). Evidence for a helium flux in the lower thermosphere. Journal of Geophysical Research, 74(3):894–896.

Keating, G. M. and Prior, E. J. (1967). The distribution of helium and atomic oxygen in the lower exosphere. In Ann. Meeting of the Am. Geophys. Union.

Kelley, M. C. (2009). The Earth's ionosphere: Plasma physics and electrodynamics. Academic press.

Kelley, M. C., Wong, V. K., Aponte, N., Coker, C., Mannucci, A. J., and Komjathy, A. (2009). Comparison of COSMIC occultation-based electron density profiles and TIP observations with Arecibo incoherent scatter radar data. Radio Science, 44(4):n/a–n/a.

Kitagawa, G. (1996). Monte Carlo Filter and Smoother for Non-Gaussian Nonlinear State Space Models. Journal of Computational and Graphical Statistics, 5(1):1.

Knipp, D. J., Pette, D. V., Kilcommons, L. M., Isaacs, T. L., Cruz, A. A., Mlynczak, M. G., Hunt, L. A., and Lin, C. Y. (2017). Thermospheric nitric oxide response to shock-led storms. Space Weather, 15(2):325–342.

Knipp, D. J., Tobiska, W. K., and Emery, B. A. (2004). Direct and indirect thermospheric heating sources for solar cycles 21-23. Solar Physics, 224(1-2):495–505.

Kockarts, G. (1980). Nitric oxide cooling in the terrestrial thermosphere. Geophysical Research Letters, 7(2):137–140.

Kodikara, T., Zhang, K., Pedatella, N. M., and Borries, C. (2021). The Impact of Solar Activity on Forecasting the Upper Atmosphere via Assimilation of Electron Density Data. Space Weather, 19(5):e2020SW002660.

Kursinski, E. R., Hajj, G. A., Schofield, J. T., Linfield, R. P., and Hardy, K. R. (1997). Observing Earth's atmosphere with radio occultation measurements using the global positioning system. Journal of Geophysical Research Atmospheres, 102(19):23429–23465.

Lee, I.-T. (2013). Assimilation of radio occultation data observed by FORMOSAT-3/COSMIC into a coupled Thermosphere/Ionosphere model. PhD thesis, National Central Univ., Zhongli, Taoyuan, Taiwan.

Lee, I. T., Matsuo, T., Richmond, A. D., Liu, J. Y., Wang, W., Lin, C. H., Anderson, J. L., and Chen, M. Q. (2012). Assimilation of FORMOSAT-3/COSMIC electron density profiles into a coupled thermosphere/ionosphere model using ensemble Kalman filtering. Journal of Geophysical Research: Space Physics, 117(10):1–11.

Lee, I. T., Tsai, H. F., Liu, J. Y., Lin, C. H., Matsuo, T., and Chang, L. C. (2013). Modeling impact of FORMOSAT-7/COSMIC-2 mission on ionospheric space weather monitoring. Journal of Geophysical Research: Space Physics, 118(10):6518–6523.

Lei, J., Syndergaard, S., Burns, A. G., Solomon, S. C., Wang, W., Zeng, Z., Roble, R. G., Wu, Q., Kuo, Y. H., Holt, J. M., Zhang, S. R., Hysell, D. L., Rodrigues, F. S., and Lin, C. H. (2007). Comparison of COSMIC ionospheric measurements with ground-based observations and model predictions: Preliminary results. Journal of Geophysical Research: Space Physics, 112(7):1–10.

Lei, J., Thayer, J. P., Burns, A. G., Lu, G., and Deng, Y. (2010). Wind and temperature effects on thermosphere mass density response to the November 2004 geomagnetic storm. Journal of Geophysical Research: Space Physics, 115(5):1–18.

Lei, J., Thayer, J. P., Lu, G., Burns, A. G., Wang, W., Sutton, E. K., and Emery, B. A. (2011). Rapid recovery of thermosphere density during the October 2003 geomagnetic storms. Journal of Geophysical Research: Space Physics, 116(3):1–10.

Li, Z., Knipp, D., and Wang, W. (2019). Understanding the Behaviors of Thermospheric Nitric Oxide Cooling During the 15 May 2005 Geomagnetic Storm. Journal of Geophysical Research: Space Physics, 124(3):2113–2126.

Li, Z., Knipp, D., Wang, W., Sheng, C., Qian, L., and Flynn, S. (2018). A Comparison Study of NO Cooling Between TIMED/SABER Measurements and TIEGCM Simulations. Journal of Geophysical Research: Space Physics, 123(10):8714–8729.

Licata, R. J., Mehta, P. M., Weimer, D. R., Drob, D. P., Tobiska, W. K., and Yoshii, J. (2022). Science Through Machine Learning: Quantification of Post-Storm Thermospheric Cooling. Space Weather, 20(9).

Lin, C. Y., Lin, C. C. H., Liu, J. Y., Rajesh, P. K., Matsuo, T., Chou, M. Y., Tsai, H. F., and Yeh, W. H. (2020). The Early Results and Validation of FORMOSAT-7/COSMIC-2 Space Weather Products: Global Ionospheric Specification and Ne-Aided Abel Electron Density Profile. Journal of Geophysical Research: Space Physics, 125(10):1–12.

Lin, C. Y., Matsuo, T., Liu, J. Y., Lin, C. H., Huba, J. D., Tsai, H. F., and Chen, C. Y. (2017). Data Assimilation of Ground-Based GPS and Radio Occultation Total Electron Content for Global Ionospheric Specification. Journal of Geophysical Research: Space Physics, 122(10):10,876–10,886.

Lin, C. Y., Matsuo, T., Liu, J. Y., Lin, C. H., Tsai, H. F., and Araujo-Pradere, E. A. (2015). Ionospheric assimilation of radio occultation and ground-based GPS data using non-stationary background model error covariance. Atmospheric Measurement Techniques, 8(1):171–182.

Liu, H. and Lühr, H. (2005). Strong disturbance of the upper thermospheric density due to magnetic storms: CHAMP observations. Journal of Geophysical Research: Space Physics, 110(A9):1–9.

Liu, H. L. (2016). Variability and predictability of the space environment as related to lower atmosphere forcing. Space Weather, 14(9):634–658.

Liu, J. Y., Lin, C. Y., Lin, C. H., Tsai, H. F., Solomon, S. C., Sun, Y. Y., Lee, I. T., Schreiner, W. S., and Kuo, Y. H. (2010). Artificial plasma cave in the low-latitude ionosphere results from the radio occultation inversion of the FORMOSAT-3/COSMIC. Journal of Geophysical Research: Space Physics, 115(7):1–8.

Liu, X., Thayer, J. P., Burns, A., Wang, W., and Sutton, E. (2014). Altitude variations in the thermosphere mass density response to geomagnetic activity during the recent solar minimum. Journal of Geophysical Research: Space Physics, 119:2160–2177.

Lomidze, L., Knudsen, D. J., Shepherd, M., Huba, J. D., and Maute, A. (2023). Equinoctial Asymmetry in the Upper Ionosphere: Comparison of Satellite Observations and Models. Journal of Geophysical Research: Space Physics, 128(5).

Lu, G. (2017). Large Scale High-Latitude Ionospheric Electrodynamic Fields and Currents. Space Science Reviews, 206(1-4):431–450.

Lu, G., Hagan, M. E., Häusler, K., Doornbos, E., Bruinsma, S., Anderson, B. J., and Korth, H. (2014). Global ionospheric and thermospheric response to the 5 April 2010 geomagnetic storm: An integrated data-model investigation. Journal of Geophysical Research: Space Physics, 119(12):10,358–10,375.

Lu, G., Mlynczak, M. G., Hunt, L. A., Woods, T. N., and Roble, R. G. (2010). On the relationship of Joule heating and nitric oxide radiative cooling in the thermosphere. Journal of Geophysical Research: Space Physics, 115(5).

Lugaz, N. (2020). PROSWIFT Bill and the 2020 Space Weather Operations and Research Infrastructure Workshop From the National Academies of Sciences, Engineering, and Medicine. Space Weather, 18(10):e2020SW002628.

Maeda, S., Fuller-Rowell, T. J., and Evans, D. S. (1992). Heat budget of the thermosphere and temperature variations during the recovery phase of a geomagnetic storm. Journal of Geophysical Research: Space Physics, 97(A10):14947–14957.

March, G., Van Den Ijssel, J., Siemes, C., Visser, P. N., Doornbos, E. N., and Pilinski, M. (2021). Gas-surface interactions modelling influence on satellite aerodynamics and thermosphere mass density. Journal of Space Weather and Space Climate, 11.

Maruyama, N., Sun, Y. Y., Richards, P. G., Middlecoff, J., Fang, T. W., Fuller-Rowell, T. J., Akmaev, R. A., Liu, J. Y., and Valladares, C. E. (2016). A new source of the midlatitude ionospheric peak density structure revealed by a new Ionosphere-Plasmasphere model. Geophysical Research Letters, 43(6):2429–2435.

Masutani, M., Andersson, E., Terry, J., Reale, O., Jusem, J. C., Riishojgaard, L. P., Schlatter, T., Stoffelen, A., Woollen, J., Lord, S., and Others (2007). Progress in Joint OSSEs A new nature run and international collaboration. In Proceedings of the 12th Conference on Integrated Observing and Assimilation Systems for Atmospheres, Oceans, and Land Surface (IOAS-AOLS).

Matsuo, T. and Araujo-Pradere, E. A. (2011). Role of thermosphere-ionosphere coupling in a global ionospheric specification. Radio Science, 46(6):1–7.

Matsuo, T. and Hsu, C. T. (2021). Inference of Hidden States by Coupled Thermosphere-Ionosphere Data Assimilation: Applications to Observability and Predictability of Neutral Mass Density. Space Physics and Aeronomy, Upper Atmosphere Dynamics and Energetics, pages 343–363.

Matsuo, T., Kilcommons, L. M., Mirkovich, W., Ruohoniemi, J., Chakraborty, S., Anderson, B., and Vines, S. (2020). Assimilative Mapping of Geospace Observations (AMGeO): Unified Global and Local Perspectives on High-latitude Ionospheric Electrodynamics. In AGU Fall Meeting Abstracts, volume 2020, pages SA026–03.

Matsuo, T., Lee, I. T., and Anderson, J. L. (2013). Thermospheric mass density specification using an ensemble Kalman filter. Journal of Geophysical Research: Space Physics, 118(3):1339–1350.

Mehta, P. M., Walker, A. C., Sutton, E. K., and Godinez, H. C. (2017). New density estimates derived using accelerometers on board the CHAMP and GRACE satellites. Space Weather, 15(4):558–576.

Meier, R. R. (2021). The Thermospheric Column O/N2 Ratio. Journal of Geophysical Research: Space Physics, 126(3):1–12.

Mikhailov, A. and Schlegel, K. (1997). Self-consistent modelling of the daytime electron density profile in the ionospheric F region. Annales Geophysicae, 15(3):314–326.

Minter, C. F., Fuller-Rowell, T. J., and Codrescu, M. V. (2004). Estimating the state of the thermospheric composition using Kalman filtering. Space Weather, 2(4).

Mlynczak, M., Martin-Torres, F. J., Rusell, J., Beaumont, K., Jacobson, S., Kozyra, J., Lopez-Puertas, M., Funke, B., Mertens, C., Gordley, L., Picard, R., Winick, J., Wintersteiner, P., and Paxton, L. (2003). The natural thermostat of nitric oxide emission at 5.3 μm in the thermosphere observed during the solar storms of April 2002. Geophysical Research Letters, 30(21):3–7.

Mlynczak, M. G. (1997). Energetics of the mesosphere and lower thermosphere and the saber experiment. Advances in Space Research, 20(6):1177–1183.

Moreno, B., Radicella, S., de Lacy, M. C., Herraiz, M., and Rodriguez-Caderot, G. (2011). On the effects of the ionospheric disturbances on precise point positioning at equatorial latitudes. GPS Solutions, 15(4):381–390.

Morozov, A. V., Ridley, A. J., Bernstein, D. S., Collins, N., Hoar, T. J., and Anderson, J. L. (2013). Data assimilation and driver estimation for the Global Ionosphere-Thermosphere Model using the Ensemble Adjustment Kalman Filter. Journal of Atmospheric and Solar-Terrestrial Physics, 104:126–136.

Murphy, R. E., Lee, E. T., and Hart, A. M. (1975). Quenching of vibrationally excited nitric oxide by molecular oxygen and nitrogen. The Journal of Chemical Physics, 63(7):2919–2925.

NASA (2020). NASA Debris Mitigation. Technical report, NASA.

Oberheide, J., Hagan, M. E., Richmond, A. D., and Forbes, J. M. (2015). Dynamical Meteorology: Atmospheric Tides, volume 2. Elsevier, second edi edition.

Pedatella, N. M., Anderson, J. L., Chen, C. H., Raeder, K., Liu, J., Liu, H. L., and Lin, C. H. (2020). Assimilation of Ionosphere Observations in the Whole Atmosphere Community Climate Model with Thermosphere-Ionosphere EXtension (WACCMX). Journal of Geophysical Research: Space Physics, 125(9):1–15.

Pedatella, N. M., Liu, H. L., Marsh, D. R., Raeder, K., Anderson, J. L., Chau, J. L., Goncharenko, L. P., and Siddiqui, T. A. (2018). Analysis and Hindcast Experiments of the 2009 Sudden Stratospheric Warming in WACCMX+DART. Journal of Geophysical Research: Space Physics, 123(4):3131–3153.

Pedatella, N. M., Raeder, K., Anderson, J. L., and Liu, H. L. (2014). Ensemble data assimilation in the Whole Atmosphere Community Climate Model. Journal of Geophysical Research: Atmospheres, 119(16):9793–9809.

Pedatella, N. M., Yue, X., and Schreiner, W. S. (2015). An improved inversion for FORMOSAT-3 / COSMIC. Journal of Geophysical Research : Space Physics, pages 8942–8953.

Pelz, D. T., Reber, C. A., Hedin, A. E., and Carignan, G. R. (1973). A neutral-atmosphere composition experiment for the Atmosphere Explorer-C, -D, and -E. Radio Science, 8(4):277–285.

Pham, K. H., Zhang, B., Sorathia, K., Dang, T., Wang, W., Merkin, V., Liu, H., Lin, D., Wiltberger, M., Lei, J., Bao, S., Garretson, J., Toffoletto, F., Michael, A., and Lyon, J. (2022). Thermospheric Density Perturbations Produced by Traveling Atmospheric Disturbances During August 2005 Storm. Journal of Geophysical Research: Space Physics, 127(2):1–14.

Picone, J. M., Hedin, A. E., Drob, D. P., and Aikin, A. C. (2002). NRLMSISE-00 empirical model of the atmosphere: Statistical comparisons and scientific issues. Journal of Geophysical Research: Space Physics, 107(A12):SIA—-15.

Pilinski, M. D. (2011). Dynamic Gas-Surface Interaction Modeling for Satellite Aerodynamic Computations. PhD thesis, University of Colorado at Boulder.

Poterjoy, J., Wicker, L., and Buehner, M. (2019). Progress toward the application of a localized particle filter for numerical weather prediction. Monthly Weather Review, 147(4):1107–1126.

Prölss, G. (2012). Physics of the Earth's space environment: an introduction. Springer Science & Business Media.

Prölss, G. W. (1987). Storm-induced changes in the thermospheric composition at middle latitudes. Planetary and space science, 35(6):807–811.

Prölss, G. W. (1996). Magnetic storm associated perturbations of the upper atmosphere. Geophysical Monograph Series, 98(1):227–241.

Prölss, G. W. (2011). Density Perturbations in the Upper Atmosphere Caused by the Dissipation of Solar Wind Energy. Surveys in Geophysics, 32(2):101–195.

Qian, L., Burns, A. G., Emery, B. A., Foster, B., Lu, G., Maute, A., Richmond, A. D., Roble, R. G., Solomon, S. C., and Wang, W. (2014). The NCAR TIE-GCM: A community model of the coupled thermosphere/ionosphere system. Modeling the ionosphere–thermosphere system, 201:73–83.

Rajesh, P. K., Lin, C. C., Lin, J. T., Lin, C. Y., Yue, J., Matsuo, T., Chen, S. P., and Chen, C. H. (2021). Day-to-day Variability of Ionosphere Electron Density During Solar Minimum Derived from FORMOSAT-7/COSMIC-2 Measurements. Terrestrial, Atmospheric and Oceanic Sciences, 32(6):959–975.

Ray, V. (2021). Advances in atmospheric drag force modeling for satellite orbit prediction and density estimation. PhD thesis, University of Colorado at Boulder.

Ray, V., Scheeres, D. J., Alnaqbi, S., Tobiska, W. K., and Hesar, S. G. (2022). A Framework to Estimate Local Atmospheric Densities With Reduced Drag-Coefficient Biases. Space Weather, 20(3).

Reber, C. A., Harpold, D. N., Horowitz, R., and Hedin, A. E. (1971). Horizontal distribution of helium in the Earth's upper atmosphere. Journal of Geophysical Research, 76(7):1845–1848.

Reid, B., Themens, D. R., McCaffrey, A., Jayachandran, P. T., Johnsen, M. G., and Ulich, T. (2023). A-CHAIM: Near-Real-Time Data Assimilation of the High Latitude Ionosphere With a Particle Filter. Space Weather, 21(3):1–26.

Richmond, A. D. (1995). Ionospheric Electrodynamics Using Magnetic Apex Coordinates. Journal of geomagnetism and geoelectricity, 47(2):191–212.

Richmond, A. D. and Kamide, Y. (1988). Mapping electrodynamic features of the high-latitude ionosphere from localized observations: Technique. Journal of Geophysical Research: Space Physics, 93(A6):5741–5759.

Richmond, A. D., Ridley, E. C., and Roble, R. G. (1992). A thermosphere/ionosphere general circulation model with coupled electrodynamics. Geophysical Research Letters, 19(6):601–604.

Rienecker, M. M., Suarez, M. J., Gelaro, R., Todling, R., Bacmeister, J., Liu, E., Bosilovich, M. G., Schubert, S. D., Takacs, L., Kim, G. K., Bloom, S., Chen, J., Collins, D., Conaty, A., Da Silva, A., Gu, W., Joiner, J., Koster, R. D., Lucchesi, R., Molod, A., Owens, T., Pawson, S., Pegion, P., Redder, C. R., Reichle, R., Robertson, F. R., Ruddick, A. G., Sienkiewicz, M., and Woollen, J. (2011). MERRA: NASA's modern-era retrospective analysis for research and applications. Journal of Climate, 24(14):3624–3648.

Rishbeth, H., Fuller-Rowell, T. J., and Rees, D. (1987). Diffusive equilibrium and vertical motion in the thermosphere during a severe magnetic storm : A computational study. Planetary and Space Science, 35(9):1157–1165.

Robie, R. G. (1993). Energetics of the Mesosphere and Thermosphere. The upper mesosphere and lower thermosphere: a review of experiment and theory, 87:1–21.

Sassi, F., McCormack, J. P., and McDonald, S. E. (2019). Whole Atmosphere Coupling on Intraseasonal and Interseasonal Time Scales: A Potential Source of Increased Predictive Capability. Radio Science, 54(11):913–933.

Scherliess, L., Schunk, R. W., Sojka, J. J., and Thompson, D. C. (2004). Development of a physics-based reduced state Kalman filter for the ionosphere. Radio Science, 39(1):231–242.

Scherliess, L., Schunk, R. W., Sojka, J. J., Thompson, D. C., and Zhu, L. (2006). Utah State University Global Assimilation of Ionospheric Measurements Gauss-Markov Kalman filter model of the ionosphere: Model description and validation. Journal of Geophysical Research: Space Physics, 111(11).

Schunk, R. and Nagy, A. (2009). Ionospheres: physics, plasma physics, and chemistry. Cambridge university press.

Schunk, R. W., Scherliess, L., Sojka, J. J., Thompson, D. C., and Zhu, L. (2005). Ionospheric weatner forecasting on the horizon. Space Weather, 3(1):24–27.

Sheng, C., Lu, G., Solomon, S. C., Wang, W., Doornbos, E., Hunt, L. A., and Mlynczak, M. G. (2017). Thermospheric recovery during the 5 April 2010 geomagnetic storm. Journal of Geophysical Research: Space Physics, 122(4):4588–4599.

Smith, A. K., Pedatella, N. M., Marsh, D. R., and Matsuo, T. (2017). On the Dynamical Control of the Mesosphere–Lower Thermosphere by the Lower and Middle Atmosphere. Journal of the Atmospheric Sciences, 74(3):933–947.

Snyder, C., Bengtsson, T., Bickel, P., and Anderson, J. (2008). Obstacles to high-dimensional particle filtering. Monthly Weather Review, 136(12):4629–4640.

Solomon, S. C. and Qian, L. (2005). Solar extreme-ultraviolet irradiance for general circulation models. Journal of Geophysical Research: Space Physics, 110(A10):1–14.

Storz, M. F., Bowman, B. R., Branson, J. I., Casali, S. J., and Tobiska, W. K. (2005). High accuracy satellite drag model (HASDM). Advances in Space Research, 36(12):2497–2505.

Sutton, E. K. (2016). Interhemispheric transport of light neutral species in the thermosphere. Geophysical Research Letters, 43(24):12,325–12,332.

Sutton, E. K. (2018). A New Method of Physics-Based Data Assimilation for the Quiet and Disturbed Thermosphere. Space Weather, 16(6):736–753.

Sutton, E. K., Nerem, R. S., and Forbes, J. M. (2007). Density and winds in the thermosphere deduced from accelerometer data. Journal of Spacecraft and Rockets, 44(6):1210–1219.

Sutton, E. K., Thayer, J. P., Pilinski, M. D., Mutschler, S. M., Berger, T. E., Nguyen, V., and Masters, D. (2021). Toward Accurate Physics-Based Specifications of Neutral Density Using GNSS-Enabled Small Satellites. Space Weather, 19(6):1–15.

Sutton, E. K., Thayer, J. P., Wang, W., Solomon, S. C., Liu, X., and Foster, B. T. (2015). A self-consistent model of helium in the thermosphere. Journal of Geophysical Research: Space Physics, 120(8):6884–6900.

Tapping, K. F. (2013). The 10.7 cm solar radio flux (F10.7). Space Weather, 11(7):394–406.

Thayer, J. P., Liu, X., Lei, J., Pilinski, M., and Burns, A. G. (2012). The impact of helium on thermosphere mass density response to geomagnetic activity during the recent solar minimum. Journal of Geophysical Research: Space Physics, 117(7):1–14.

Thayer, J. P. and Semeter, J. (2004). The convergence of magnetospheric energy flux in the polar atmosphere. Journal of Atmospheric and Solar-Terrestrial Physics, 66(10):807–824.

Thayer, J. P., Waldron, Z. C., and Sutton, E. K. (2023). Solar Flux Dependence of Upper Thermosphere Diurnal Variations: Observed and Modeled. Journal of Geophysical Research: Space Physics, 128(2).

Thiemann, E. M. and Dominique, M. (2021). PROBA2 LYRA Occultations: Thermospheric Temperature and Composition, Sensitivity to EUV Forcing, and Comparisons With Mars. Journal of Geophysical Research: Space Physics, 126(7):1–15.

Thiemann, E. M., Dominique, M., Pilinski, M. D., and Eparvier, F. G. (2017). Vertical Thermospheric Density Profiles From EUV Solar Occultations Made by PROBA2 LYRA for Solar Cycle 24. Space Weather, 15(12):1649–1660.

Tippett, M. K., Anderson, J. L., Bishop, C. H., Hamill, T. M., and Whitaker, J. S. (2003). Ensemble square root filters. Monthly Weather Review, 131(7):1485–1490.

Tobiska, W. K., Bowman, B. R., Bouwer, S. D., Cruz, A., Wahl, K., Pilinski, M. D., Mehta, P. M., and Licata, R. J. (2021). The SET HASDM Density Database. Space Weather, 19(4):1–4.

Tsai, L. C., Liu, J. Y., Schreiner, W. S., and Berkey, F. T. (2001). Comparisons of GPS/MET retrieved ionospheric electron density and ground based ionosonde data. Earth, Planets and Space, 53(3):193–205.

Tsai, L. C. and Tsai, W. H. (2004). Improvement of GPS/MET ionospheric profiling and validation using the Chung-Li ionosonde measurements and the IRI model. Terrestrial, Atmospheric and Oceanic Sciences, 15(4):589–607.

Tulasi Ram, S., Su, S. Y., Tsai, L. C., and Liu, C. H. (2016). A self-contained GIM-aided Abel retrieval method to improve GNSS-Radio Occultation retrieved electron density profiles. GPS Solutions, 20(4):825–836.

van den IJssel, J., Doornbos, E., Iorfida, E., March, G., Siemes, C., and Montenbruck, O. (2020). Thermosphere densities derived from Swarm GPS observations. Advances in Space Research, 65(7):1758–1771.

Van Leeuwen, P. J. (2009). Particle filtering in geophysical systems. Monthly Weather Review, 137(12):4089–4114.

Van Leeuwen, P. J. (2010). Nonlinear data assimilation in geosciences: An extremely efficient particle filter. Quarterly Journal of the Royal Meteorological Society, 136(653):1991–1999.

van Leeuwen, P. J., Künsch, H. R., Nerger, L., Potthast, R., and Reich, S. (2019). Particle filters for high-dimensional geoscience applications: A review.

Vourlidas, A., Turner, D., Biesecker, D., Coster, A., Engell, A., Ho, G., Immel, T., Keys, C., Lanzerotti, L., Lu, G., Lugaz, N., Luhmann, J., Leila Mays, M., O'Brien, P., Semones, E., Spence, H., Upton, L., White, S., and Spann, J. (2023). The NASA space weather science and observation gap analysis. Advances in Space Research.

Waldron, Z. C. (2020). Investigation of the Day-to-Night Ratio in the Thermosphere Mass Density. Master's thesis, University of Colorado Boulder.

Wang, C., Hajj, G., Pi, X., Rosen, I. G., and Wilson, B. (2004). Development of the Global Assimilative Ionospheric Model. Radio Science, 39(1):260–270.

Wang, N., Mlynczak, M. G., Emmert, J. T., López-Puertas, M., and Funke, B. (2024). Nitric Oxide Concentration: A New Data Set Derived From SABER Measurements. Earth and Space Science, 11(5).

Weimer, D. R. (2005). Improved ionospheric electrodynamic models and application to calculating Joule heating rates. Journal of Geophysical Research: Space Physics, 110(A5):1–21.

Whitaker, J. S. and Hamill, T. M. (2002). Ensemble data assimilation without perturbed observations. Monthly Weather Review, 130(7):1913–1924.

Wu, D. L. (2018). New global electron density observations from GPS-RO in the D- and E-Region ionosphere. Journal of Atmospheric and Solar-Terrestrial Physics, 171:36–59.

Wu, M. J., Guo, P., Fu, N. F., Hu, X. G., and Hong, Z. J. (2018). Improvement of the IRI Model Using F2 Layer Parameters Derived From GPS/COSMIC Radio Occultation Observations. Journal of Geophysical Research: Space Physics, 123(11):9815–9835.

Yue, X., Schreiner, W. S., and Kuo, Y. H. (2012). A feasibility study of the radio occultation electron density retrieval aided by a global ionospheric data assimilation model. Journal of Geophysical Research: Space Physics, 117(8):1–9.

Yue, X., Schreiner, W. S., and Kuo, Y. H. (2013a). Evaluating the effect of the global ionospheric map on aiding retrieval of radio occultation electron density profiles. GPS Solutions, 17(3):327–335.

Yue, X., Schreiner, W. S., Kuo, Y. H., Braun, J. J., Lin, Y. C., and Wan, W. (2014a). Observing system simulation experiment study on imaging the ionosphere by assimilating observations from ground GNSS, LEO-based radio occultation and ocean reflection, and cross link. IEEE Transactions on Geoscience and Remote Sensing, 52(7):3759–3773.

Yue, X., Schreiner, W. S., Kuo, Y. H., Wu, Q., Deng, Y., and Wang, W. (2013b). GNSS radio occultation (RO) derived electron density quality in high latitude and polar region: NCAR-TIEGCM simulation and real data evaluation. Journal of Atmospheric and Solar-Terrestrial Physics, 98:39–49.

Yue, X., Schreiner, W. S., Lei, J., Sokolovskiy, S. V., Rocken, C., Hunt, D. C., and Kuo, Y. H. (2010). Error analysis of abel retrieved electron density profiles from radio occultation measurements. Annales Geophysicae, 28(1):217–222.

Yue, X., Schreiner, W. S., Pedatella, N., Anthes, R. A., Mannucci, A. J., Straus, P. R., and Liu, J. Y. (2014b). Space weather observations by GNSS radio occultation: From FORMOSAT-3/COSMIC to FORMOSAT-7/COSMIC-2. Space Weather, 12(11):616–621.

Zesta, E. and Oliveira, D. M. (2019). Thermospheric Heating and Cooling Times During Geomagnetic Storms, Including Extreme Events. Geophysical Research Letters, 46(22):12739–12746.

Zhang, S., Wu, X., and Hu, X. (2023). Ionospheric Vertical Correlation Distance Calculation Based on COSMIC Electron Density Profile Data. Journal of Geophysical Research: Space Physics, 128(7):e2023JA031453.

Appendix A

Glossary

LEO – low Earth orbit
SDA – space domain awareness
TLE – two-line element
$\mathbf{a}_{drag}$ – atmospheric drag force
$\boldsymbol{C_D}$ – drag coefficient

I-T – ionosphere-thermosphere
$\boldsymbol{\rho}$ – neutral mass density (or neutral density)
$\boldsymbol{e^-}$ – electron density
$\boldsymbol{O^+}$ – atomic oxygen ion density
Tn – neutral temperature
UN – zonal wind (east-west)
VN – meridional wind (north-south)
He – helium composition
NO – nitric oxide

F10.7 index – daily index proxy for solar ultraviolet radiation at the 10.7 cm wavelength
Kp index – geomagnetic activity index on a quasi-logarithmic scale.
Kp values greater than 4 indicates a geomagnetic storm
Ap index – geomagnetic activity index equivalent to the Kp index on a linear scale
HP – hemispheric power
Φ – cross-tail potential
SYM-H / Dst – geomagnetic activity indices
IMF – interplanetary magnetic field

GNSS – global navigation satellite system
RO – radio occulation(s)
EDP – electron density profile
EIA – equatorial ionization anomaly
$\mathbf{N}_m\mathbf{F}_2$ – peak electron density of F2 layer
$\mathbf{h}_m\mathbf{F}_2$ – height of peak electron density of F2 layer

TEC – total electron content
sTEC – slant total electron content

COSMIC-1/2 (F3/F7) – Constellation Observing System for Meteorology, Ionosphere, and Climate - 1/2 (FORMOSAT3/FORMOSAT-7)
GRACE-FO – Gravity Recovery and Climate Experiment Follow-On
CHAMP – CHAllenging Minisatellite Payload
TIMED-SABER – Thermosphere Ionosphere Mesosphere Energetics and Dynamics - Sounding of the Atmosphere using Broadband Emission Radiometry

GCM – general circulation model
TIEGCM – thermosphere ionosphere electrodynamics general circulation model
WAM-IPE – whole atmosphere model - ionosphere plasmasphere electrodynamics
GSWM – global scale wave model

DA – data assimilation
PDF – probability distribution function
EnKF – ensemble Kalman filter
EAKF – ensemble adjustment Kalman filter
DART – data assimilation research testbed
PF – particle filter
OSE – observing system experiment
OSSE – observing system simulation experiment
GC – Gaspari-Cohn

RMSE – root mean square error
UT – universal time

Appendix B

Control and Experiment Ensemble Configurations for Data Assimilation Experiment Runs

This appendix contains the control and experiment run configurations used in each Chapter's data assimilation experiments. Data assimilation performance in OSSE and OSE frameworks is assessed against a control ensemble identical to the experiment ensemble but without data assimilation. Each experiment ensemble is initialized with a spin-up period for $7-15$ days to reach a steady state from model input forcing. The thesis uses the TIEGCM developed by NCAR HAO as the I-T experiment model, with model and documentation available from `https://www.hao.ucar.edu/modeling/tgcm/tie.php`. The TIEGCM v2.0 is used. EAKF is developed by NCAR DART and available from `http://dart.ucar.edu` for the Lanai and Manhattan versions. A tutorial for DART is available here: `https://dart.ucar.edu/tutorials/`. The Whole Atmosphere Model Ionosphere Plasmasphere Electrodynamics (WAM-IPE) software was developed by the NOAA Space Weather Prediction Center and is available from https://github.com/CU-SWQU/GSMWAM-IPE. In-line matrices are defined using the following column stack notation:

$$\left[\boldsymbol{a};\boldsymbol{b}\right] = \begin{bmatrix}\boldsymbol{a}\\ \boldsymbol{b}\end{bmatrix} \tag{B.1}$$

B.1 Chapter 2 Runs

The experiment period for the results for this chapter spans the St. Patrick's Day storm of 2015, from March 13th - March 18th. RO EDP observations are retrieved from the WAM-IPE truth run and assimilated into TIEGCM to update plasma states. Experiment configurations are listed in Tables B.1 and B.2.

B.2 Chapter 3 Runs

The experiment period is June 23rd - 24th, 2008. RO EDP observations are retrieved from the TIEGCM truth run and assimilated into TIEGCM to update neutral and plasma states in a strongly coupled framework. Experiment configurations are listed in Tables B.3 and B.4.

B.3 Chapter 4 Runs

The experiment period is July 5th - July 10th, 2022 including a geomagnetic storm on July 7th. COSMIC-2 EDPs are assimilated into TIEGCM to update neutral temperature and plasma states in a strongly coupled DA framework. Experiment configurations are listed in Tables B.5 and B.6. Ensembles are initialized through external forcing perturbations, and details for how solar irradiance, magnetospheric forcing, and lower boundary conditions were perturbed are as follows.

Solar irradiance spread, illustrated in the top panel of Figure 4.1, is added through F10.7 index perturbations using the daily observed value, $d_{F10.7}$, as the mean and is sampled from a time-correlated multivariate Gaussian distribution, $\hat{d}_{F10.7d} \sim \mathcal{N}(d_{F10.7}, 20^2)$. Correlations are defined in time by an exponential function with a scale parameter of 27 days. The F10.7 index is the most influential forcing parameter for introducing state spread and adjusting biases, as also found in Hsu et al. (2021a). TIEGCM additionally uses $\hat{d}_{F10.7a}$ as input, defined as the 81-day average of $\hat{d}_{F10.7d}$.

Table B.1: Ensemble configuration for the Chapter 2 experiment runs

	Truth Run	**Experiment Ensemble**
Model (if applicable)	WAM-IPE	TIEGCM
Model Resolution	2-deg (spectral output)	5-deg
Model Altitude Span	*WAM*: 0 km to $\sim 500-600$ km *IPE*: 90 km to $10,000$ km	$\sim$ 97 km to $\sim$ 500$-$600 km
Solar Irradiance	Daily observed F10.7 index Period range: $110-125$	Constant F10.7 index $d_{F10.7} \sim \mathcal{N}(120, 4^2)$
Magnetospheric Forcing	Weimer forcing specified with input solar wind parameters	Constant Heelis forcing specified with hemispheric power HP and cross-tail potential (Φ) *Quiet period*: $d_{HP} \sim \mathcal{N}(22, 4^2)$, $d_{\Phi} \sim \mathcal{N}(46, 8^2)$ *Storm period*: $d_{HP} \sim \mathcal{N}(115, 10^2)$, $d_{\Phi} \sim \mathcal{N}(135, 20^2)$
Lower Boundary	Free-run from lower atmosphere	GSWM input $\sim$ 97 km
Ensemble Size	1	90

Table B.2: Filter configuration for the Chapter 2 experiment runs

Filter Configuration	
Filter	DART EAKF (Lanai version)
Assimilated Observations	Abel inverted synthetic RO EDPs Retrieved from four RO s
Localization	Horizontal: 0.2-radian radius GC No vertical localization
Update Cycle	1-hour
Observation Altitude Span	$160-500$ km at 10 km intervals
Observation Uncertainty	Calculated against WAM-IPE truth
Updated State Vector	$[\boldsymbol{f}_{e^-}; \boldsymbol{f}_{O^+}]$

Table B.3: Ensemble configuration for the Chapter 3 experiment runs

	Truth Run	**Experiment Ensemble**
Model (if applicable)	TIEGCM	TIEGCM
Model Resolution	5-deg	5-deg
Model Altitude Span	~ 97 km to $\sim 500-600$ km	~ 97 km to $\sim 500-600$ km
Solar Irradiance	Constant F10.7 index $d_{F10.7} = 74$	Constant F10.7 index $d_{F10.7} \sim \mathcal{N}(69, 5^2)$
Magnetospheric Forcing	Constant Heelis forcing specified with hemispheric power (HP) and cross-tail potential (Φ) $d_{HP} = 55$, $d_{\Phi} = 18$	Heelis forcing specified with constant HP and Φ $d_{HP} \sim \mathcal{N}(45, 10^2)$, $d_{\Phi} \sim \mathcal{N}(16, 2^2)$
Lower Boundary	GSWM input ~ 97 km	GSWM input ~ 97 km
Ensemble Size	1	90

Table B.4: Filter configuration for the Chapter 3 experiment runs

Filter Configuration	
Filter	DART EAKF (Lanai version)
Assimilated Observations	Directly sampled and perturbed synthetic RO EDPs Sampled at COSMIC-1 RO tangent points
Localization	Horizontal: 0.2-radian radius GC No vertical localization
Update Cycle	1-hour
Observation Altitude Span	$160-450$ km at 10 km intervals
Observation Uncertainty	Linear dependence in altitude: $1\ std = 3\times10^5 - \lvert(0.105\times alt[m] - 3\times10^5)\rvert$ $[\#/cm^3]$
Updated State Vector	$[\boldsymbol{f}_{e^-}; \boldsymbol{f}_{O^+}; \boldsymbol{f}_{TN}; \boldsymbol{f}_{UN}; \boldsymbol{f}_{VN}]$

Samples of solar wind IMF parameters are illustrated in Figure 4.1. These parameters are sampled from a time-correlated, multivariate Student's t-distribution, defined as $t(\mu, \sigma^2, \nu)$, where μ is the mean, σ^2 is the variance and ν is the degrees of freedom. The t-distribution is chosen to represent the heavy-tail distribution of solar wind parameters. Correlations are defined in time by an exponential function with a scale parameter of 2 days. We perturb the B-field, B_{sw}, solar wind velocity, V_{sw}, and density n_{sw}, where for each state is sampled from $\widehat{SW} = t\big(\bar{SW}_{obs}, (\sigma_{daily} + \sigma_{SW-scale})^2, 2.1\big)$. Observed solar wind parameters from the ACE satellite at Earth's L1 point (NASA OMNIWeb) are used as the mean, $\bar{SW}_{obs}$, and to calculate the variances: $\sigma^2_{B-scale} = 0.88$ nT, $\sigma^2_{V-scale} = 2.41$ km/s, $\sigma^2_{n-scale} = 0.16$ #/cm^3. An additional daily variance is added, σ^2_{daily}, and is scaled by 0.2. A few noted details are as follows: only the IMF B-field magnitude is perturbed, retaining constant relative B_x, B_y, and B_z components; parameters are kept > 0 to avoid negative values; IMF parameters for TIEGCM input have 1-minute frequency, and back-smoothed by 10-minutes. These solar wind perturbations have little impact on state spreads during the quiet period but greatly benefit storm-time state spreads.

For lower boundary perturbations, we only perturb the amplitudes for the migrating diurnal and semidiurnal tides, sampled from $\hat{A}_{mig} = \mathcal{N}(A_{mig}, (0.5 \times \sigma_{Amig})^2)$, where A_{mig} is the tidal amplitude, and σ^2_{Amig} is the longitudinal tidal amplitude variance. Added perturbations are proportional to the longitudinal tidal amplitude, scaled by 0.5, to perturb only major tidal modes. Perturbed GSWM lower boundary input states include neutral temperature, meridional and zonal winds, and geopotential height. While adding tidal perturbations did not greatly benefit model spread, they did have a positive impact on neutral density and electron density biases, and improve vertical correlation length scales.

One additional perturbation is included to account for internal process uncertainties, specifically the collision factor between O^+ and O, defined as ν_{O^+-O}, and sample from $\hat{\nu}_{O^+-O} \sim \mathcal{N}(1.5, 0.2^2)$. These perturbations account for chemistry and ion-drag uncertainties, and these perturbations were not used in the final reanalysis ensemble.

Table B.5: Ensemble configuration for the Chapter 4 reanalysis

	Truth Run	**Experiment Ensemble**
Model (if applicable)	True atmosphere	TIEGCM
Model Resolution		2.5-deg
Model Altitude Span		~ 97 km to $\sim 500 - 600$ km
Solar Irradiance		Time-series F10.7 index $\hat{d}_{F10.7} \sim \mathcal{N}(d_{F10.7}, 20^2)$
Magnetospheric Forcing		Weimer forcing specified with observed solar wind parameters (solar wind velocity, density, magnetic magnitude)
Lower Boundary		GSWM perturbed tidal amplitude ~ 97 km
Ensemble Size	1	90

Table B.6: Filter configuration for the Chapter 4 reanalysis

Filter Configuration	
Filter	DART EAKF (Manhattan version)
Assimilated Observations	COSMIC-2 RO EDPs
Localization	Horizontal: 0.4-radian radius GC No vertical localization
Update Cycle	1-hour
Observation Altitude Span	$160 - 500$ km at 10 km intervals
Observation Uncertainty	Assigned uncertainties quantified in Yue et al. (2010); Liu et al. (2010); Lee (2013)
Updated State Vector	$[\boldsymbol{f}_{e^-}; \boldsymbol{f}_{O^+}; \boldsymbol{f}_{TN}]$

Table B.7: Ensemble configuration for the Chapter 5 experiment runs

	Truth Run	**Experiment Ensemble**
Model (if applicable)	True atmosphere	TIEGCM
Model Resolution		5-deg
Model Span		~ 97 km to $\sim 400 - 500$ km
Solar Irradiance		F10.7 index
Magnetospheric Forcing		Heelis forcing specified with Ap index
Lower Boundary		GSWM perturbed tidal amplitude ~ 97 km
Ensemble Size	1	100

B.4 Chapter 5 Runs

The experiment period is July 5th - July 10th, 2022 including a geomagnetic storm on July 7th. GRACE-FO neutral densities are assimilated into TIEGCM to estimate forcing parameters. Experiment configurations are listed in Tables B.7 and B.8.

Table B.8: Filter configuration for the Chapter 5 experiment runs

Filter Configuration	
Filter	Particle filter
Assimilated Observations	GRACE-FO neutral densities
Update Cycle	6-hour, 3-hour, 1-hour
Observation Uncertainty	15% error
Updated State Vector	$[\boldsymbol{d}_{F10.7}; \boldsymbol{d}_{Ap}]$

Appendix C

Supplement to Chapter 2

C.1 Supporting Figures for Chapter 2

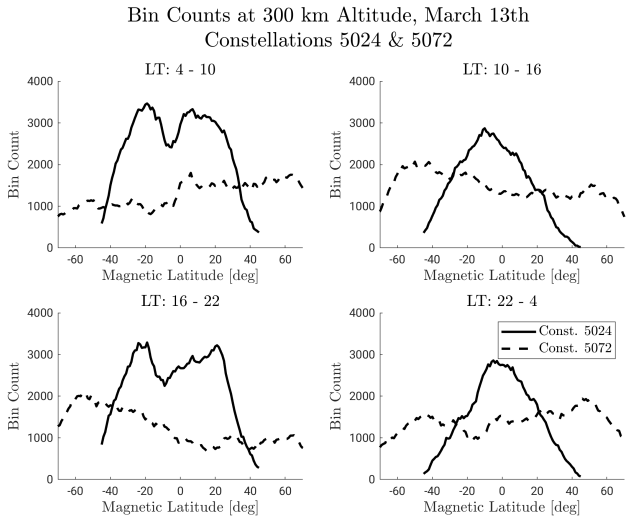

Figure C.1: Same as Figure 2.3 in Chapter 2, shown instead for bin counts used to calculate standard deviation.

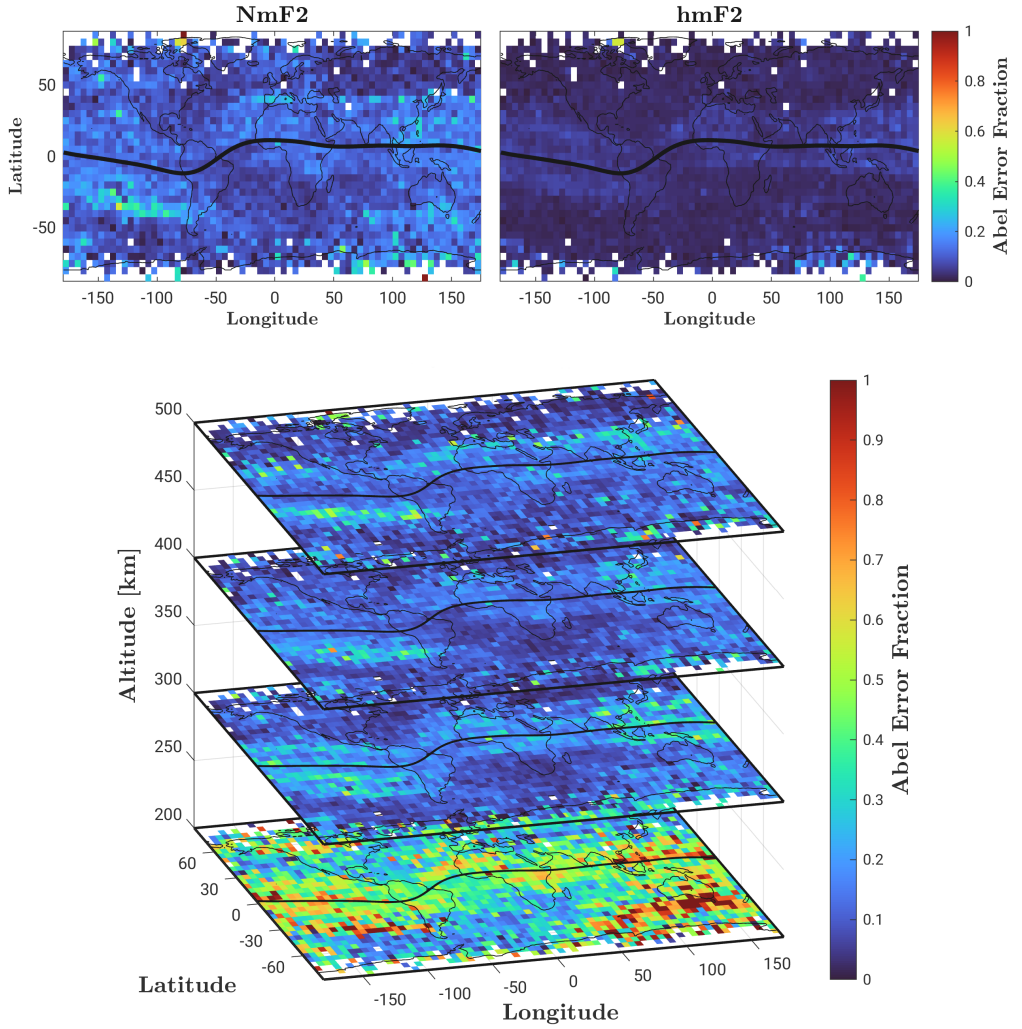

Figure C.2: Binned average fractional error due to Abel Retrieval, across local times 10−16. Shown for NmF2, hmF2 and at each EDP altitude, and black line indicates the magnetic equator. Blank regions are due to lack of observation coverage.

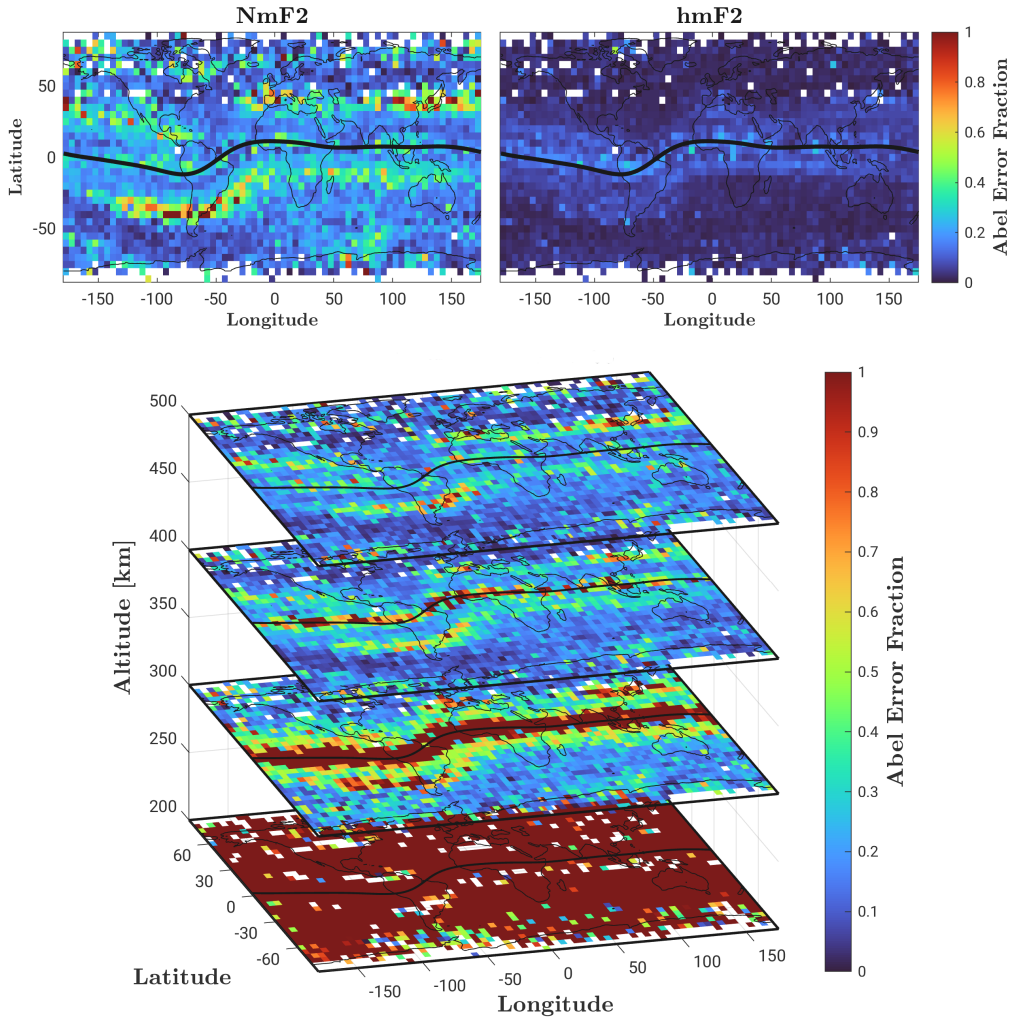

Figure C.3: Same as Figure C.2, shown for local times $16 - 22$

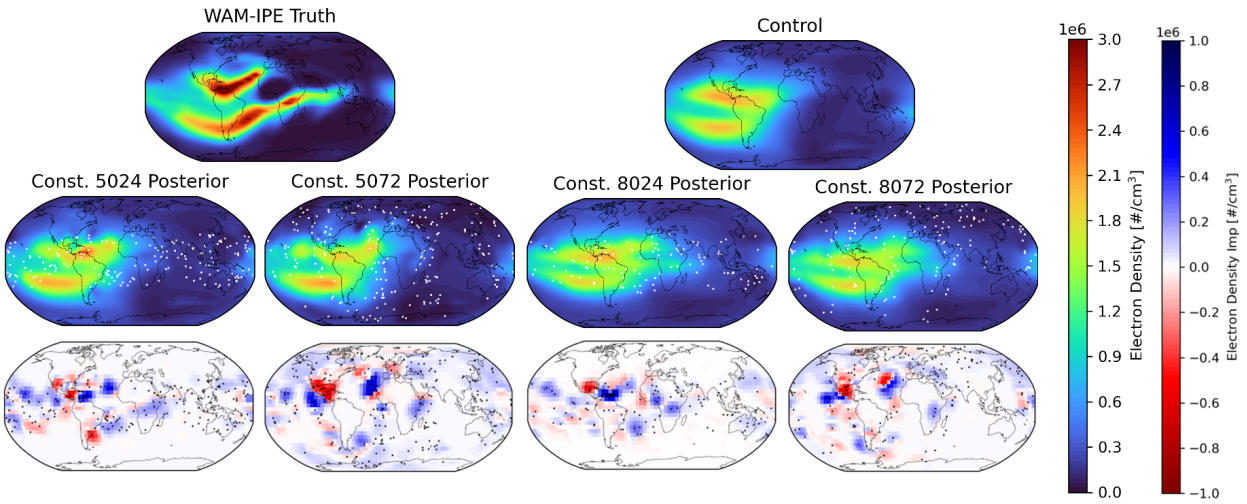

Figure C.4: Electron density shown for the truth, control, and OSSEs 1-4 posteriors at 300 km altitude at UT 20 on March 17th, during the storm period. The middle row shows posterior states, where white points are the assimilated tangent-point observations at 300 km altitude. Bias improvement, shown on bottom row, is illustrated with blue regions providing improvement and red regions worsening.

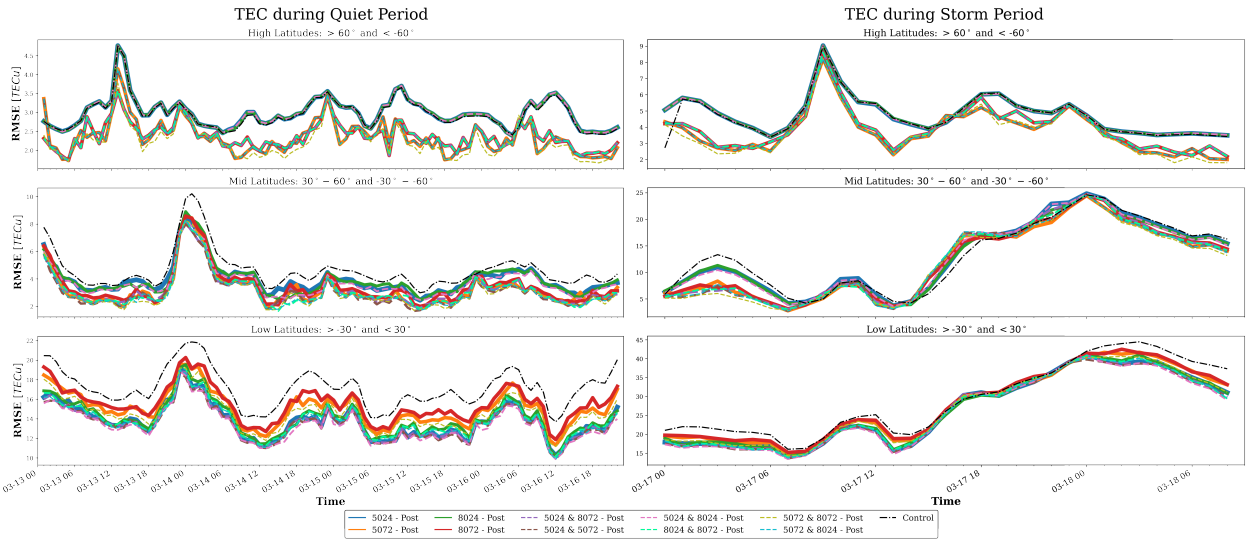

Figure C.5: The TEC RMSE for each OSSE throughout the quiet period (left) and storm period (right). Solid lines indicate single constellation OSSEs and dashed lines indicate two constellation OSSEs. Performance is assessed compared to a no-assimilation control in the dashed black curve.

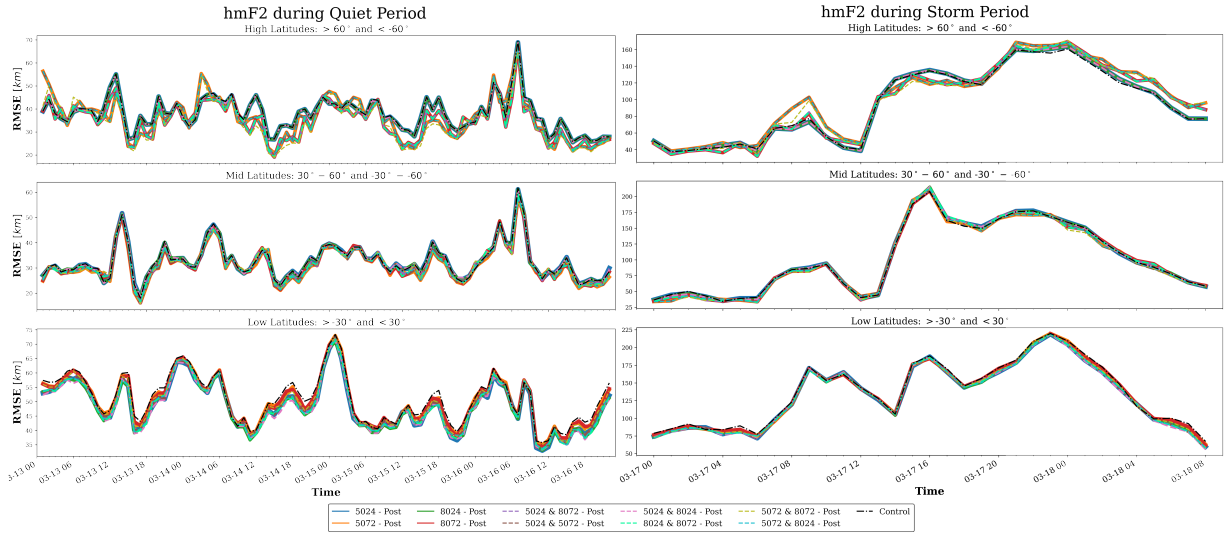

Figure C.6: The h_mF_2 RMSE for each OSSE, same as Figure C.5.

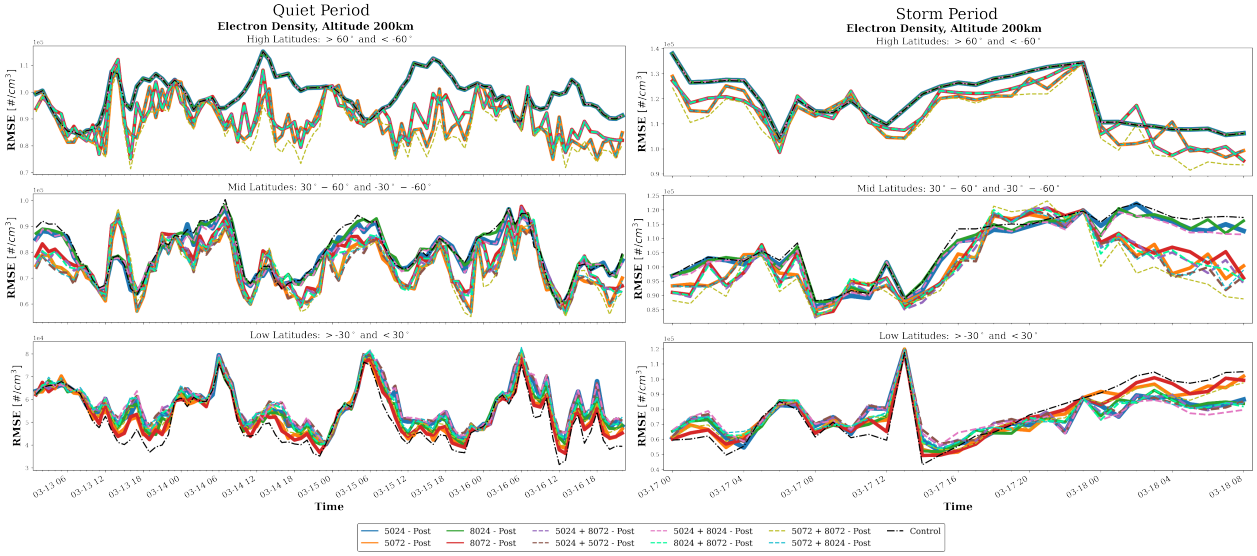

Figure C.7: The 200 km electron density altitude RMSE for each OSSE, same as Figure C.5.

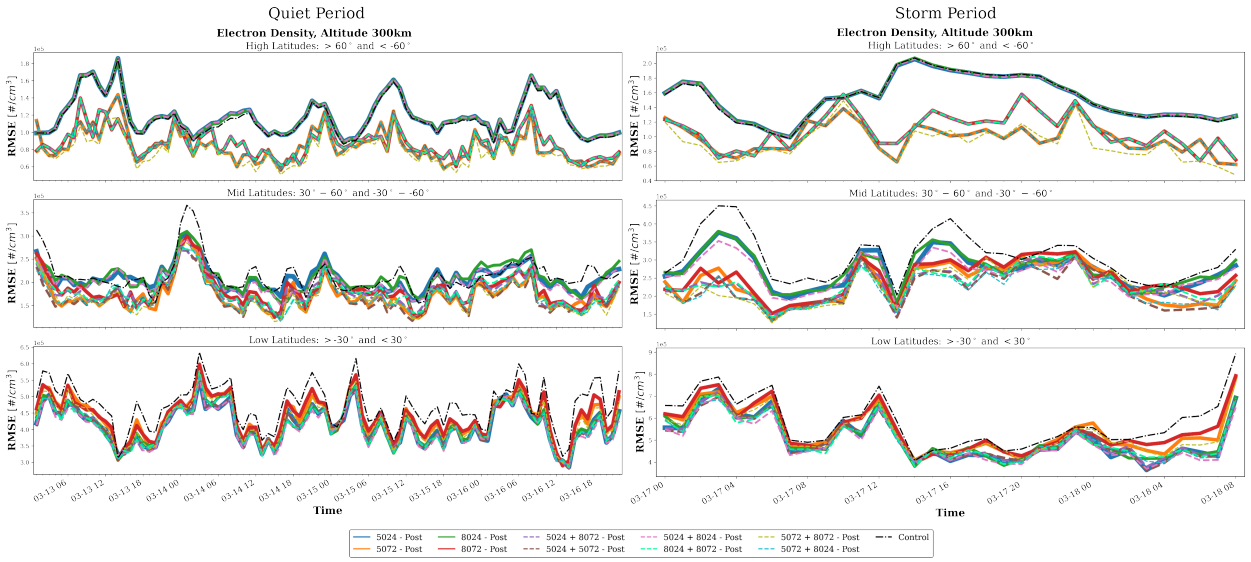

Figure C.8: The 300 km electron density altitude RMSE for each OSSE, same as Figure C.5.

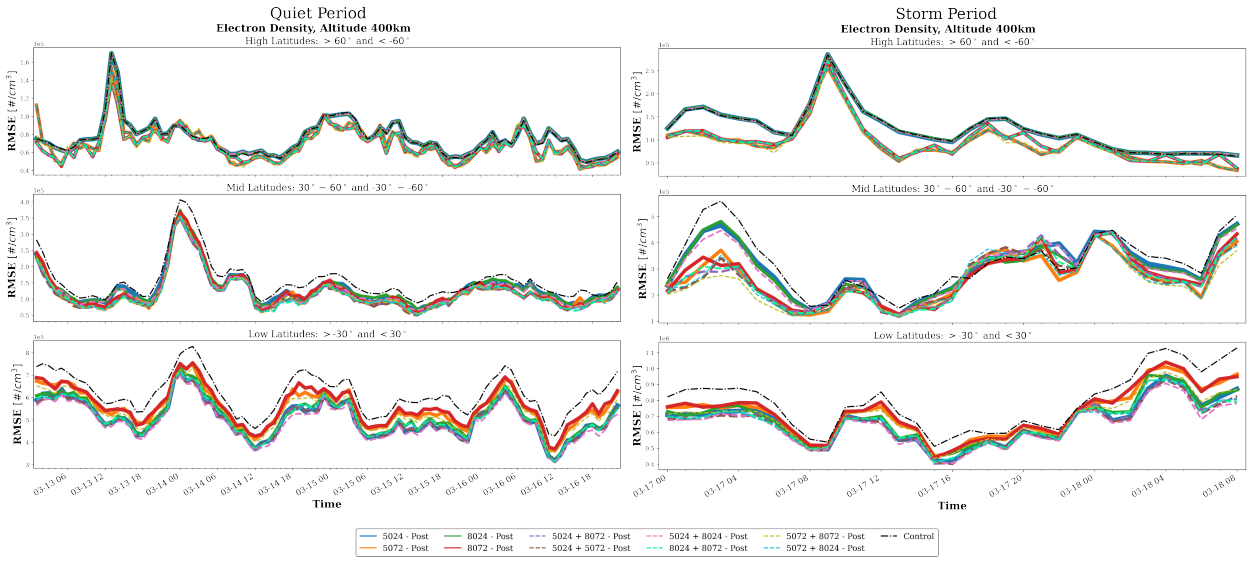

Figure C.9: The 400 km electron density altitude RMSE for each OSSE, same as Figure C.5.

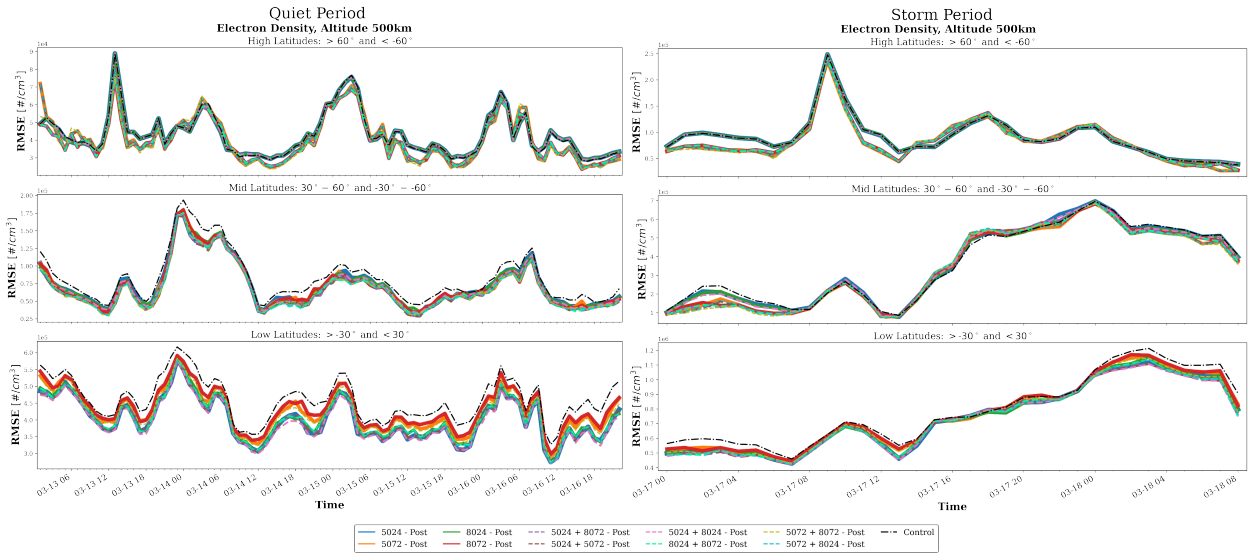

Figure C.10: The 500 km electron density altitude RMSE for each OSSE, same as Figure C.5.

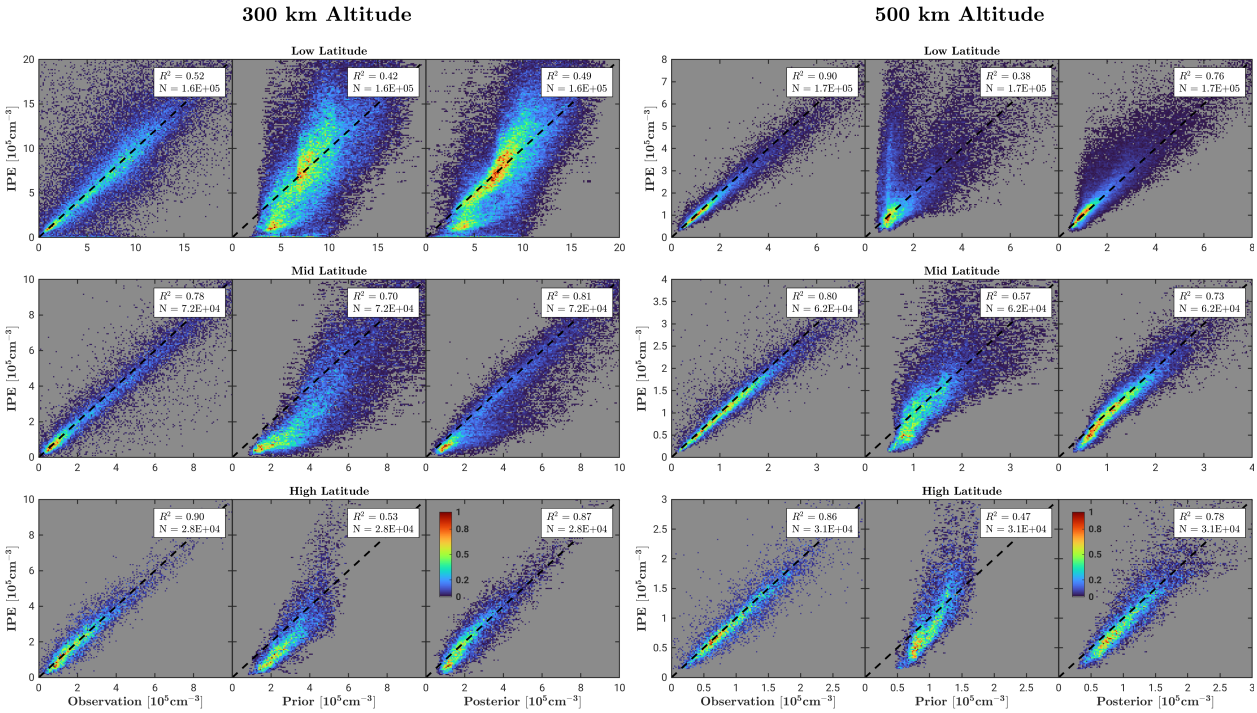

Figure C.11: Comparison of electron density observations at given altitudes (300 and 500 km), with the true IPE state shown against the Abel retrieval, TIEGCM prior and TIEGCM posterior states. Density heat maps are shown, with counts normalized by the max bin count for that subplot. Units are all in $10^5 \#/cm^3$.

			Low Lat	Mid Lat	High Lat	Low Lat	Mid Lat	High Lat
Altitude	**Experiment Name**	**Constellations**	**Quiet**			**Storm**		
200 km	**OSSE 1**	**5024**	5.12	7.53	8.36	5	6.67	7.67
300 km			5.24	9	8.49	5.21	7.52	8
400 km			4.71	8.76	8.38	6.27	8.03	8.39
500 km			3.81	8.79	7.57	5.97	7.21	6.58
200 km	**OSSE 2**	**5072**	2.72	3.77	4.28	5.27	5.3	4.58
300 km			8.63	3.34	3.71	8.67	5.48	3.64
400 km			9.18	5.9	5.28	9.73	4.61	4.3
500 km			9.1	6.68	5.48	8.39	4.42	4.73
200 km	**OSSE 3**	**8024**	4.22	8.22	7.72	5.76	7.85	6.7
300 km			5.34	9.4	9.05	5.94	9.15	8.97
400 km			6.32	8.94	8.12	2.97	7.76	7.03
500 km			5.51	8.47	7.48	4.42	7.27	6.09
200 km	**OSSE 4**	**8072**	2.53	6.06	5.32	5.85	6.79	3.85
300 km			9.11	5.87	4.48	7.03	7.61	6.88
400 km			9.82	7.13	4.21	6.61	5.94	5.27
500 km			9.9	6.93	4.77	7.85	6.7	6.18
200 km	**OSSE 5**	**5024 & 8072**	7.29	6	5.20	5.73	4.42	5.39
300 km			4	5.04	5.22	4.79	4.64	4.97
400 km			3.65	3.69	3.98	4.73	5.64	4.64
500 km			4.52	3.65	4.40	5.45	5.97	5.09
200 km	**OSSE 6**	**5024 & 5072**	8.12	3.28	5.00	6	4.09	5
300 km			4.38	3	4.15	4.33	2.85	3.36
400 km			3.13	2.86	5.05	3.88	4.67	4
500 km			3.26	3.51	5.03	4.21	4.94	4.94
200 km	**OSSE 7**	**5024 & 8024**	7.62	7.5	8.20	5.55	6.27	8.58
300 km			2.16	8.12	9.36	2.52	6	8.24
400 km			1	6.83	7.87	2.24	7.24	8.7
500 km			1.02	6.76	7.04	3	6.82	7
200 km	**OSSE 8**	**8024 & 8072**	6.11	5.77	4.77	5.12	5.06	5.27
300 km			4.26	5.57	5.05	4.7	4.97	5.3
400 km			5.01	4.21	3.63	5.61	4.7	5.09
500 km			5.63	3.5	4.32	4.52	4.67	5.18
200 km	**OSSE 9**	**5072 & 8072**	4.28	3.57	2.05	5.39	3.55	2.97
300 km			7.38	2.63	1.50	7.55	3.91	1.82
400 km			8	3.55	3.84	8.18	2.91	3.3
500 km			8	3.54	4.09	7	2.85	4.82
200 km	**OSSE 10**	**5072 & 8024**	7	3.7	4.10	5.61	5	5
300 km			4.2	3.35	3.98	4.27	2.88	3.73
400 km			4.18	3.13	4.64	4.79	3.52	4.27
500 km			4.29	3.18	4.82	4.21	4.15	4.79

Figure C.12: OSSE ranking metric for each electron density altitude. Contains quiet period defined from March 13th UT 01 to March 16th UT 22 and storm period defined from March 17th UT 00 to March 18th UT 08. Values of 1 indicate the best performance and values of 10 indicate the worst performance.

		Low Lat	Mid Lat	High Lat	Low Lat	Mid Lat	High Lat
Experiment Name	**Constellations**	**Quiet**			**Storm**		
OSSE 1	5024	5.32	9.23	8.70	7	7.7	8.12
OSSE 2	5072	9.1	4.26	3.70	9.39	4.67	3.88
OSSE 3	8024	6.68	9.34	9.05	2.12	8.82	9.18
OSSE 4	8072	9.88	6.49	4.46	4.88	5.82	5.33
OSSE 5	5024 & 8072	3.59	5	5.16	5.82	5.73	4.55
OSSE 6	5024 & 5072	2.65	2.73	4.26	4	4.24	4
OSSE 7	5024 & 8024	1.2	7.88	9.15	2.88	7.03	8.21
OSSE 8	8024 & 8072	4.97	5.09	4.87	6.12	4.85	4.88
OSSE 9	5072 & 8072	7.85	2.15	1.61	8.39	2.85	2.73
OSSE 10	5072 & 8024	3.77	2.95	4.04	4.73	3	4

Figure C.13: Same as Figure C.12, shown for N_mF_2.

		Low Lat	Mid Lat	High Lat	Low Lat	Mid Lat	High Lat
Experiment Name	**Constellations**	**Quiet**			**Storm**		
OSSE 1	5024	4.31	7.56	7.66	6	5.64	4.36
OSSE 2	5072	9.15	3.21	6.26	7.82	5.97	6.88
OSSE 3	8024	2.9	7.9	7.15	5.06	6.64	4.88
OSSE 4	8072	8.39	4.86	5.40	6.03	5.97	3.73
OSSE 5	5024 & 8072	5.03	5	4.24	5.52	5.58	5.79
OSSE 6	5024 & 5072	6.37	4.03	5.28	5	5.64	7
OSSE 7	5024 & 8024	2.3	8.16	6.52	3.64	4.94	3.82
OSSE 8	8024 & 8072	3.61	5.51	4.11	4.82	5.09	5.64
OSSE 9	5072 & 8072	8.01	4.24	3.52	6.3	4.27	6.06
OSSE 10	5072 & 8024	4.93	4.13	4.86	4.58	5	7

Figure C.14: Same as Figure C.12, shown for h_mF_2.

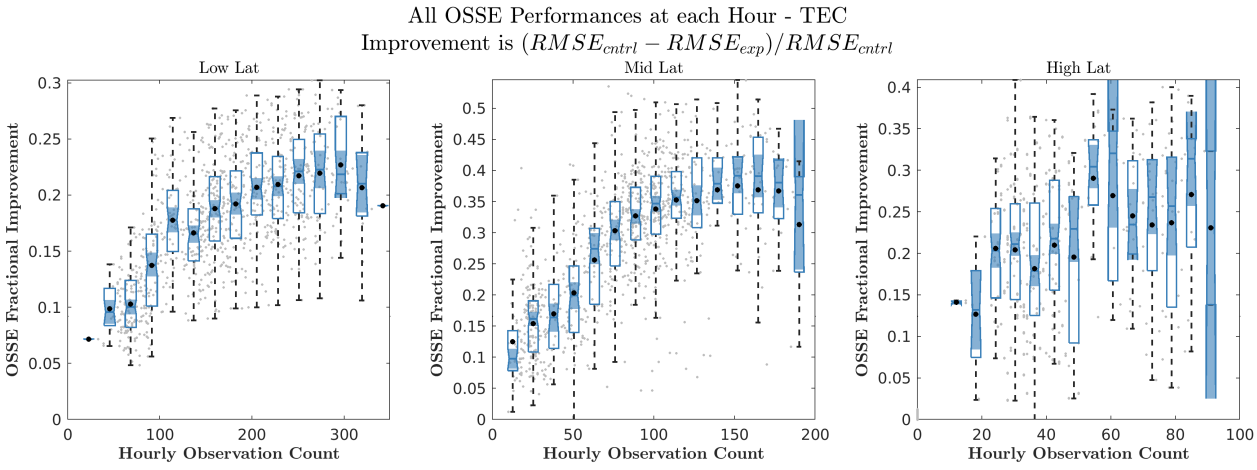

Figure C.15: OSSE TEC RMSE fractional improvement over the control as a function of observation count, defined in Equation 2.1 Calculated for the entire TEC grid RMSE within each latitude band. Gray points are all samples and averaged over count bins to give the mean (black dots) and notched box plots. Shaded regions not overlapping indicate the significant difference between medians (5% confidence).

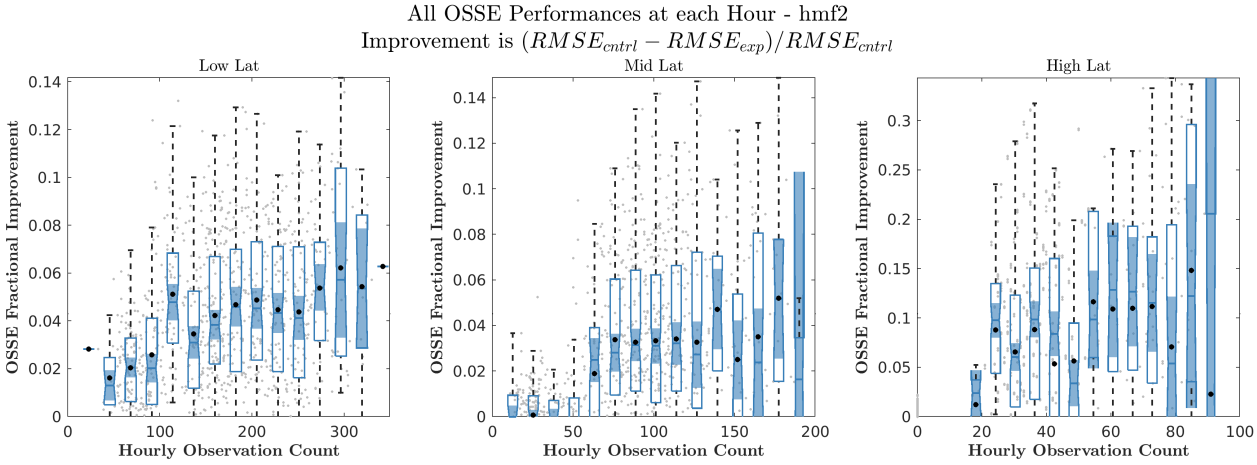

Figure C.16: Same as Figure C.15, shown for h_mF_2.

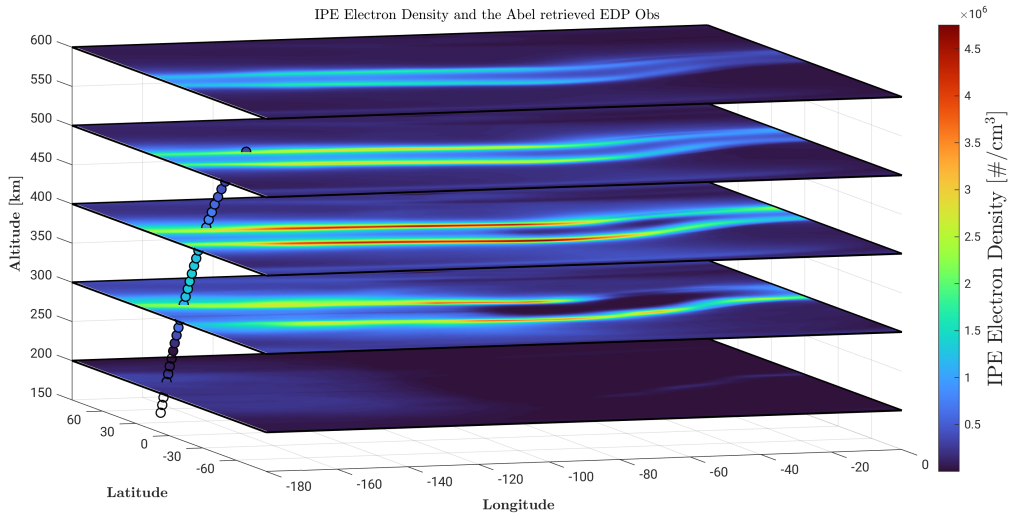

Figure C.17: Highlighted poor EDP observation update, with scatter showing the observation EDP and grids showing IPE electron density at that given altitude. RO EDP tangent points are quasi-vertical, with higher altitude tangent points moving into higher density regions, creating a double-peaked structure.

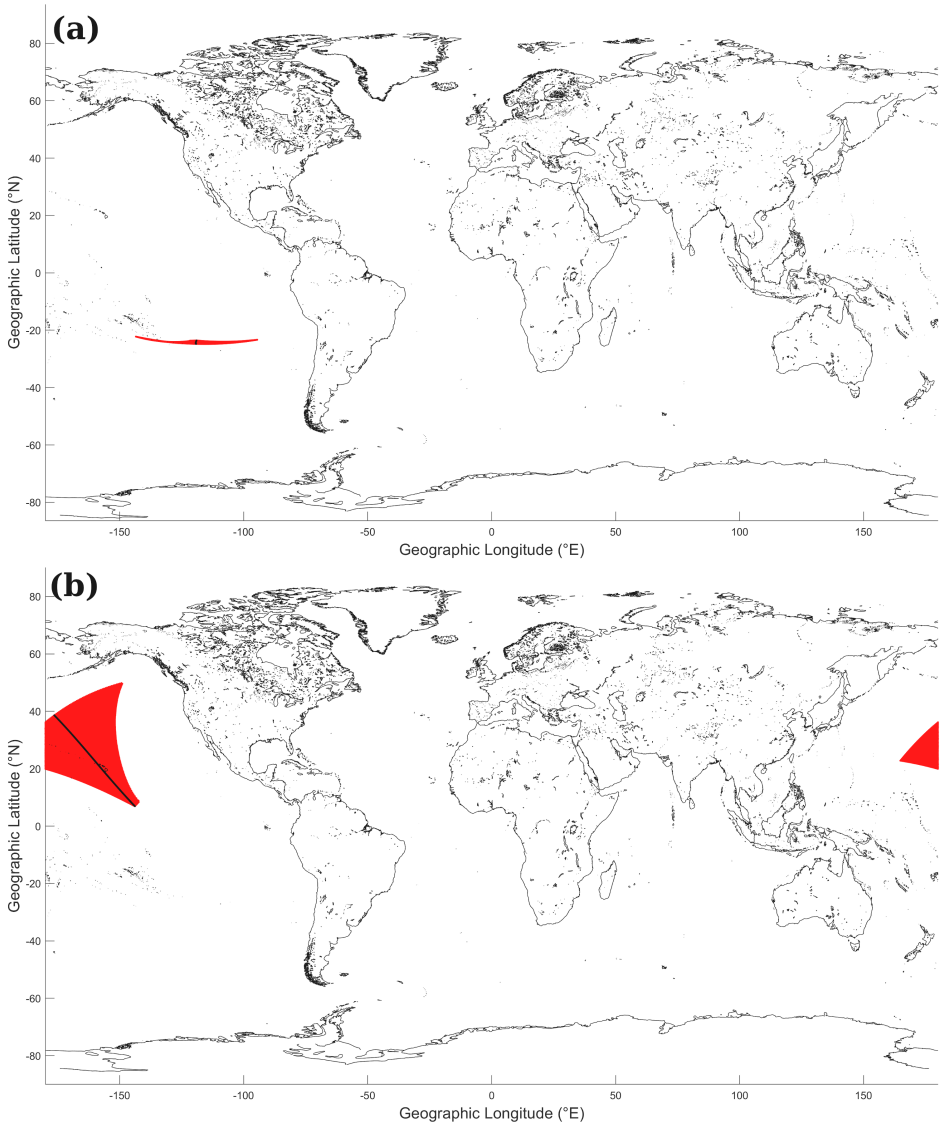

Figure C.18: GNSS ray passes for profiles (a) and (b) highlighted in the Discussion Figure 13. Black points are the RO tangent point locations and red shaded area are the occultation ray paths below the orbit height of the receiving RO satellite.

Appendix D

Supplement to Chapter 4

This appendix includes supporting figures and information for the Chapter 4 storm-time reanalysis.

D.1 Further Experiment Testing Diagnostics

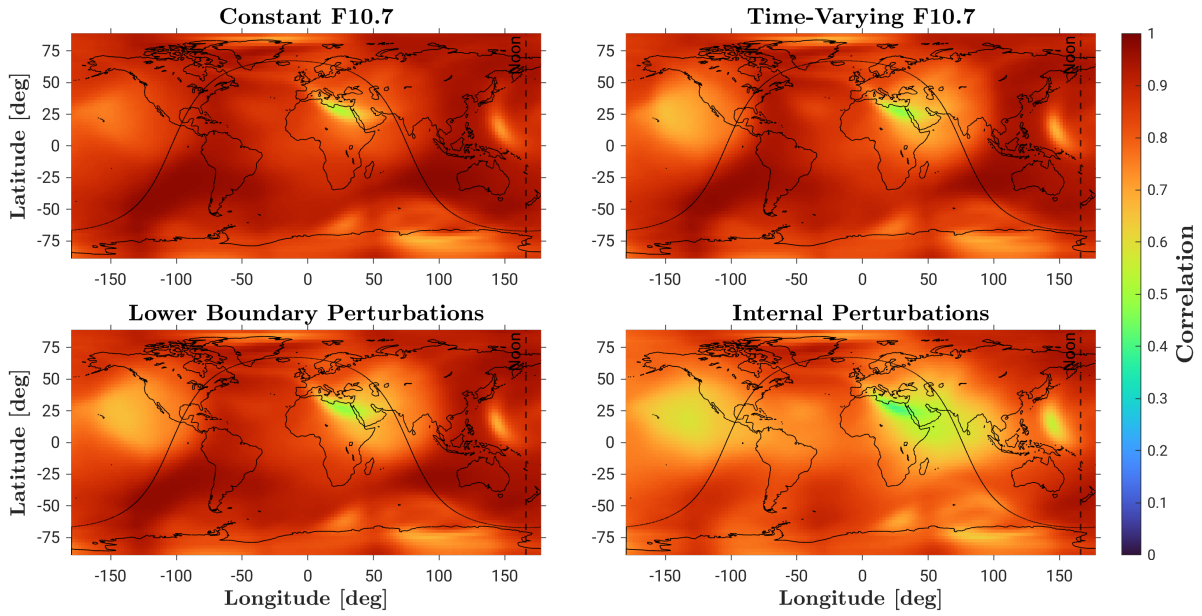

Figure D.1: Locally averaged quiet period (UT01 on July 5th) correlations shown from electron density to neutral temperature. Each point shows the average correlation within a distance of 40°. Shown for a pressure surface about ∼400 km altitude.

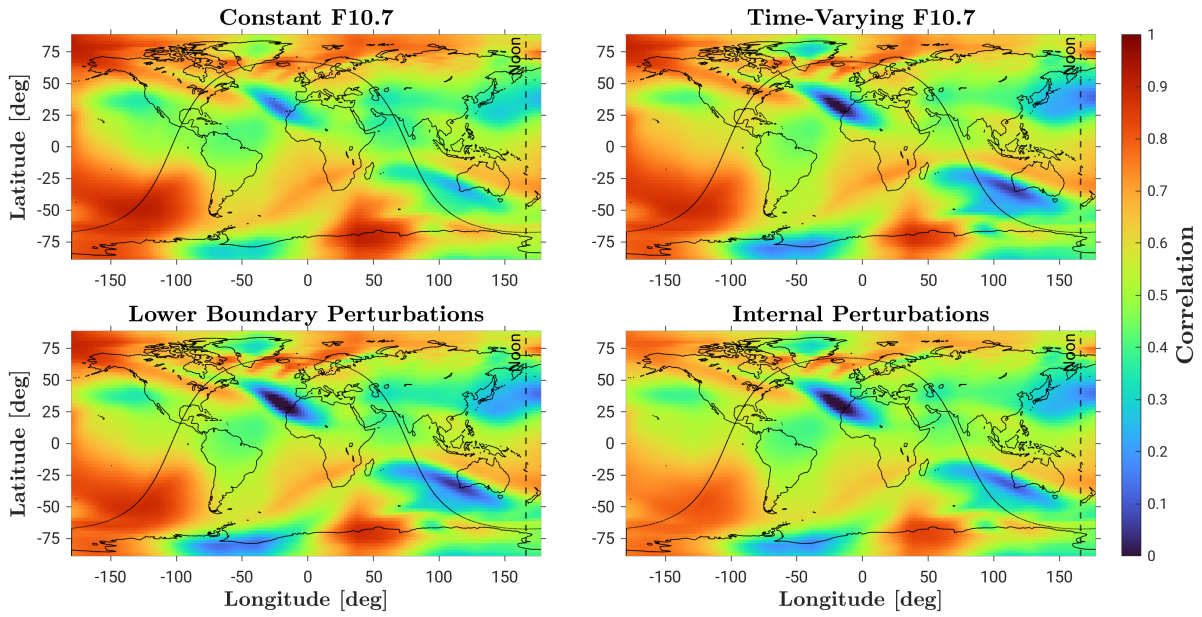

Figure D.2: Locally averaged storm period (UT01 on July 8th) correlations shown from electron density to neutral temperature. Each point shows the average correlation within a distance of 40°. Shown for a pressure surface about ∼430 km altitude.

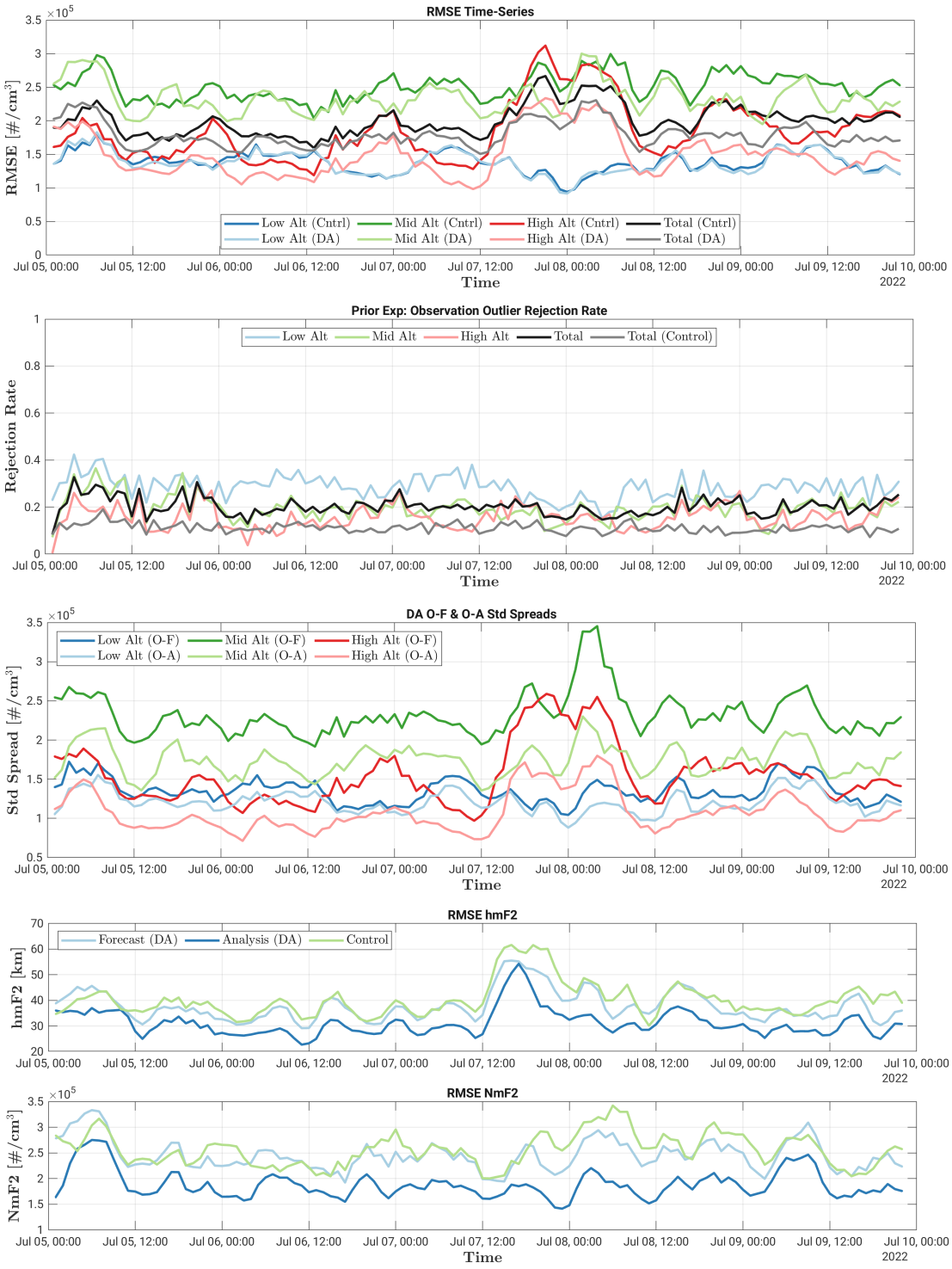

Figure D.3: Forecast COSMIC-2 EDP verification diagnostics shown for the control ($\text{Cntrl}_{*-\nu}$) and reanalysis ($\text{Exp}_{*-\nu}$). Includes the time series of RMSEs, outlier rejection rate, observation-forecast (O-F) and observation-analysis (O-A) standard deviation (std) spreads, RMSE of EDP parameters h_mF_2 and N_mF_2, and normalized standard deviation spread.

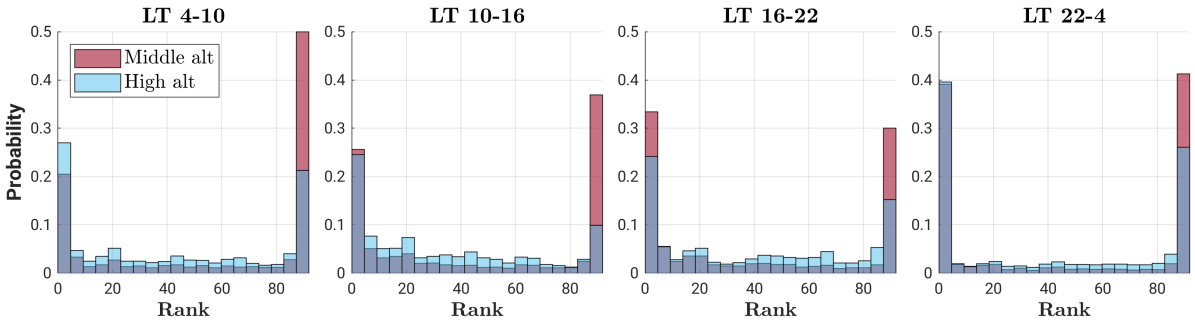

Figure D.4: Rank histogram of control run Cntrl$_*$ for the quiet period, separated by local time and altitude.

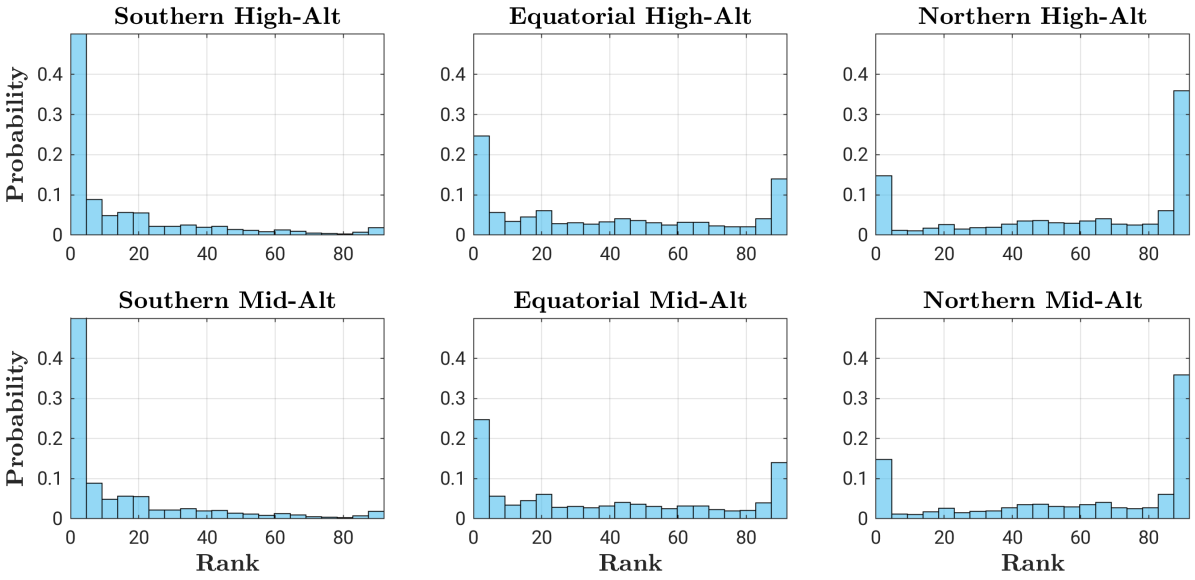

Figure D.5: Rank histogram of control run Cntrl$_*$ for the quiet period, separated by altitude and latitude.

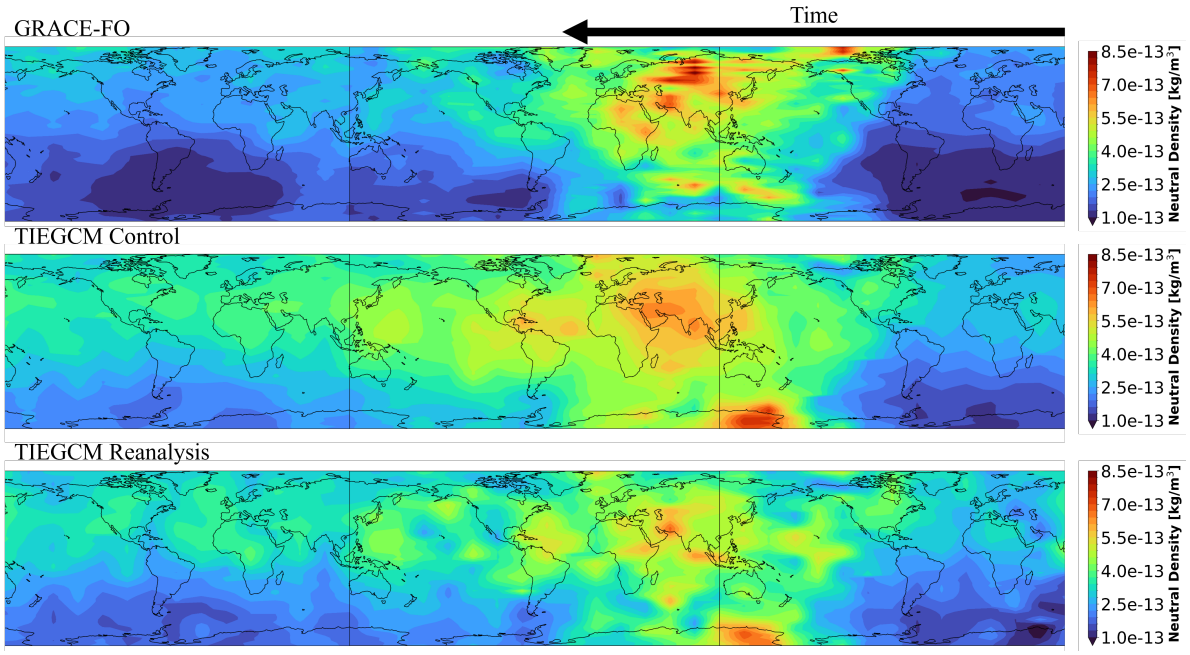

Figure D.6: Keogram of the dawn-side GRACE-FO neutral densities, Cntrl$_*$, and forecast Exp$_{*-Storm}$ states. Plotted with latitude slices with time moving to the left.

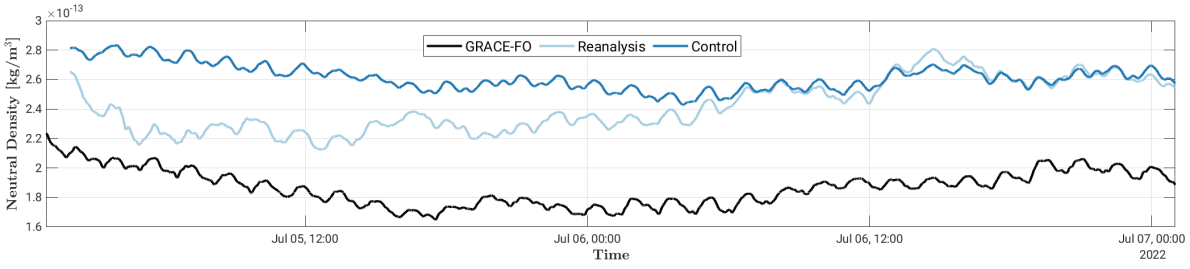

Figure D.7: GRACE-FO, control and reanalysis neutral density comparison for the quiet period, with the reanalysis beginning at UT01 on July 5th. Smoothed ±45 minutes.

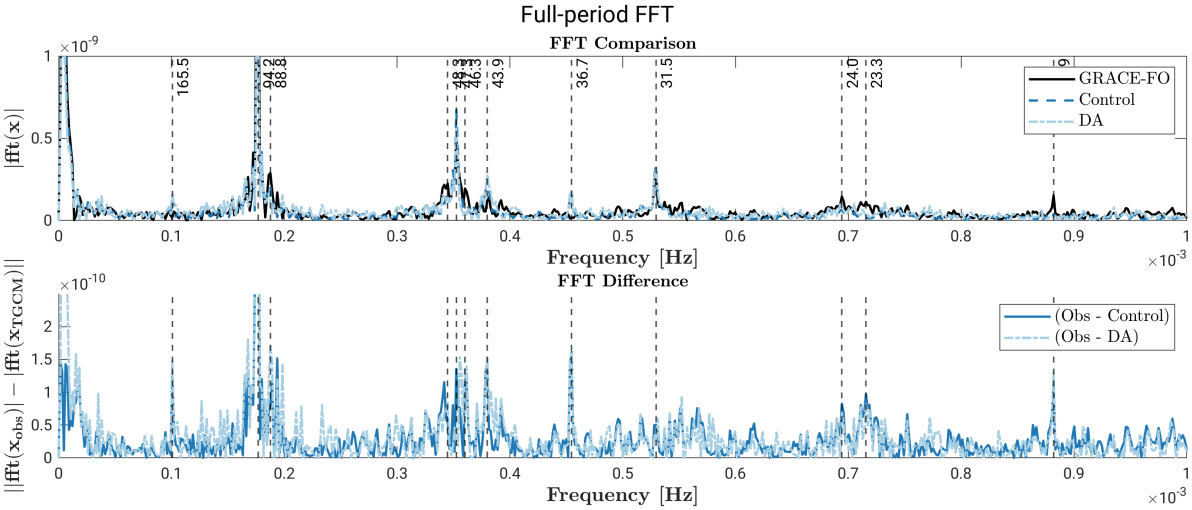

Figure D.8: Fast Fourier Transform (FFT) GRACE-FO, TIEGCM control (Cntrl_*), and TIEGCM reanalysis (Exp_*) for the full experiment period. Shown for the absolute value of frequency magnitudes. Vertical lines denote selected frequency peaks, with their corresponding period (in hours). The bottom plot shows the difference between the GRACE-FO FFT to the control and reanalysis FFTs.

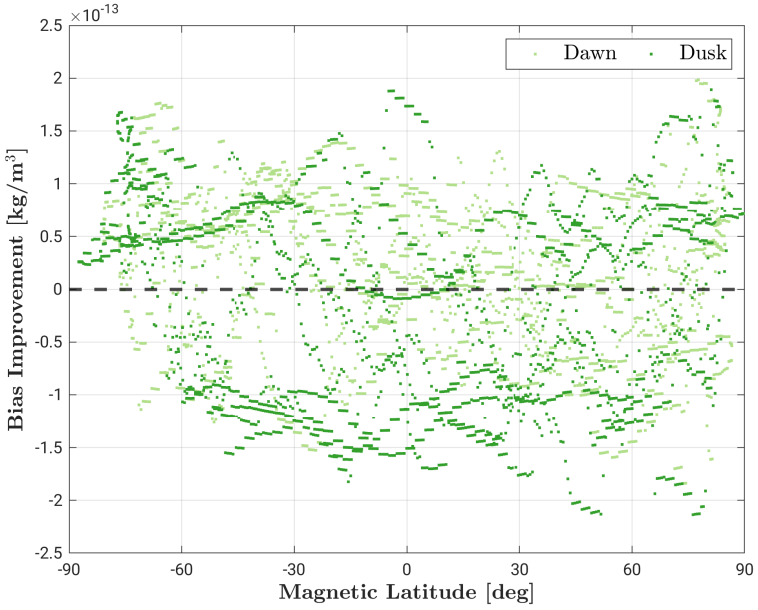

Figure D.9: GRACE-FO bias improvement metric defined in Equation 4.2, using the control (Cntrl_*) and reanalysis ($\text{Exp}_{*-Storm}$). Shown for magnetic latitude and separated by dawn and dusk LT sides.

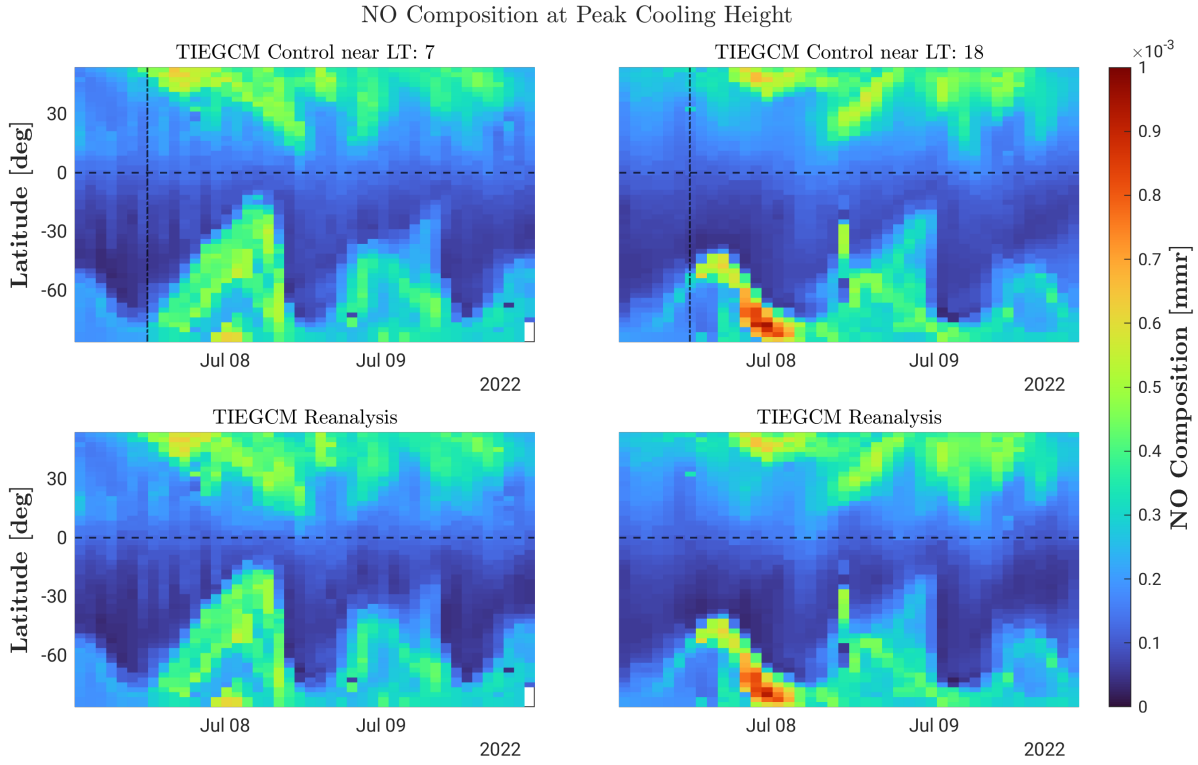

Figure D.10: TIEGCM control and reanalysis NO composition (in mixing ratio) at NO peak cooling altitudes, shown at TIMED-SABER observation locations.

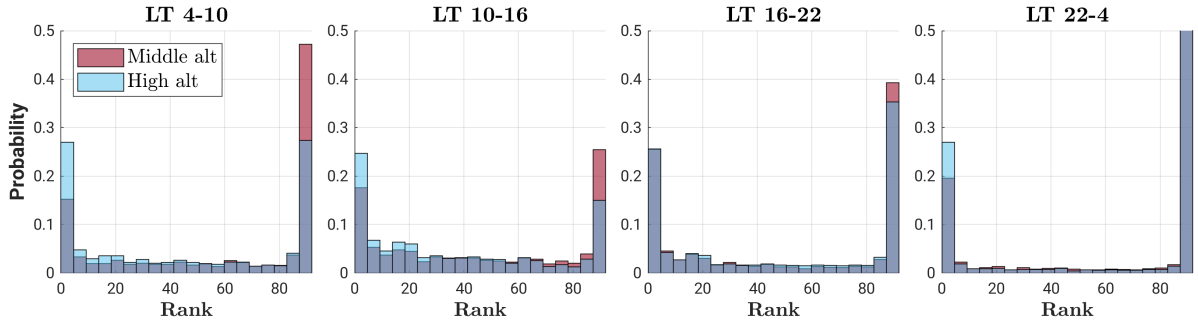

Figure D.11: Rank histogram of an inflation run for the quiet period, separated by local time and altitude. Includes EDP assimilation.

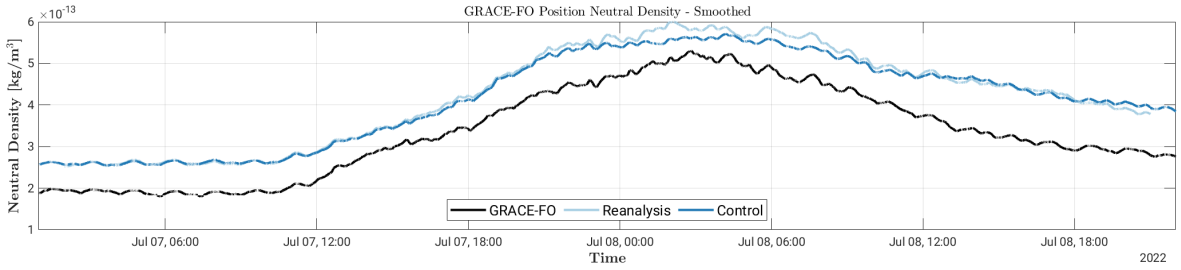

Figure D.12: GRACE-FO, control and experiment neutral density comparison for the storm period, using adaptive inflation to inflate plasma and neutral temperature states. Smoothed ±45 minutes.

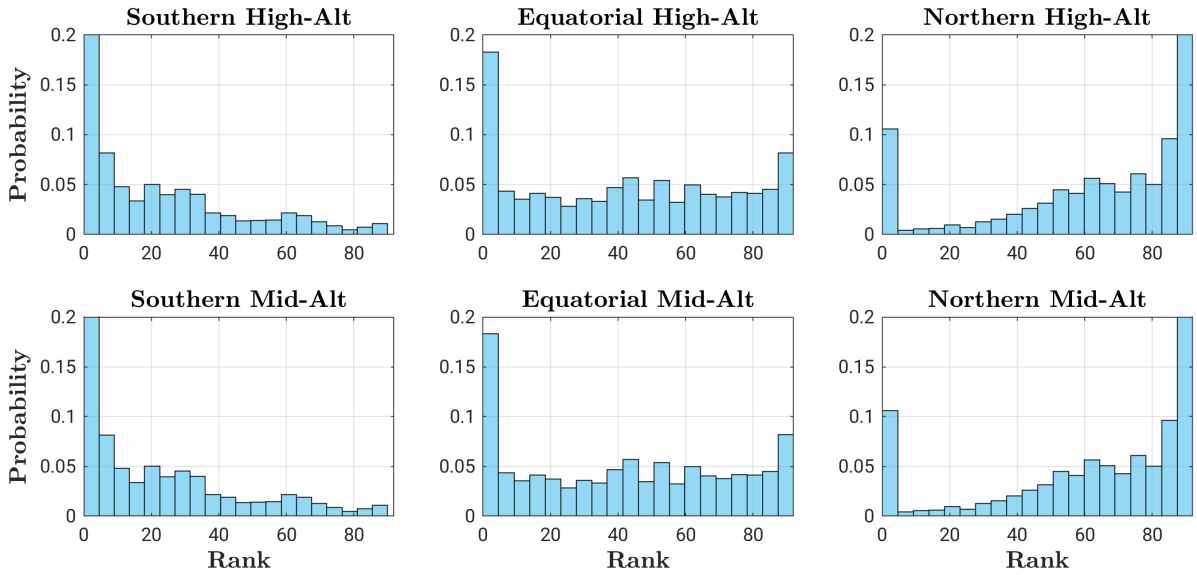

Figure D.13: Rank histogram following adding direct state perturbations to atomic oxygen and neutral density. Control TIEGCM run. Separated by latitude and altitude. Shown for the quiet period from UT01-UT04 on July 5th.

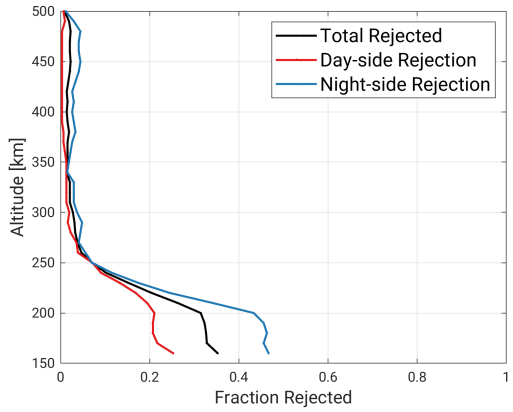

Figure D.14: COSMIC-2 rejection rate profile following adding direct state perturbations to atomic oxygen and neutral density. Shown for a control TIEGCM run and is separated by day and night local times. Shown for the quiet period from UT01-UT04 on July 5th.

D.2 Altitude Data Assimilation Impact

An interesting reanalysis result of Chapter 4 is the forecast coupling impact that different altitudes have on temperature specification. Figures D.15 and D.16 show the altitude profile of neutral density impact between the forecast and control, plotted for pressure levels along the GRACE-FO orbit track locations. For the magnitude of updates, there are as expected larger temperature differences for the middle and high-altitude regions. However, when temperature differences are normalized, relatively consistent neutral temperature impact is seen throughout the whole vertical atmosphere that begins to reduce below an altitude of $\sim$150 km. This suggests the reanalysis sees impacts across altitude regions, and raises questions as to what vertical coupling impacts are controlling neutral density estimation. The reanalysis impact could come either from high altitude temperatures thermally conducting down to lower altitudes, or from low altitudes neutral temperatures where there is greater density vertically influencing high altitudes through coupling. As an additional complication, the filter does not include vertical localization instead relying on the vertical background covariance, and as such analysis updates can reach across altitudes regions. Neutral temperature increments in the analysis step are shown in Figure D.17. It is unclear the vertical impact of this estimation, and investigating the altitude dependence of the relative forecast memory is an important question that warrants future investigation.

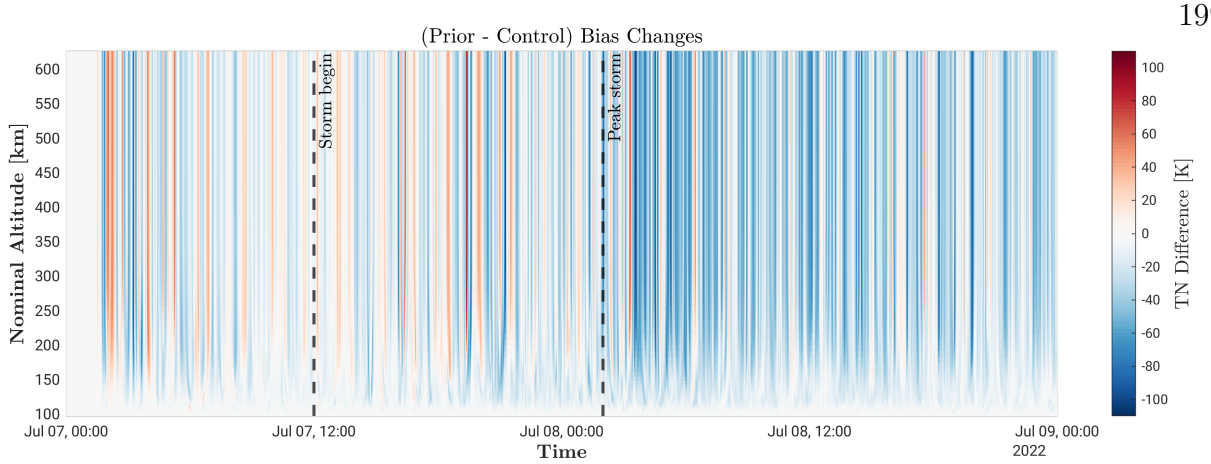

Figure D.15: Neutral temperature data assimilation difference between the prior (forecast), ($\text{Exp}_{*-Storm}$), and control, (Cntrl_{*}). Shown for neutral temperature magnitude for vertical pressure levels along GRACE-FO track locations.

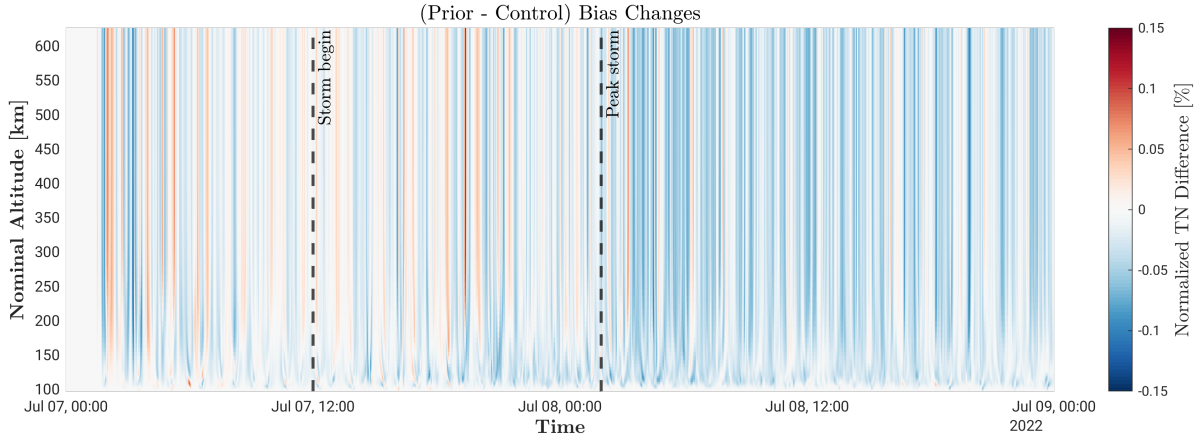

Figure D.16: Same as Figure D.15, normalized by the mean neutral temperature.

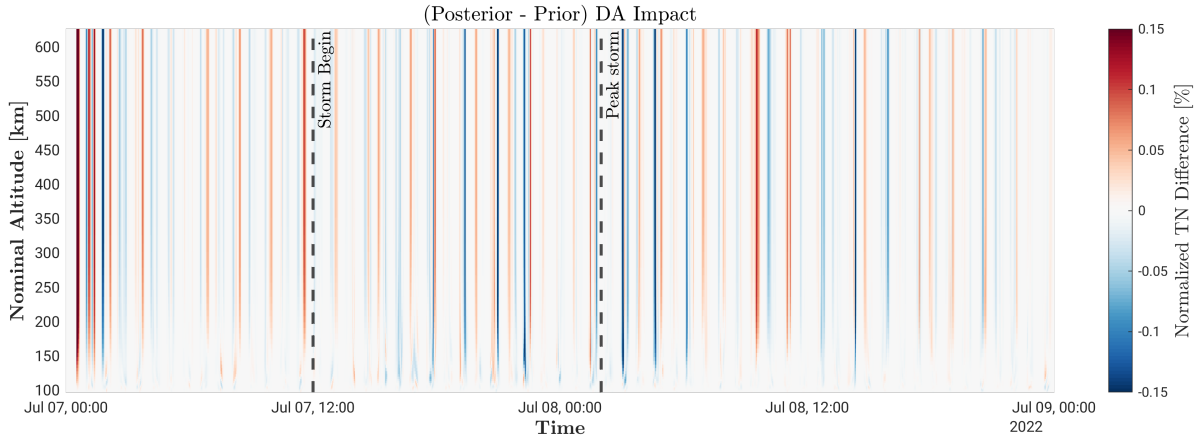

Figure D.17: Same as Figure D.15, shown for posterior (analysis) and prior (forecast) difference, showing the analysis step impact